



NAVAL POSTGRADUATE SCHOOL

MONTEREY, CALIFORNIA

DISSERTATION

**MODELING INTERACTION OF A TROPICAL CYCLONE
WITH ITS COLD WAKE**

by

Sue Chen

September 2014

Dissertation Supervisors:

Patrick A. Harr
Russell L. Elsberry

Approved for public release; distribution is unlimited

THIS PAGE INTENTIONALLY LEFT BLANK

REPORT DOCUMENTATION PAGE			<i>Form Approved OMB No. 0704-0188</i>	
Public reporting burden for this collection of information is estimated to average 1 hour per response, including the time for reviewing instruction, searching existing data sources, gathering and maintaining the data needed, and completing and reviewing the collection of information. Send comments regarding this burden estimate or any other aspect of this collection of information, including suggestions for reducing this burden, to Washington headquarters Services, Directorate for Information Operations and Reports, 1215 Jefferson Davis Highway, Suite 1204, Arlington, VA 22202-4302, and to the Office of Management and Budget, Paperwork Reduction Project (0704-0188) Washington DC 20503.				
1. AGENCY USE ONLY (Leave blank)		2. REPORT DATE September 2014	3. REPORT TYPE AND DATES COVERED Dissertation	
4. TITLE AND SUBTITLE MODELING INTERACTION OF A TROPICAL CYCLONE WITH ITS COLD WAKE			5. FUNDING NUMBERS N/A	
6. AUTHOR(S) Sue Chen			8. PERFORMING ORGANIZATION REPORT NUMBER N/A	
7. PERFORMING ORGANIZATION NAME(S) AND ADDRESS(ES) Naval Postgraduate School Monterey, CA 93943-5000			10. SPONSORING/MONITORING AGENCY REPORT NUMBER N/A	
9. SPONSORING /MONITORING AGENCY NAME(S) AND ADDRESS(ES) N/A			11. SUPPLEMENTARY NOTES The views expressed in this dissertation are those of the author and do not reflect the official policy or position of the Department of Defense or the U.S. Government. IRB Protocol number ____N/A____.	
12a. DISTRIBUTION / AVAILABILITY STATEMENT Approved for public release; distribution is unlimited			12b. DISTRIBUTION CODE	
13. ABSTRACT (maximum 200 words) This dissertation examines the tropical cyclone (TC) intensity response to its cold wake first with five idealized cold wakes using an uncoupled version of the Coupled Ocean/Atmosphere Mesoscale Modeling System for Tropical Cyclone (COAMPS-TC) and then with simulated cold wakes from the coupled version. These simulations reveal a new dynamical pathway induced by the ocean cold wake that acts in concert with the conventional thermodynamic pathway to modulate the TC structure and intensity change. Wakes with a long trailing part or an irregular shape below the eyewall region force a dynamic response that tends to offset the negative feedback effect of reduced enthalpy flux. In particular, a low-level jet-like feature referred to as the "wake jet" is found at the top of the atmospheric boundary layer above the trailing cold wake. Significant wake cooling underneath the eye also tends to damp the vorticity gradient in the eyewall region, which forces the eyewall to transition from an unstable ring vortex to a stable Rankine-like vortex.				
14. SUBJECT TERMS Modeling, Tropical cyclone prediction, Battle Space Environment.			15. NUMBER OF PAGES 269	
			16. PRICE CODE	
17. SECURITY CLASSIFICATION OF REPORT Unclassified	18. SECURITY CLASSIFICATION OF THIS PAGE Unclassified	19. SECURITY CLASSIFICATION OF ABSTRACT Unclassified	20. LIMITATION OF ABSTRACT UU	

THIS PAGE INTENTIONALLY LEFT BLANK

Approved for public release; distribution is unlimited

**MODELING INTERACTION OF A TROPICAL CYCLONE WITH ITS COLD
WAKE**

Sue Chen
Civilian, U.S. Naval Research Laboratory
B.S., Central Taiwan University, 1983
M.S., Colorado State University, 1986

Submitted in partial fulfillment of the
requirements for the degree of

DOCTOR OF PHILOSOPHY IN METEOROLOGY

from the

**NAVAL POSTGRADUATE SCHOOL
September 2014**

Author: Sue Chen

Approved by:	Patrick A. Harr Professor of Meteorology Dissertation Committee Chair	Russell L. Elsberry Professor of Meteorology Dissertation Supervisor
	Rebecca Stone Professor of Meteorology	Frank Giraldo Professor of Mathematics
	Melinda Peng Naval Research Laboratory	Peter Black Naval Research Laboratory

Approved by: Wendell Nuss, Chair, Department of Meteorology

Approved by: Douglas Moses, Vice Provost for Academic Affairs

THIS PAGE INTENTIONALLY LEFT BLANK

ABSTRACT

This dissertation examines the tropical cyclone (TC) intensity response to its cold wake first with five idealized cold wakes using an uncoupled version of the Coupled Ocean/Atmosphere Mesoscale Modeling System for Tropical Cyclones (COAMPS-TC) and then with simulated cold wakes from the coupled version. These simulations reveal a new dynamical pathway induced by the ocean cold wake that acts in concert with the conventional thermodynamic pathway to modulate the TC structure and intensity change.

Wakes with a long trailing part or an irregular shape below the eyewall region force a dynamic response that tends to offset the negative feedback effect of reduced enthalpy flux. In particular, a low-level jet-like feature referred to as the “wake jet” is found at the top of the atmospheric boundary layer above the trailing cold wake. Significant wake cooling underneath the eye also tends to damp the vorticity gradient in the eyewall region, which forces the eyewall to transition from an unstable ring vortex to a stable Rankine-like vortex.

THIS PAGE INTENTIONALLY LEFT BLANK

TABLE OF CONTENTS

I.	INTRODUCTION.....	1
II.	REVIEW ON THE INTERACTION OF A TC WITH ITS COLD WAKE.....	5
A.	FORMATION OF THE COLD WAKE.....	5
B.	LOCATION AND AMPLITUDE OF THE COLD WAKE	9
C.	EFFECTS OF PRE-EXISTING OCEAN EDDIES.....	16
D.	PRECIPITATION EFFECT ON THE OCEAN MIXING.....	17
E.	SURFACE WAVE EFFECTS ON THE UPPER-OCEAN MIXING.....	18
F.	AIR-SEA INTERACTION	21
G.	PRECONDITION OF THE PRE-STORM OCEAN ENVIRONMENT..	26
H.	OCEAN COLD WAKE IMPACT ON THE TC KINEMATIC FLOW ..	27
I.	OBJECTIVES OF THIS STUDY	28
III.	COAMPS-TC MODEL DESCRIPTION AND EXPERIMENT SET-UP	31
A.	MODEL PHYSICS	31
B.	TRAJECTORY AND 3D MOMENTUM BUDGET ANALYSIS.....	35
C.	AXISYMMETRIC IDEALIZED TC CONFIGURATION	36
D.	EXPERIMENT DESIGN	41
1.	Uncoupled and One-Way Coupled Experiments	41
2.	Air-Ocean Coupled Experiments	43
IV.	UNCOUPLED CONTROL SIMULATION.....	45
A.	CONTROL DYNAMIC STRUCTURE.....	52
B.	CONTROL THERMODYNAMIC STRUCTURE.....	75
V.	ONE-WAY COUPLED COLD WAKE EXPERIMENTS.....	83
A.	COLD WAKE EXPERIMENTS.....	83
B.	ASYMMETRIC RESPONSE FROM WAKE COOLING	109
C.	ORIGIN OF WAKE JET	166
D.	ANALYSIS OF MOMENTUM BUDGET	174
1.	A Thought Experiment.....	174
2.	COAMPS Wake 3 Momentum Budget Analysis	177
3.	Analysis of Surface Fluxes.....	187
VI.	TWO-WAY AIR-OCEAN COUPLED SIMULATIONS.....	193
A.	COMPARISON OF COUPLED AND UNCOUPLED SIMULATIONS	193
B.	TRAJECTORY AND MOMENTUM BUDGET ANALYSES OF EXPB EXPERIMENT	207
C.	ANALYSIS ON THE POTENTIAL TEMPERATURE SURFACE	214
D.	ANALYSIS OF THE SURFACE FLUXES.....	217
VII.	SUMMARY AND DISCUSSION	221
A.	HYPOTHESIS I.....	222
B.	HYPOTHESIS II	225
C.	HYPOTHESIS III.....	228

LIST OF REFERENCES	233
INITIAL DISTRIBUTION LIST	243

LIST OF FIGURES

Figure 1.	(a) TC image, and (b) a schematic depiction of the physical processes forced by hurricane winds such as shear-induced mixing and OML deepening, upwelling due to transport away from the center, and surface heat fluxes from the ocean to atmosphere, all of which may contribute to ocean cooling during TC passage (from Chan and Kepert 2010).....	7
Figure 2.	Average ocean mixed-layer temperature change rate ($^{\circ}\text{C}/\text{h}$, contour interval is $0.02^{\circ}\text{C}/\text{h}$) at 42 h predicted by the two-way coupled model of Chen et al. (2010). The total temperature change is the sum of the vertical mixing (VMIX), vertical advection (VADV), and horizontal advection (HADV) plus some smaller terms (from Chen et al. 2010).....	8
Figure 3.	Rightward displacements and magnitudes of the SST decrease for hurricane translation speeds at $U_h = 4$ and 16 ms^{-1} from the Price (1981) model simulation. Line definitions for the SST responses for the complete (solid) pressure field and two sensitivity tests with no TC pressure effects are indicated in the inset.	11
Figure 4.	Plain views of the ocean response to Hurricane Frances in a storm-centered coordinate system: (top) SST ($^{\circ}\text{C}$) , (middle) change of depth (m) of the 24°C isotherm, and (bottom) change of the ocean heat content relative to the 26°C isotherm. Arrows show mixed layer velocity from the EM-APEX floats. The storm moves to the left along the horizontal axis (from D’Asaro et al. 2007).....	15
Figure 5.	Simulated ocean mixed layer cooling in (top) warm-core eddy WEC1 and (bottom) CCE2 cold-core eddy with two turbulent mixing closure schemes (from Jaimes and Shay 2011). Vertical velocity (m s^{-1} , scale on the right margin) has a dipole structure. Color is the OML cooling, vectors are OML geostrophic currents, the black line is the storm track and, and black dots are model moorings in the cross-track direction.	17
Figure 6.	Schematic illustration of Langmuir circulation (from http://jerry.ucsd.edu/JSmith_PDF/2001-Smith-aStoryOfMixing.pdf).	19
Figure 7.	Normalized two-point spatial correlation $R_{ww}(x', y', z_{max})$ along the track $X = 60 \text{ km}$ from the idealized LES simulation by Sullivan et al. (2012). The solid (dotted) contour levels are 0.1 (-0.05). The positive contour level encloses a region of strong downwelling while the negative contour level encloses a broad region of weaker upwelling. The vectors (arrows) show the magnitude and direction of the horizontal perturbation velocities (u' , v') induced by a Langmuir cell. (a) – (f) $t - t_m = (-30.2, -12.5, -3.04, -0.003, 3.37, 12.8) \text{ h}$ respectively. Note the change in the horizontal and vertical scales between the lower and upper panels. Here $t_m = 45.625 \text{ h}$ is based on a constant storm translation speed $V_h = 5.5 \text{ m s}^{-1}$ and the initial storm center location. Thus for time $t - t_m < 0$ is ahead of the storm and $t - t_m > 0$ is behind the storm (from Sullivan et al. 2012)	20

Figure 8.	Wind speed (U_{10} ; m s^{-1}) dependence of (top) momentum, and (bottom) heat and moisture transfer coefficients from eddy covariance observations and from models (from C. Fairall 2012, personal communication). Note that the models have more spread than do the observations.	23
Figure 9.	Various momentum drag coefficients as a function of surface wind speed reported in the literature from (a) Andreas et al. (2012), (b) Bell et al. (2012), (c) Donelan et al. (2012), (d) Fan et al. (2010), (e) Jarosz et al. (2007), (f) Black et al. (2007), (g) Moon et al. (2004c), and (h) Donelan et al. (2004).	25
Figure 10.	Enthalpy flux drag coefficient measurements at wind speeds $< 20 \text{ m s}^{-1}$ from (a) Drennan et al. (2007) and (b) at higher wind speeds from Haus et al. (2010).	26
Figure 11.	Flow chart of the air, ocean, and wave forecast components of the fully coupled COAMPS-TC system, where the exchanges between the components are through the Earth System Framework (ESMF). The coupling between each pair of component models is two-way (from Chen et al. 2011).	32
Figure 12.	An illustration of the COAMPS-TC limited-area analysis and modeling system that uses the global atmospheric, ocean, and wave models to provide cold start initial and lateral boundary updates (from Chen et al. 2014).	35
Figure 13.	Nighttime mean tropical summer soundings from the West Indies (Jordan 1958, blue lines), western North Pacific (Gray et al. 1975, magenta lines), and non-SAL West Indies (Dunion and Marron 2008, red lines).	39
Figure 14.	Schematic illustration of the ocean cold Wake 1 through Wake 4 sensitivity experiments: (a) a circle-shape wake, (b) a half-a-circle-shape wake, (c) an oval-shape wake, and (d) a crescent-shape wake. The magnitude of the SST cold anomaly (blue color) is 2°C	42
Figure 15.	Initial ocean temperature and salinity profile for the two-way coupled TC-wake experiment. The composite is derived from ITOP surface and subsurface moorings A1, A2, A4, SA1, SA2, and SA4 for pre-Fanapi during 14-16 September 2010.	44
Figure 16.	Maximum 10 m wind speed (m s^{-1} , blue dashed line) and minimum SLP (hPa, green line) during the first 72 h of the CNTL experiment.	47
Figure 17.	Minimum SLP (hPa) and maximum 10 m wind (kt) relationship for the CNTL experiment (blue circles). These data are fitted with a polynomial of 2 degree (black line) for comparison with other P-W relationships (see inset for sources).	48
Figure 18.	Time evolution (forecast hour at top) of the relative vorticity (s^{-1}) at 400 hPa (blue) and at 850 hPa (red) in the CNTL experiment on a $200 \text{ km} \times 200 \text{ km}$. The contour interval is 0.05 s^{-1} and 0.01 s^{-1} for the 850 hPa and 400 hPa vorticity, respectively.	49
Figure 19.	Predicted 400 hPa vorticity (s^{-1} , scale on right) at 38 h, 41 h, 43 h, and 46 in the CNTL experiment. At these four times, the vortex was undergoing	

	trochoidal oscillations, and the vortex had multiple mesovortices and a polygonal eyewall.	51
Figure 20.	Azimuthal and vertical average of the vorticity (10^{-3} s^{-1}) with radius at various times (see inset) in the CNTL experiment.	52
Figure 21.	Composites of the azimuthal-mean (a) tangential wind (m s^{-1}), (b) radial wind (m s^{-1}), (c) mean tangential wind deviation from the value at 24 h, and (d) mean radial wind deviation from 24-72 h as the intensity increases from CAT3 to CAT5. The time-averaged location of RMW as a function of height is indicated by the dashed black line.	55
Figure 22.	As in Figure 21, except for relative vorticity (s^{-1} , contour interval of 0.01 s^{-1}) and for divergence (s^{-1} , contour interval of 10^{-4} s^{-1}).	57
Figure 23.	As in Figure 21, except for vertical velocity (m s^{-1}) and turbulent kinetic energy ($\text{m}^2 \text{ s}^{-2}$).	59
Figure 24.	Composites of the axisymmetric (a) tangential wind, (c) radial wind, and (e) vertical velocity from swath data. Composites of the axisymmetric (b) tangential wind, (d) radial wind, and (f) vertical velocity from dropsonde data [From Rogers et al. (2012)].	63
Figure 25.	Composites of the axisymmetric (a) vorticity, (b) divergence, and (c) TKE from Doppler radar swath data [From Rogers et al. (2012)].	64
Figure 26.	Composites of the 12-24 h azimuthal-mean (a) tangential wind (m s^{-1}), and (b) radial winds (m s^{-1}), (c) mean deviation of the mean tangential wind relative to the 12 h values, and (d) mean deviation of the radial winds from the 12 h values. The variation of the RMW in the vertical is indicated by the dashed black line.	66
Figure 27.	As in Figure 26, except for vertical velocity (m s^{-1}) and relative vorticity (s^{-1}).	68
Figure 28.	As in Figure 26, except for TKE ($\text{m}^2 \text{ s}^{-2}$) and divergence (s^{-1}).	70
Figure 29.	Composites of the (a) axisymmetric transverse streamlines (blue) and wind vectors, (b) absolute angular momentum, (c) baroclinicity, and (d) static stability during 24 – 72 h of the CNTL experiment.	73
Figure 30.	Latent heat flux (color shaded) and sensible heat flux (contours) averaged over 6-h periods at selected times between 36 – 66 h in the CNTL simulation. The contour interval is 300 W m^{-2}	76
Figure 31.	Time series of total (a) latent (solid) and sensible (dashed) heat flux (W m^{-2}) averaged over the grid 3 domain, and (b) rain (mm, dashed) and wind stress (N m^{-2} , solid).	77
Figure 32.	Time series of azimuthal-mean total latent (top panel) and sensible (bottom panel) heat fluxes (W m^{-2}) within 1 (blue), 5 (green), 10 (red), and 15 (green) RMW, respectively. The time evolution of the RMW (km) is shown in the bottom panel.	78
Figure 33.	Composites of azimuthal-mean (a) potential temperature (K), (b) diabatic heating rate (units), and (e) vapor mixing ratio (kg/kg during the CAT3 – CAT5 period, and deviations from the predicted values at 24 h for the azimuthal-mean (c) potential temperature, (d) diabatic heating rate, and (f)	

	mean vapor mixing ratio. The dashed black line indicates the time-averaged locations of the RMW as a function of height.....	79
Figure 34.	Comparison of the (top panel) maximum wind speeds (m s^{-1}) and (bottom) minimum sea-level pressures (hPa) between the CNTL and the wake experiments, in which the coupling begins instantaneously at hour 36. The line definitions for the wake experiments are in the insets.....	87
Figure 35.	Comparison of azimuthal- and time-mean (36 h to 72 h) RMW (km, red bar) and radius of gale winds (blue bar) for the wake 1 to wake 5 experiments.....	88
Figure 36.	Total enthalpy flux (10^4 W m^{-2}) within the RMW (green bar) and within 200 km radius (blue bar) at 36-72 h for the wake 1 to wake 5 experiments....	89
Figure 37.	Composites of the azimuthal-mean tangential wind (contour interval 5 m s^{-1}) at 36-72 h from (a) CNTL, (b) wake 1, (c) wake 2, (d) wake 3, (e) wake 4, and (f) wake 5 experiments. Dashed black line represents the RMW at each level.	90
Figure 38.	Composite of the 36 h – 72 h azimuthal-mean radial wind component (m s^{-1} ; scale on right) from the (a) CNTL experiment, and then the deviations from the CNTL for: (b) wake 1-CNTL, (c) wake 2-CNTL, (d) wake 3-CNTL, (e) wake 4-CNTL, and (f) wake 5-CNTL. The contour interval in panels (b) to (f) is 2 m s^{-1} and the scale is on the right.	95
Figure 39.	As in Figure 38, except for the water vapor mixing ratio (kg/kg) from the CNTL experiment in (a) and then the deviations from the CNTL for the wake 1 to wake 5 experiments in panels (b) to (f).	98
Figure 40.	Composite of the wake 3 experiment 49 h azimuthal-mean mixing ratio (g kg^{-1} ; scale on right) deviation from the CNTL experiment.	101
Figure 41.	As in Figure 39, except for the vertical velocity (ms^{-1}) from the CNTL experiment in (a) and then the deviations from the CNTL for the wake 1 to wake 5 experiments in panels (b) to (f).	103
Figure 42.	Composites of the azimuthal-mean radial pressure gradients (hPa/km) from (a) CNTL, (b) wake 1, (c) wake 2, (d) wake 3, and (e) wake 4, and (f) wake 5 experiments at 36-72 h.	106
Figure 43.	Time evolution at selected times from 36 h to 72 h of vorticity at 850 hPa (red) exceeding $5 (10^{-3} \text{ s}^{-1})$ and at 400 hPa (blue) exceeding $1 (10^{-3} \text{ s}^{-1})$ from (a) CNTL, (b) wake 1, (c) wake 2, (d) wake 5, (e) wake 3, and (f) wake 4 experiments. Black contour indicates the cold wake area.....	110
Figure 44.	Low-level vortex tracks from (a) CNTL, (b) wake 1, (c) wake 2, (d) wake 3, (e) wake 4, and (f) wake 5 experiments. Black circles are the 3 hourly locations of vortex centers beginning at 36 h and ending at 72 h as indicated by the red numbers. Numbers along the ordinate and abscissa are grid 3 positions (km).....	114
Figure 45.	Histograms of eddy enstrophy percentage of the total enstrophy at 25 km radii from 36-72 h at (a) 850 hPa and (b) 400 hPa levels decomposed to WN1-WN5 components for the control and five wake experiments (see inset for bar definitions).....	116

Figure 46.	Time and azimuthal plot of wavenumber 2 eddy vorticity (s^{-1} ; scale on right) from (a) CNTL, (b) wake 1, (c) wake 2, (d) wake 3, (e) wake 4, and (f) wake 5 experiments. Only positive eddy vorticity is shown here. Positive slope (left to right with increasing time) means downwind propagation.	118
Figure 47.	As in Figure 46, except for the wavenumber 1 eddy vorticity.....	121
Figure 48.	Time and radius plots of the wake 5 experiment eddy enstrophy decomposed into azimuthal (a)WN1, (b) WN2, (c) WN3, (d) WN4, and (e) WN5 at 850 hPa level. The black line represents the radius of maximum wind.	125
Figure 49.	As in Figure 48, except for the 400 hPa levels.	127
Figure 50.	Time and radius plot of 850 hPa WN1 eddy enstrophy from (a) CNTL, (b) wake 1, (c) wake 2, (d) wake 3, (e) wake 4, and (f) wake 5 experiments. The contour interval is $10^{-4} s^{-2}$. The black line represent the radius of maximum wind.	132
Figure 51.	As in Figure 50, except for the wavenumber 2.	135
Figure 52.	Radial distributions of 850 hPa azimuthal-mean (a) tangential wind ($m s^{-1}$), (b) tangential wind gradient (s^{-1}), (c) relative vorticity (s^{-1}), (d) relative vorticity gradient ($m^{-1}s^{-1}$), and (e) angular velocity ($rad s^{-1}$) from the various wake experiments (see inset for definitions).	141
Figure 53.	Plan views of composite wavenumber 1 divergence (color shaded) and vorticity (contoured) at 850 hPa level for the CNTL (upper-left) and the five wave experiments. The time period of the composite is from 36-72 h. The vorticity contour interval is $5*10^{-5} s^{-1}$ and the white contours mark the boundaries of each cold wake.	144
Figure 54.	As in Figure 53, except for the wavenumber 2.	148
Figure 55.	Azimuth-height cross-sections of composite WN1 vorticity (s^{-1} , color scale on right) and divergence (s^{-1} , solid white and dashed black contours) at RMW from (a) CNTL, (b) wake 1, (c) wake 2, (d) wake 3, (e) wake 4, and (f) wake 5 experiments. The contour interval is $2*10^{-4}s^{-1}$. The RMW for the CNTL experiment is 10 km and for the wake experiments is 25 km.	152
Figure 56.	As in Figure 55, except for the WN2 vorticity and divergence.	156
Figure 57.	Radial-height cross-sections of WN1 composite vorticity (s^{-1} , color shaded) and divergence (s^{-1} , contours) from (a) CNTL, (b) wake 1, (c) wake 2, (d) wake 3, (e) wake 4, and (f) wake 5 experiments. The contour interval is $5*10^{-4} s^{-1}$	160
Figure 58.	As in Figure 57, except for the WN2 vorticity and divergence.	163
Figure 59.	Six-hour evolutions of trajectories TJ8-TJ10 (see inset for definitions) released at (a) 42 h, (b) 45 h, (c) 48 h, and (d) 51 h.....	168
Figure 60.	(a) Inflow angle ($^{\circ}$) and (b) vertical distance traveled (m) for the TJ10 releases between 42 h – 51 h.....	170
Figure 61.	North-south cross sections of the wake 3 potential temperature every three hours from (a) 48 h – 72 h. (b) Location of the cross section with respect to the cold wake (black oval) and the plan view of the 48 h potential temperature ($^{\circ}K$, colored) averaged over the 1-2 km layer.	171

Figure 62.	As in Figure 61, except for the sensible heat flux from -50 to 400 Wm^{-2} . The contour interval is every 50 Wm^{-2}	172
Figure 63.	As in Figure 61, except for the long wave fluxes averaged over the lowest 500 m. The contour interval is every 0.5 Wm^{-2}	173
Figure 64.	Wake 3 experiment 48 h radial wind (ms^{-1}) budgets (a) upwind, (b) over, and (c) downwind from the cold wake at a radius 150 km from the eye. The budget terms are the total tendency (yellow), pressure gradient (magenta), horizontal advection (green), vertical advection (red), and Coriolis (blue), and vertical mixing (cyan).	178
Figure 65.	As in Figure 64, except for the tangential wind budget.	180
Figure 66.	As in Figure 64, except for the radial wind budget at 30 km from the eye. ..	182
Figure 67.	As in Figure 66, except for the tangential wind budget at 30 km from the eye.	184
Figure 68.	(a) Radial wind and (b) tangential wind budgets following trajectory 10 air parcel across the cold wake.	186
Figure 69.	Azimuthal-mean (a) latent heat flux, (b) sensible heat flux, and (c) total enthalpy flux averaged within five RMW for the control and the five one-way coupled wake experiments (see inset). The unit for the fluxes is 10^5 Wm^{-2} for (a) and (c), but 10^4 Wm^{-2} for (b).	189
Figure 70.	Scatter plots of (a) day time and (b) nighttime normalized potential vorticities, (c) day time and (d) night time normalized maximum tangential wind speeds in the lowest 2 km versus normalized enthalpy flux averaged within 5 RMW. The symbol colors (see insets) indicate the one-way coupled wake experiments and the control (ctl) simulation.	190
Figure 71.	As in Figure 70, except for averaged within one RMW.	191
Figure 72.	Sea-surface temperature anomaly ($^{\circ}\text{C}$, color shading bar on right) and 10 m wind speeds (m s^{-1} , magenta contours) from (a) EXPA and (b) EXPB simulation after 42 h. The contour interval for the SST anomaly is 0.5°C and for wind speed is 5 m s^{-1} . The 10 m wind vectors are plotted every 20 grid points.	195
Figure 73.	Time series of the maximum wind speeds (m s^{-1}) from the coupled EXPA and EXPB and the uncoupled uncEXPA and uncEXPB experiments (see inset). The coupling with the ocean in EXPA and EXPB starts at 36 h.	197
Figure 74.	Time evolution at selected times of 850 hPa vorticity (red) exceeding $1 (10^{-3} \text{ s}^{-1})$ and 400 hPa vorticity (blue) exceed $1 (10^{-4} \text{ s}^{-1})$ from (a) 36 h to 60 h from EXPA experiment and (b) 36 h to 72 h from EXPB experiment. Color shadings indicate the cold wake area with contour interval of 1°C . The domain is re-centered around the TC eye in (a) from 36 h – 42 h and in (b) from 36 h – 72 h.	199
Figure 75.	Vertical vortex tilt of the 850 hPa and 400 hPa vortex centers from 36 h to 72 h in EXPA and EXPB experiments (see inset for definition).	200
Figure 76.	Displacement each hour from 36 h through 72 h of the minimum SLP centers for (a) EXPB and (b) uncEXPB experiments.	201
Figure 77.	As in Figure 76, except for the 850 hPa maximum vorticity center. Note that the scale on the ordinate is much smaller than on the abscissa.	201

Figure 78.	Composite radial wind speed (m s^{-1}) and mixing ratio (kg kg^{-1}) anomalies from EXPA (a and b) and EXPB (c and d). The contour interval is 1 m^{-1} for the wind speed and $0.5 \times 10^{-4} \text{ kg kg}^{-1}$ for the mixing ratio.....	203
Figure 79.	(a) Magnitude of the mean azimuthal 850 hPa eddy enstrophy for EXPB and uncEXPB simulations (see inset for definitions) from WN1 and WN2-5, and (b) Normalized wave eddy enstrophy in wave numbers 1 to 5 with respect to the total enstrophy.	206
Figure 80.	Eleven-hour evolutions of trajectories TJ8-TJ10 (see inset for definitions) released at (a) 42 h, (b) 45 h, (c) 48 h, and (d) 51 h. The shaded area is the SST distribution in the coupled EXPB experiment at the release time with a contour interval of $0.5 \text{ }^{\circ}\text{C}$	208
Figure 81.	Plot of TJ10 (a) inflow angle ($^{\circ}$) and ascent distance (m) during the same 11 h trajectories as in Figure 80.	210
Figure 82.	(a) Tangential wind and (b) radial wind budgets from two-way coupled EXPB experiment following trajectory 10 air parcel across the cold wake. .	212
Figure 83.	Low-level winds (m s^{-1} , magenta vectors), upward vertical velocity (m s^{-1} , red contours), and the column-integrated mixing ratio (kg kg^{-1} , white contours) at (a) 37 h and (b) 42 h on the $302 \text{ }^{\circ}\text{K}$ potential temperature surface from the EXPB experiment. The upward vertical velocity contour interval is 0.2 m s^{-1} from 0.2 to 3 m s^{-1} . The column integrated mixing ratio contour interval is 0.1 kg kg^{-1} from 0.001 to 3 kg kg^{-1} . The black arrows represent the wind differences between the EXPB and uncEXPB experiments.	215
Figure 84.	Azimuthal-mean (a) latent heat flux, (b) sensible heat flux, and (c) total enthalpy flux averaged within five RMW for experiment EXPB and uncoupled uncEXPB (see inset). The unit for the fluxes is 10^5 Wm^{-2} for (a) and (c), but 10^4 Wm^{-2} for (b).....	218
Figure 85.	Scatter plots of (a) day-time and (b) night-time normalized maximum tangential wind speeds in the lowest 2 km versus normalized enthalpy flux averaged within 5 RMW for the two-way coupled experiment EXPA and EXPB (see insets). (c) and (d) as in (a) and (b), except for the average within one RMW.....	219
Figure 86.	Conceptual model of the physical processes affecting the atmospheric response in a TC moving from right to left while interacting with an ocean cold wake (green color) and the atmospheric cold pool (light blue) above that cold wake. In addition to the thermodynamic processes related to a reduction in the enthalpy flux from the ocean to the TC boundary layer, a dynamic response of a low-level wake jet leads to inflow of moist air that delays or offsets the thermodynamic response to the cold wake. The gray shading depicts the locations of clouds, and the blue column represents the eye of the TC. The white arrows are the winds. The cooling underneath the eyewall forces an outward expansion of the eyewall.....	230

THIS PAGE INTENTIONALLY LEFT BLANK

LIST OF TABLES

Table 1.	Sea-surface temperature (SST) decreases ($^{\circ}\text{C}$) observed in the inner-core (IC; radius < 60 km) relative to the pre-storm SST_A (column 4) compared to the corresponding SST decreases in the cold wake in outer radii (60-200 km); column 5) for 33 Atlantic hurricanes surveyed by Cione and Uhlhorn (2003). The hurricanes with year (column 2) and observing platform (buoy number, AXBT, or publication) are listed according to magnitude of the inner-core hurricane ΔSST magnitude in column 4.....	12
Table 2.	Key observational studies of the ocean response to Category 3-5 TCs from AXBT, AXCP, AXCTD, mooring, and ocean profiler observations.	14
Table 3.	COAMPS namelist variables for the trajectory and momentum budget outputs.....	36
Table 4.	Nighttime temperature and moisture values from the mean tropical cloud cluster sounding of Gray et al. (1975).	40
Table 5.	Description of five prescribed wake sensitivity experiments	42

THIS PAGE INTENTIONALLY LEFT BLANK

LIST OF ACRONYMS AND ABBREVIATIONS

CBLAST	Coupled Boundary Layers Air-Sea Transfer
COAMPS5	Version 5 of Coupled Ocean and Atmosphere Mesoscale Prediction System
COAMPS-OS	Coupled Ocean and Atmosphere Mesoscale Prediction System—On Scene
COAMPS-TC	Coupled Ocean and Atmosphere Mesoscale Prediction System—Tropical Cyclone
COARE	Coupled Ocean-Atmosphere Response Experiment
ESMF	Earth System Modeling Framework
HYCOM	HYbrid Coordinate Ocean Model
ITOP	Impact of Typhoon on the Ocean in the Pacific
NAVDAS	NRL Atmospheric Variational Data Assimilation System
NAVGEN	NAVy Global Environmental Model
NAVO	Naval Oceanographic Office
NCODA	Navy Coupled Ocean Data Assimilation
NCOM	Navy Coastal Ocean Model
NDBC	National Weather Service National Data Buoy Center
NOAA	National Oceanic and Atmospheric Administration
NOGAPS	Navy Operational Global Atmospheric Prediction System
NRL	Naval Research Laboratory
UTC	Coordinated Universal Time

THIS PAGE INTENTIONALLY LEFT BLANK

EXECUTIVE SUMMARY

Despite a large body of literature that discusses the TC structure and intensity changes owing to air-sea interaction or describes the ocean response to passing TCs, several key questions need to be further studied: What are the key physical processes in the TC response to the ocean cooling during the storm stage? How do the location relative to the TC center and the shape of the ocean cold wake affect the TC intensity change? To address these questions, the responses in one-way and two-way coupled model-simulated CAT3-5 TCs are examined in an ocean cold wake parameter space that includes the cold wake magnitude, shape, and location. Key advancements in understanding have been achieved through validation of the following three hypotheses:

- Hypothesis I: The TC intensity is sensitive to the location and magnitude of the wake relative to the track. A cold wake centered underneath the TC core has more important impacts on reducing the intensity than a cold wake located to the right or left of the TC center.
- Hypothesis II: Differential surface enthalpy fluxes over the ocean cold wake introduce an asymmetric structure in the TC circulation. In a certain region of moderate winds outside the radius of maximum wind, the cold wake forces a low-level wake jet that is deflected toward the center of the storm. The strength of the wake jet depends on the magnitude of the wake cooling.
- Hypothesis III: The TC intensity reduction due to the cold wake may arise dynamically from the growth of vortex Rossby and baroclinic waves excited by the cold wake at the expense of the mean vortex as well as by thermodynamic influences resulting from a change in the surface enthalpy fluxes over the colder water.

The main new findings presented in this dissertation can be summarized as illustrated by the conceptual model, which outlines the physical processes governing the model-simulated TC interaction with its cold wake. First, these processes include complex dynamical pathway induced by the ocean cold wake that act in concert with the enthalpy flux to modulate the TC intensity change. Second, the shape and location of the wake are relevant to the TC intensity change because they affect the time delay of the vortex spin-down. A long-trailing wake or irregularly shaped wake within the eyewall

region forces a dynamic response that tends to offset the negative effect of reduced enthalpy flux and increase the time delay of the vortex spin-down. Third, a $1 - 2 \text{ m s}^{-1}$ increase of low- to mid-level inflow referred to as the “wake jet” occurs above an atmospheric cold pool that is induced by the reverse sensible flux transfer over the trailing cold wake that is augmented by negative long wave fluxes at night-time. As the low-level boundary level boundary inflow crosses the ocean wake, air parcels can be deflected upward and turned toward the center of TC, which helps retain the moisture within and above the boundary layer. Fourth, a strong 4°C cold wake underneath the eyewall significantly damps the vorticity gradient in the eyewall region, which in turns forces the TC to transition from an unstable annulus ring vortex to a stable Rankine-like vortex. The wavenumber 1 VRW is reduced and is replaced by amplifying DVRWs and an increase in spiral rainband activity associated with the IG wave emission.

The significance of this dissertation stems from the discovery that a dynamic pathway that governs the time scale of the TC intensity reduction due to interaction with its cold wake, which has not been previously shown in the literature. This discovery has been made possible from an advancement in the state-of-the-art, high-resolution, coupled atmospheric-ocean model at the Naval Research Laboratory-Monterey. The transition of this advanced model to operations will improve predictions of TCs that continually threaten U. S. Navy ships and Department of Defense bases.

ACKNOWLEDGMENTS

The guidance and encouragement provided by Professors Russell Elsberry and Pat Harr during the course of this dissertation research are greatly appreciated. Thanks go to committee member Professors Rebecca Stone and Frank Giraldo, and Drs. Melinda Peng and Peter Black for their input that helped to improve the dissertation. Penny Jones of the Department of Meteorology assisted in the preparation of the dissertation. This research is supported by the Naval Postgraduate School long-term training program from the Naval Research Laboratory. The computing resource for the model simulations was from the Department of Defense High Performance Computing Modernization Program.

THIS PAGE INTENTIONALLY LEFT BLANK

I. INTRODUCTION

The improvements of our understanding on how the ocean modulates the TC intensity and track change are relevant for the Navy's need to better observe, assimilate, and forecast the TC. Given the complexity of isolating the governing physical processes in a full physics coupled model, a simpler and controlled framework is needed to investigate the wake-imposed TC intensity and structure changes as the circulation crosses the cold wake.

The energy input from the ocean to a tropical cyclone (TC) may be modulated by low sea-surface temperatures (SST) that are induced by the TC winds. The cold SST anomaly known as the TC cold wake puts a unique footprint on the ocean that sometimes persists up to several weeks after the passage of the TC (Mrvaljevic et al. 2013). Thus, the upper-ocean conditions may be greatly altered by the TC during and after the passage of a storm. However, the amounts of the wake cooling forced by a TC and the wake feedback to subsequent TC intensity changes are complex processes that are influenced by a combination of several environment factors. The parameter space that determines the evolution of the cold wake and influences TC intensity change has been examined by many previous studies. For example, given the same TC forcing, a faster translating TC generates less wake cooling than a slower translating TC (Price 1981; Schade and Emanuel 1999; Chaing et al. 2011). Vertical mixing is suppressed (enhanced) as a TC passes over a pre-storm warm (cold) eddy region due to dispersion (trapping) of near-inertial shear into the thermocline (Jaimes and Shay 2010). The TC-induced upwelling and mixing is increased (decreased) in cold (warm) eddies (Jaimes and Shay 2010). Shallower mixed layer (ML) depth and weaker thermal stratification encourage larger wake cooling (Lin et al. 2008). In summary, the wake cooling is stronger with a slower TC translation speed, weaker upper-ocean stability, and shallower mixed-layer depth.

The conventional approach to study the ocean feedback to the TC intensity change has been to focus on the thermodynamic processes through the reduction of surface enthalpy flux transfer from the ocean to the TC. Numerous studies have suggested that TC intensity change is positively correlated to the upper-ocean thermal

structure. Studies by Lin et al (2008, 2009) demonstrated that the pre-storm ocean conditions modulate the TC intensity change. With a deeper thermocline, the negative impact of the cold wake to TC intensity change is reduced. Furthermore, a negative correlation exists for storm intensification between the TC translation speed and ocean heat content, which is defined as the heat content above the level at which the ocean temperature is equal to 26°C. The TC intensity is decreased with a stronger cold wake, while the TC intensification is favored over a region of higher ocean heat content regions.

Although the upper-ocean response to a TC is relatively well understood, less attention has been paid to how the TC interacts with the cold wake. Specifically, the following questions need to be addressed: How does the TC surface wind field adjust to the presence of the cold wake? What thermodynamic or dynamic processes occurring in the cold wake lead to significant TC intensity and structure changes? How does the mature TC spin-down due to the presence of a strong cold wake? Does the wake affect the TC track? These are important issues that require further attention. To investigate the wake-imposed TC structure change as the circulation crosses the cold wake, a simpler and controlled modeling framework is needed.

In preparation for this modeling study of the interaction of TC with its cold wake, a literature review on the ocean response to TC forcing and the ocean feedback to TC intensity changes is given in Chapter II. The review provides an update of current knowledge, which provides a foundation to test hypotheses toward understanding the physical processes that govern the interaction of a TC with its cold wake. The description of the Coupled Ocean Atmospheric Mesoscale Prediction System (COAMPS-TC) model and influences numerical experiment design with coupled/uncoupled versions are described in Chapter III. The TC responses to the wake parameter space such as magnitude, shape, location, and vertical shear will be first examined in the one way-coupled experiments. The idealized TC structure from the control simulation is discussed in Chapter IV. Discussion of the one-way coupled experiments is presented in Chapter V. The one-way results then are compared with the flow response under the storm motion with the fully coupled air-ocean coupled experiments. The idealized coupled model results using the Typhoon Fanapi (2010) ocean profiles are discussed in Chapter VI.

Chapter VII gives a summary of these idealized results with a conceptual model of the interaction of a TC with its cold wake.

THIS PAGE INTENTIONALLY LEFT BLANK

II. REVIEW ON THE INTERACTION OF A TC WITH ITS COLD WAKE

Progress in understanding the upper-ocean processes and air-sea interaction during the passage of TCs has been summarized in a chapter review article by Shay (Chan and Kepert 2010). The first objective of this section is to describe physical factors that affect the wake characteristics such as shape, location, and amplitude. The second objective is to review studies of the negative oceanic feedback that arises from reduction of the enthalpy flux over the cold wake and the dynamic response, which were only briefly touched on in the Shay (Chan and Kepert 2010) review. Previous studies of the kinematic variations in the TC inner core with respect to the horizontal and vertical distributions of heating profiles are also summarized. Finally, progress achieved from updates of recent research and current gaps in knowledge will be reviewed with an emphasis on the TC-wake interaction during the storm stage.

A. FORMATION OF THE COLD WAKE

Upper-ocean response to TC forcing has been the subject of numerous modeling and observational studies. It is well established that the formation of the cold wake involves three mechanisms, namely the wind mixing, upwelling, and horizontal advection. Each mechanism operates on a different part of the ocean under the TC as depicted in Figure 1 by Shay (Chan and Kepert 2010). This schematic illustration depicts the upwelling under the eye while the wind mixing regime extends to outer radii with the maximum extent to the right of the track in the Northern Hemisphere.

What is not shown in Shay's figure is the horizontal advection by the ocean currents that move cold water from the rear part of the wake to the front and extend the width of the wake (Chen et al. 2010; Vincent et al. 2012). Using a two-way coupled model, Chen et al. (2010) showed the distinct spatial separation among these three primary forcing terms that are generating the bulk of the cooling (Figure 2). Note the total tendency has two primary centers of cooling – one centered along the TC track and the other displaced to the northeast of the TC at the leading edge of the wake. The

northeastern center is primarily due to the horizontal advection term. The cooling near the center of the track is nearly equally due to the contributions from the vertical mixing and vertical advection terms (upwelling). In these modeling studies, the horizontal advection is in the same order of magnitude in the upper-ocean temperature budget as the wind mixing and upwelling. A recent global general circulation model study by Vincent et al. (2012) of 3000 TCs forced by idealized TC wind patterns with the observed intensities and tracks suggested the along-track advection of cold water significantly contributes to the asymmetric cooling distribution in stronger TCs. However, this advection effect on the TC wake cooling has not been well-documented from observations.

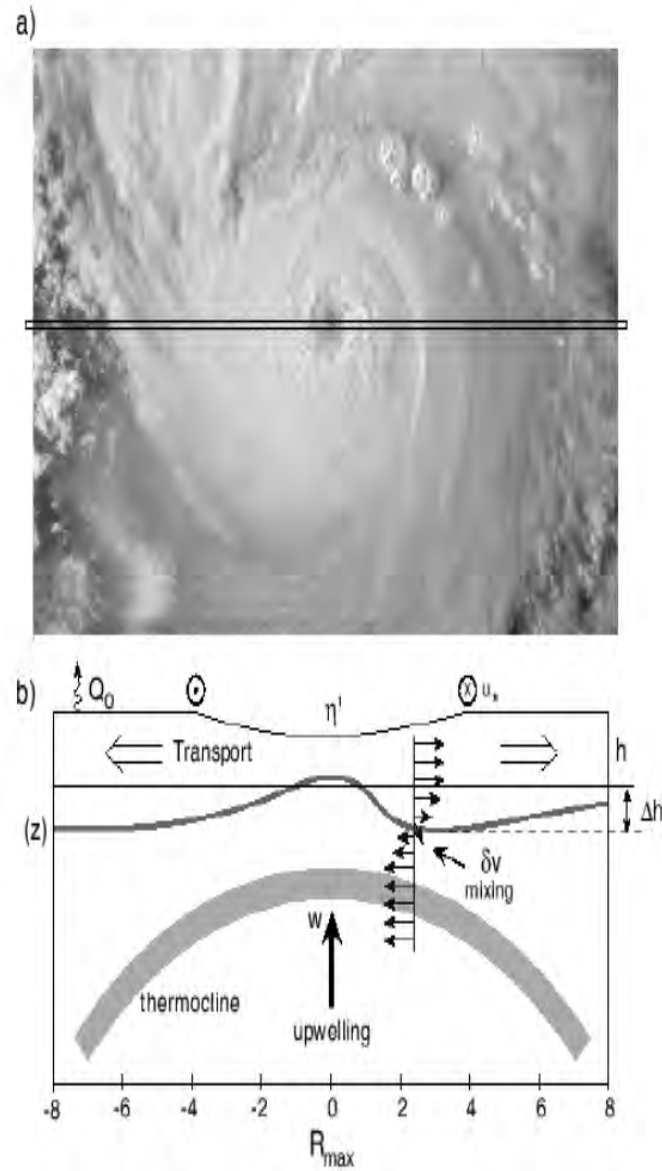


Figure 1. (a) TC image, and (b) a schematic depiction of the physical processes forced by hurricane winds such as shear-induced mixing and OML deepening, upwelling due to transport away from the center, and surface heat fluxes from the ocean to atmosphere, all of which may contribute to ocean cooling during TC passage (from Chan and Kepert 2010).

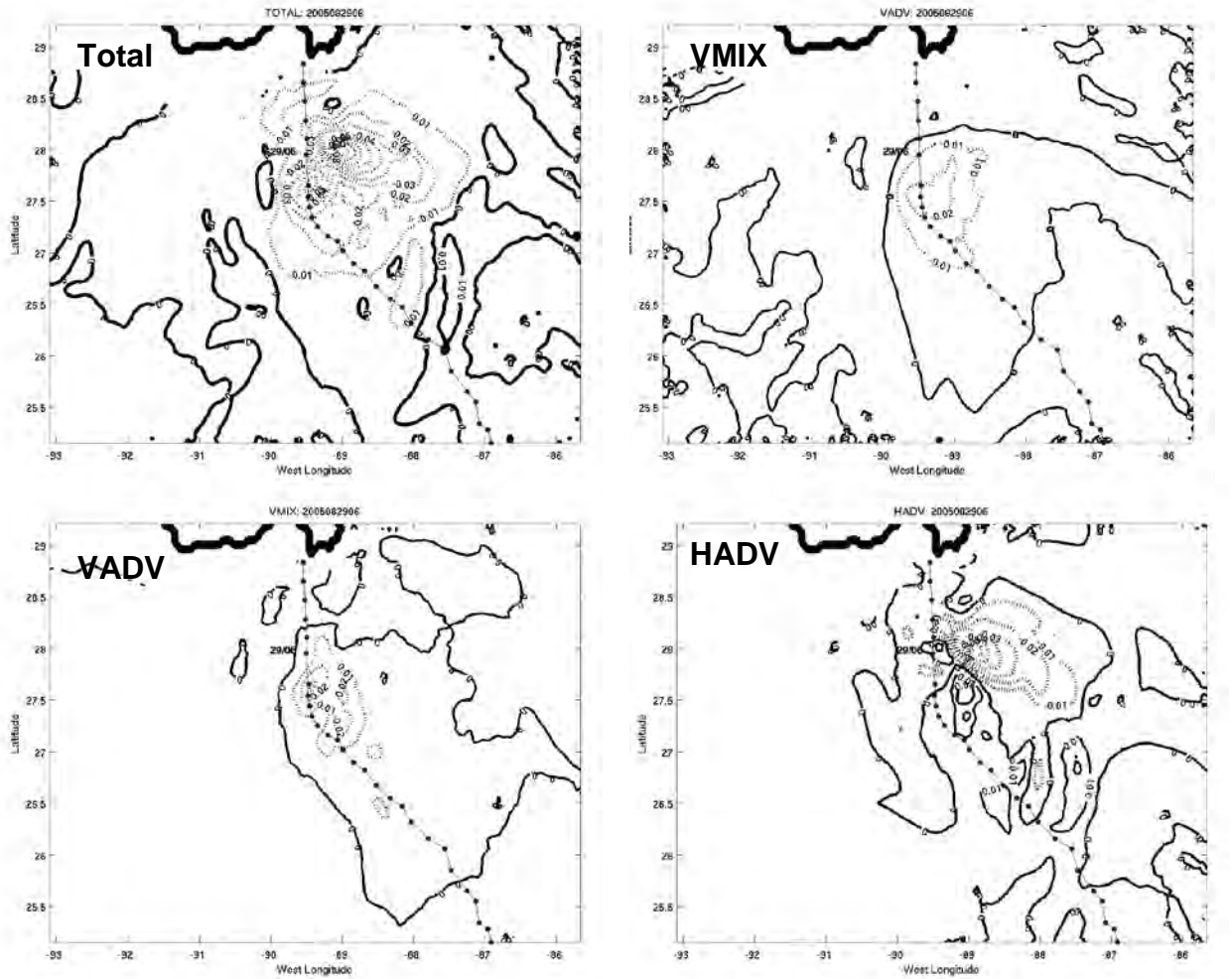


Figure 2. Average ocean mixed-layer temperature change rate ($^{\circ}\text{C}/\text{h}$, contour interval is $0.02^{\circ}\text{C}/\text{h}$) at 42 h predicted by the two-way coupled model of Chen et al. (2010). The total temperature change is the sum of the vertical mixing (VMIX), vertical advection (VADV), and horizontal advection (HADV) plus some smaller terms (from Chen et al. 2010).

The spatial and temporal changes of ML temperature during the storm stage are dominated by the wind mixing, upwelling, and horizontal advection. In the wake, cooling from the air-sea fluxes is generally smaller compared to these three mechanisms (Prasad and Hogan 2007; Chen et al. 2010). In the warm eddy region, the air-sea flux can

be as high at 30% of the total cooling (Jacob and Shay 2003). Strong divergence in the ML velocity beneath the TC center results in Ekman pumping and upwelling. The model simulation of Price (1981) had an upwelling magnitude that rapidly decayed away from the center. In an extreme case of 10.8°C wake cooling in association with a very slowly moving (2 ms^{-1}) Typhoon Kai-Tak (2000), cooling from upwelling was twice as large as the wind mixing (Chiang et al. 2011). They attributed the unusually strong upper-ocean response to a combination of a slow-moving storm and a subsurface cold eddy that was capped by a shallow warm surface layer.

B. LOCATION AND AMPLITUDE OF THE COLD WAKE

Early modeling studies by Chang and Anthes (1978) and Price (1981) described the location of the cold wake relative to the TC center due to a translating TC. Using both prescribed symmetric and asymmetric TC wind forcings for 3D ocean models and various TC translation speeds, both modeling studies demonstrated the rightward bias of the wake location with respect to the TC track in the Northern Hemisphere is due to translation rather than the asymmetric wind forcing. Price (1981) suggested the near-resonant effect of the wind stress and ocean current causes the cold wake to form to the right of the TC track. This wind-current resonate occurs due to anti-clockwise turning of the TC wind stress in time that is then roughly in the same direction as the clockwise-rotating inertial ocean currents that are induced by the translating TC. The wind-current resonant effect enhances the upper ocean current, which leads to increased current shear and enhanced entrainment mixing at the base of the mixed layer (ML). On the left side of the track, the direction of the wind stress nearly opposes the direction of inertial current within the ML and hence reduced mixing.

Price (1981) also noted the maximum wind-current coupling shifted to the TC outer radii when the wind-stress vector turns slower, e.g. the inertial motion of the TC is slower (Figure 3). Price also showed that given the same initial TC stress forcing, the rightward shift of the cold wake is reduced (but the magnitude is increased) with smaller TC translation speed. A near-symmetric wake was obtained with a very slow translation

speed of 2 ms^{-1} , which then more resembles the schematic in Figure 1b, with significant upwelling due to the slow translation speed.

Cione and Uhlhorn (2003) summarized the observations of SST cooling from 33 Atlantic TCs using the Air-eXpendable BathyThermographs (AXBT) or moored buoys. They examined the SST cooling in the TC inner-core region (60 km) compared to outer radii ($< 200 \text{ km}$). The cooling in the inner-core is about half of that of outer radii ($0\text{-}2^{\circ}\text{C}$ compared to $4\text{-}5^{\circ}\text{C}$, see Table 1). However, because of larger wind speed in the TC inner-core, they suggested a moderate 1°C cooling in inner-core SST reduces by about 40% of the enthalpy flux transfer from the ocean to the TC. Cione and Uhlhorn (2003) showed a linear increase of ocean heat content extracted by TC with respect to inner-core SST change, and the radius of maximum inner-core SST cooling is about 1.2 degree latitude. The inner-core SST cooling was less for lower-latitude and faster-moving TCs due to deeper and warmer pre-storm upper-ocean environment at the lower latitudes and the faster translation lead to a shorter ocean response time. These observational results are consistent with the model results of Price (1981). Thus, reducing the SST below the inner-core region of the TC is an effective thermodynamic pathway to reduce the TC intensity.

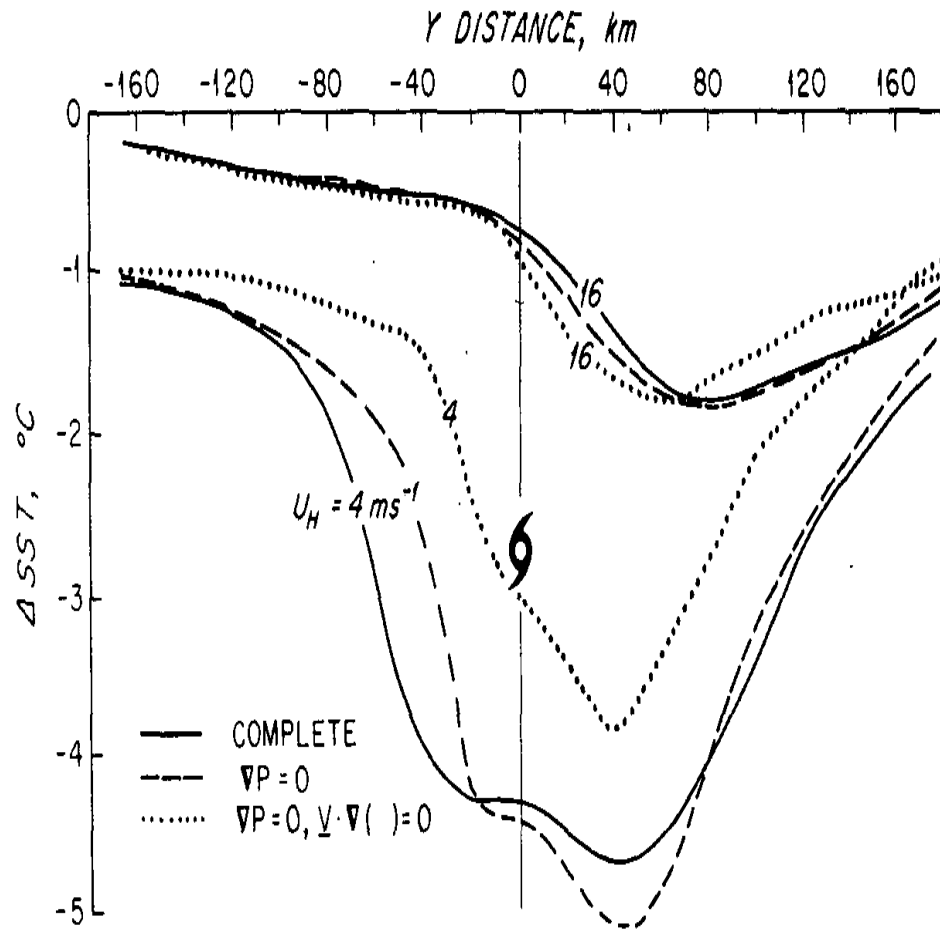


Figure 3. Rightward displacements and magnitudes of the SST decrease for hurricane translation speeds at $U_h = 4$ and 16 ms^{-1} from the Price (1981) model simulation. Line definitions for the SST responses for the complete (solid) pressure field and two sensitivity tests with no TC pressure effects are indicated in the inset.

Table 1. Sea-surface temperature (SST) decreases ($^{\circ}\text{C}$) observed in the inner-core (IC; radius < 60 km) relative to the pre-storm SST_A (column 4) compared to the corresponding SST decreases in the cold wake in outer radii (60-200 km); column 5) for 33 Atlantic hurricanes surveyed by Cione and Uhlhorn (2003). The hurricanes with year (column 2) and observing platform (buoy number, AXBT, or publication) are listed according to magnitude of the inner-core hurricane ΔSST magnitude in column 4.

Hurricane	Year	Observing platform	$\Delta\text{SST}_{\text{IC}} (^{\circ}\text{C})$ $\text{SST}_{\text{IC}} - \text{SST}_A$	$\Delta\text{SST}_{\text{ICW}} (^{\circ}\text{C})$ $\text{SST}_{\text{ICW}} - \text{SST}_A$
Alicia	1983	42008	-1.8	-2.7
Georges	1998	42040	-1.5	-3.4
Emily	1993	44019	-1.5	-1.5
Erika	1997	AXBT	-1.5	-1.5
Belle	1976	41002	-1.2	-1.5
Elena	1985	42007	-1.0	-1.7
Earl	1998	42003	-0.9	—
Luis	1995	41519	-0.9	—
Georges	1998	SANF1	-0.8	-1.4
Dennis	1999	AXBT	-0.8	—
Georges	1998	DRYF1	-0.8	-0.9
Dennis	1999	AXBT	-0.8	—
Lili	2002	42001	-0.7	-1.9
Georges	1998	SMKF1	-0.7	-1.2
Danielle	1998	AXBT	-0.7	—
Andrew	1992	FWYF1	-0.7	—
Allison	1995	42003	-0.6	-0.6
Bob	1991	DSLN	-0.6	-0.6
Anita	1977	42002	-0.6	-1.4
Irene	1999	AXBT	-0.6	—
Frederic	1979	42003	-0.5	-0.8
Dennis	1999	AXBT	-0.5	-0.5
Earl	1998	42040	-0.4	-0.5
Eloise	1975	42001	-0.3	-0.8
Bonnie	1998	AXBT	-0.3	-0.3
Bret	1999	AXBT	-0.3	-0.4
Lili	2002	AXBT	-0.3	-0.7
Opal	1995	42001	-0.1	-0.3
Earl	1998	AXBT	-0.1	-0.8
Isidore	2002	AXBT	-0.1	-0.2
Edouard	1996	41611	0.0	0.0
Edouard	1996	41614	0.0	-0.2
Andrew	1992	42003	0.0	-0.1

A survey of some key studies of the wake cooling magnitudes in Category 3-5 TCs is summarized in Table 2. The locations of maximum SST cooling in the studies by Shay et al. (1992), Jaimes and Shay (2009), D'Asaro et al. (2007), and Sanford et al. (2011) are mostly in the outer radii in the rear- right quadrant relative to the TC center. Strong 4-5°C cooling is detected in the cases of Felix, Ivan, Katrina, Rita, and Lupit. By contrast, Category 4 Hurricane Frances and Category 3 Typhoon Fanapi have a moderate 1-3 °C cooling (D'Asaro et al. 2007; Sanford et al. 2011; Mrvaljevic et al. 2013). In some cases, not enough information is given to estimate where the maximum cooling occurred during the storm. However, the maximum wake cooling in the Hurricane Frances case occurs in the outer radii and the cooling magnitude in the inner-core is about 1-2°C (Figure 4). In general, these results are within the range of SST cooling magnitudes described by Cione and Uhlhorn (2003).

Table 2. Key observational studies of the ocean response to Category 3-5 TCs from AXBT, AXCP, AXCTD, mooring, and ocean profiler observations.

Tropical Cyclone	Year	Observing platform	ΔSST(°C)	TC translation speed (ms⁻¹)	Reference
Norbert	1984	AXBT,AXCP	2.6	4	Shey et al. (1992)
Josephine	1984	AXCP	1.8		Black et al. (1988)
Gilbert	1985	AXBT	3.5-4	6-7	Jacob et al. (2000)
Felix	1995	Mooring	3.5-4	6.9	Dickey et al. (1998)
Ivan	2004	AXBT	6.5	5.5	Jaimes and Shay (2009)
France	2004	Profiler, EM-APEX	2.2	6	D'Asaro et al. (2007), Sanford et al (2011)
Katrina	2005	AXCP,AXCTD ,AXBT	4-5	6.3	Jaimes and Shay (2009)
Rita	2005	AXCP,AXCTD ,AXBT	4-5	4.5	Jaimes and Shay (2009)
Fanapi	2010	AXBT	>2.5		Mrvaljevic et al. (2013)

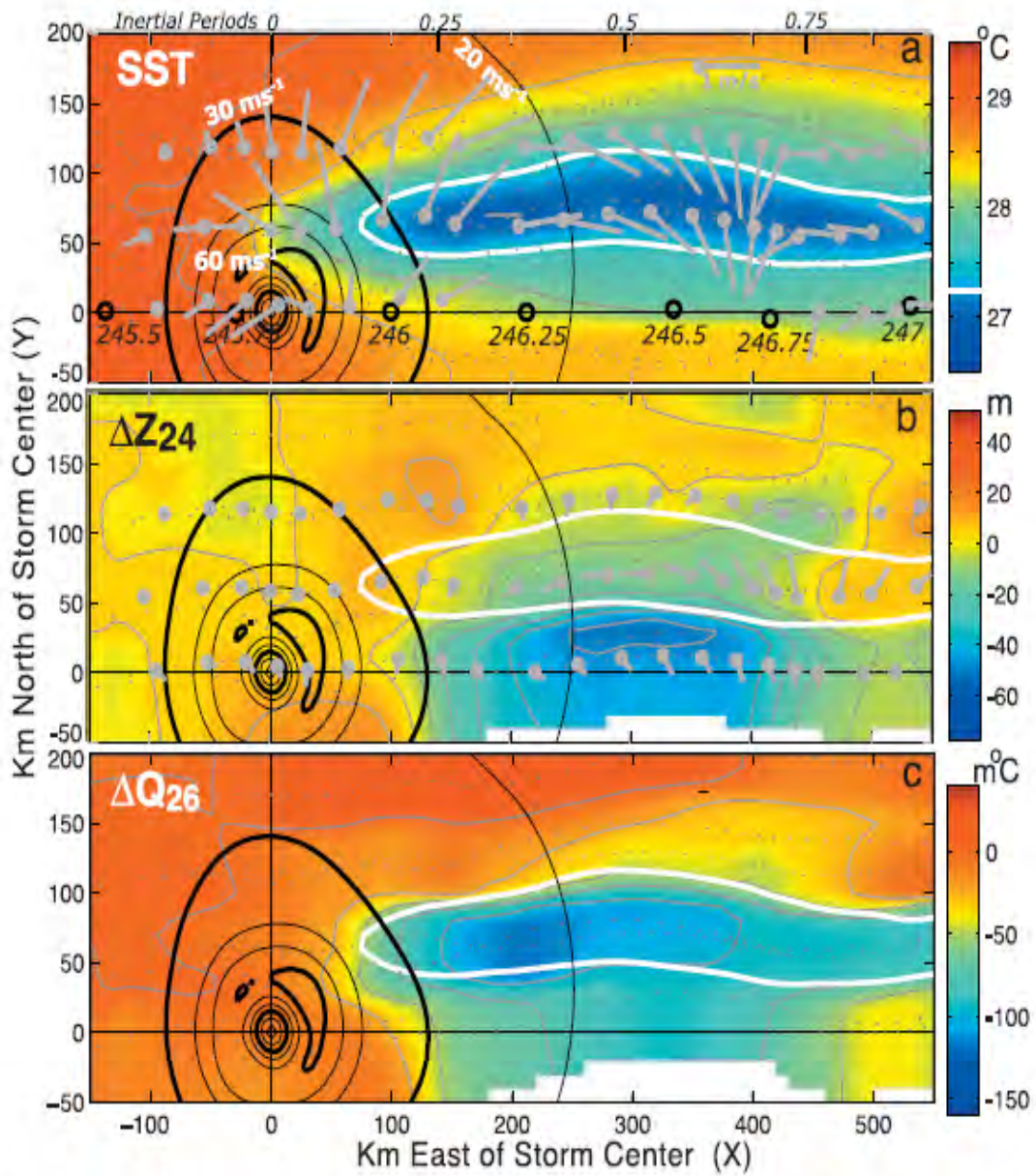


Figure 4. Plain views of the ocean response to Hurricane Frances in a storm-centered coordinate system: (top) SST ($^{\circ}\text{C}$), (middle) change of depth (m) of the 24°C isotherm, and (bottom) change of the ocean heat content relative to the 26°C isotherm. Arrows show mixed layer velocity from the EM-APEX floats. The storm moves to the left along the horizontal axis (from D'Asaro et al. 2007).

C. EFFECTS OF PRE-EXISTING OCEAN EDDIES

The upper-ocean wind mixing forced by a TC is different in a region of pre-existing ocean eddies. In the warm-core eddies (WCEs) region, the mixed layer is usually deeper than in the cold –core eddies (CCEs), or in the eddy-free region. Thus, the TC-forced wake cooling is smaller in deeper WCE mixed layer (Price 1981, Shay et al. 2000, Jacob and Shay 2003, Hong et al. 2000, Wu et al. 2007, Jaimes and Shay 2011).

Based on satellite altimetry study of 13 years of CAT5 typhoons in the western North Pacific, Lin et al. (2007) found a higher percentage of CAT5 typhoons over WCEs compared to an eddy-free region shallower mixed-layer depth (MLD). A subsequent modeling study by Wu et al. (2007) further suggested that the amplitude of the cold wake cooling, and thus the potential negative impact of the wake on the TC intensity, is affected more by the MLD associated with the large-scale ocean eddies than on the TC translation speed or upper-ocean stratification. Wu et al. (2007) suggested the slower moving storm has a longer interaction time with the eddies and thus is more likely to be affected by the dynamic response of the eddy to the forcing.

The interaction of a TC with WCEs and CCEs was recently examined in an idealized study by Jaimes and Shay (2011), who found the vertical mixing is indeed suppressed (enhanced) as the TC passes through a pre-storm warm (cold) core eddy region due to dispersion (versus a trapping) of near-inertial currents into the thermocline. The wake cooling is three times larger in cyclonic CCEs than in anticyclonic WCEs given the same TC wind forcing (Figure 5). In addition, a dipole vertical velocity appears inside the WCEs and CCEs, which is attributed to differential advection of geostrophic vorticity by the wind stress.

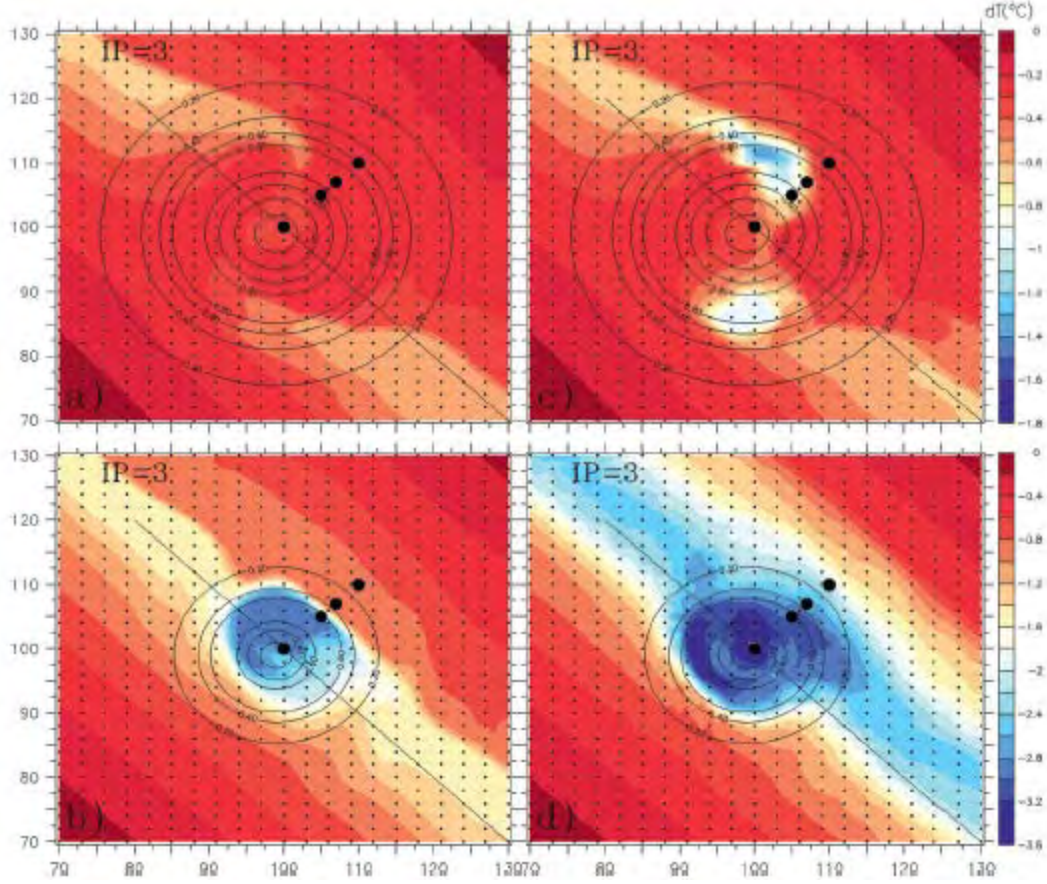


Figure 5. Simulated ocean mixed layer cooling in (top) warm-core eddy WEC1 and (bottom) CCE2 cold-core eddy with two turbulent mixing closure schemes (from Jaimes and Shay 2011). Vertical velocity (m s^{-1} , scale on the right margin) has a dipole structure. Color is the OML cooling, vectors are OML geostrophic currents, the black line is the storm track and, and black dots are model moorings in the cross-track direction.

D. PRECIPITATION EFFECT ON THE OCEAN MIXING

The freshwater input to the ocean has two effects on the upper-ocean thermal structure change. The first effect is to increase the stability, which reduces the mixing and favors formation of a barrier layer. The second effect is the heat lost from rain flux (Gosnell et al. 1995). For heavy precipitation conditions in a TC, the rain flux effects in reducing the stability and heat lost are small, e.g., about 10% of the total ocean heat flux lost and $0.03\text{ }^{\circ}\text{C}$ increase in cooling in an idealized study by Jacob and Kobalinsky (2007). They also showed the main effect of the rain in a quiescent ocean was to reduce

ocean cooling by about 0.2-0.5 °C at the location of heavy precipitation (specified to be between the inner and outer eyewalls) due to reduced mixing since the rate of freshening exceeds the rate of mixing.

E. SURFACE WAVE EFFECTS ON THE UPPER-OCEAN MIXING

In the high wind speed conditions of a TC, a mixture of wind-seas and swells exist. Both of these ocean surface conditions may have a large impact on the upper-ocean mixing by changing the vertical current shear, and by transferring energy to the current from wave breaking dissipation (Craig and Banner 1994), radiation stress (Longuet-Higgins and Stewart 1964), wave-enhanced bottom stress due to wave orbital motion, and altering the momentum drag. The dynamics of the surface wave and ocean current interaction are driven by Stokes' drift that creates alternating horizontal roll vortices (Figure 6) that are known as the 'Langmuir Circulation (LC)' (Langmuir 1938). An extensive review of observations and modeling of LCs is given by Smith (1992). These rolls are driven by a mechanical instability (Leibovich and Ulrich 1972; Craik 1977; Leibovich 1983) produced by the tilting of the depth-varying Stokes' drift, which stretches the vertical vorticity horizontally. This effect then leads to lines of surface convergence in the center of each pair of counter-rotating roll vortices, which may be reinforced by wind-induced shear in the down-wind direction. Because the mixing process produces bubble streaks along the axis of the convergence, characteristics of LC can then be inferred from bubble observations using the Doppler sonar (Melville et al., 2002).

Under high wind speed conditions in the TC, the net effect of the Langmuir-induced mixing depends on the alignment of the wind and Stokes drift current and the penetration depth of the Stokes drift. The Langmuir mixing is strong when the alignment angle of wind and wave is small. When the alignment angle is large and the wind direction opposes the wave direction, the waves become steeper and break, which is a larger effect than the Langmuir mixing. Idealized large eddy simulations (LES) by Sullivan et al. (2012) suggested a 25% increase in turbulent mixing and a 0.25°C more cooling on the right side of the TC due to Langmuir mixing. By contrast, cooling is

reduced on the left side of TC due to reduction of Langmuir mixing. The clockwise rotation of Langmuir cells and their associated Stokes currents on the right hand side of TC are illustrated in Figure 7. Rapid growth of Langmuir cells and a broad region of weak upwelling on the flank of cells occurred at the time of maximum wind.

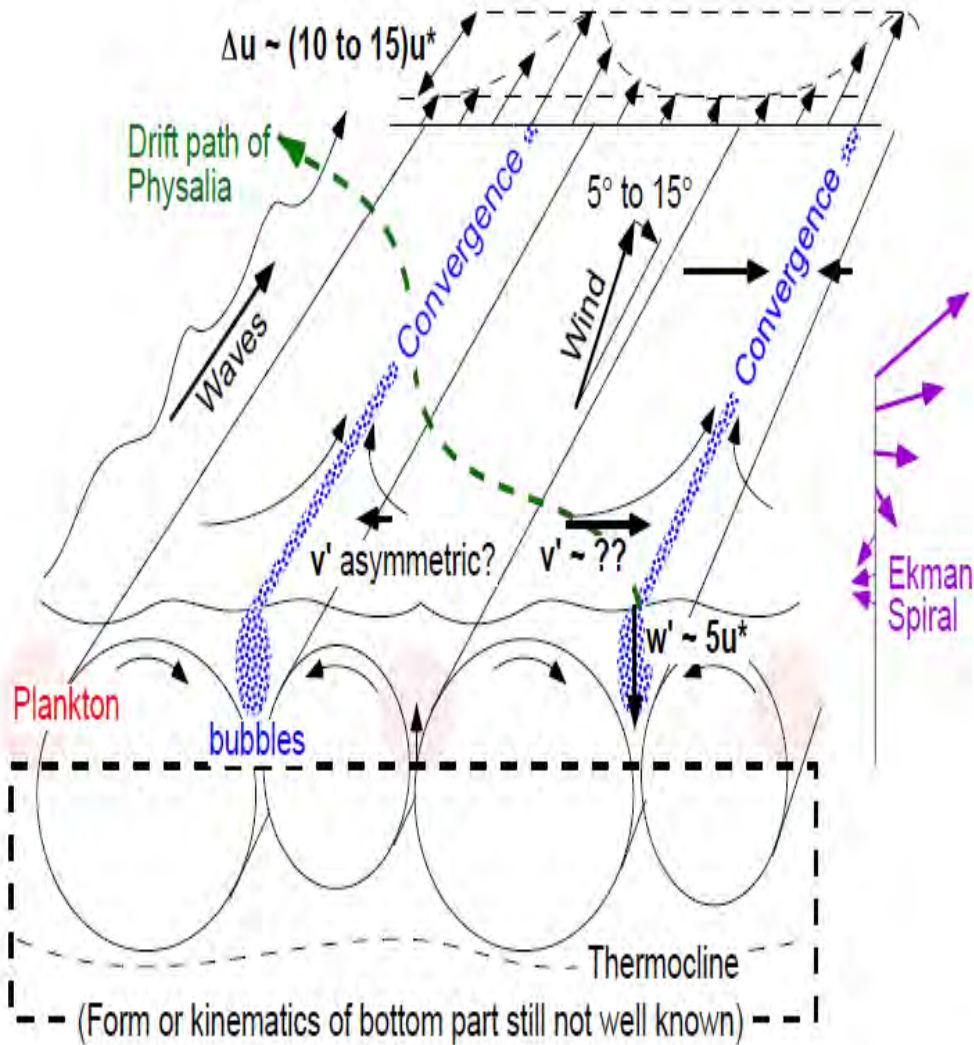


Figure 6. Schematic illustration of Langmuir circulation (from http://jerry.ucsd.edu/JSmith_PDF/2001-Smith-aStoryOfMixing.pdf).

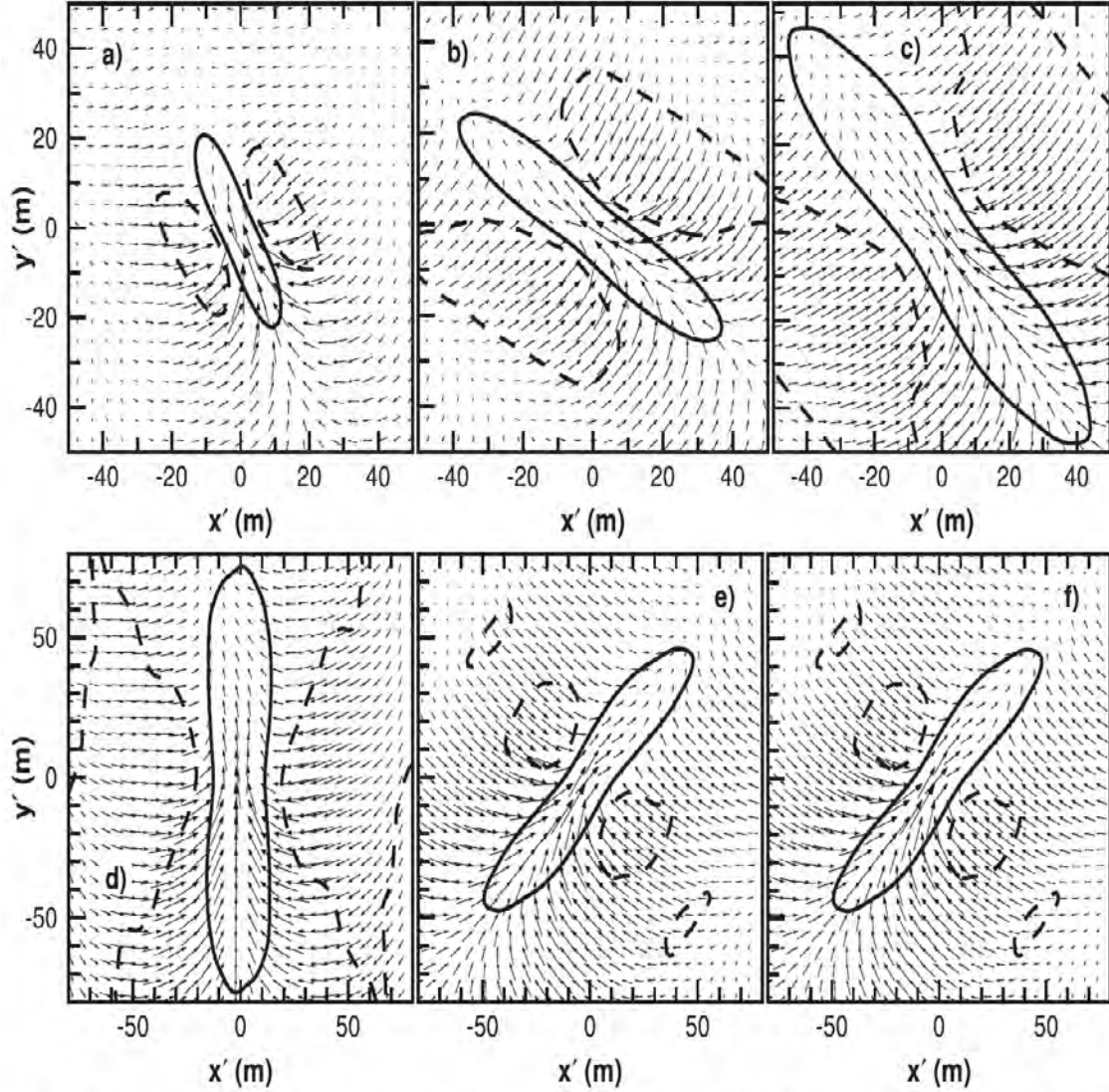


Figure 7. Normalized two-point spatial correlation $R_{ww}(x', y', z_{max})$ along the track $X=60$ km from the idealized LES simulation by Sullivan et al. (2012). The solid (dotted) contour levels are 0.1 (-0.05). The positive contour level encloses a region of strong downwelling while the negative contour level encloses a broad region of weaker upwelling. The vectors (arrows) show the magnitude and direction of the horizontal perturbation velocities (u' , v') induced by a Langmuir cell. (a) – (f) $t - t_m = (-30.2, -12.5, -3.04, -0.003, 3.37, 12.8)$ h respectively. Note the change in the horizontal and vertical scales between the lower and upper panels. Here $t_m = 45.625$ h is based on a constant storm translation speed $V_h = 5.5$ m s⁻¹ and the initial storm center location. Thus for time $t - t_m < 0$ is ahead of the storm and $t - t_m > 0$ is behind the storm (from Sullivan et al. 2012)

F. AIR-SEA INTERACTION

Enthalpy fluxes across the air-sea interface are proportional to the surface wind speed, which is tied to the momentum drag (C_d) formulation. Direct flux measurements over tropical ocean basins from selected field experiments have shown a very good agreement for wind speeds $< 20 \text{ ms}^{-1}$ (Figure 8, C. Fairall 2012, personal communication). Notice the spread of transfer coefficients from the models is larger than from the observations. However, the uncertainty on the fluxes in the TC high wind speed regime is much larger for both observations and models (Figure 9). The flux measurements from the wave tank, aircraft dropsonde, and momentum budget analysis of radar winds have a larger spread of momentum drag for wind speed $> 20 \text{ ms}^{-1}$ (Large and Pond 1981; Powell *et al.* 2003; Black *et al.* 2007; Andreas *et al.* 2012; Bell *et al.* 2012). For example, the momentum drag values for a wind speed of 50 ms^{-1} is as low as 0.001 (Jarosz *et al.* 2007) and as high as 0.003 (Bell *et al.* 2012). Recent research suggests that the momentum drag does not continue to increase with wind speed. However, whether the momentum drag asymptotes at a certain wind speed or it begins to decrease in higher winds remains controversial.

One interesting aspect from the published momentum drag coefficients is that the magnitude of the drag is near the lower bound of the spread if it is estimated from the ocean observation (Jarosz *et al.* 2007; D’Asaro *et al.* 2007; Sanford *et al.* 2011; Fan *et al.* 2010). A possible explanation is that part of the wind momentum deposited in the ocean is advected away by swell and thus not all of the energy from wave breaking is transferred to the ocean currents, and then to the vertical current shear to generate the upper-ocean mixing. If these effects are not negligible, then an important consideration for the parameterizations of air-sea momentum exchange for the coupled ocean-TC model is that the model must directly include wave coupling or some parameterization to account for the local loss of momentum due to advection by the swell.

Most formulations of the atmospheric model surface physics are based on the Monin-Obukhov similarity theory. The fluxes of the momentum, sensible heat, and latent heat between the atmosphere and ocean are determined by three bulk transfer coefficients and the atmospheric stability. The atmospheric stability plays a minor role in the air-sea

energy exchange in an unstable regime, but may be important over the cold wake where the atmosphere boundary layer is stable (warm air over cold water). The sensible and latent heat fluxes at the air-sea interface are determined by heat and moisture exchange coefficients. Both the Coupled Boundary Layer Air-Sea Transfer (CBLAST) hurricane results (Drennan *et al.* 2007) and recent wave tank experiments (Jeong *et al.* 2012, Haus *et al.* 2010) all suggest the heat and moisture transfer coefficients (C_k) do not change much as wind speed increases (Figure 10). The upper bound of C_k is around 1.2×10^{-3} for wind speeds $> 20 \text{ ms}^{-1}$. Using the upper bound of C_k and the upper and lower bounds of C_d , the C_k/C_d ratios are 1.2 and 0.4, respectively.

Because a large uncertainty exists as to the exact value of the momentum drag coefficient, it is important to understand the sensitivity in the coupled model to different momentum drag coefficients, and specifically on the collective impacts on the predictions of the TC structure, ocean cooling, and surface wave forecasts. Recent advancements in coupling the surface wave model to the atmosphere and the ocean models now allow derivation of the sea state-dependent momentum drag, which provides a non-uniform drag distribution in the model TC. Research has suggested that the surface wave conditions such as wave age (Doyle 2002; Moon *et al.* 2004a,b; Fan *et al.* 2009a,b), breaking waves (Donelan *et al.* 2012), sea spray (Andreas *et al.* 2007; Fairall *et al.* 2009; Bao *et al.* 2011), and Langmuir circulations may affect the spatial distribution of momentum drag and upper-ocean mixing (Kantha and Clayson 2004).

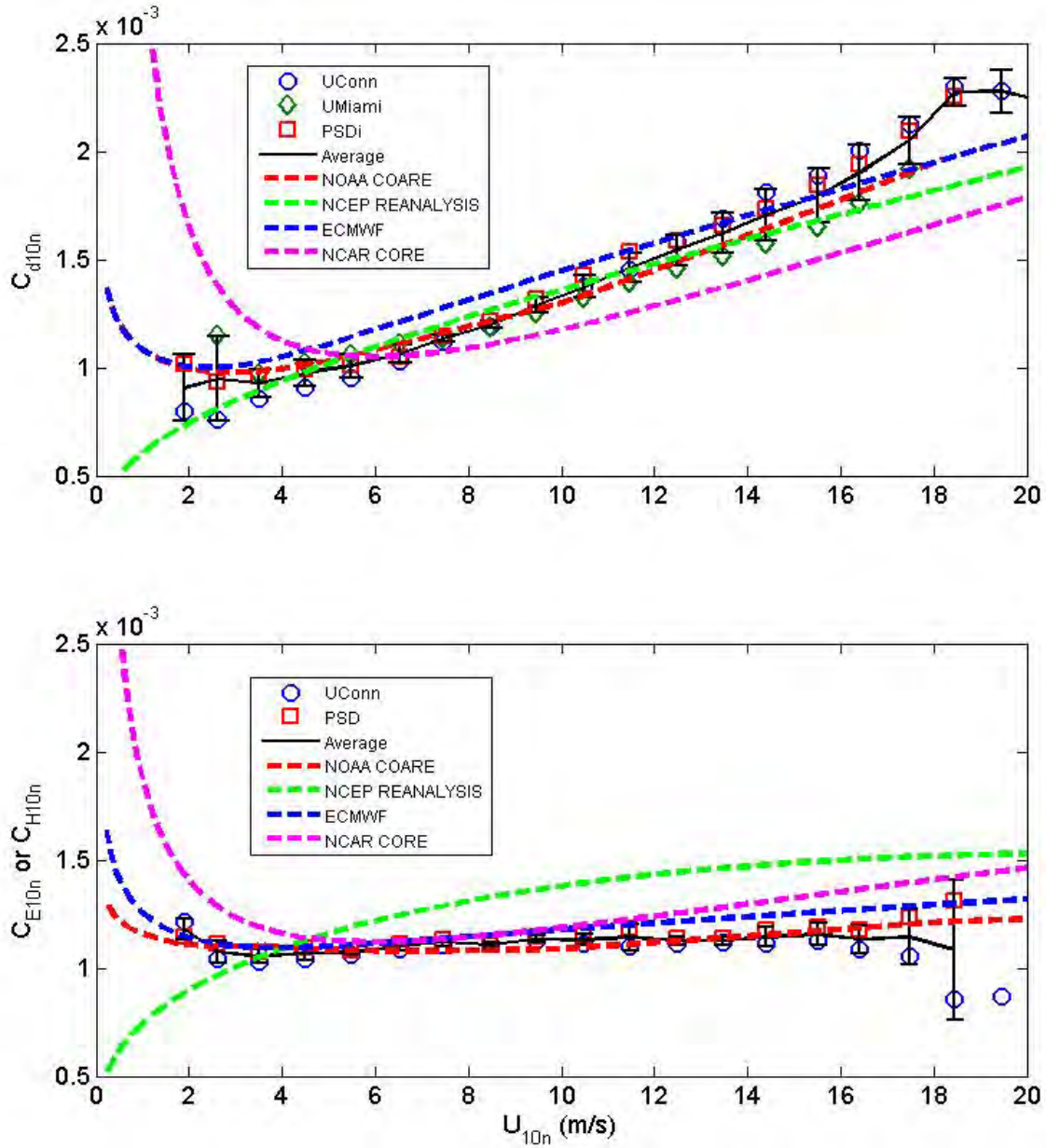


Figure 8. Wind speed (U_{10} ; m s^{-1}) dependence of (top) momentum, and (bottom) heat and moisture transfer coefficients from eddy covariance observations and from models (from C. Fairall 2012, personal communication). Note that the models have more spread than do the observations.

The impacts of wave coupling on the TC intensity change remain uncertain. Doyle (2002) found that including atmosphere-surface wave coupling for three simulated hurricanes produced negligible instantaneous maximum wind speeds ($< 0.1 \text{ ms}^{-1}$ average of three cases over four time periods) and led to a one meter smaller significant wave heights compared to the uncoupled simulations. However, idealized air-ocean-wave coupled model hurricane simulations by Liu et al. (2011) indicated the atmosphere-surface wave coupling increased the maximum wind speed by 8 ms^{-1} . In their idealized simulations, the TC intensity in the coupled atmosphere-ocean-wave model was generally reduced relative to the uncoupled simulation due to the larger ocean cooling underneath the TC. Recently Lee and Chen (2012) found the air-ocean-wave coupling simulation was superior to the uncoupled and air-ocean coupled simulations. Ocean coupling and ocean-wave coupling were not considered in the studies by Doyle (2002) and Lee and Chen (2012), respectively.

Discrepancies among these results may be attributed to the different treatments of the air-sea interaction processes, parameterization of the air-sea enthalpy and momentum fluxes, ocean-wave coupling, wind-wave coupling, and the nonlinear interaction of component model errors within the coupled system. The TC structure changes may also change the spatial distribution of momentum drag as well as the wake cooling modulated by the surface waves. It is clear from the aforementioned studies that the magnitude of the wake cooling is primary determined by wind induced mixing at the base of the mixed layer, upwelling under the TC eye, and modulated by wind-wave interaction. The transfer of momentum flux to the ocean is parameterized by the momentum drag formulation. How the momentum flux across the air-sea interface is computed varies widely in the coupled models.

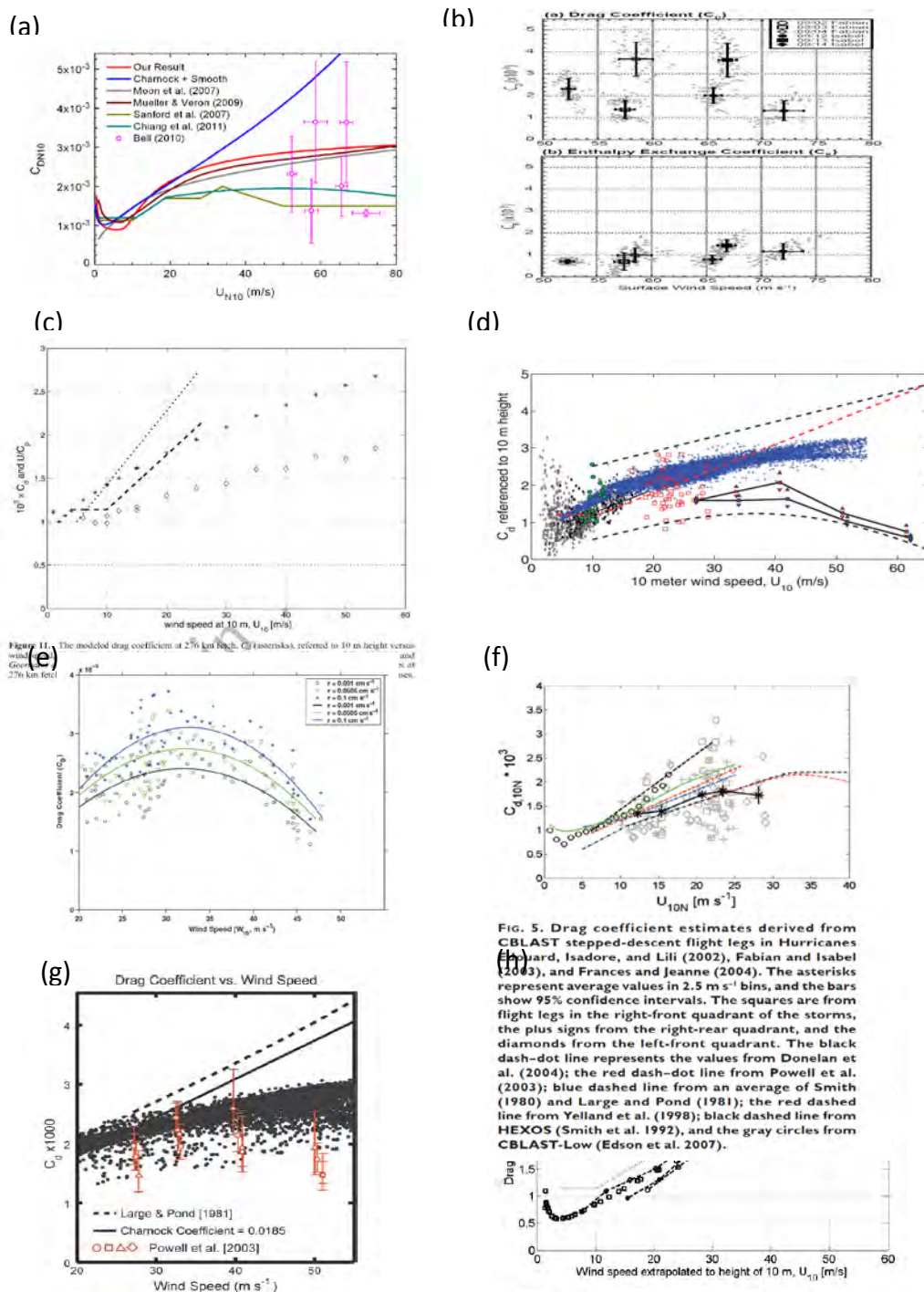


Figure 9. Various momentum drag coefficient estimates. (a) Large and Pond (1981), (b) Bell et al. (2012), (c) Moon et al. (2004c), (d) Donelan et al. (2004), (e) Jarosz et al. (2007), (f) Black et al. (2007), (g) Moon et al. (2004c), and (h) Donelan et al. (2004).

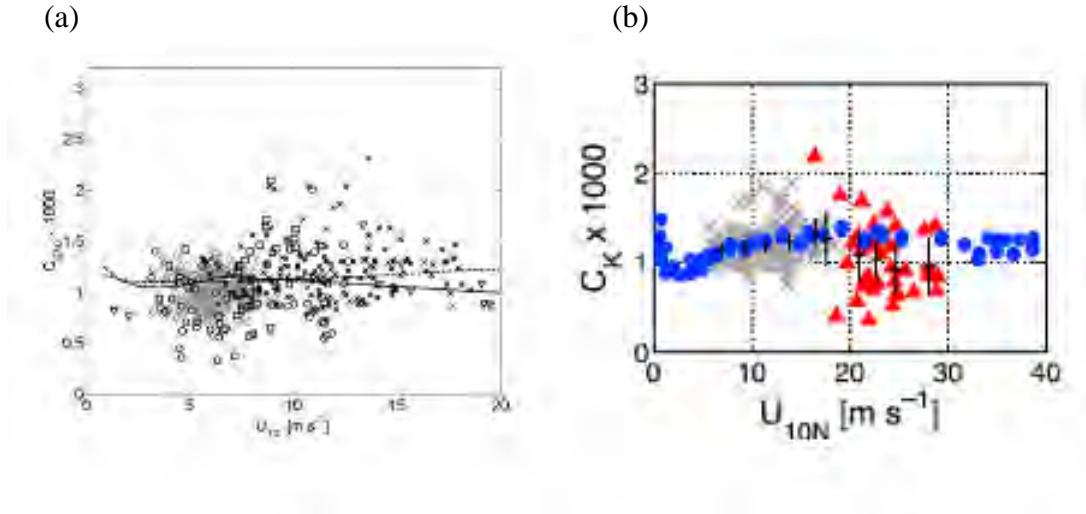


Figure 10. Enthalpy flux drag coefficient measurements at wind speeds $< 20 \text{ m s}^{-1}$ from (a) Drennan et al. (2007) and (b) at higher wind speeds from Haus et al. (2010).

G. PRECONDITION OF THE PRE-STORM OCEAN ENVIRONMENT

A limited parameter space of ocean effects on TC intensity was explored by Schade and Emanuel (1999) using a very simple idealized, axisymmetric coupled TC model. They found that smaller ocean mixed layers, stronger upper-ocean stratification, larger atmospheric boundary layer moisture, slower TC translation speed, larger storm size, higher storm intensity, or lower latitude will contribute to a stronger cold wake and a less intense TC.

Subsequent studies by Lin et al. (2008, 2009) reaffirmed that the pre-storm ocean conditions have an important role in the ocean response to TC forcing. With a deeper thermocline, the negative impact of the cold wake to TC intensity change is reduced. Furthermore, a negative correlation exists for storm intensification between TC translation speed and ocean heat content. If the TC is passing over a pre-existing cold oceanic eddy, the wake cooling is enhanced (Jaimes and Shay 2011). Passage over a deep warm-core eddy favors intensification of the TC due to inhibition of the wake cooling (Hong et al. 2000).

H. OCEAN COLD WAKE IMPACT ON THE TC KINEMATIC FLOW

Dynamic impact of the cold wake on the TC circulation was first demonstrated with a simple idealized hurricane model (Zou et al. 2004), and subsequently by a coupled simulation of Hurricane Katrina (Chen *et al.* 2010). Using the ocean-coupled version of the Coupled Ocean Atmosphere Mesoscale Prediction System (COAMPS), Chen *et al.* (2010) demonstrated the cold wake induced a broadening of the inner-core TC circulation, but not in the outer region, and the strongest convergence was shifted to downwind of the cold wake. Their coupled simulation also showed the equivalent potential temperature is decreased in the inner core, but is increased in the outflow region compared to the uncoupled run. Both studies indicated an increased asymmetry in the simulated TC vortex. Associated with the increase asymmetry is the reduction of the atmospheric mixed-layer depth and the depth of inflow layer over the ocean cold wake quadrant (Lee and Chen 2012). The mechanisms by which the wake affects the TC transverse circulation are not well understood. A recent coupled model study suggested an enhanced low-level inflow that transports the warm and moist air into the inner core region (Lee and Chen 2014). However, whether a dynamic pathway exists is still illusive and will be examined in this study.

The Eliassen (1952) vortex equations have been used to study the role of the secondary circulation in the vortex development. Using a transform form of Eliassen equations, the analytical solutions of Schubert and Haack (1983) indicate the thermally- or frictionally-forced balanced vortex circulation is proportional to the square root of the ratio of the vortex inertial stability and static stability ratio. Both solutions are affected by the 3D distribution of diabatic heating profile (Haack and Shubert 1986). When the maximum inner-core heating moves to a lower vertical level, more energy is projected onto higher order modes with smaller Rossby radii. The vortex with the lower-level heating profile develops quicker than with the higher-level heating profile. Shifting the heating toward outer radii with the same vertical heating profile, the tangential wind speed is decreased and the radius of maximum wind is increased. The conversion of potential energy to kinetic energy becomes less efficient as the heating is moved outward from the inner-core region of high vorticity.

In summary, many investigations have been conducted as to how the TC cold wake is generated, what kind of physical processes might influence the magnitude and location of the wake, and how TC intensity is related to its interaction with the cold wake. The magnitude of the wake cooling is primarily determined by ocean current-induced mixing at the base of the mixed layer, upwelling under the TC eye, and modulated the effects of precipitation, wind-wave, and wind-current interactions. The wake cooling is amplified over a pre-existing cold eddy, shallower mixed layer, and less stable pre-storm upper-ocean environment. Wake cooling underneath the TC eye reduces the air-sea energy exchange and thus tends to reduce the TC intensity. Numerical simulations suggest the cold wake increases the TC asymmetry, the region of convergence rotates to downwind of the wake, and increases the eye radius and secondary circulation. However, up to this date, the exact flow response imposed by the wake is still elusive and raises the question: Is there a dynamic pathway to the TC circulation change in response to the formation of cold wake?

I. OBJECTIVES OF THIS STUDY

In this study, various aspects of TC response to the cold wake are first investigated using a fully air-ocean-wave coupled version of the COAMPS-TC in an idealized axisymmetric setting. This, idealized axisymmetric COAMPS-TC is configured in both one-way influence and two-way interactive coupled models to systematically examine the sensitivity of TC intensity and structure changes to wake location, size, and magnitude to test the following three hypotheses:

- Hypothesis I: The TC intensity is sensitive to the location and magnitude of the cold wake relative to the track, such that a cold wake centered underneath the TC core has a more important impact on the intensity than a cold wake located to the right or left of the TC center. Starting first with simplified conditions, the objective is to understand the contributions of the physical mechanisms represented in the fully-coupled air-ocean-wave model as the TC interacts in different locations with the cold wake.
- Hypothesis II: Differential surface enthalpy fluxes over the ocean cold wake are the primary factor in creating an asymmetric structure in the TC circulation in a certain region of moderate winds outside the radius of maximum wind. In this region, the cold wake forces a low-level wake jet

that is deflected toward the center of the storm, and the strength of the wake jet depends on the magnitude of the wake cooling.

- Hypothesis III: The TC intensity reduction due to the cold wake has a significant dynamic contribution from the growth of baroclinic waves excited by the cold wake at the expense of the mean vortex as well as the thermodynamic contribution resulting from a change in the surface fluxes over the colder water.

THIS PAGE INTENTIONALLY LEFT BLANK

III. COAMPS-TC MODEL DESCRIPTION AND EXPERIMENT SET-UP

A. MODEL PHYSICS

The air-ocean-wave coupled COAMPS-TC system consists of three forecast models for the atmosphere, ocean, and waves. The atmospheric component uses an improved suite of atmospheric physics (Hodur 1997; Chen et al. 2003; Doyle et al. 2012) compared to the operational version of COAMPS. These new physics were specifically designed for TC prediction. The coupling between the atmosphere and ocean is described in Chen et al. (2010). An important difference from the two previously developed systems is a new fully coupled air-ocean-wave COAMPS-TC system that includes two inter-changeable wave component options - Simulating Wave Near shore (SWAN) and Wave Watch III. It also has the full interactive physics for the air-wave coupling and ocean current-wave coupling (Chen et al. 2011).

The atmospheric physics include the Fu-Liou four stream radiation scheme (Liu 2009), Mellor-Yamada (MY) 2.5 turbulent kinetic energy (TKE) closure mixing scheme (Mellor and Yamada 1974), Kain-Fritsch (KF) cumulus scheme (Kain and Fritsch 1990, Kain 2004), and a new COAMPS generalized microphysics scheme (J. Schmidt 2012, personal communication). The surface flux formula over the ocean follows COARE 3.0 (Fairall et al. 2003). For wind speeds greater than 27 ms^{-1} , the uncoupled and air-ocean coupled momentum drag coefficient asymptotes to a value of 0.025, which is similar to Powell et al. (2003).

Several variations of the MY TKE schemes are available in COAMPS-TC. A recent analysis of the approximations made to the first law of thermodynamics that are used to derive the conservative thermodynamic variables upon which the TKE closures are based, e.g., the ice-liquid potential temperature (θ_{il}) or the equivalent potential temperature (θ_e). These approximations to the first law leading to θ_{il} strongly over-predict the true thermodynamic state in the case of deep convection while those based on θ_e strongly under-predict the true state. This error increases in tropical environments in which the conditions at the lifted condensation level are warmer and more moist. The

calculation of buoyancy term in the COAMPS MY closure was recently modified to compute the mean turbulent eddy fluxes directly without the need for a mixing length assumption (J. Schmidt 2012, personal communication).

This fully coupled air-sea-wave model of Chen et al. (2014) provides a mechanism for examining frequent two-way feedbacks between the air-ocean, air-wave, and ocean-wave components. Several model variables are exchanged between each set of coupled components during the course of the coupled time-step (Figure 11).

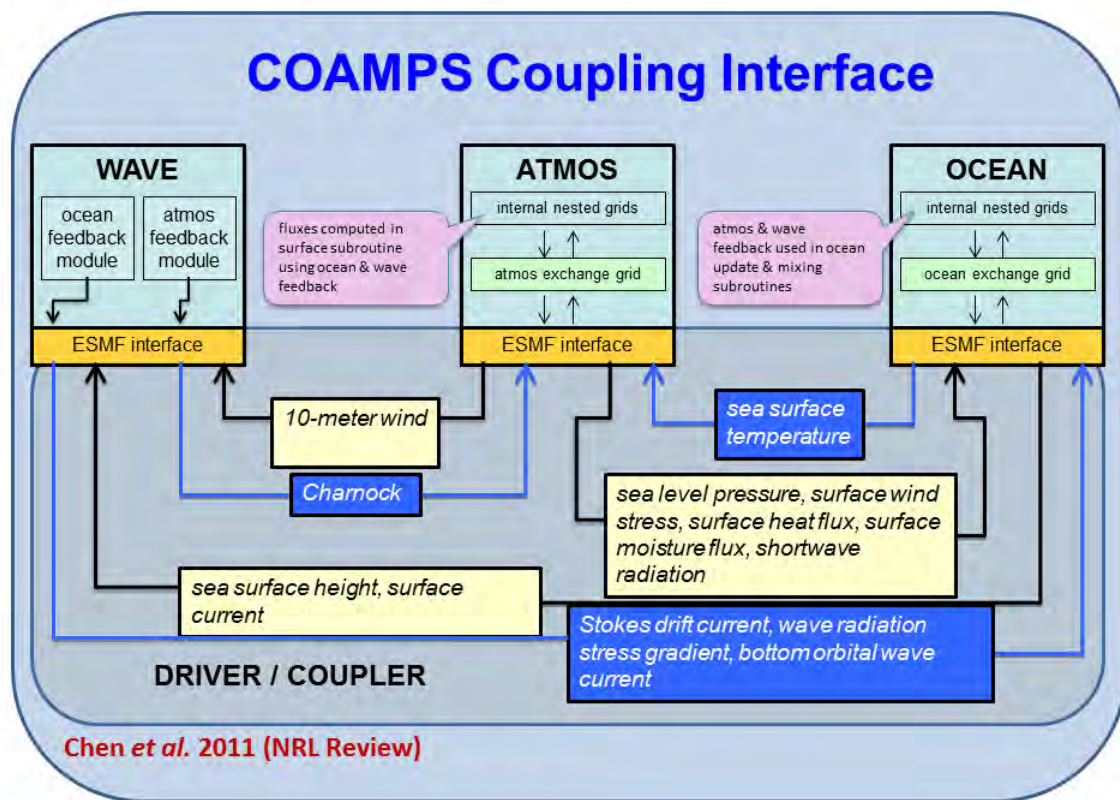


Figure 11. Flow chart of the air, ocean, and wave forecast components of the fully coupled COAMPS-TC system, where the exchanges between the components are through the Earth System Framework (ESMF). The coupling between each pair of component models is two-way (from Chen et al. 2011).

The atmospheric component provides a total of six ocean surface boundary forcing fields to the ocean component, and the ocean model returns a new sea-surface

temperature to the atmosphere model that then influences prediction of the atmospheric surface fluxes and wind stress in the next time step. The ocean component also provides the current field and sea-surface height to the wave component, and the atmospheric component impacts the waves through the wind-driven momentum drag. The feedback from the wave component to the ocean consists of ten forcing terms including the Stokes drift current, wave radiation stress gradients, wave-bottom current, and wave-bottom current radian frequency. When the COAMPS-TC is coupled with the wave model, a non-dimensional roughness length (Charnock) is used to relate to the atmospheric momentum drag. The sea-state dependent Charnock number is a function of wind speed and wave age following the Moon (2004) formulation for hurricane wind conditions. For wind speeds less than 10 ms^{-1} , a constant Charnock number of 0.016 is used, and the drag formulation utilized is the COARE 3.0 scheme.

For the wind-wave coupling, three options are available within the coupled COAMPS-TC (Figure 11) These options include an empirical wave age and wind speed coupling described by Moon et al. (2004c), which is a recent update of a similar scheme from the University of Rhode Island (I. Ginis 2011, personal communication), and the Jenssen scheme (Doyle 2002). All three schemes return a wave state-dependent Charnock number to feedback to the atmospheric surface flux scheme based on the surface roughness length. The wave state-dependent Charnock number is updated at the coupled interval. For the currents and wave interaction, an improved observation-based wave breaking and drag formulation is used in SWAN (Smith *et al.* 2012). The ocean-wave coupling considers the effect of Stokes' drift and wave radiation stress due to horizontal gradients of the energy in the surface waves. Direct energy dissipation from wave breaking to currents is not currently considered in the coupled version of COAMPS-TC, but empirically enters in the wind-wave coupling parameterization.

Along with the component forecast models, the fully coupled COAMPS-TC system has the option of two independent 3DVAR data assimilation systems (Figure 12). The atmosphere uses the Navy Atmospheric Variational Data Assimilation System (NAVDAS; Daley and Barker 2001) that includes TC relocation and initialization algorithms. At the analysis time, the first-guess fields are relocated to the observed TC

location. Next, the new first- guess fields are combined with 49 synthetic atmospheric temperature, moisture, and wind profiles at nine vertical levels to better define the TC and its immediate environment. Next, NAVDAS uses a reduced correlation length scale and relaxation of the geostrophic balance near the TC center to improve the covariance used in the analysis (Liou and Sashegyi 2011).

The ocean component is the Navy Coastal Ocean Model (NCOM) that uses the Navy Coupled Ocean Data Assimilation (NCODA), which is an equivalent oceanographic implementation of NAVDAS (Cummings 2005; Smith et al. 2011). In the two-dimensional mode, NCODA analyzes the SST, sea ice, significant wave height (SWH), and sea-surface height (SSH) using a univariate data assimilation method. The 3D analysis of sea temperature, salinity, and u and v currents is multivariate. NCODA has options to perform the data assimilation on either the native ocean model sigma grid or at constant depth levels. When the COAMPS-TC system is run in the cycling mode, the NAVDAS and NCODA data assimilations are run sequentially prior to the forecast every six or 12 hours.

Air-Ocean-Wave Coupled COAMPS Forecast and Data Assimilation System

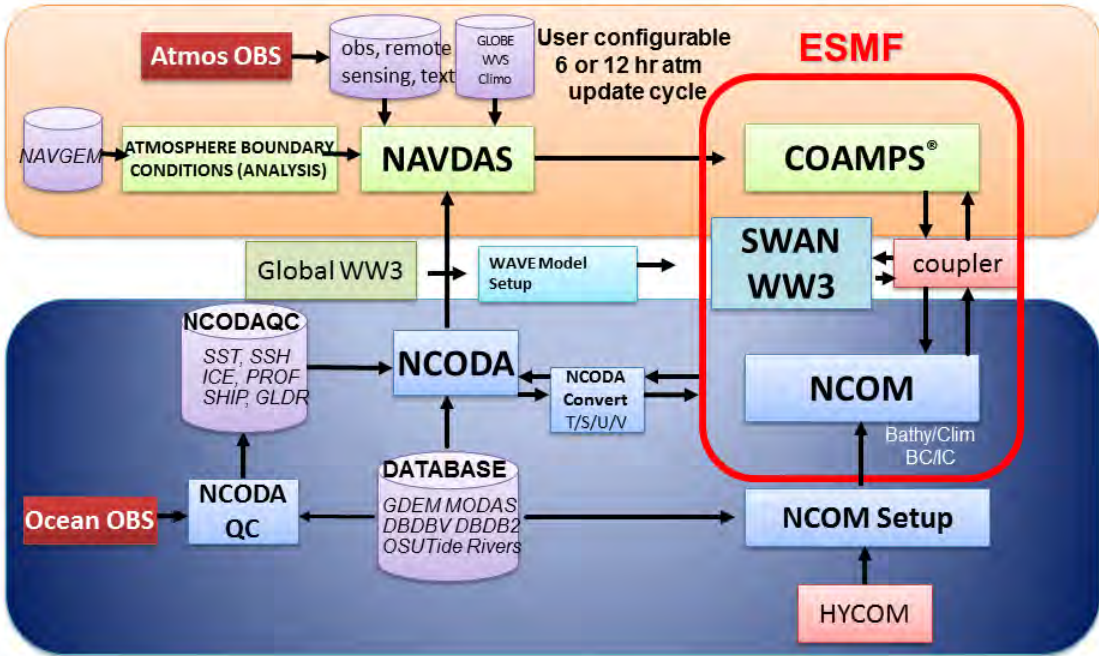


Figure 12. An illustration of the COAMPS-TC limited-area analysis and modeling system that uses the global atmospheric, ocean, and wave models to provide cold start initial and lateral boundary updates (from Chen et al. 2014).

B. TRAJECTORY AND 3D MOMENTUM BUDGET ANALYSIS

Two new capabilities in COAMPS-TC have been developed for this research to improve the interpretation of the model results presented here. These two analysis tools are the parallel implementation of Lagrangian particle trajectories and a 3D momentum budget of the model output. Both utilities are set by the user at the compilation stage using the “-DMBUDGET” and “-DTRAJECT” compilation flags. The corresponding namelist variables to activate the trajectory and momentum budget output are listed in Table 3. The trajectory is calculated at each model large time-step from the 3D wind information from the inner-most nest. The mass fields such as temperature, moisture, and pressure as well as u and v momentum budget terms are interpolated to the trajectory locations.

Table 3. COAMPS namelist variables for the trajectory and momentum budget outputs.

Namelist	ltraj	itraj	rttraj	lmbudg	ksavm
description	Logical flag =t turn on trajectory	Integer array trajectory release (i,j,k) locations	Real array trajectory release time (hr, min, sec)	Logical flag =t turn on 3D momentum budget output	Integer array output interval (hr, min, sec)

The changes of horizontal momentum are calculated in the Cartesian sigma coordinate as the sum of the local change, geostrophic forcing, damping, horizontal advection, vertical advection, Coriolis, vertical mixing, and horizontal diffusion (Eqs. 1-2).

$$\frac{\partial u}{\partial t} + c_p \theta_v \left[\frac{\partial \pi'}{\partial x} + G_x \frac{\partial \pi'}{\partial \sigma} \right] - K_D \left[\frac{\partial D_3}{\partial x} + G_x \frac{\partial D_3}{\partial \sigma} \right] = -u \left(\frac{\partial u}{\partial x} \right)_\sigma - v \left(\frac{\partial u}{\partial y} \right)_\sigma - \sigma \left(\frac{\partial u}{\partial \sigma} \right) + fv + D_u + K_H \nabla^4 u \quad (1)$$

$$\frac{\partial v}{\partial t} + c_p \theta_v \left[\frac{\partial \pi'}{\partial y} + G_y \frac{\partial \pi'}{\partial \sigma} \right] - K_D \left[\frac{\partial D_3}{\partial y} + G_y \frac{\partial D_3}{\partial \sigma} \right] = -u \left(\frac{\partial v}{\partial x} \right)_\sigma - v \left(\frac{\partial v}{\partial y} \right)_\sigma - \sigma \left(\frac{\partial v}{\partial \sigma} \right) - fu + D_v + K_H \nabla^4 v \quad (2)$$

The second term on the left side is the geostrophic forcing, G is the metric of coordinate transform to the sigma surfaces, D_3 is the density- and potential temperature-weighted 3D divergence together with the use of diffusion coefficient K_D that filters the sound waves, f is the Coriolis, D_u and D_v are the subgrid scale mixing, and the last term represents the horizontal diffusion that controls the nonlinear instability. This horizontal momentum budget is output at the trajectory time and then is transformed to cylindrical coordinates centered on the feature for further analysis.

C. AXISYMMETRIC IDEALIZED TC CONFIGURATION

The idealized axisymmetric TC configuration option that also exists in COAMPS-TC will be utilized to set up simplified conditions to understand the physical mechanisms in the TC-cold wake interaction.. The underlying physics options are the same as in the

real-data COAMPS-TC. Instead of using an initial bogus vortex as in the real-data integrations, the idealized vortex is spun up based on a user-specified initial tropical environment sounding. The spin-up process starts with an initial annulus of low-level wind speed of 25 ms^{-1} . The radii of the two concentric circles that form the annulus are 90 and 240 km, respectively. The surface friction forces the low-level convergence and vertical motion within the annular ring. Model mass fields adjust to winds by means of convection. The initial environment wind profile is also user-specified. A mean wind speed can be subtracted from the model winds to account for the movement of the model-simulated TC and thus to keep the TC close to the center of the model domain.

A digital filter (Lynch and Huang 1992) with a 2 h integration time window is applied prior to the start of the model to ensure the wind and mass fields in the initial idealized vortex are balanced. During the digital filter integration time window, all model physics are turned off. Similar to the real-data COAMPS-TC, the idealized COAMPS-TC has the nesting capability with a nesting ratio of 1:3. The interaction between the inner and outer domains is two-way and the update of the nests is performed on the seven grid points along the nested domain lateral boundaries using the Davies (1976) lateral boundary condition. Prior to the inner to outer domain feedback, a nine point smoother is applied to the values on the inner domain. The upper boundary condition uses a radiation-type condition (Klemp and Wilhelmson 1978) that allows the inertial gravity waves excited by the TC convection to exit the model upper boundary. Similarly, the coarse domain also uses a radiative lateral boundary condition (Klemp and Wilhelmson 1978) to allow the inertial gravity waves excited by the convection to propagate out of the model coarse domain.

All idealized model experiments presented here have the atmospheric model top set at around 29 km. The model domains consist of: a coarse mesh of 201×201 grid points with 9 km horizontal spacing, nest 2 of 301×301 grid points at 3 km spacing, and nest 3 of 499×499 grid points at 1 km spacing. There are a total of 70 vertical sigma levels with vertical resolution ranging from 20 m throughout the lowest 560 m to 1000 m at the top four model levels. A forward-in-time integration scheme is used for all model scalar fields (J. Schmidt 2012, personal communication), while the model momentum

fields are calculated with a leap-frog time scheme with the Robert (1966) time filter to filter out the sound waves. The hybrid forward time scheme performs better in preserving the sharp gradients in the model than does the leap-frog scheme. The coarse domain model time step is 20 seconds.

In the two-way coupled experiments, the ocean model domain contains 601x601 grid points with horizontal grid spacing of 3 km and 51 vertical layers, of which 20 layers are in the upper 100 m of ocean. The ocean depth is 4000 m with a flat bottom. The model time step for the ocean model is 15 seconds. The coupling interval is 2 minutes.

The initial atmospheric thermodynamic sounding profile for all experiments is from a two-year composite mean nighttime tropical cloud cluster sounding over the western North Pacific (Gray et al. 1975). While the Gray mean temperature profile extends to 80 hPa, the relative humidity profile is only up to 400 hPa, so the initial mixing ratios above that level are set to zero. The conversion of relative humidity to mixing ratio is from the Smithsonian tables (Bolton 1980). Since the model top is much higher than the mean Gray cloud cluster sounding, the temperature above 80 hPa is assumed to be isothermal, i.e., the value at 80 hPa. This sounding is compared in Figure 13 with the Atlantic mean tropical sounding from Jordan (1958) and non-SAL mean Atlantic sounding from Dunion and Marron (2008). Compared to the Jordan mean sounding, the Gray mean cloud cluster sounding is slightly warmer in the mid-troposphere above 600 hPa. The Gray mean sounding moisture above 900 hPa is also much larger than in the Jordan or Dunion and Marron non-SAL sounding. Temperature, mixing ratio, and relative humidity values for the Gray tropical mean cloud cluster sounding are provided in Table 4.

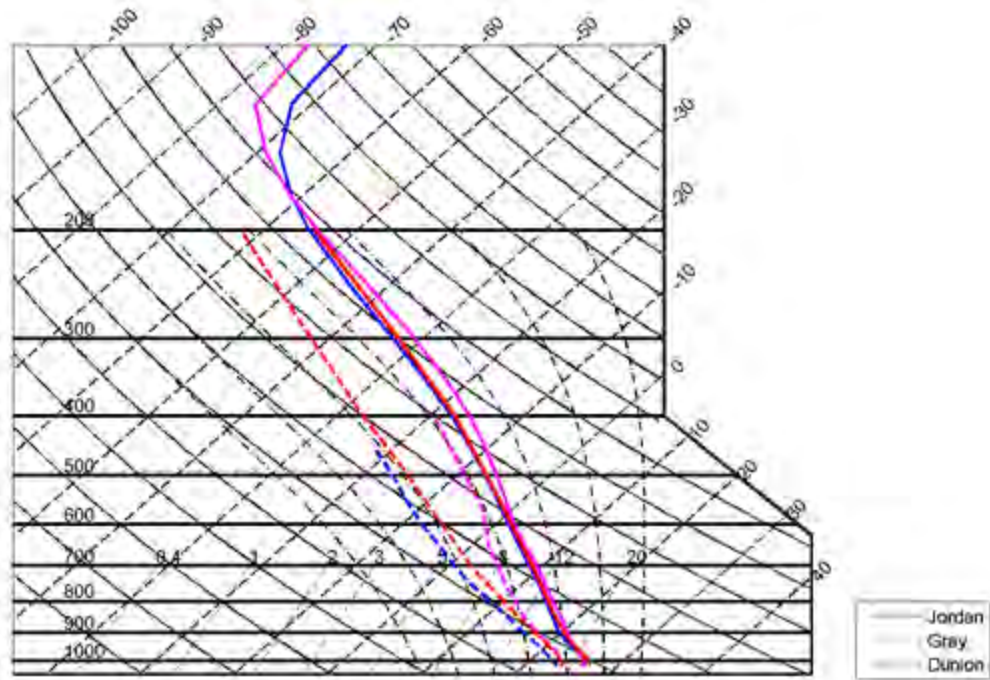


Figure 13. Nighttime mean tropical summer soundings from the West Indies (Jordan 1958, blue lines), western North Pacific (Gray et al. 1975, magenta lines), and non-SAL West Indies (Dunion and Marron 2008, red lines).

Table 4. Nighttime temperature and moisture values from the mean tropical cloud cluster sounding of Gray et al. (1975).

Pressure (mb)	Temperature (°C)	Mixing ratio (g/kg)	Relative humidity (%)
1015 (sfc)	26.1	18.8	88
1000	25.9	18.6	87
950	23.2	16.6	87
900	20.7	14.2	82
850	18.2	12.2	78
800	15.4	10.7	77
750	12.5	9.1	75
700	9.4	8.0	75
650	5.7	6.7	76
600	2.0	5.9	80
550	-1.7	5.0	81
500	-5.7	3.9	77
450	-10.4	2.9	74
400	-15.8	2.0	72
350	-22.6	0	
300	-30.9	0	
250	-41.3	0	
200	-54.3	0	
175	-61.6	0	
150	-69.1	0	
125	-76.0	0	
100	-77.5	0	
80	-72.9	0	
30	-72.9	0	
10	-72.9	0	

D. EXPERIMENT DESIGN

1. Uncoupled and One-Way Coupled Experiments

Two groups of the idealized experiments are designed to systematically quantify the interaction of the TC and its cold wake. Considering the nonlinearity and the complexity of the interaction between the TC and its cold wake, a more controlled examination of the wake is required. All model simulations are on an f -plane and the short-wave radiative forcing is calculated at 20°N and 120°E, which eliminates the differential radiative forcing from the latitudinal and longitudinal differences. In the group 1 experiments, the basic flow is at rest with a prescribed time-invariant cold wake. The response of the TC flow fields is first studied by comparing one-way influence simulations with and without the SST cold anomaly. In the group 1 simulations, the SST is updated with a prescribed cold wake after the simulated idealized TC has spun-up to CAT4 strength at 36 h, and this SST cold anomaly is fixed to the end of the 72 h simulation. Although the instantaneous switch-on of the cold wake does not represent conditions in nature, the shock to the simulated TC is quickly adjusted. In the group 2 experiments, a two-way interaction of the TC circulation with its cold wake is simulated.

The control run (CNTL) is also uncoupled with a horizontally uniform SST of 303 K that is invariant in time. For Hypothesis I, five sensitivity experiments are performed to examine the TC response to the location, shape, and magnitude of the cold wake (Table 5). A schematic illustration of the characteristics of these prescribed cold wakes is given in Figure 14. Experiment 1 (Wake 1, Figure 14a) has a circular-shape wake that is of 2°C colder than the surrounding area underneath a TC with an initial eyewall radius of 60 km. Experiment 2 (Wake 2) is similar to Wake 1 except the wake is a half circle that is of 4°C colder than the surrounding area and is located on the north side of the eye (Figure 14b). Experiment 3 (Wake 3) has an oval-shape wake that is about the same size as the circle-shaped wake in Wake 1 (Figure 14c). The length of the Wake 3 is 270 km and it is located to the right-rear side of the eye. Experiment 4 (Wake 4) has a crescent-shaped wake that is 10% larger than the wake in Wake 1 (Figure 14d). Experiment 5 has the same circular shape as in Wake 1, except the magnitude of the

wake is increased from 2°C to 4°C. Environmental vertical wind shear effects are not considered in the Wake 1 through Wake 5 experiments.

Table 5. Description of five prescribed wake sensitivity experiments

Experiment Name	Shape of cold anomaly	Magnitude of cold anomaly (°C)	Basic environmental flow
Wake 1	circle	2	At rest
Wake 2	Half a circle	4	At rest
Wake 3	oval	2	At rest
Wake 4	crescent	2	At rest
Wake 5	circle	4	At rest

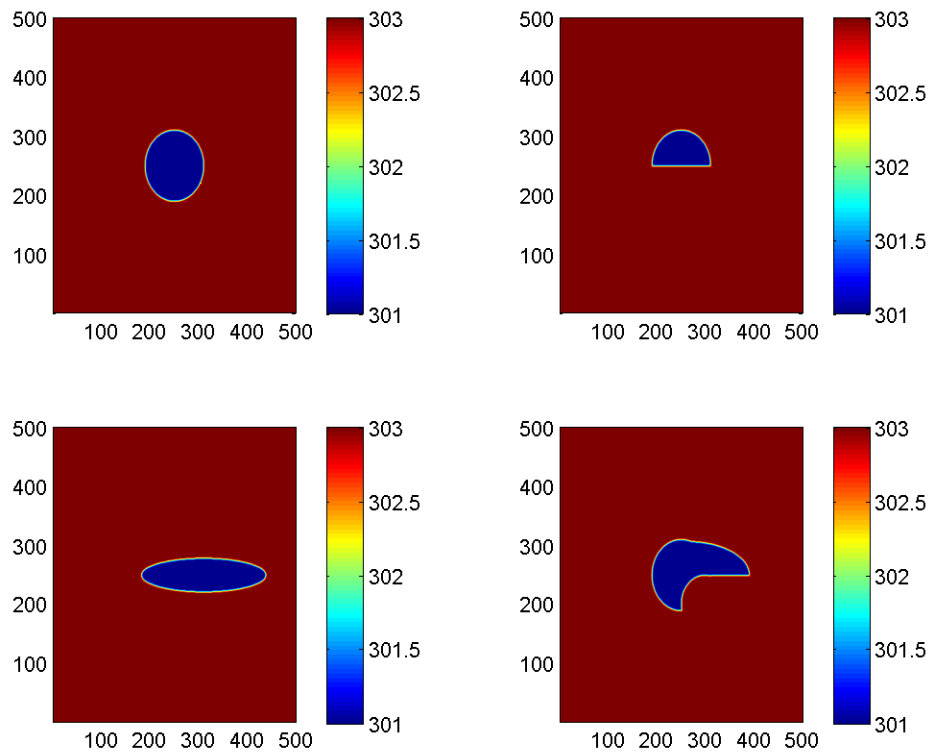


Figure 14. Schematic illustration of the ocean cold Wake 1 through Wake 4 sensitivity experiments: (a) a circle-shape wake, (b) a half-a-circle-shape wake, (c) an oval-shape wake, and (d) a crescent-shape wake. The magnitude of the SST cold anomaly (blue color) is 2°C.

2. Air-Ocean Coupled Experiments

Two-way interaction of TC with its cold wake will also be investigated using two idealized air-ocean coupled experiments (EXPA and EXPB). The initial ocean temperature and salinity profiles (Figure 15) are from a composite of six ITOP surface and subsurface moorings A1, A2, A4, SA1, SA2, and SA4 from 14-16 September 2010, prior to the passage of Typhoon Fanapi. The salinity profile above 130 m and below 500 m is extrapolated from the composite. These characteristics of the Fanapi pre-storm composite include a SST that is close to 30°C (i.e., about the same magnitude as in the uncoupled control run), a mixed layer depth of 60 m, and an ocean heat content (ohc100) of 1.3 kJ. The temperature jump criteria used to specify the mixed layer depth is 0.15°C and the ohc100 is the heat integrated from the surface to 100 m depth. A quiescent initial ocean and wave field is specified. Predicted currents and surface wave developments subsequently are forced by the TC wind and motion. The initial atmospheric temperature and humidity profiles are as in group 1, which is the Gray et al. (1975) mean western North Pacific tropical cloud cluster nighttime sounding.

Slow (2 m s^{-1}) and moderate (5 m s^{-1}) westward-moving storm translation speeds are used to reproduce cold wakes similar to wake 3 and wake 4 (trailing cold wake). Early uncoupled ocean model experiments with less complicated atmospheric and oceanic models have shown a slow (faster) TC translation speed promotes more (less) cold wake response (Chang and Anthes 1978; Price 1981). Larger initial ocean heat content and a more stable upper-thermocline temperature profile also reduce the magnitude of the cold wake.

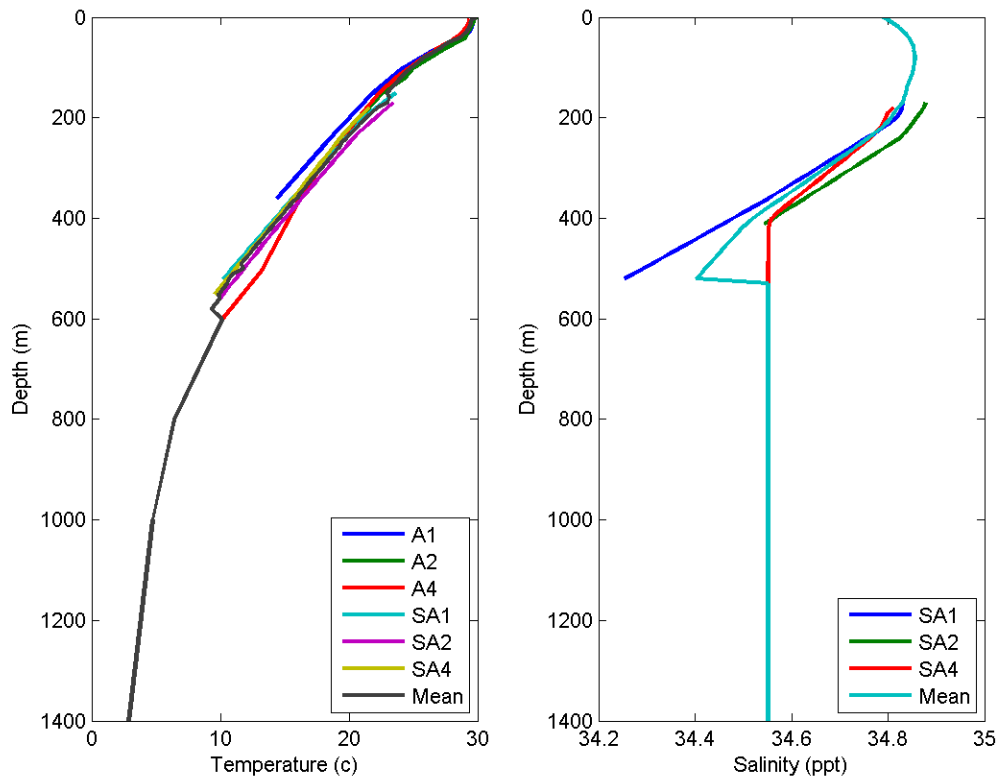


Figure 15. Initial ocean temperature and salinity profile for the two-way coupled TC-wake experiment. The composite is derived from ITOP surface and subsurface moorings A1, A2, A4, SA1, SA2, and SA4 for pre-Fanapi during 14-16 September 2010.

IV. UNCOUPLED CONTROL SIMULATION

The axisymmetric and asymmetric structure of the TC kinematic and thermodynamic responses to the cold wake will be described in this chapter. Discussion of the control (uniform and constant SST) experiment will be given in Chapter IV and the five cold wake experiments with variable SST but fixed in time will be described in Chapter V.

To remove transient features, an azimuthal- and time-mean composite in radial-height coordinates is used to examine the axisymmetric structures. The asymmetric deviations relative to the axisymmetric vortex are revealed by a wavenumber decomposition using the discretized Fast Fourier Transform (FFT). First, the model field is transformed from the Cartesian to cylindrical coordinates. Next, the perturbation is obtained by removing the azimuthal mean at each vertical level and radius. Finally, an azimuthal 1-D FFT is applied. By filtering the FFT series using a box window in the middle of the FFT series (i.e., set the coefficients of higher wave numbers to zero inside the box), discretized wave 1-5 fields are obtained after inverting the FFT of the filtered field back to the original field.

The intensification of the TC in the uncoupled control (CNTL) experiment is with a time invariant 303K SST. The maximum wind speed increases rapidly from Saffir-Simpson category (CAT) 1 at 12 h forecast time to a CAT5 by 42 h (Figure 16). After 42 h, the maximum wind speed oscillates between 80-90 m s⁻¹. The maximum wind speed and minimum SLP at 72 h are 95 m s⁻¹ and 936 hPa, respectively (Figure 16).

The relationship between surface pressure (P) and maximum sustained surface wind speed (W) has been studied frequently, and numerous P-W relationships have been developed (Knaff and Zehr 2007, Holland 2008). A polynomial fit of degree 2 calculated for the CNTL SLP and maximum 10 m wind V_{\max} (Figure 17) gives the relation

$$V_{\max} = -0.01(1010 - P)^2 + 2.5(1010 - P) + 45 \quad (3)$$

This nonlinear equation predicts 98% of the CNTL maximum 10 m wind variance. Compared with previous P-W relationships using the CNTL SLP, the CNTL P-W curve lies to the right side of P-W curves derived from observations. The maximum wind predicted by the P-W relationship is larger than the P-W derived from a dataset that includes both the Atlantic and eastern North Pacific (Knaff and Zehr 2007; Holland 2008). Since no environmental vertical wind shear is imposed in the CNTL experiment, a stronger TC intensity is expected. Although the maximum wind from the CNTL P-W relationship is larger than suggested by Knaff and Zehr and Holland, the COAMPS P-W curve has a similar slope as the Knaff and Zehr curve.

One effect of vertical wind shear is to decrease the TC intensity by inducing a vertical tilt of the vortex in the downshear left direction (Jones 1995, 2000a,b; Frank and Ritchie 1999, 2001). Since no background vertical wind shear is imposed in the CNTL experiment, any vertical tilt of CNTL vortex may be attributed to the local shear produced by internal vortex dynamics. During the CAT3 - CAT5 stage intensification, the magnitude of the vertical tilt below 5 km height is small (~ 4 km in the horizontal). The vorticity maxima at 400 hPa and 850 hPa are almost vertically aligned until 72 h (Figure 18).

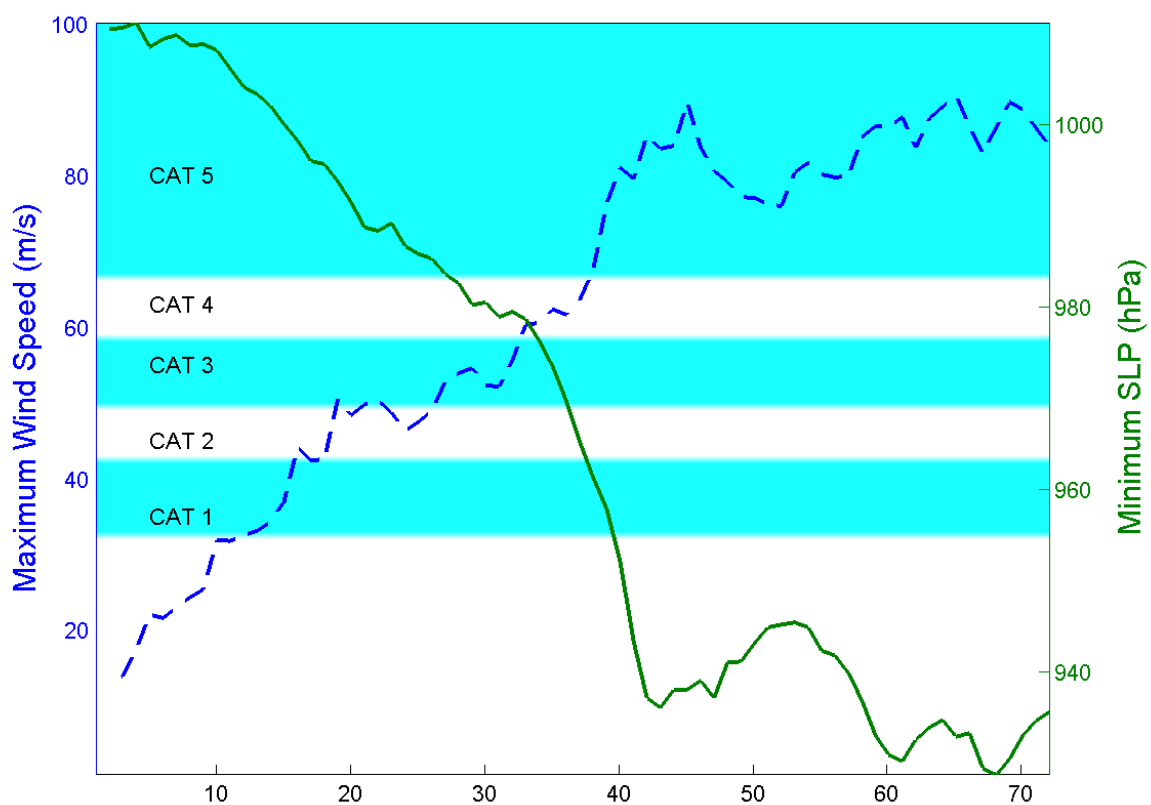


Figure 16. Maximum 10 m wind speed (m s^{-1} , blue dashed line) and minimum SLP (hPa, green line) during the first 72 h of the CNTL experiment.

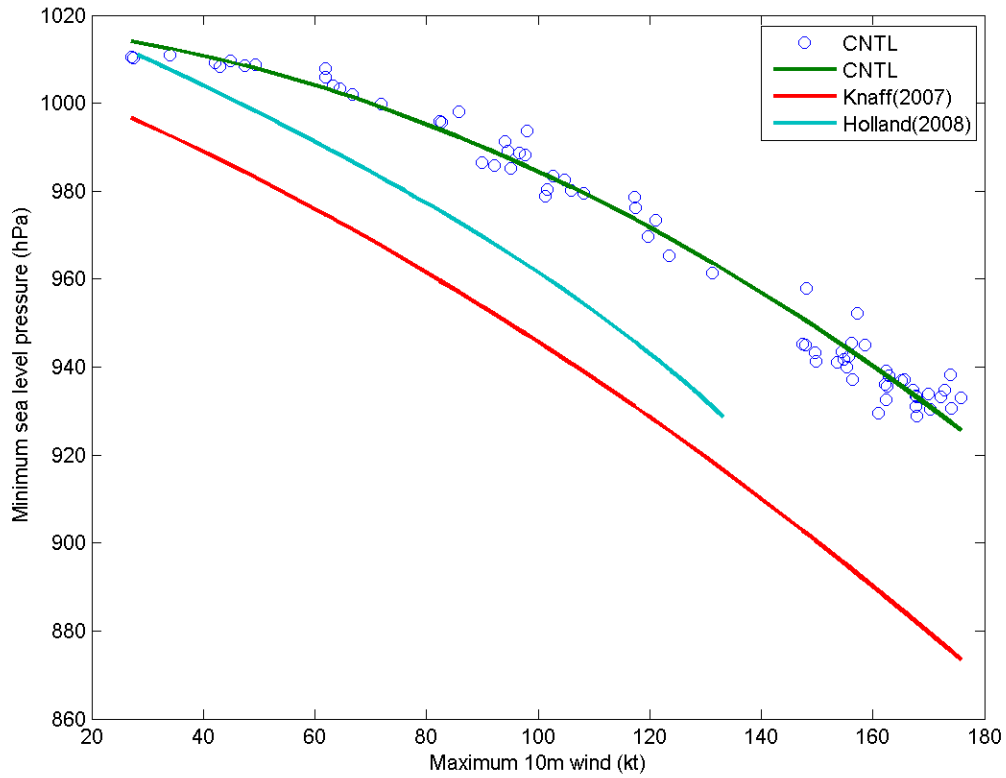


Figure 17. Minimum SLP (hpa) and maximum 10 m wind (kt) relationship for the CNTL experiment (blue circles). These data are fitted with a polynomial of 2 degree (black line) for comparison with other P-W relationships (see inset for sources).

Similar to previous studies (Montgomery and Kallenbach 1997; Carr and Williams 1989), the model-simulated vortex ring is not in a steady state; rather, the vortex alternates between axisymmetrization processes and asymmetric structures. Due to these asymmetries, the center of the vortex that was initially at the center of grid 3 has moved 55 km northwestward at 72 h (Figure 18). The movement initially starts around 36 h, when the TC reaches CAT4 intensity. After this time, the vorticity ring continuously evolves from triangular to elliptical and finally to a monopole vortex between 36-48 h. After 48 h, the vortex maintains a monopole structure. During this trochoidal oscillation period, 3-4 smaller mesovortices developed within the eye (Figure 19). These polygonal eyewalls, mesovortices, and the asymmetric eyewall contraction were similar to previous

studies (Schubert et al. 1999; Kossin and Schubert 2001, 2004; Montgomery et al. 2002; Hendricks et al. 2008). These studies attributed the inner-core vortex features to the asymmetric dynamics of potential vorticity (PV) mixing in the hurricane inner core, because PV is not conserved in the presence of diabatic heating. The PV mixing causes the vortex ring to become barotropically unstable, which destabilizes the vortex.

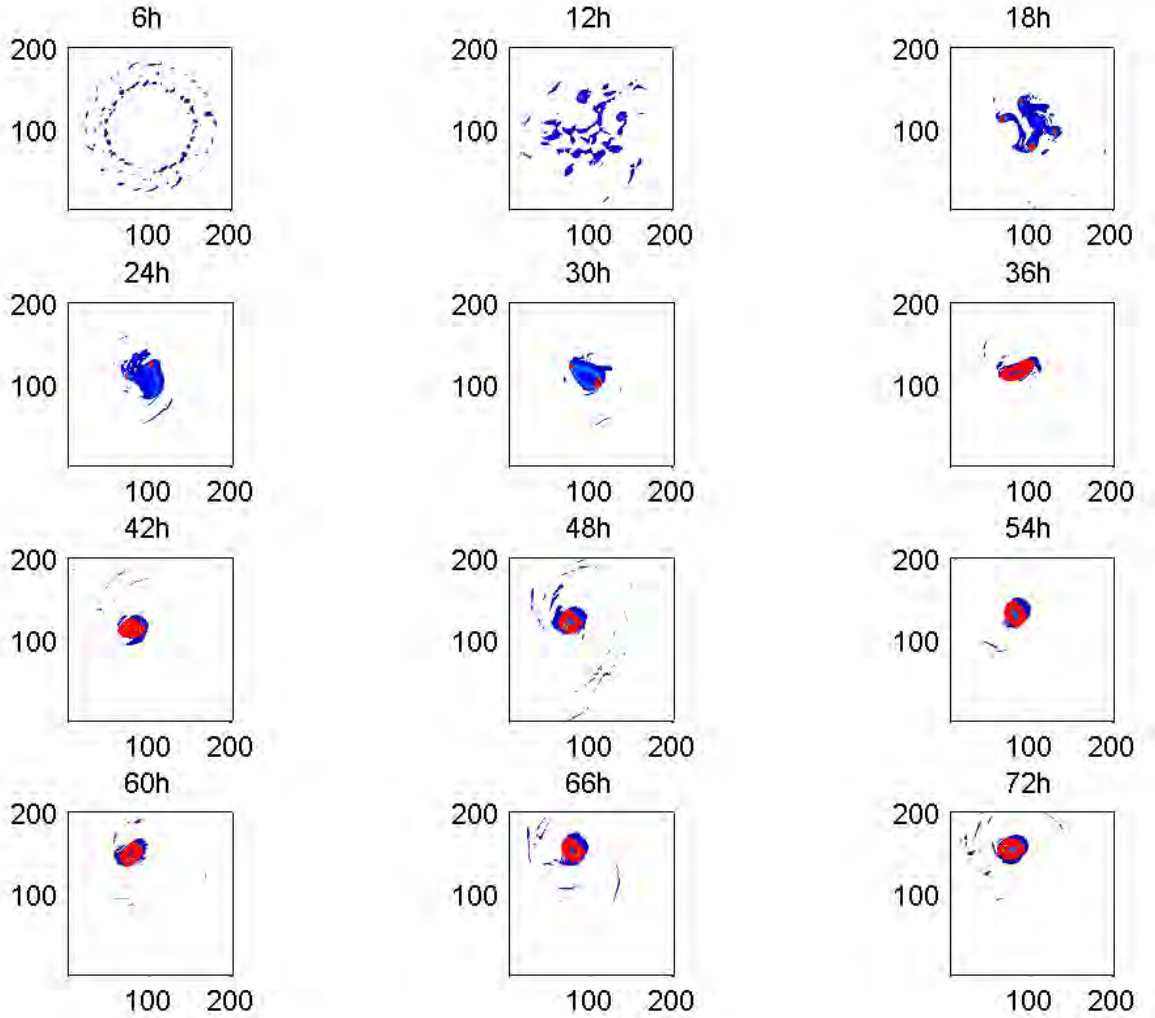


Figure 18. Time evolution (forecast hour at top) of the relative vorticity (s^{-1}) at 400 hPa (blue) and at 850 hPa (red) in the CNTL experiment on a 200 km x 200 km. The contour interval is 0.05 s^{-1} and 0.01 s^{-1} for the 850 hPa and 400 hPa vorticity, respectively.

The barotropic instability is evident from the time evolution of the azimuthal-mean 400 hPa vorticity (Figure 20). There is a steady increase of vorticity with time except between 42-48 h, when a reversal in the sign of the vorticity gradient is simulated. The radial gradient of vorticity changes sign twice, which is an indication of the development of barotropic instability and possible exponential growth in the inner-core region. This period is also the time of the trochoidal oscillation. The location of maximum vorticity is around 10 km from the center of the eye. After 60 h, the axis of maximum vorticity moves inward, which indicates a contraction of the eyewall. Outside the eyewall, a band of a small mean positive vorticity associated with the outer rainbands extends to about 70 km. The vorticity is predicted to approach zero at larger radius (> 100 km). The vortex center used to compute the azimuthal-mean vorticity for forecast times prior to 24 h is the center of the third nest. After 24 h, the location of minimum SLP is used to define the vortex center.

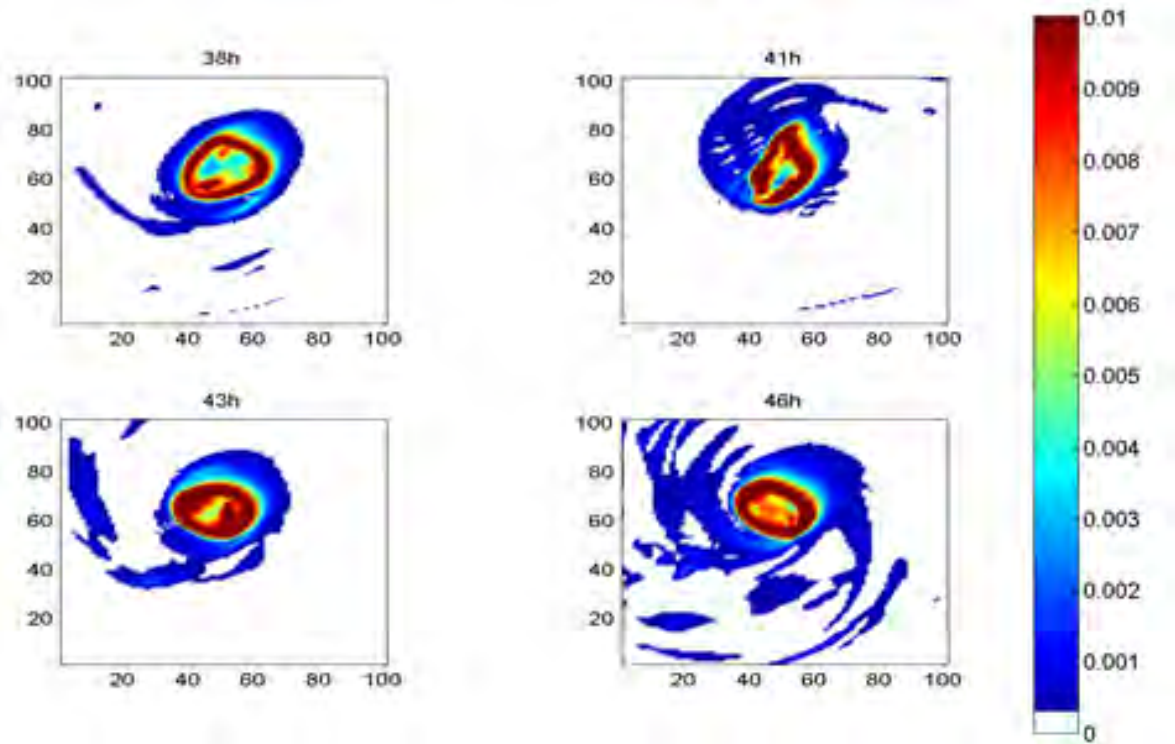


Figure 19. Predicted 400 hPa vorticity (s^{-1} , scale on right) at 38 h, 41 h, 43 h, and 46 in the CNTL experiment. At these four times, the vortex was undergoing trochoidal oscillations, and the vortex had multiple mesovortices and a polygonal eyewall.

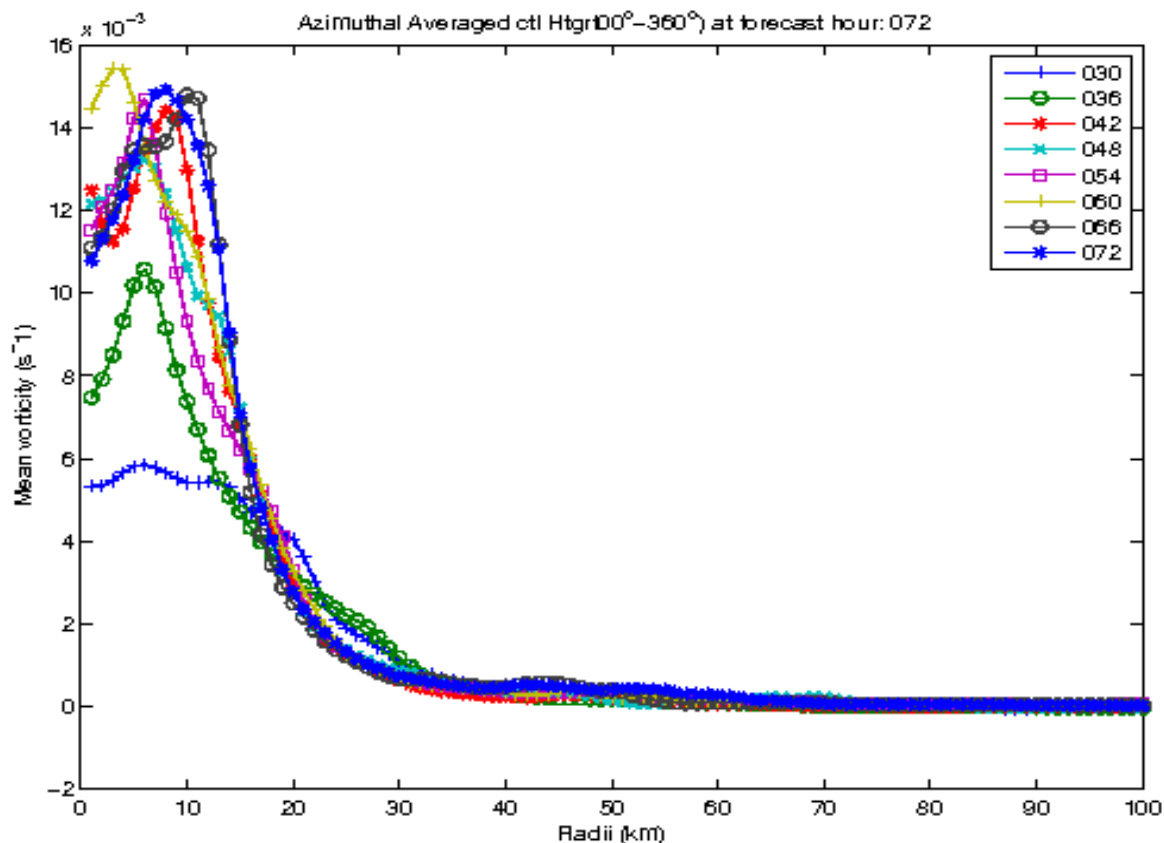


Figure 20. Azimuthal and vertical average of the vorticity (10^{-3} s^{-1}) with radius at various times (see inset) in the CNTL experiment.

The axisymmetric structures of the kinematic and thermodynamics fields in the CNTL experiment are investigated using composites obtained by first computing the azimuthal mean of each field at each forecast time. A time average of the azimuthal-mean fields is calculated over 24-72 h, which is the time period that the TC spins-up to CAT3-CAT5 intensity. In these composites of tangential and radial winds, the horizontal axis is normalized with mean radius of maximum tangential wind (RMW) in the vertical, which has a value of 30.3 km.

A. CONTROL DYNAMIC STRUCTURE

The maximum tangential wind of 84.8 m s^{-1} is predicted around 1 km height in the eyewall region above the leading edge of the low-level inflow (Figure 21a). The maximum low-level inflow extends from one to two RMW with a wind speed of 26.8 m

s^{-1} . The outer extent of the low-level inflow is around 9 RMW (126 km). The inflow layer of the secondary circulation extends up to 7 km and extends radially beyond the grid3 lateral boundary. The top of the upward-sloping outflow layer is located at 16 km with a maximum outflow speed of 25.7 m s^{-1} (Figure 21b). The tangential wind is extended vertically with time and is accompanied by an increase in both the low-level radial inflow and upper-level outflow (Figure 21 c and d). These mean perturbation fields over 24-72 h have been computed as deviations from the values at 24 h. The upper-level outflow maximum is slightly larger ($\sim 3 \text{ m s}^{-1}$) than the low-level inflow maximum. In addition, two regions of reduced outflow are predicted above and below the axis of maximum upper-level outflow, which indicates the vertical extent of the outflow is shrinking while the anticyclonic outflow is increasing in time.

Vertical stretching of the tangential wind with time is also implied in the vorticity field. The mean maximum relative vorticity of 0.02 s^{-1} is located inside the RMW at low levels, which indicates the model TC development is dominated by a bottom-up spin-up process. Negative vorticity is simulated in the upper-level anticyclone above 16 km. A deep broad region with small negative vorticity is predicted outside 4 RMW from the surface up to 18 km. The perturbation vorticity evolution indicates the upper-level anticyclone and low-level cyclone increased with time. Negative vorticity perturbations extend radially outward from the RMW (Figure 22 a and c). An area of low-level convergence extends from about 3 RMW to the eye and upward at the RMW to 10 km (Figure 22b). Mid- and upper-level convergence is also predicted above the low-level inflow and at the base of upper-level outflow. The perturbation divergence evolution indicates the convergence is increased with time inside about 0.5 RMW and at the location of low-level inflow (Figure 22d).

In a nonlinear primitive equation model such as COAMPS, the prediction of vertical motion preserves mass continuity and thermal wind balance. In the CNTL experiment, the core of the maximum vertical velocity of 8 m s^{-1} is at 6-12 km elevation along the axis of RMW (Figure 23a). Upward vertical motion extends beyond the RMW to 2-4 RMW at levels of 6-12 km. The largest upward motion is associated with the eyewall convection. The region outside 4 RMW and below 4 km is dominated by

downward vertical motion. Large turbulent kinetic energy (TKE) is simulated inside the RMW with two maxima with magnitudes of 25 and 15 $\text{m}^2 \text{s}^{-2}$ near the surface and 5 km, respectively (Figure 23b). The upward vertical velocity and TKE maxima, plus the inward movement toward the eye in time, are consistent with continuing TC intensification and contraction of the eyewall. Correlations of TKE, wind, and reflectivity from airborne Doppler radar observations suggest the large near-surface TKE is produced by strong horizontal and vertical shears of the radial and tangential winds, while the mid-level TKE is generated by the strong turbulent motion in the convective core (Lorsolo et al. 2010).

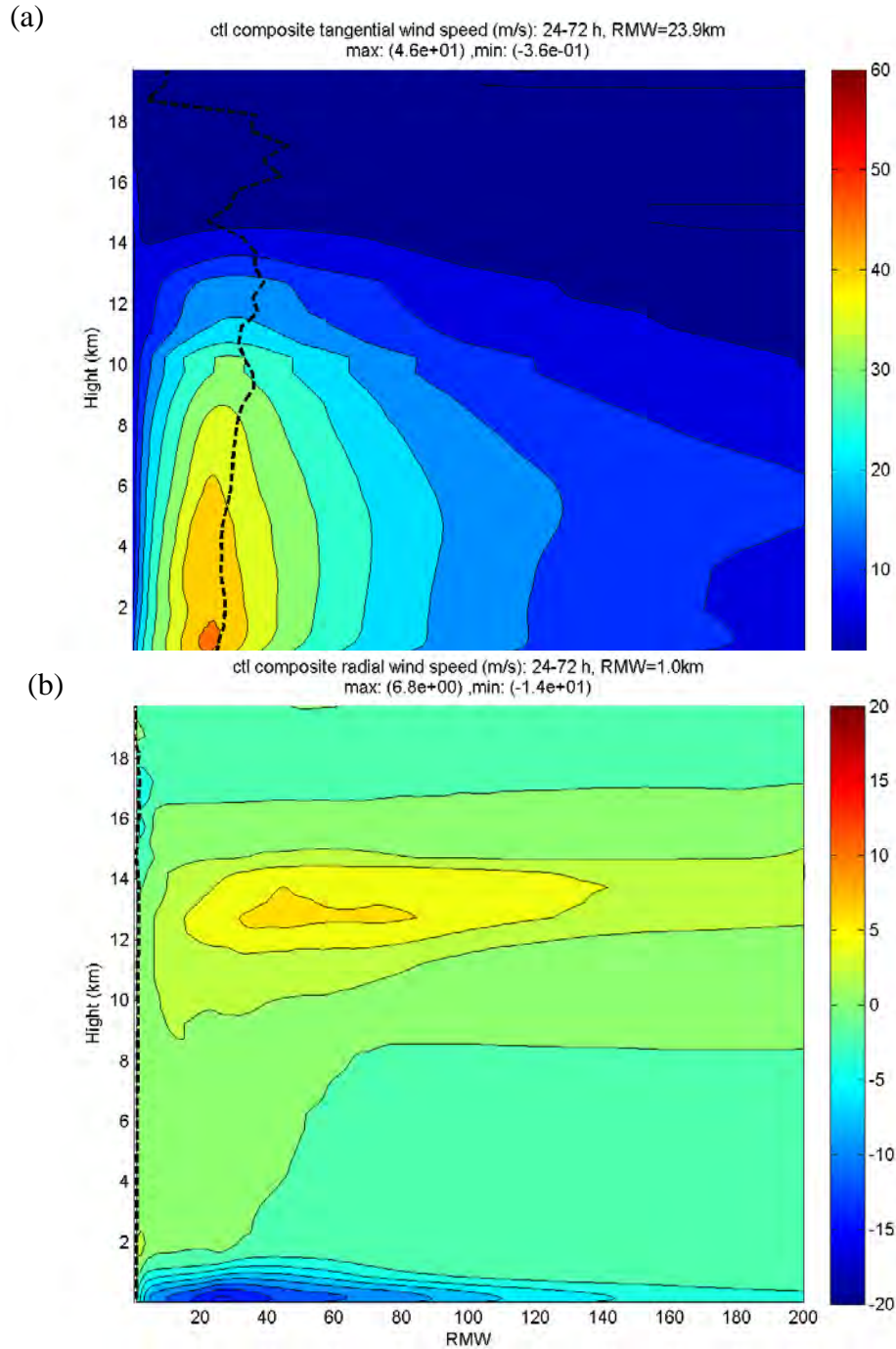
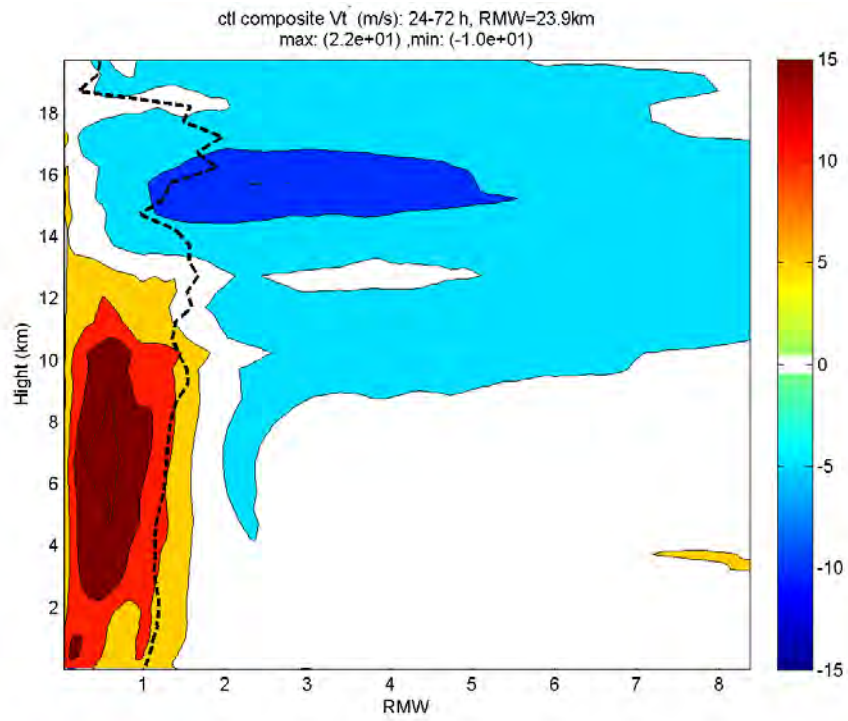
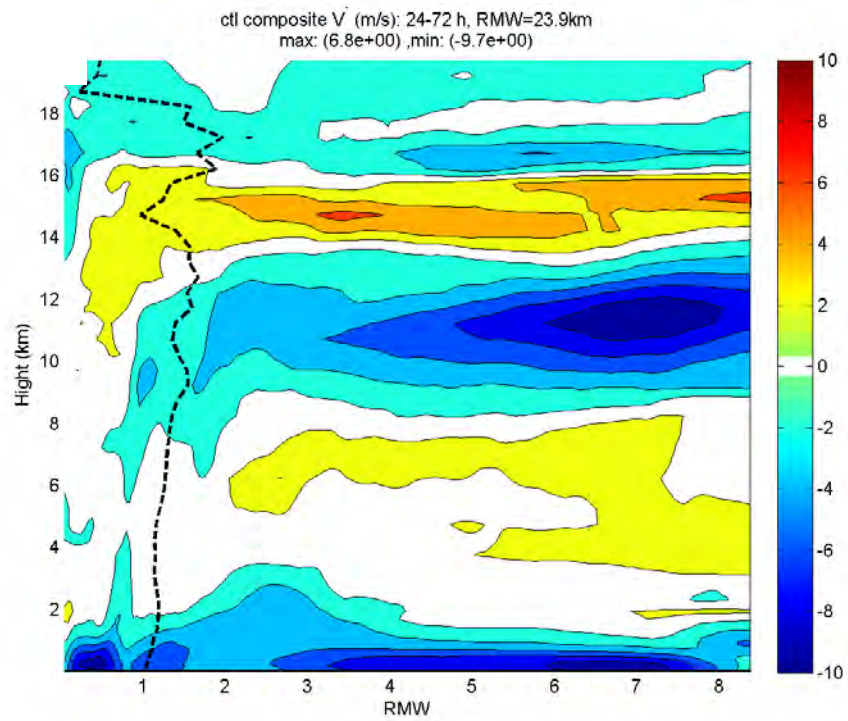


Figure 21. Composites of the azimuthal-mean (a) tangential wind (m s^{-1}), (b) radial wind (m s^{-1}), (c) mean tangential wind deviation from the value at 24 h, and (d) mean radial wind deviation from 24-72 h as the intensity increases from CAT3 to CAT5. The time-averaged location of RMW as a function of height is indicated by the dashed black line.

(c)



(d)



(Figure 21 continued)

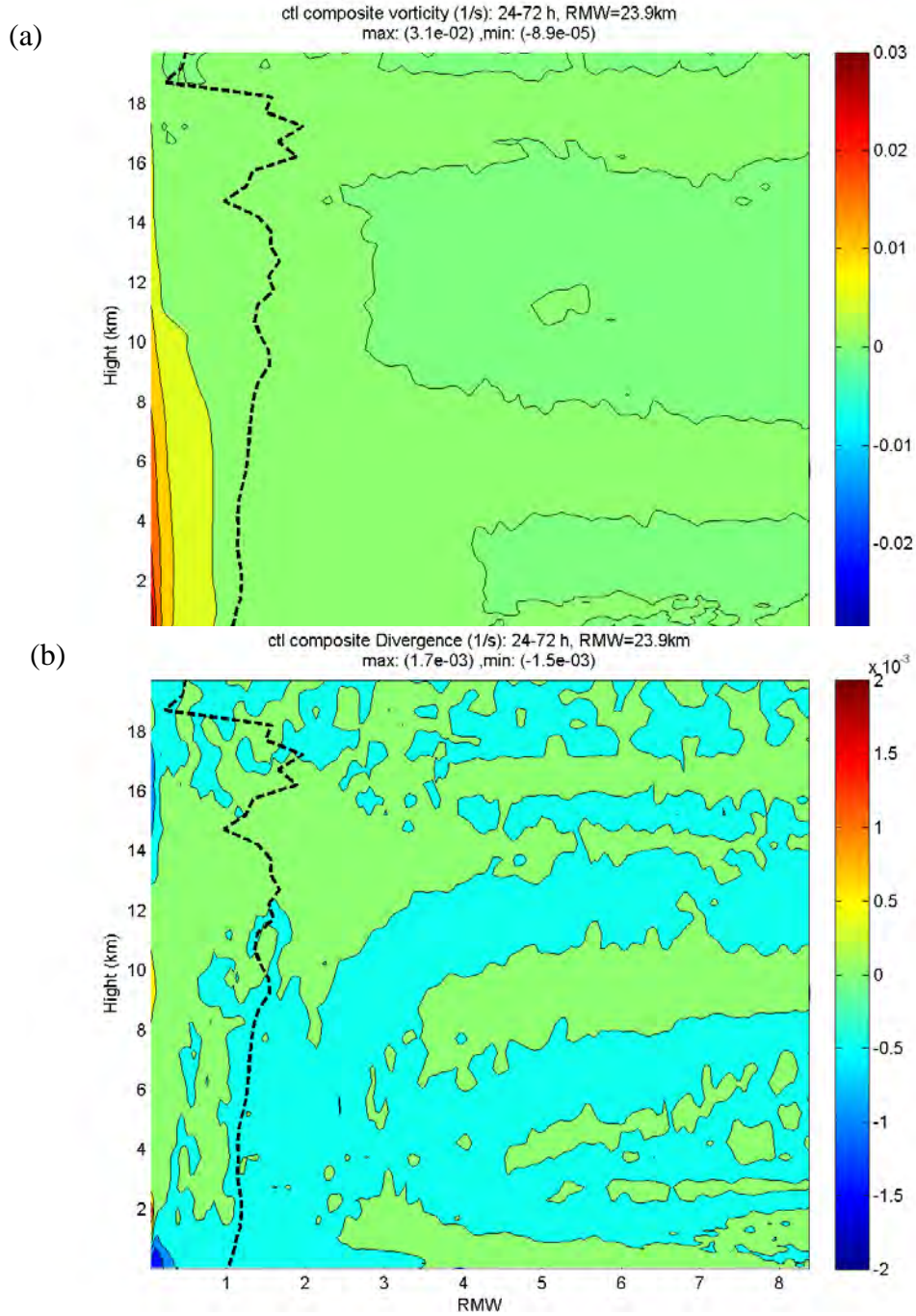
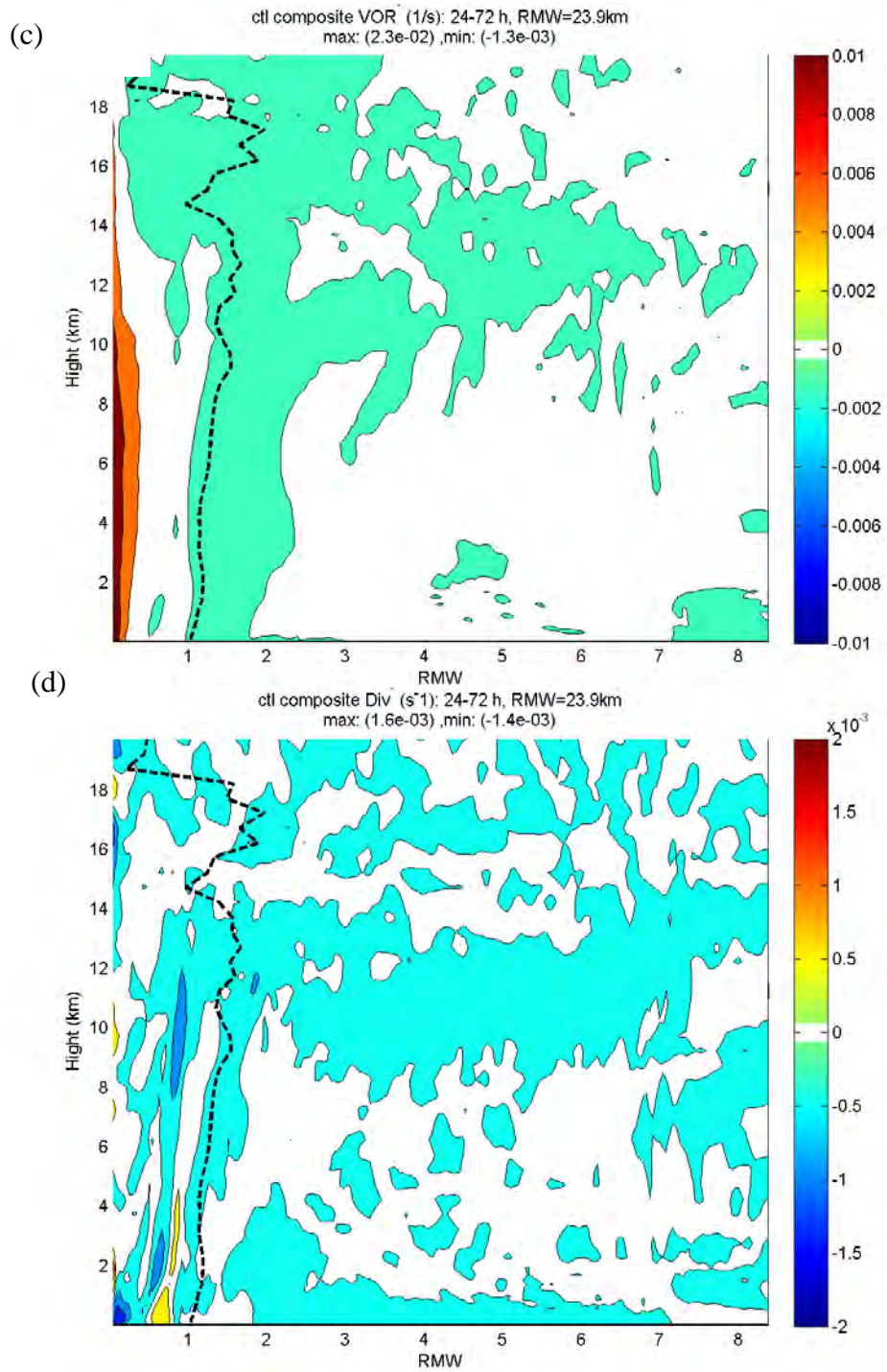


Figure 22. As in Figure 21, except for relative vorticity (s^{-1} , contour interval of 0.01 s^{-1}) and for divergence (s^{-1} , contour interval of 10^{-4} s^{-1}).



(Figure 22 continued)

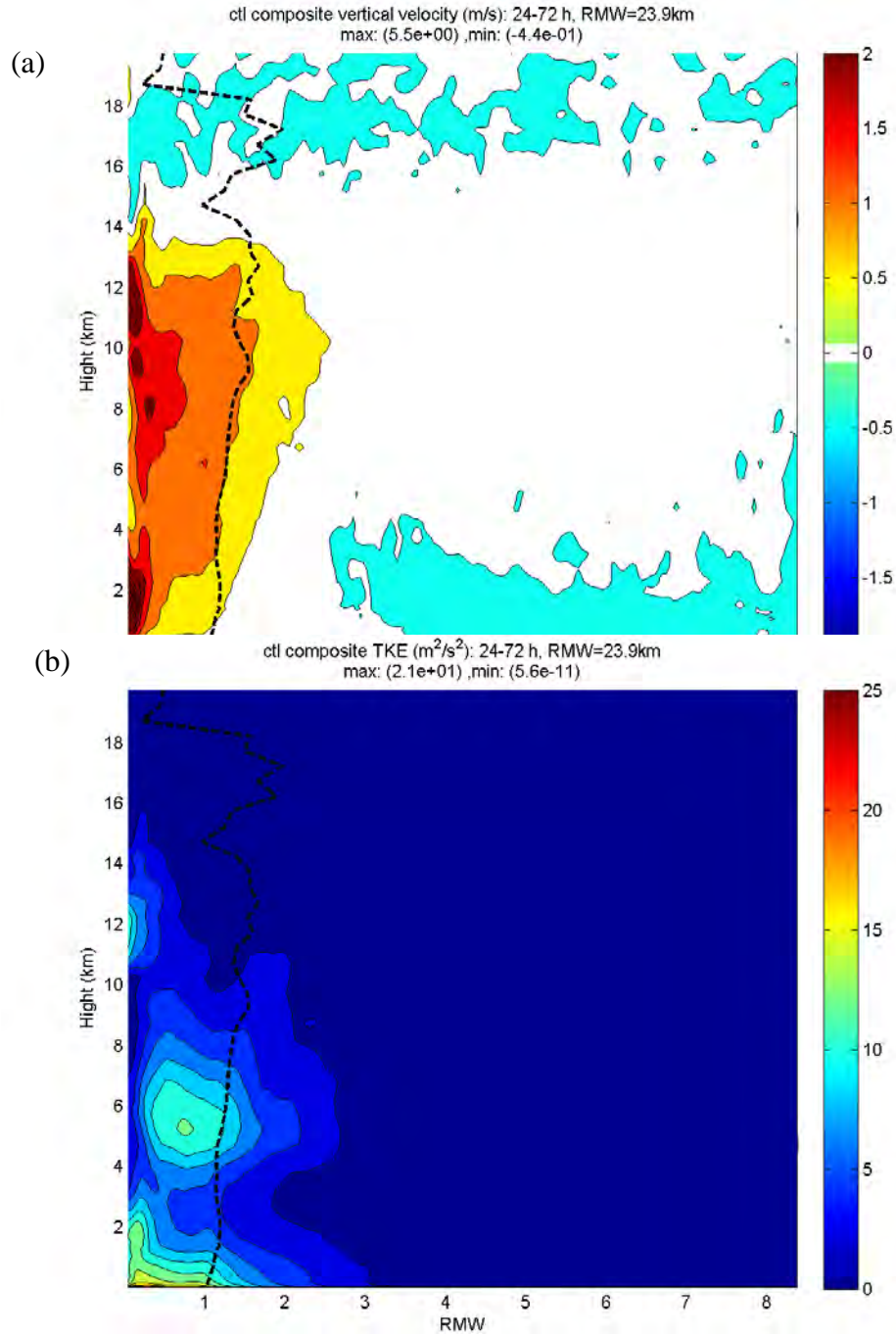
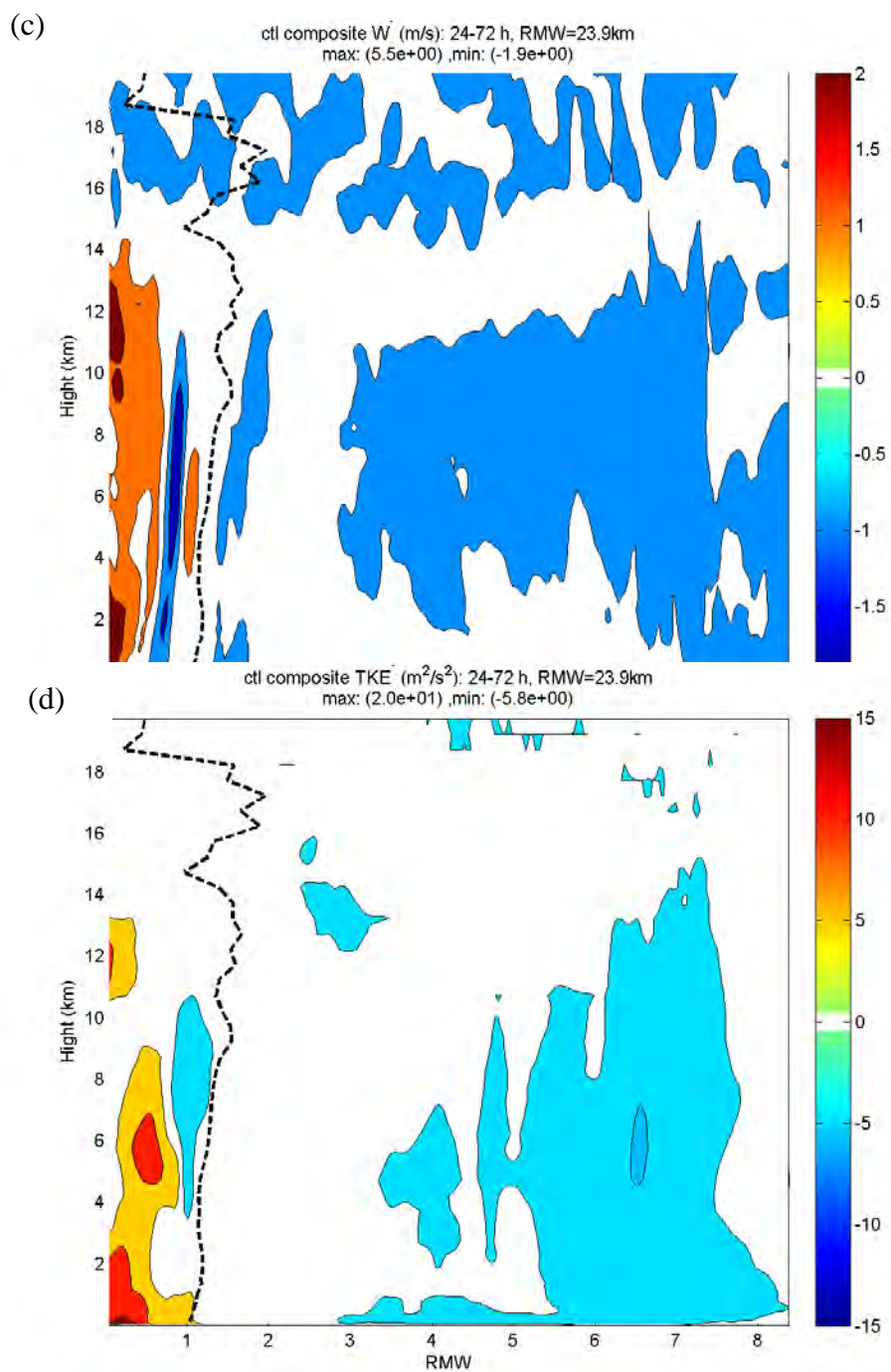


Figure 23. As in Figure 21, except for vertical velocity (m s^{-1}) and turbulent kinetic energy ($\text{m}^2 \text{s}^{-2}$).



(Figure 23 continued)

The model-simulated TC structure during the CAT3 – CAT5 intensity period is compared with the Doppler radar composite of axisymmetric wind structure from eight CAT 3-5 Atlantic hurricanes (Rogers et al. 2012, Figures 7, 8, and 11). The CNTL composite tangential wind, low-level inflow, vertical velocity, vorticity, and TKE structure are remarkably similar to the composites from the airborne Doppler radar analysis (Figure 24 - Figure 25). Similarities between CNTL and the Rogers et al. composites include: (a) strong low-level inflow and upper-level outflow; (b) maximum vorticity inside RMW; (c) two maximum TKE centers; (d) maximum vertical velocity inside the RMW; and (e) an upward and outward sloping RMW. The differences are that the CNTL simulation has a weaker mid-level outflow just above the low-level inflow, maximum low-level TKE is near the surface instead of about 1.5 km, and a broader region of mid-level TKE extends from inside the RMW to 3 RMW. However, the lowest observations from the radar are at 150 m and the radar-derived TKE does not include the full spectrum of turbulent motion. In addition, the CNTL TKE magnitudes are within the range of TKE values analyzed by Lorsolo et al. (2010) from five Atlantic hurricanes during various development stages, e.g. $> 15 \text{ m}^2 \text{ s}^{-2}$ inside RMW, $> 4 \text{ m}^2/\text{s}^2$ inside the boundary layer, and $> 8 \text{ m}^2 \text{ s}^{-2}$ around 2.5 RMW (see their Fig. 8).

Using a smaller time window during the trochoidal oscillation period (36-48 h) yields an almost identical kinematic structure as the composite during the CAT3-CAT5 period. This similarity is because considerable asymmetry exists during the trochoidal oscillation period. The axisymmetric mean does not provide additional insight regarding the fluctuations in the model TC inner core during this period. An examination of the model asymmetric structure during the CNTL simulation trochoidal period is deferred to Chapter V where the TC asymmetries during the cold wake experiments will be discussed.

Before the transition to CAT3 in the CNTL simulation, the composite axisymmetric kinematic structure is very different from the mature CAT3-CAT5 TC structure in many aspects. The RMW is at 36.4 km, or about 10 km larger than in the CAT3-CAT5 composite. The RMW axis also has a larger vertical tilt between the surface and 10 km (25.6 km compared to 7.6 km from the CAT3-CAT5 composite). The

maximum tangential wind speed is only 30.7 m s^{-1} , which is half of the CAT3-CAT5 maximum tangential wind speed (Figure 26a). Unlike the CAT3-CAT5 composite, radial outflow at 2 km is predicted outside the RMW. Maximum inflow (outflow) speed is 7 (17) m s^{-1} , which is almost four (two) times smaller than in the CAT3-CAT5 composite. The outflow speed increases at about half of the rate of the inflow speed as during the transition from CAT1-CAT2 to CAT3-CAT5 (Figure 26b).

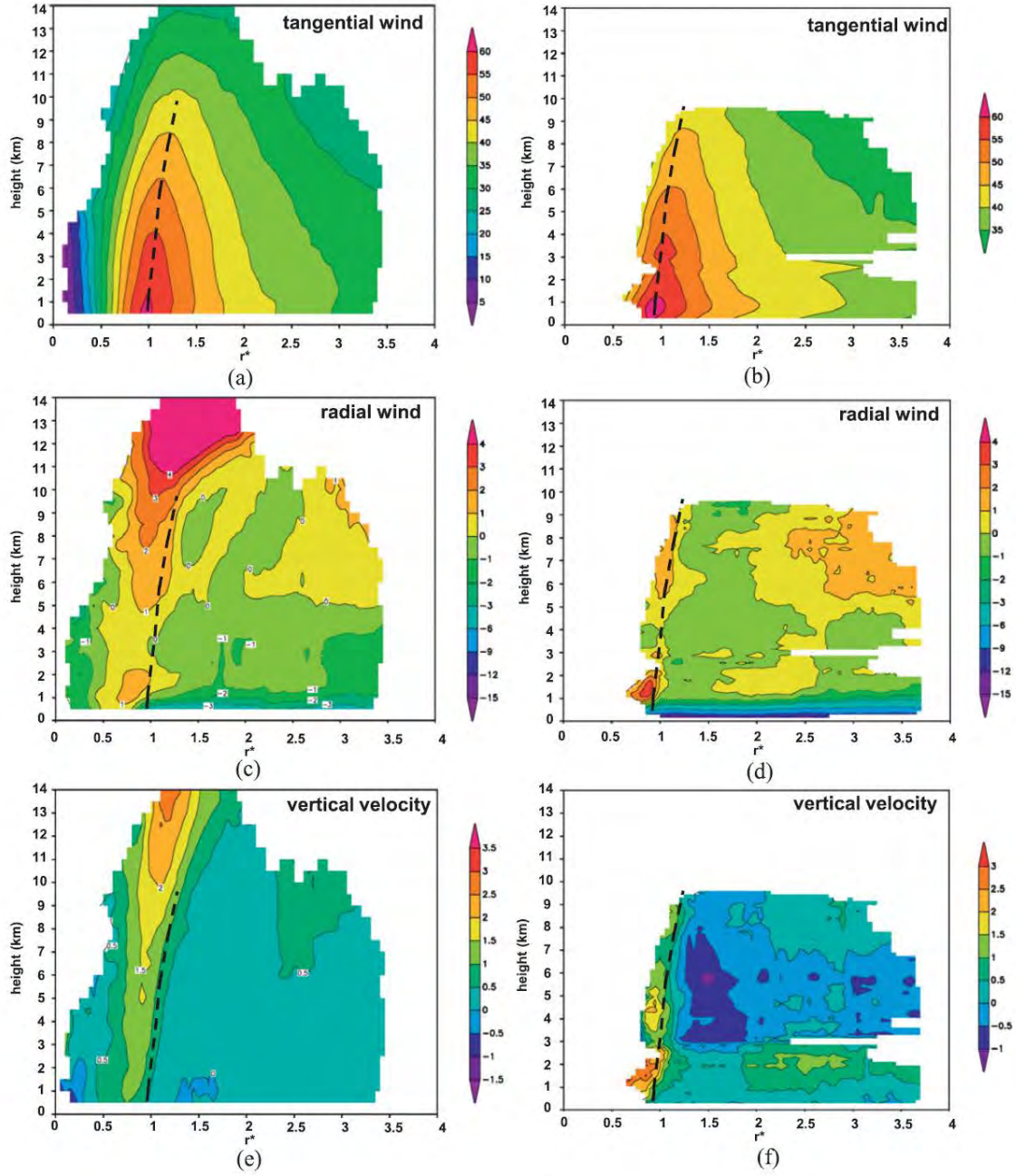


Figure 24. Composites of the axisymmetric (a) tangential wind, (c) radial wind, and (e) vertical velocity from swath data. Composites of the axisymmetric (b) tangential wind, (d) radial wind, and (f) vertical velocity from dropsonde data [From Rogers et al. (2012)].

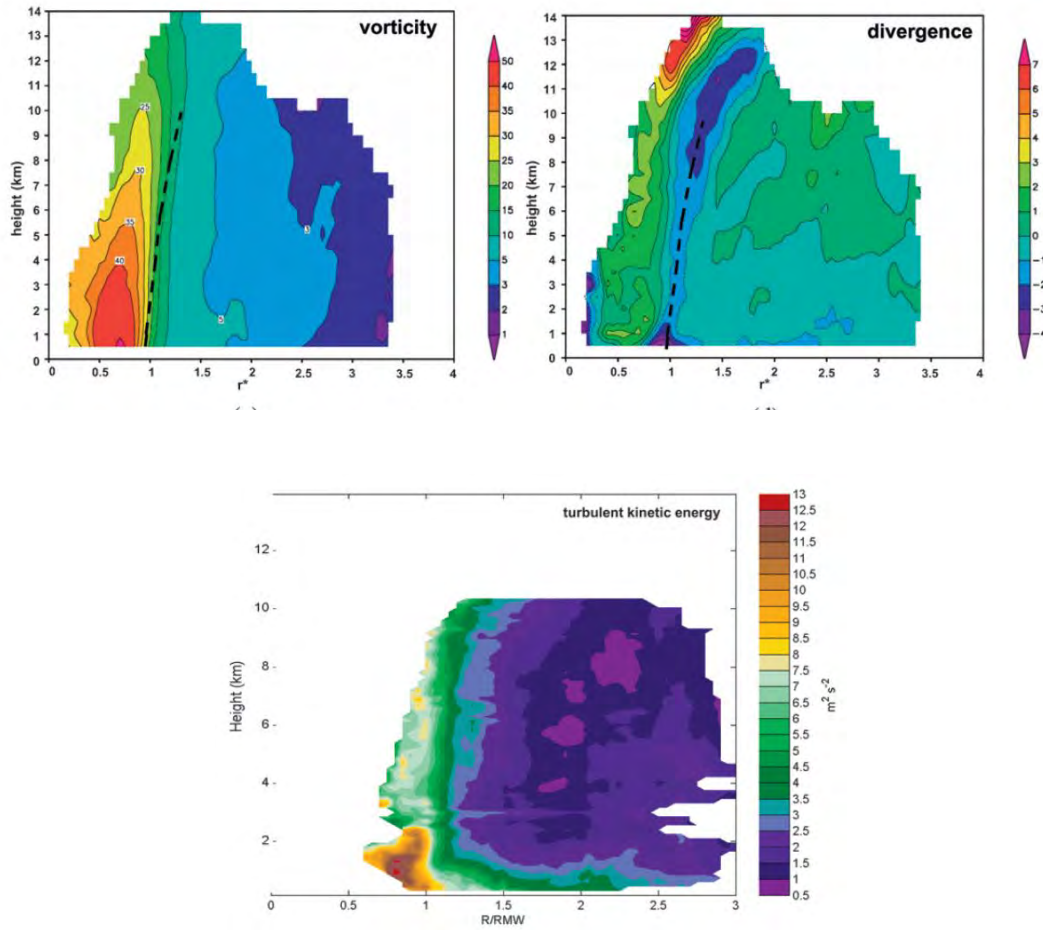


Figure 25. Composites of the axisymmetric (a) vorticity, (b) divergence, and (c) TKE from Doppler radar swath data [From Rogers et al. (2012)].

Defining a perturbation as a deviation from the simulated values at hour 12, increased stretching of the tangential wind also is predicted at CAT1-CAT2 stage (Figure 26c). Increased low-level inflow with time near the RMW and reduced inflow beyond 2.5 RMW is simulated (Figure 26d). Unlike the CAT3-CAT5 stage, the CAT1-CAT2 stage vertical velocity has a pair of mid-level (8-10 km) maxima on the opposite sides of the RMW. One vertical velocity maximum of 1.7 m s^{-1} is located at about 2.5 RMW, which indicates more active rainbands in the outer radii than during the CAT3-CAT5 stage (Figure 27). The low-level positive vorticity maximum of $3.8 \times 10^{-4} \text{ s}^{-1}$ inside the RMW then has a larger vertical tilt than for the CAT3-CAT5 stage (Figure 27b). Negative vorticity in the upper-level anticyclone is not as large or as wide as in the CAT3-CAT5 stage (Figure 27d).

The maximum mid-level TKE during the CAT1 – CAT2 stage is outside the RMW at about 2.5 RMW (Figure 28a). As the TC continues to intensify, both the low-level and mid-level TKE maxima are inside the RMW and the mid-level TKE at 2.5 RMW increases in magnitude. This mid-level TKE maximum is associated with the outer rainband convection (Figure 28b).

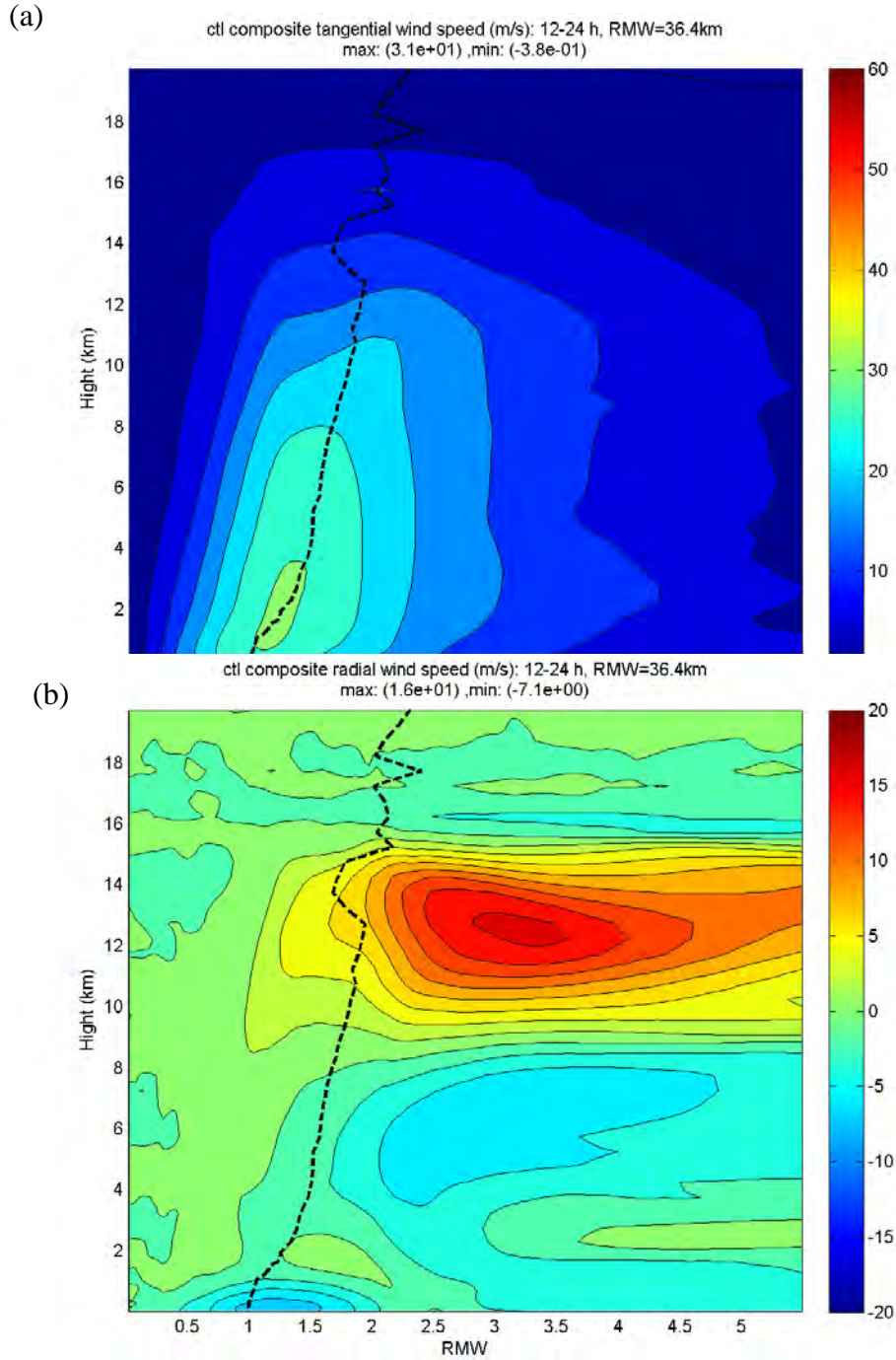
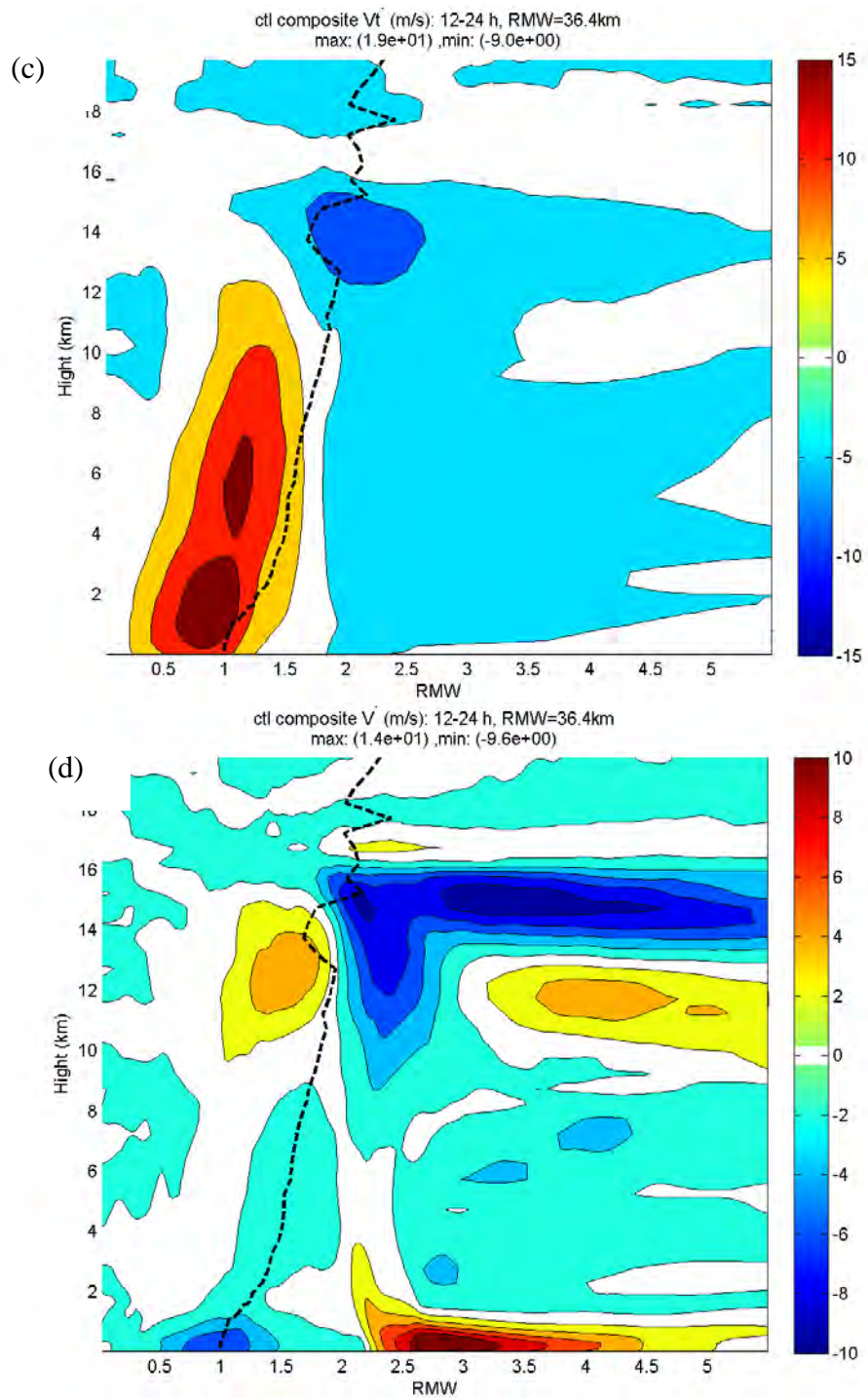


Figure 26. Composites of the 12-24 h azimuthal-mean (a) tangential wind (m s^{-1}), and (b) radial winds (m s^{-1}), (c) mean deviation of the mean tangential wind relative to the 12 h values, and (d) mean deviation of the radial winds from the 12 h values. The variation of the RMW in the vertical is indicated by the dashed black line.



(Figure 26 continued)

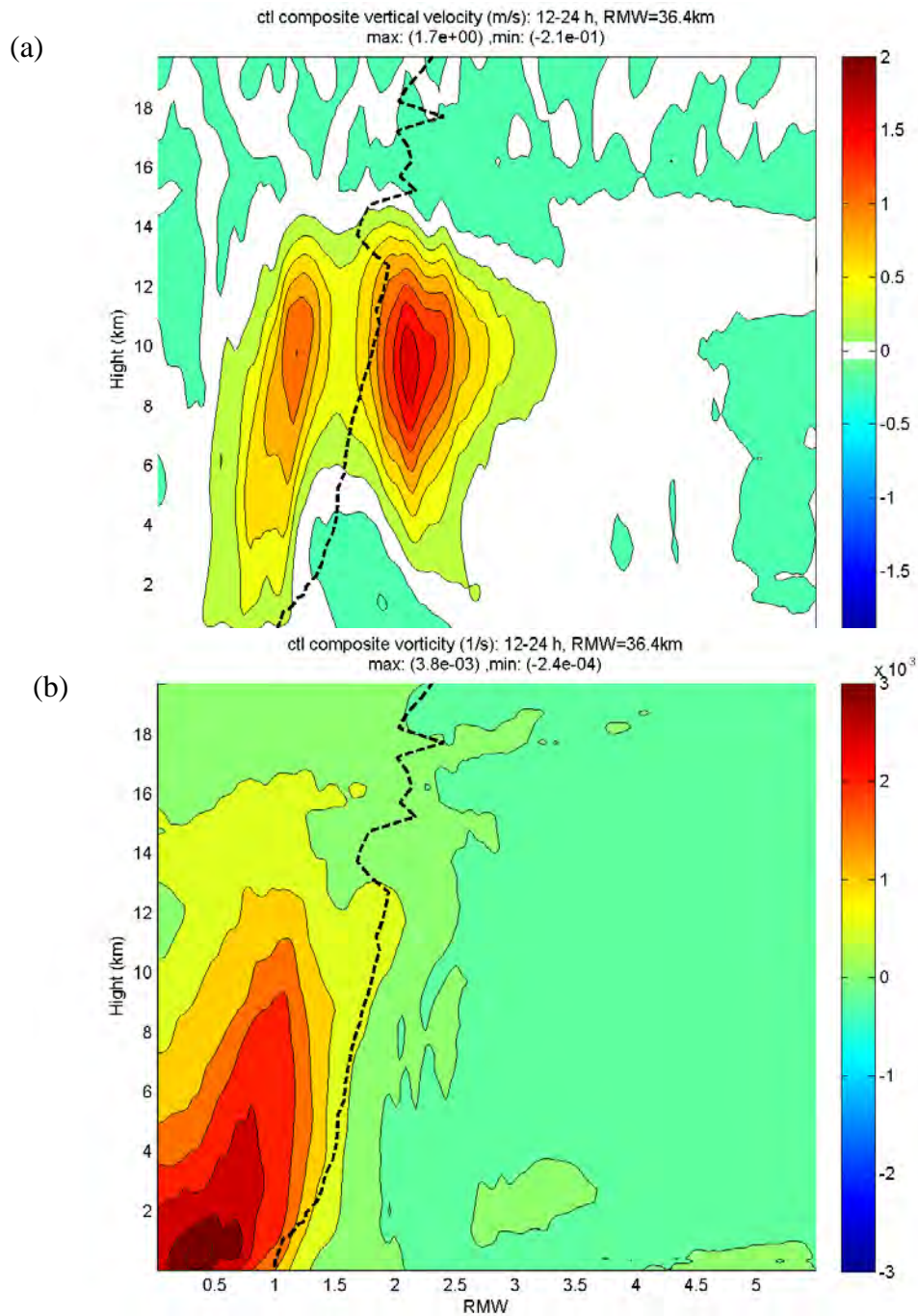
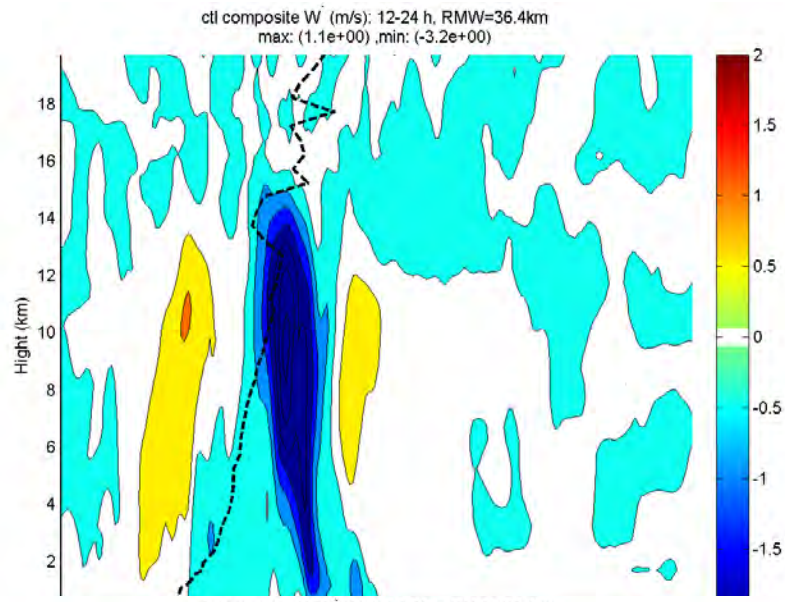
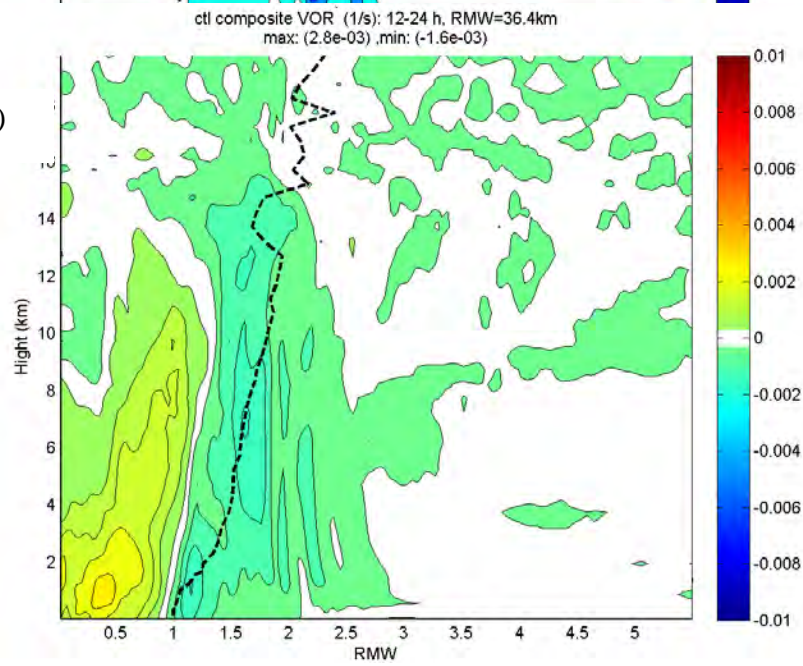


Figure 27. As in Figure 26, except for vertical velocity (m s^{-1}) and relative vorticity (s^{-1}).

(c)



(d)



(Figure 27 continued)

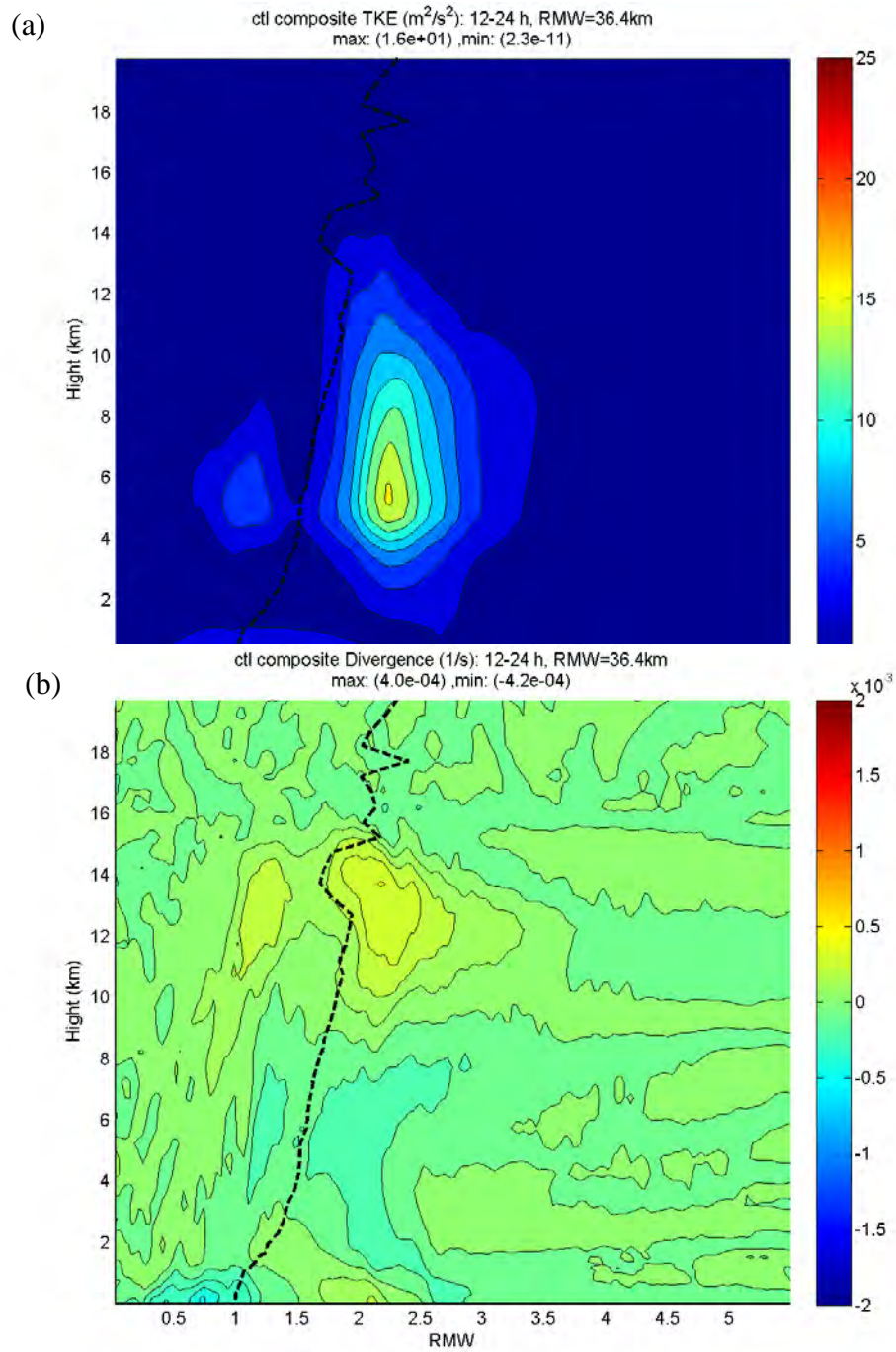
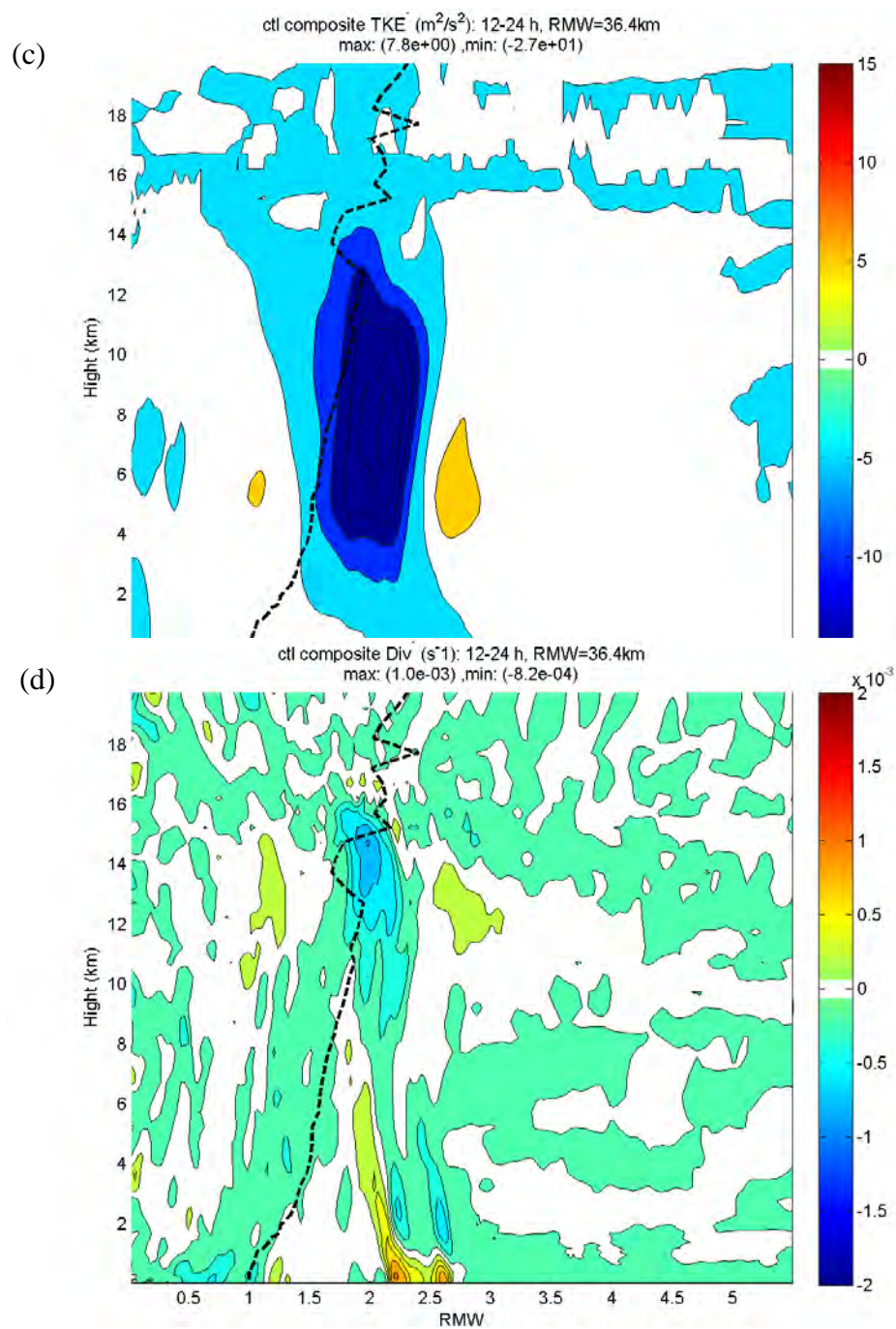


Figure 28. As in Figure 26, except for TKE ($\text{m}^2 \text{s}^{-2}$) and divergence (s^{-1}).



(Figure 28 continued)

The composite of the radial-height structure of the axisymmetric transverse circulation during the CAT3 – CAT5 stage has a broad, open single cell with upward vertical motion near the RMW that is nearly vertical to 14 km before turning outward (Figure 29a). A considerable vertical tilt of the angular momentum surfaces is predicted between 2-6 km elevation beyond 6 RMW (Figure 29b). The baroclinicity has a maximum in the outflow layer, and the baroclinicity is also large in the low-level inflow layer and at mid-levels (2-4 km) in the inner-core region (Figure 29c). The static stability is large inside the RMW in the inner-core region at around 1 km height. Outside the RMW, the static stability is relatively smaller. Both the low-level static stability and radial gradient of the angular momentum are large in the inner-core region (Figure 29d). In general, the angular momentum is the restoring force for radial displacements, static stability for vertical displacements, and baroclinicity for the vertical tilt of the vortex. Therefore, these three restoring forces determine the structure of the axisymmetric transverse circulation.

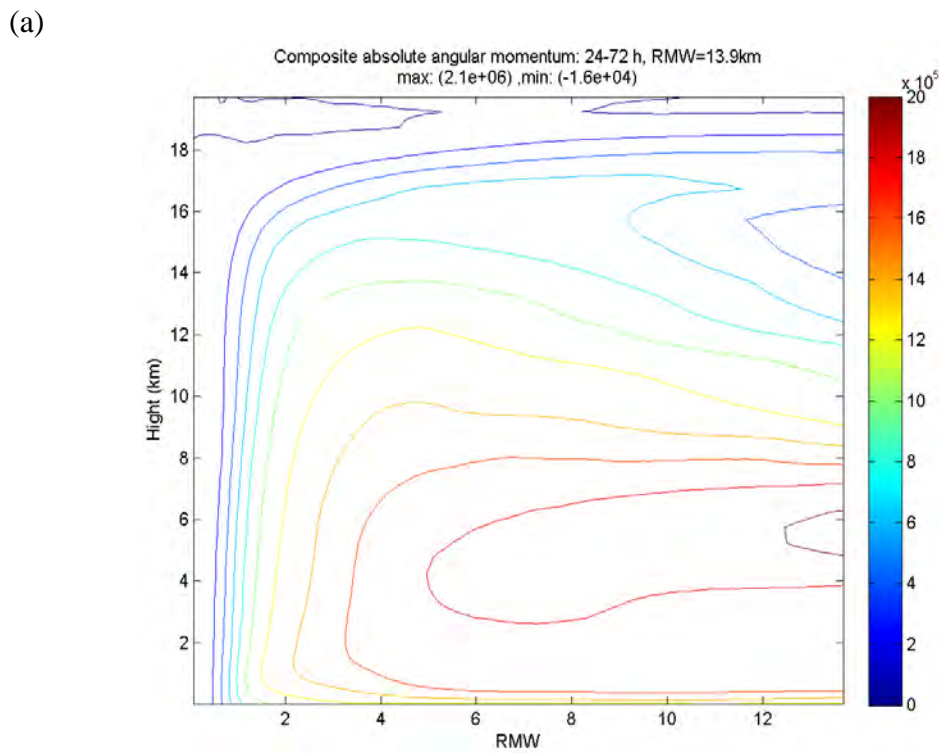
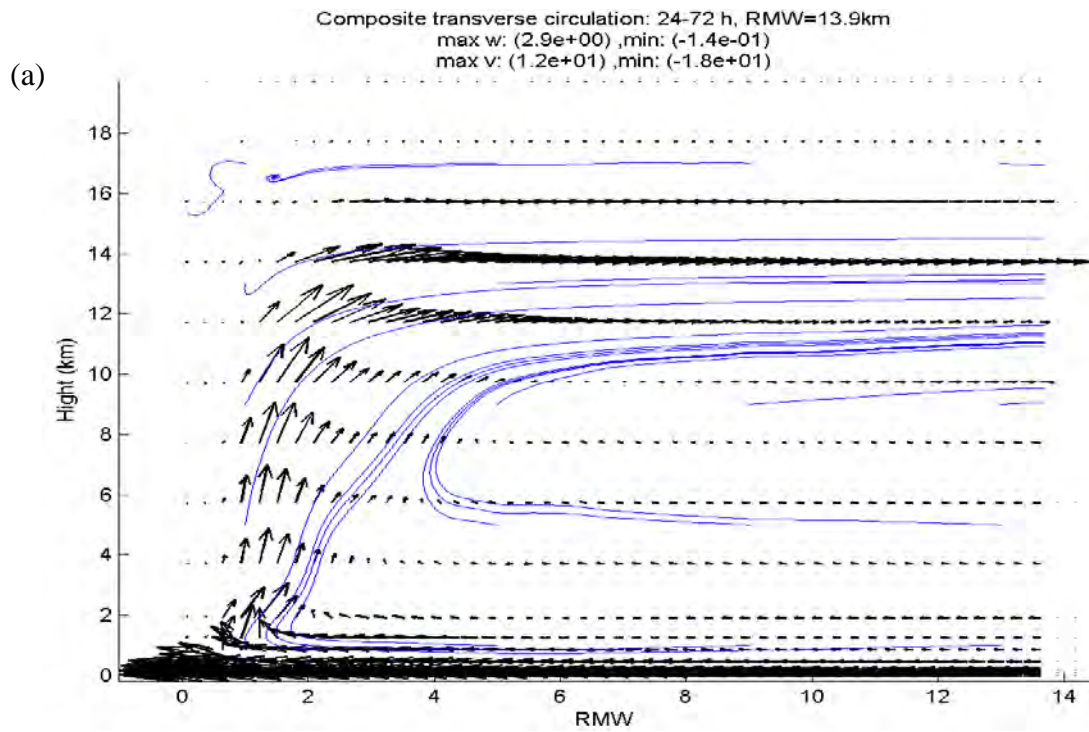
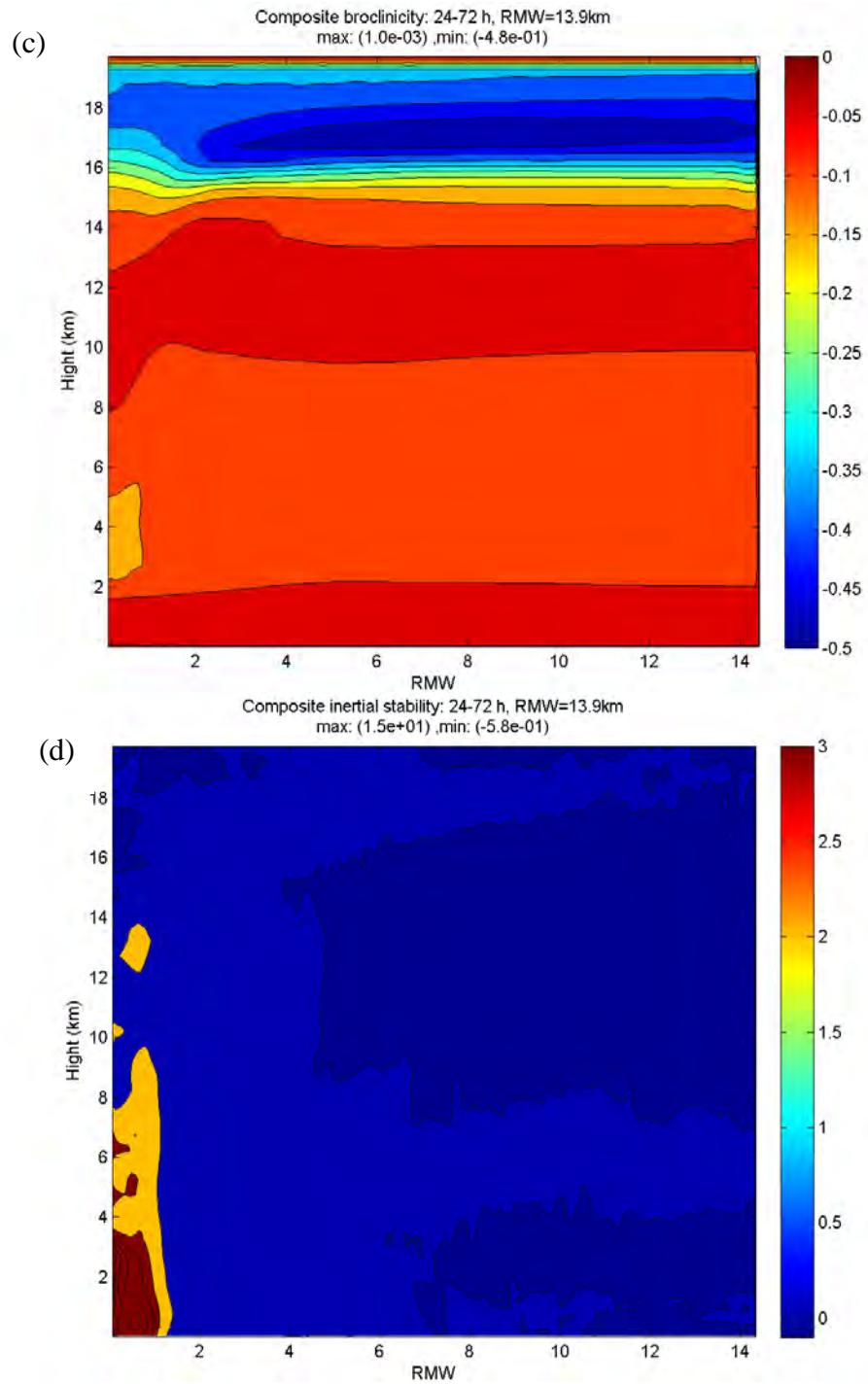


Figure 29. Composites of the (a) axisymmetric transverse streamlines (blue) and wind vectors, (b) absolute angular momentum, (c) baroclinicity, and (d) static stability during 24 – 72 h of the CNTL experiment.



(Figure 29 continued)

B. CONTROL THERMODYNAMIC STRUCTURE

The thermodynamic structure of TC is influenced by the enthalpy transfer through the air-sea interface and is closely related to the wind speed. The sensible and latent heat fluxes averaged over 6 h at selected times from 36 – 66 h in the CNTL experiment are shown in Figure 30. Considerable spatial variability is predicted in outer radii due to vortex rotation and variations in the size of the secondary circulation.

Total enthalpy (latent+sensible) flux averaged over the grid 3 domain has a bimodal evolution (Figure 31a). A similar variability is also predicted in the total rain field (Figure 31b). By contrast, the wind stress generally has an upward trend of increased momentum flux within grid 3. These maxima of latent (sensible) heat flux of 60 (32) and 87 (6.7) mega W/m² occur around 22 and 51h, respectively. The time period between the two maxima is 29 h, which is longer than the diurnal cycle. Note that this rain maxima leads the flux maxima by about 4-10 h. Recall the SST in CNTL is fixed at 30°C. Since the wind stress increases with time, the decrease of enthalpy flux after each maximum must then be due to reduced low-level air-sea temperature and moisture differences (warmer and more moist atmosphere) in the outer radii. Analysis of the azimuthal mean fluxes normalized to the RMW shows most of the total enthalpy flux contribution is from within the radius of 5 RMW, and is about 3-4 times larger than the flux contribution from the far field (15 RMW). Oscillations of the latent heat flux summed over the area inside 5 RMW has an amplitude about 6-7 mega W/m² (Figure 32).

The composite of axisymmetric potential temperature in the CAT3 – CAT5 period reveals an increasing warm core magnitude inside the RMW (Figure 33c). The mean potential temperature change from hour 24 indicates warming in time that extends from 4-14 km with the maximum amplitude of 10 °C between 12-15 km. Note that the inner-core air below 4 km is cooling with time. The corresponding inner-core, upper-level warming is caused by subsidence (compare with the vertical velocity in Figure 23). This inner-core warming produces a concave bow-shaped isotherm within the eyewall. The latent heat release from eyewall convection (Figure 33b) contributes to the inner-core warming. The maximum diabatic heating rate is located at 2 km and extends up to 10 km, which indicates deep convection. Sustained deep convection inside RMW is supported by

a deep layer of moisture inside the RMW (Figure 33e). The moisture deviations from the 24 h values (Figure 33f) reveal increased moisture in the inner core between 1-8 km, and also just above the radial inflow layer. This moisture increase above the radial inflow is attributed to the increased radial inflow and increased turbulent mixing with time that transports up moisture from the air-sea interface. A deep layer of increased drying is predicted below the outflow layer.

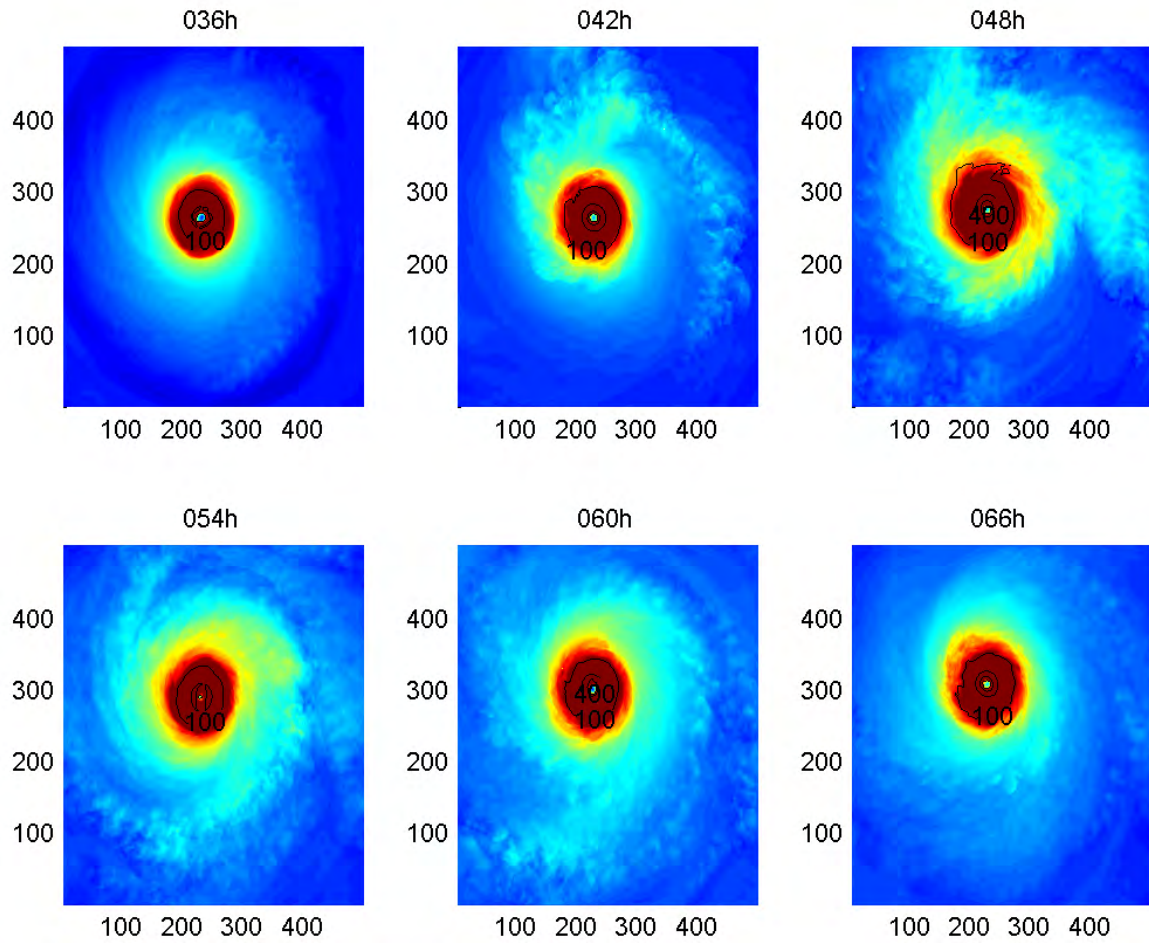


Figure 30. Latent heat flux (color shaded) and sensible heat flux (contours) averaged over 6-h periods at selected times between 36 – 66 h in the CNTL simulation. The contour interval is 300 W m^{-2} .

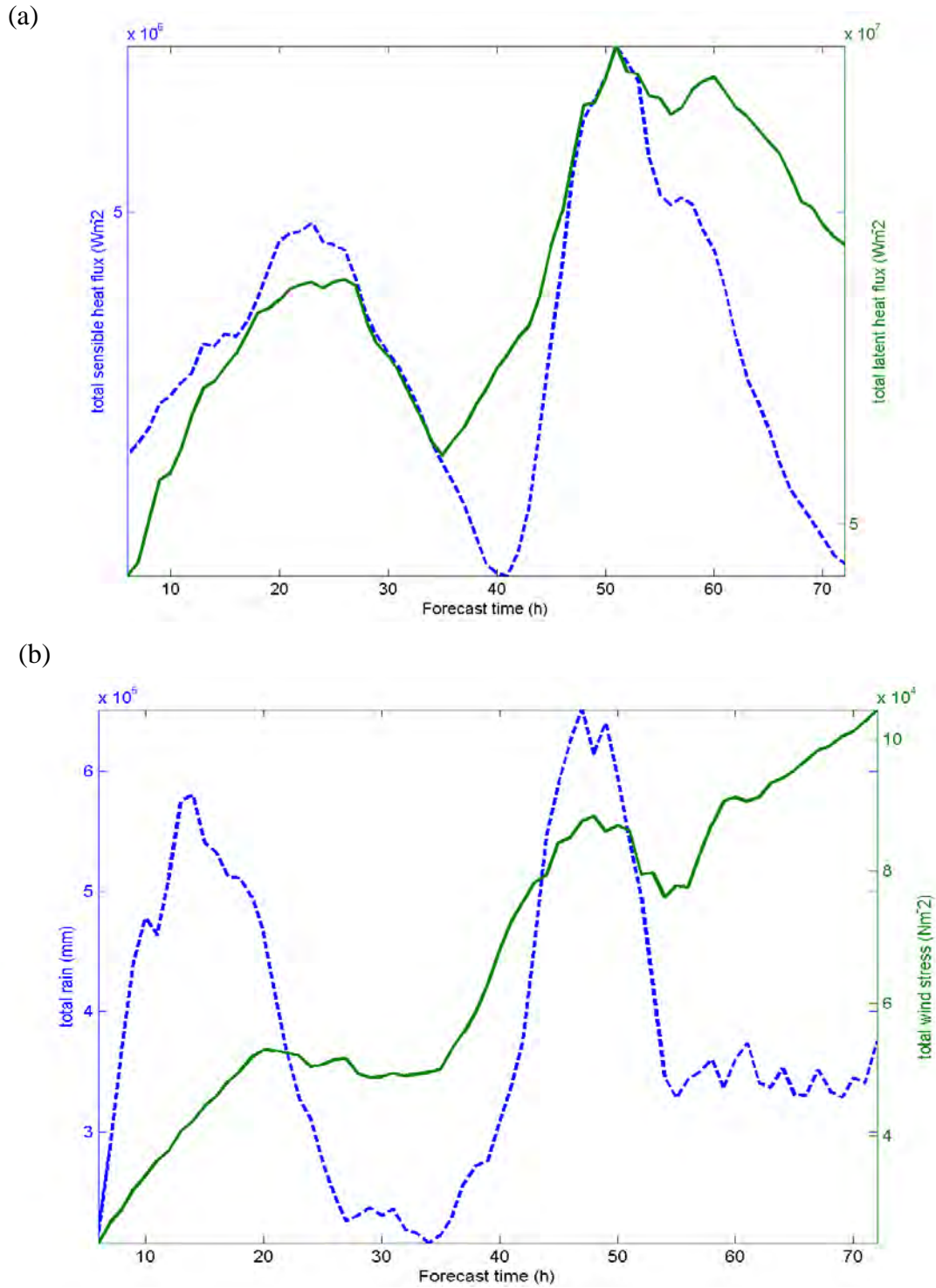


Figure 31. Time series of total (a) latent (solid) and sensible (dashed) heat flux (W m^{-2}) averaged over the grid 3 domain, and (b) rain (mm, dashed) and wind stress (N m^{-2} , solid).

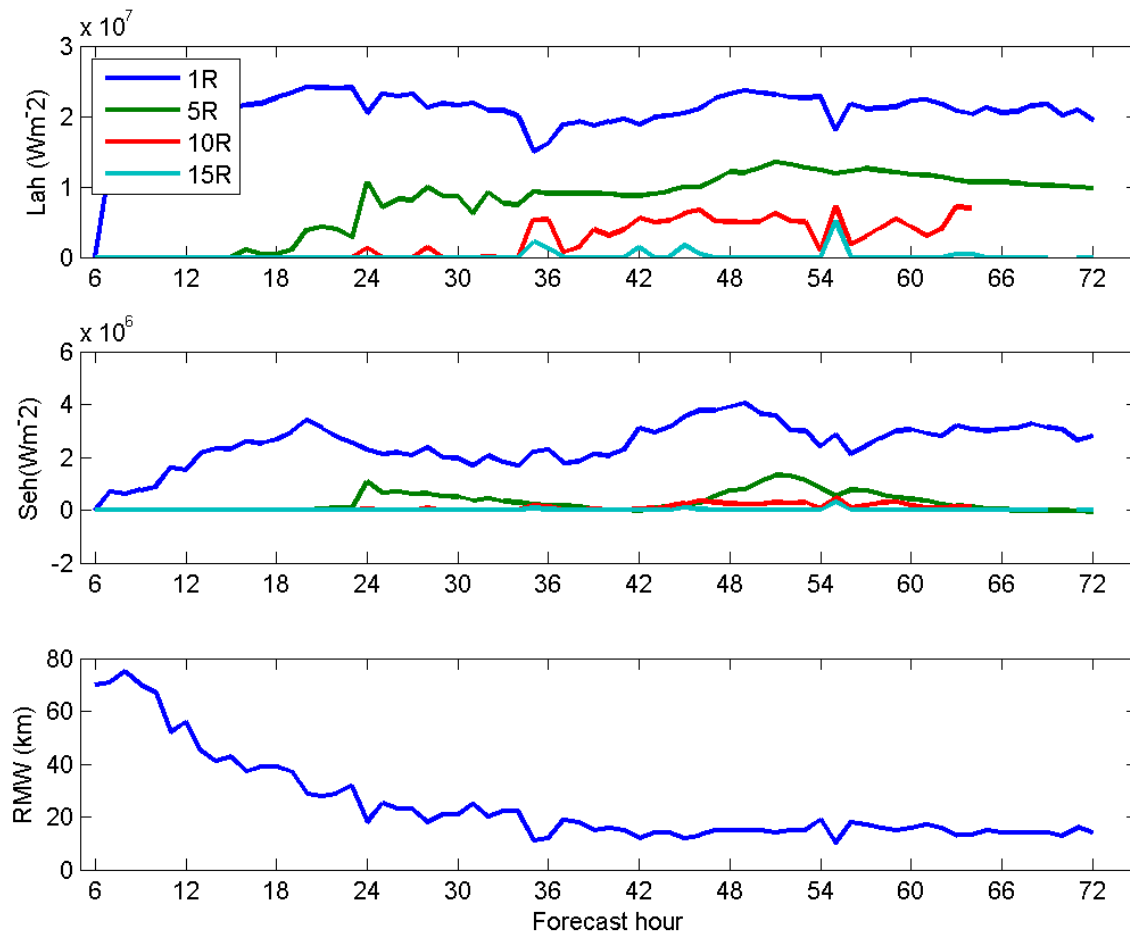


Figure 32. Time series of azimuthal-mean total latent (top panel) and sensible (bottom panel) heat fluxes ($W m^{-2}$) within 1 (blue), 5 (green), 10 (red), and 15 (green) RMW, respectively. The time evolution of the RMW (km) is shown in the bottom panel.

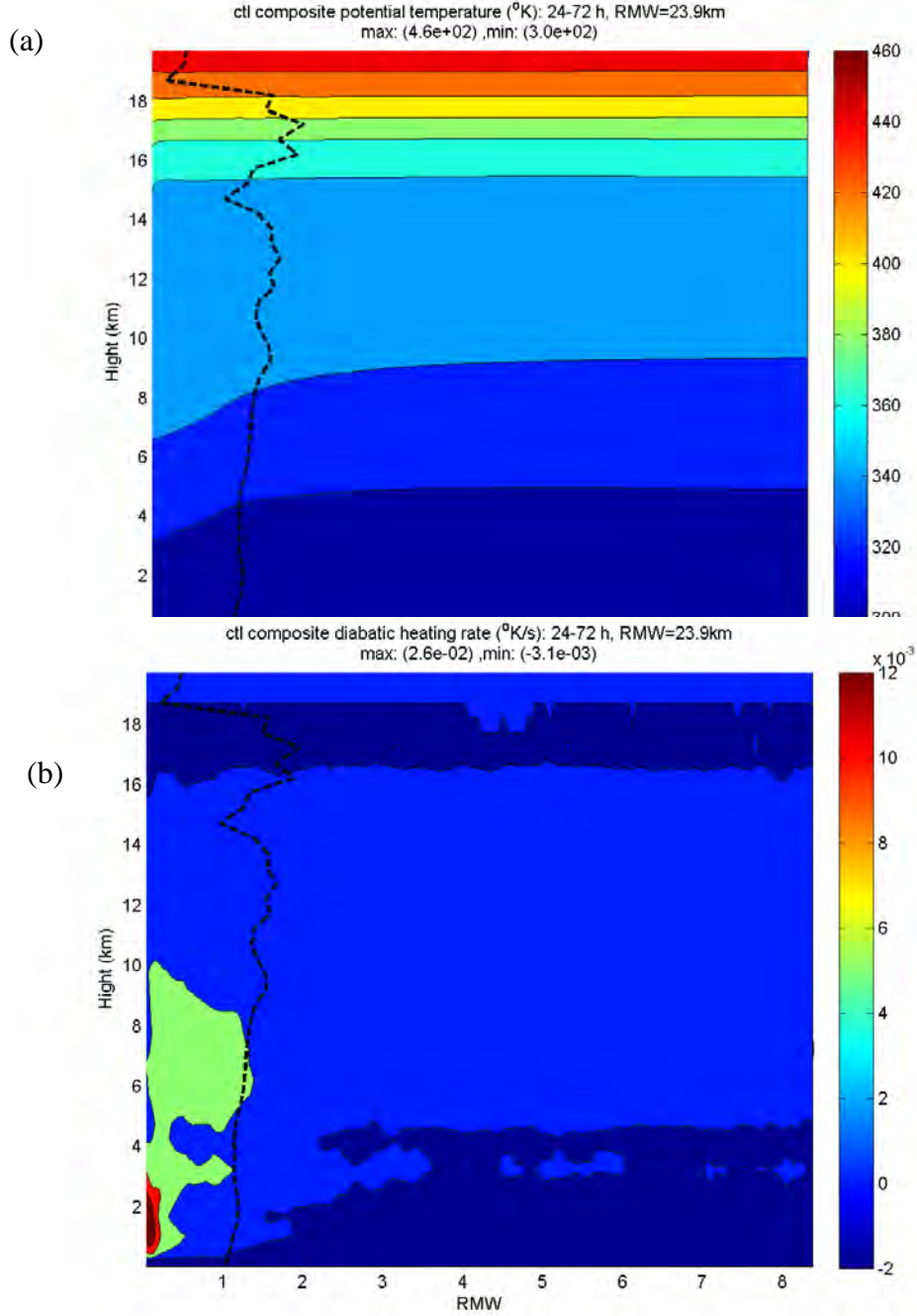
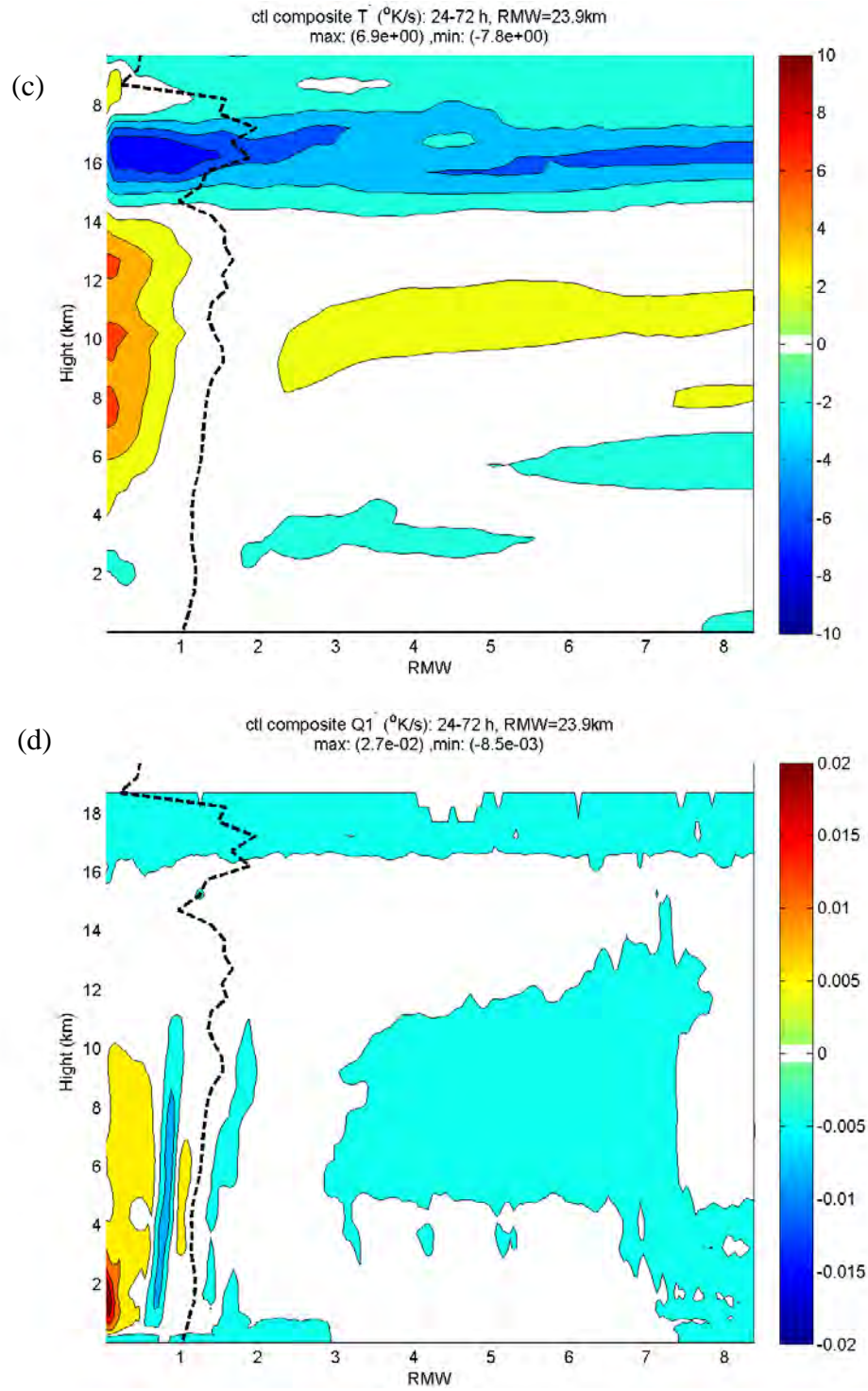
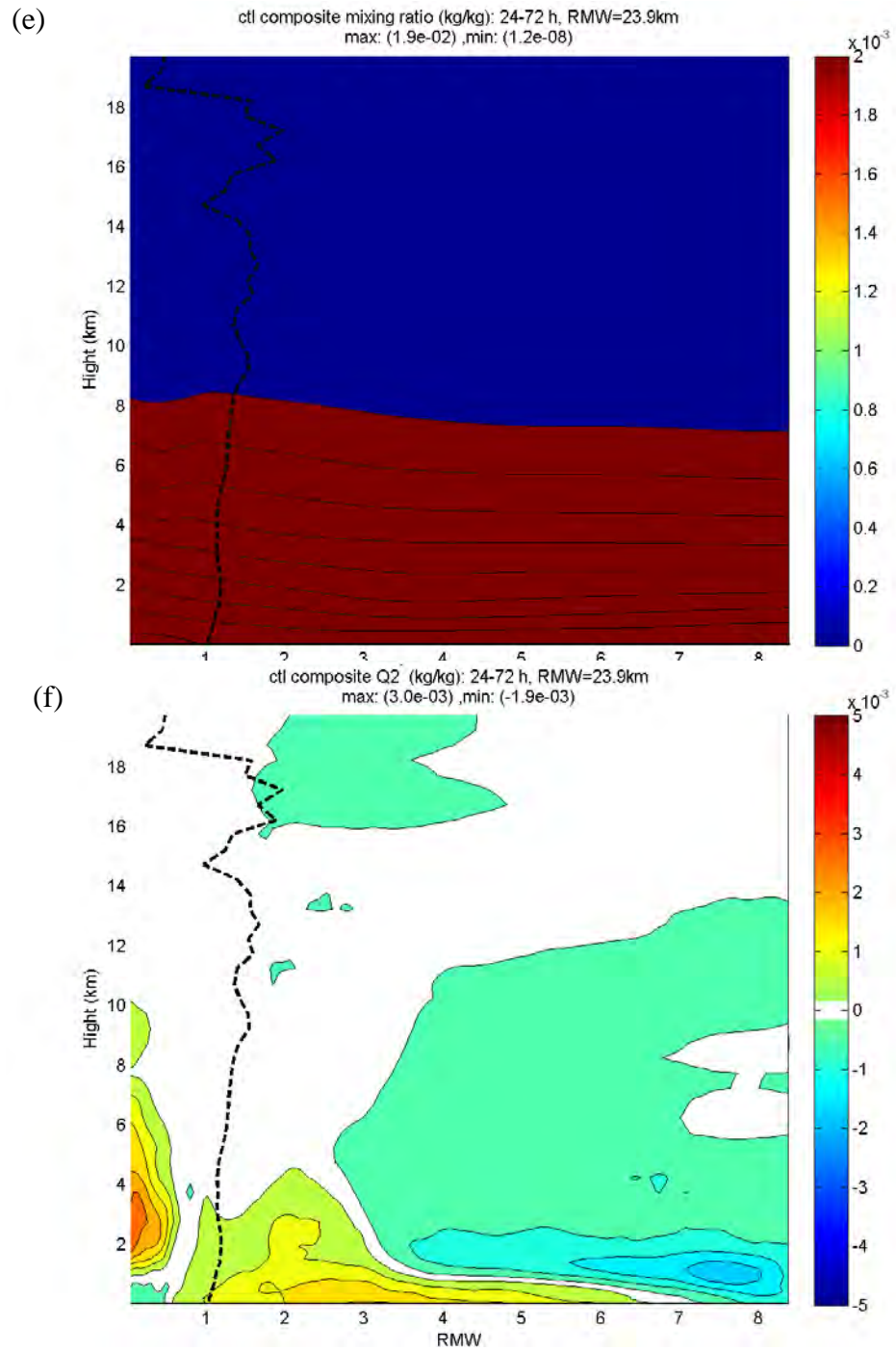


Figure 33. Composites of azimuthal-mean (a) potential temperature (K), (b) diabatic heating rate (units), and (e) vapor mixing ratio (kg/kg) during the CAT3 – CAT5 period, and deviations from the predicted values at 24 h for the azimuthal-mean (c) potential temperature, (d) diabatic heating rate, and (f) mean vapor mixing ratio. The dashed black line indicates the time-averaged locations of the RMW as a function of height.



(Figure 33 continued)



(Figure 33 continued)

THIS PAGE INTENTIONALLY LEFT BLANK

V. ONE-WAY COUPLED COLD WAKE EXPERIMENTS

A. COLD WAKE EXPERIMENTS

Recall from Chapter III section D that the wake experiments are designed to test three hypotheses proposed in Chapter I by using an idealized cold wake underneath the eyewall or a combination of an eyewall cold wake with a trailing cold wake. By comparing the wake 1, 2, and 5 experiments with wake 3 and 4 experiments, hypothesis I: “A cold wake centered underneath the TC core has more important impacts on the intensity than a trailing cold wake” will be examined. The wake 1 and 5 experiments have exactly the same circle-shape wake with radius of 60 km that is directly beneath the TC inner-core, but the magnitude of the cold anomaly in wake 5 is 4°C compared to 2°C in wake 1. The size of the cold wake in the wake 2 experiment is only half that of the wake 1 size, but the magnitude of the cold anomaly is increased from 2°C to 4°C (Figure 14b). Wake 3 experiment has a trailing oval-shaped wake with a 270 km length and 60 km width and a 2°C cold anomaly as in wake 1. The cold anomaly is placed on the center-right side of the eye (Figure 14c). Wake 4 experiment has a crescent-shaped trailing wake (Figure 14d). In contrast to wake 1, the crescent-shaped cold wake 4 does not completely cover the region below the eyewall. The areal coverages of wake 3 and wake 4 are essentially identical to that of wake 1. Recall also that the environmental vertical wind shear is zero and f is a constant so the TC will stay over the cold wake in these experiments. Note that the reduction in the air-sea fluxes is not necessarily proportional to the size or magnitude of the cold wake due to nonlinear dynamics that alter the TC near-surface wind speed, which will be demonstrated later in this section.

The wake 1, wake 2, wake 3, and wake 4 experiments are used to test hypothesis II:

Differential surface enthalpy fluxes over the ocean cold wake introduce an asymmetric structure in the TC circulation. In a certain region of moderate winds outside the radius of maximum wind, the cold wake forces a low-level wake jet that is deflected toward the center of the storm.

The strength of the wake jet depends on the magnitude of the wake cooling. The wake 1 and wake 5 experiments represent special cases of the TC remaining stationary and interacting with cold wakes generated under the eyewall with 2-4 °C magnitudes of the cold anomalies. While the TC is also not moving in the wake 3 and wake 4 experiments, the SST pattern is also fixed in time so that a minimal direct effect on the intensity will be simulated. Thus, the focus is more on the intensity and structure changes of the TC circulation due to the interaction with these trailing cold wakes, rather than due to a direct influence under the eyewall. These experiments are intended to represent a scenario of a TC moving away from, but still interacting with, the cold wake that it had generated.

Comparisons of axisymmetric and asymmetric TC structures are used to validate hypothesis III: “The TC intensity reduction due to cold wake may arise dynamically from the growth of vortex Rossby and baroclinic waves excited by the cold wake at the expense of the mean vortex, as well as by thermodynamic influences resulting from a change in the surface fluxes over the colder water.” The axisymmetric structure is defined in composites of the azimuthal-mean fields as displayed for the CNTL experiment in Chapter IV. The asymmetric structure is defined using a 1-D FFT in the azimuthal direction, and the decomposed field is then inspected for wavenumbers 1-5.

These idealized wakes are fixed in time with one-way coupling from 36-72 h. The time evolutions of V_{\max} and minimum SLP from CNTL and the wake experiments are very similar, but are not identical prior to the switching on of the coupling at 36 h (Fig. 5.1). Some of these differences are due to nonlinear truncation errors in the COAMPS even though the computations are performed in double precision. The V_{\max} difference between the CNTL and the wake experiments is less than 10 m s^{-1} at 36 h when the coupling with the cold wakes is initiated. Since the intensity at 72 h in all of the wake experiments is considerably lower than for the CNTL experiments, these intensity differences at 36 h do not alter the interpretation of the overall TC response to the various cold wakes. The wake 1 to wake 5 intensities reach CAT4, CAT3, low CAT5, low CAT5, and CAT1, respectively (Figure 34). The wake 1, wake 2, and wake 5 experiments result in at least one hurricane intensity category decrease compared to the CNTL, while the

wake 5 experiment reaches the lowest intensity in the upper CAT1 at 72 h. The TC intensity in response to the cold wake 1 is about one category lower than for the wake 3 or wake 4 experiments despite they all have a 2°C cold anomaly and have roughly about the same size wake. Because the wake 5 experiment imposes a 4°C cold wake below the eyewall, it has a more rapid response and decreases to CAT1 at 72 h. This first set of experiments is intended to demonstrate that the cold wake underneath the eyewall region is more efficient than a trailing wake in spinning down the TC, which validates hypothesis I: “A cold wake centered underneath the TC core has a more important impact on the intensity than a trailing cold wake.”

Note that an immediate intensity decrease and pressure rise do not occur in the wake 2, wake 3, and wake 4 experiments, which have more asymmetry in the shape of the cold wake than for the wake 1 and wake 5 experiments. Reducing the wake size, but doubling the cold wake magnitude, in the wake 2 experiment delayed the start time of the TC weakening by about 4 h compared to the wake 1 experiment. However, by 72 h the response to the cold wake may be very nonlinear.

Both wake 3 and wake 4 are trailing cold wakes and the TC continues to intensify as in the CNTL until 50 h (hour 14 after imposition of the cold wake), and then the intensity decreases. The 72-h intensity in the wake 4 (crescent-shape) experiment is lower than in wake 3 (trailing oval) presumably due to the larger area of cold wake under the eyewall. Comparing wake 1 with wake 2 and wake 1 with wake 3, the differences in cold wake areas under the eyewall suggest a dynamic response that delays the TC spin-down. The effects of the trailing wake in the wake 3 and wake 4 experiments is similar to the effect of the asymmetric wake 2 underneath the eyewall as the trailing wakes prolong the adjustment time for TC spin-down. These results suggest a more complicated TC dynamic response to the cold wake forcing compared to a direct thermodynamic impact, which is in contrary to the WHISHI thermodynamic point of view (Bender and Ginis 2000). In all of the wake experiments except for wake 5, the imposition of the cold wake, and thus a reduction in the surface fluxes, did not immediately reduce the surface wind speed. These differences in intensity responses suggest that there must be a dynamic pathway that accounts for the time delay in the TC spin-down.

To identify the dynamic pathway, the TC structure changes forced by different cold wakes are further analyzed. The azimuthal-mean RMW at 10 m height averaged in time between 36-72 h from the wake experiments ranges from 32.4 km (wake 5) to 22.7 km (wake 3), for a difference of only 9.7 km (Figure 35). This larger R_{\max} in the wake 5 experiment may be expected due to the broad 4°C cold wake directly underneath the eye. Radii of gale-force wind (17.2 m s^{-1}) for the wake 5 and wake 3 (long trailing wake) experiments are 58.6 and 51.5 km, respectively. Since the R_{\max} is also larger for the wake 5 experiment, the shapes of the wind profiles outside the R_{\max} are not that different for the wake 5 and wake 3 experiments. Thus, a cold wake directly below the eye such as in wake 5 is more effective in decreasing the intensity and increasing the R_{\max} and expanding the radius of gale-force wind compared to the trailing wake 3 and wake 4 experiments.

The magnitudes of the fluxes from the ocean are implicitly related to the surface wind speed. The enthalpy fluxes within the area inside the RMW and within 200 km are shown in Figure 36. The wake 3 experiment has the largest total flux of $0.12 \text{ mega W m}^{-2}$ within 200 km radius. The total fluxes in the wake 1, wake 2, wake 4, and wake 5 experiments are around 0.11, 0.1, 0.11, $0.09 \text{ mega W m}^{-2}$, respectively. The enthalpy flux difference within 200 km is only a 23% reduction between the wake 1 and wake 5 experiments that have the same area of a cold wake directly below eyewall, and anomalies of 2°C and 4°C, respectively. This flux difference is primarily due to the reduction in surface winds associated with the large decrease in intensity in the wake 5 experiment. The wake 1 and wake 4 experiments have about the same total enthalpy flux into the atmosphere, but the TC in the wake 4 experiment has a much higher intensity than for wake 1, which is in part due to the eyewall in the wake 4 experiment is not directly over the cold wake as it is for the wake 1 experiment. This is another indication of nonlinear processes that may be induced by a cold wake then alters the TC moisture, temperature, and wind structures, and thus modulates the energy fluxes from the ocean into the atmosphere.

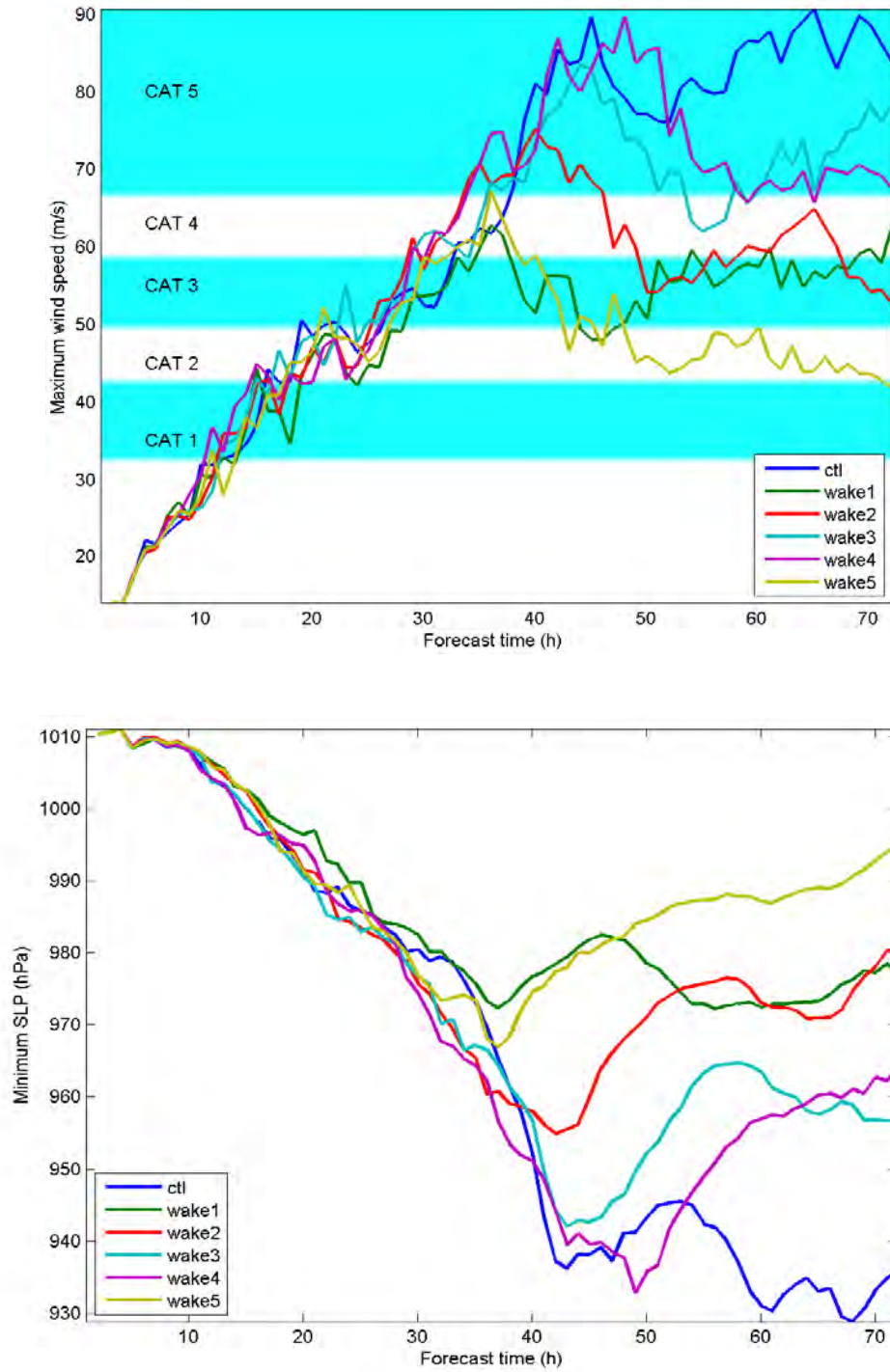


Figure 34. Comparison of the (top panel) maximum wind speeds (m s^{-1}) and (bottom) minimum sea-level pressures (hPa) between the CNTL and the wake experiments, in which the coupling begins instantaneously at hour 36. The line definitions for the wake experiments are in the insets.

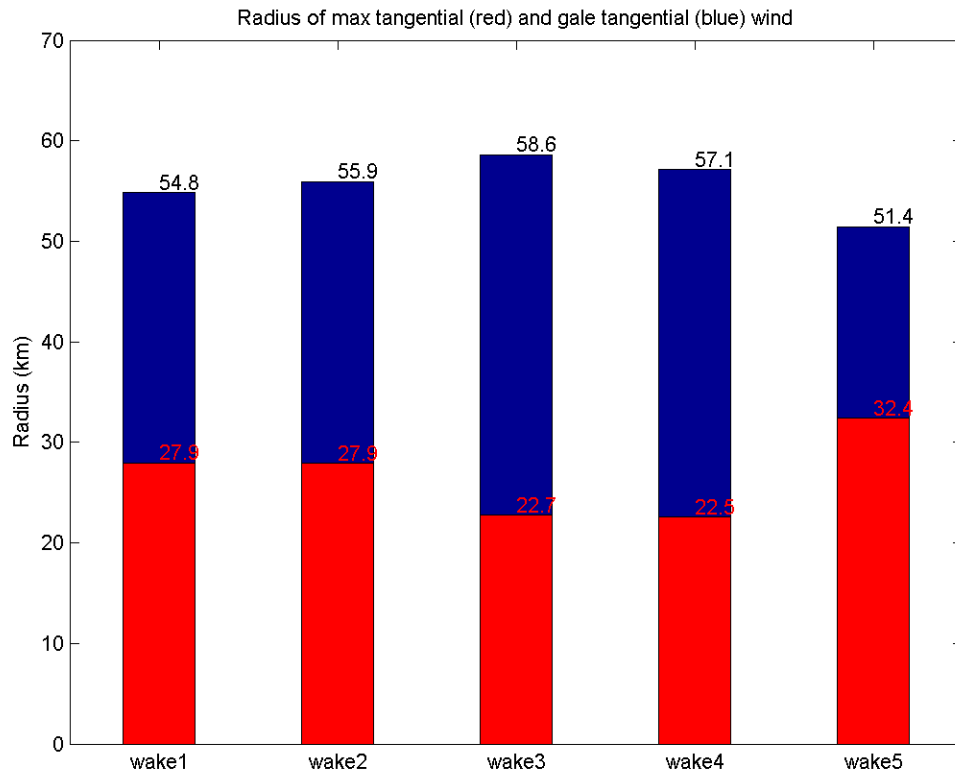


Figure 35. Comparison of azimuthal- and time-mean (36 h to 72 h) RMW (km, red bar) and radius of gale winds (blue bar) for the wake 1 to wake 5 experiments.

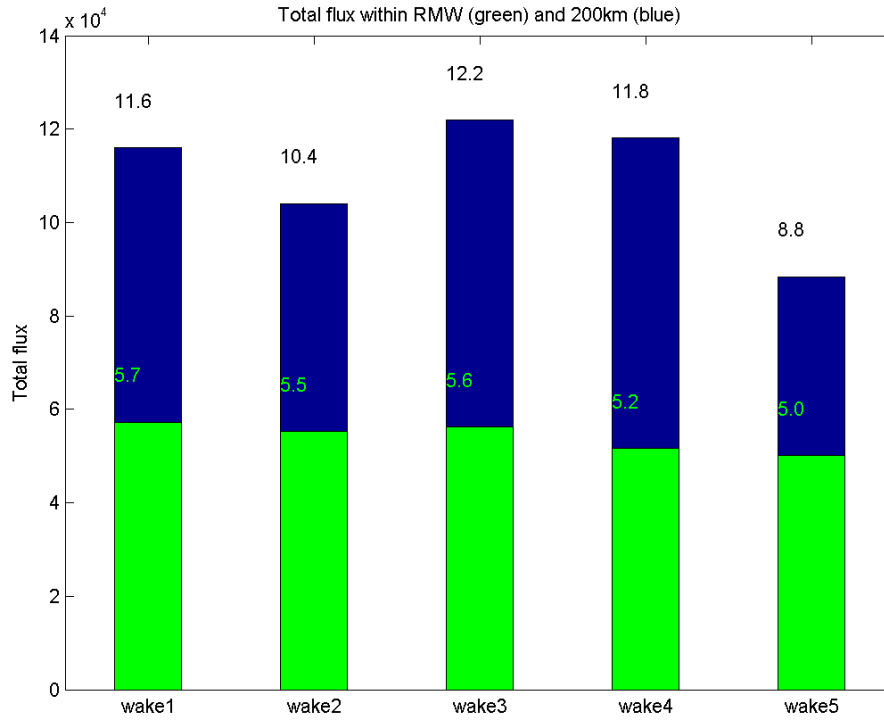


Figure 36. Total enthalpy flux (10^4 Wm^{-2}) within the RMW (green bar) and within 200 km radius (blue bar) at 36-72 h for the wake 1 to wake 5 experiments.

Although introducing these cold wakes forces an asymmetric response in the TC structure to be discussed below, the axisymmetric structure changes from the CNTL experiment are first examined (Figure 37). These composites are calculated in the same way as in Chapter VI section A, except the time window is after the time the cold wake is introduced in the model, i.e., between 36-72 h. The V_{\max} is decreased in all of the wake 1 to wake 5 experiments compared to the CNTL (Figure 37a), with the 4°C cold wake 5 (Figure 37f) having the largest reduction to a CAT 1. The horizontal and vertical structures of the tangential wind are also affected. While the RMW (at 10 m) in the CNTL, wake 1, and wake 5 experiments are 34.5, 27.9 km, and 32.4 km, respectively, the vertical tilts of the RMW for wake 1 and wake 5 are much larger (doubled and almost tripled radii at 10 km elevation compared to the RMW at 10 km in elevation) compared to the almost vertically oriented RMW for the CNTL. For the cold wake 3 and cold wake 4 that have along trailing wake, the RMW remains vertically oriented as in the CNTL.

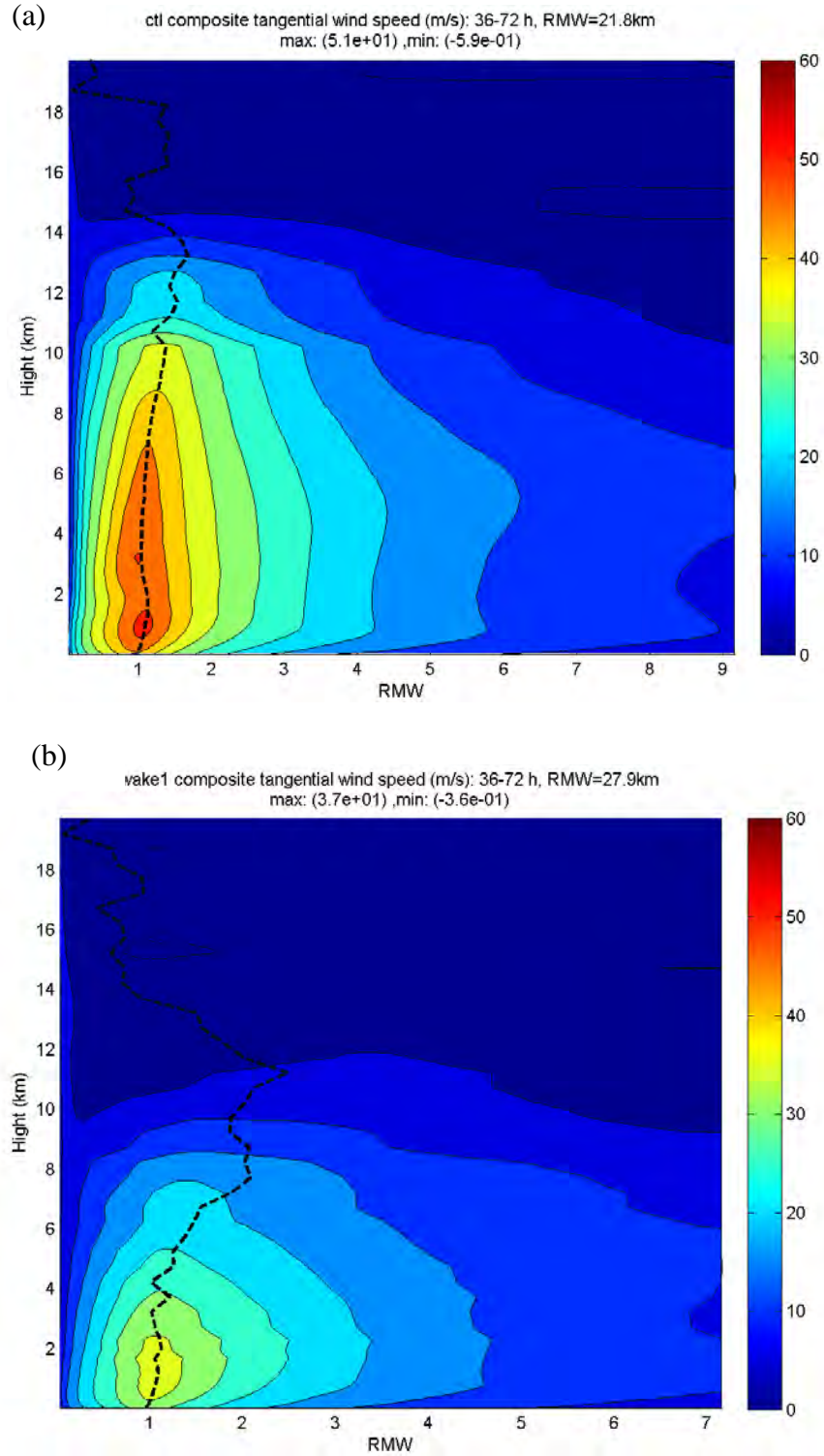
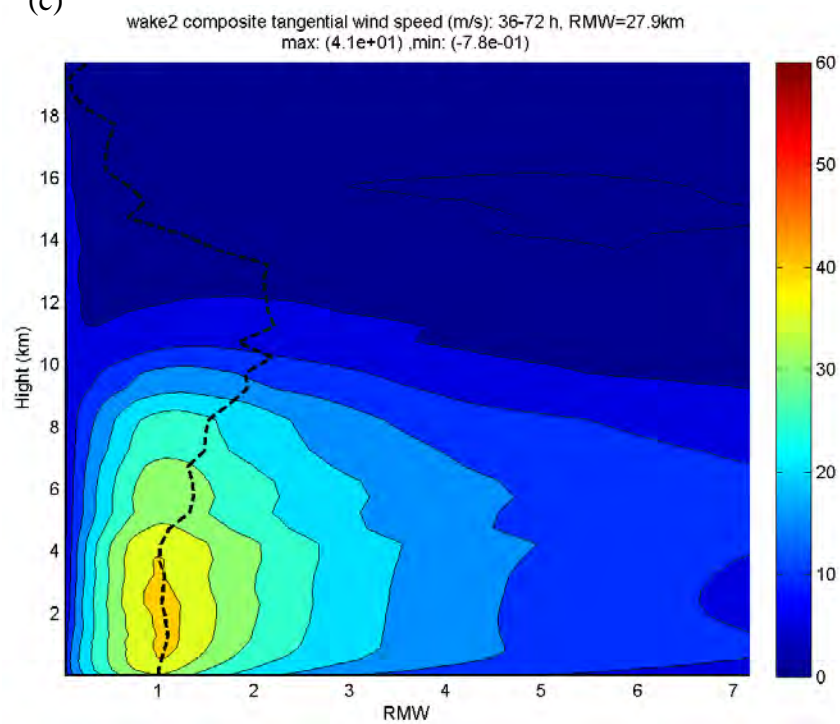
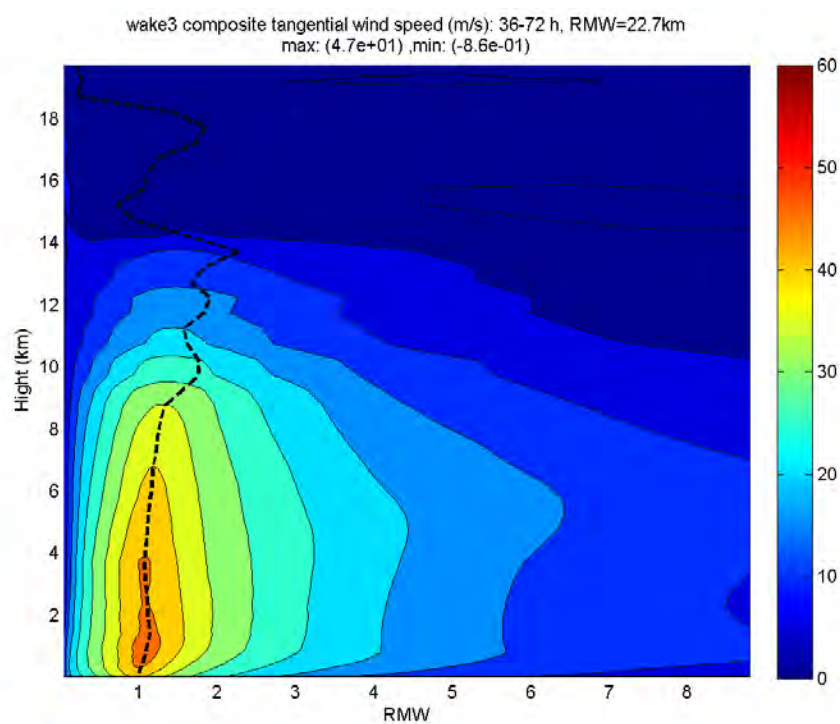


Figure 37. Composites of the azimuthal-mean tangential wind (contour interval 5 m s^{-1}) at 36-72 h from (a) CNTL, (b) wake 1, (c) wake 2, (d) wake 3, (e) wake 4, and (f) wake 5 experiments. Dashed black line represents the RMW at each level.

(c)

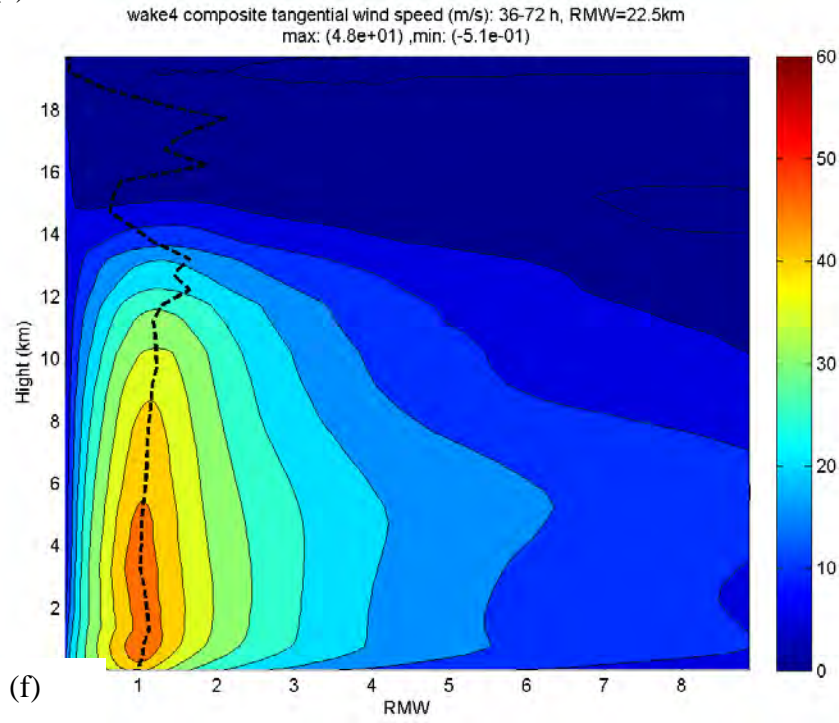


(d)



(Figure 37 continued)

(e)



(f)

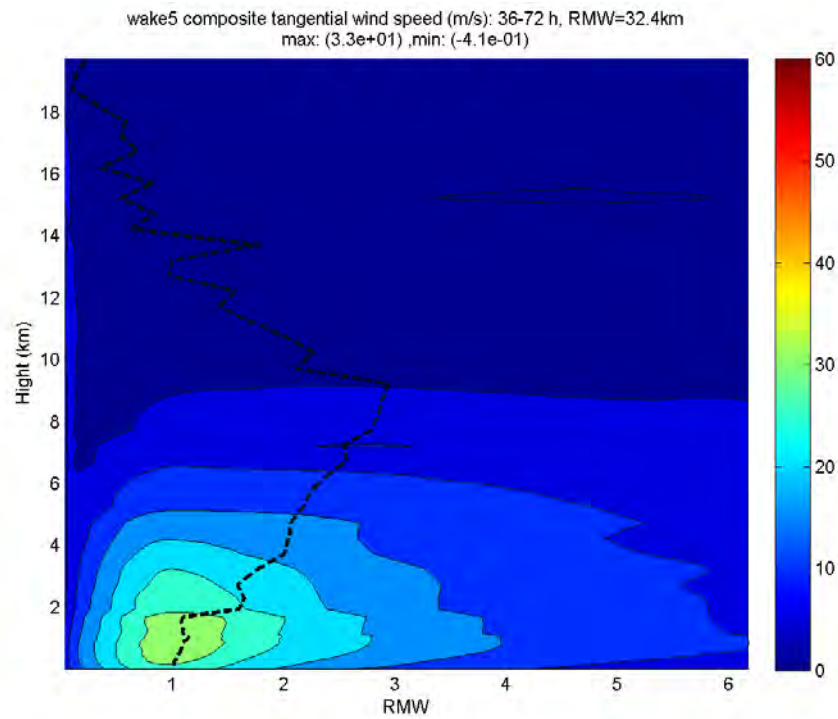


(Figure 37 continued)

Whereas the vertical extents of the maximum tangential winds in the wake 3 and wake 4 experiments are also similar to the CNTL, the TC vertical extents for wake 1, wake 2, and wake 5 experiments are much reduced, which may be attributed to weaker vertical convection since the eyewall is directly over these cold wakes. In conjunction with the reduced intensity, the sizes (horizontal extents of the tangential winds) are also reduced for the wake 1, wake 2, and wake 5 experiments compared to the CNTL.

The associated azimuthal-mean profiles of radial wind in the wake 1 to wake 5 experiments (Figure 38b–f) expressed as deviations from the CNTL experiment (Figure 38a) illustrate the changes in the secondary circulation. The near-surface inflows in the wake experiments are weaker than in the CNTL. The wake 3 and wake 4 experiments with a trailing cold wake have about a $2\text{--}3\text{ m s}^{-1}$ smaller low-level inflow. By contrast, the wake 1, wake 2, and wake 5 experiments with cold wakes directly under the eyewall have reductions in the low-level radial inflows exceeding 6 m s^{-1} . These reductions are a maximum inside the RMW, which is consistent with the larger reductions in intensity for the wake 1, wake 2, and wake 5 experiments. The upper-level outflows are also reduced. For the wake 3 and wake 4 experiments, the maximum outflows are reduced and the outflow layers are at a lower elevation compared to the CNTL. More dramatic reductions in the magnitudes of the outflow, and the elevations of the outflow, are noted for the wake 1, wake 2, and wake 5 experiments, which again are consistent with the larger reductions in the intensities for these cold wake experiments.

The latent heat supply to the inner core of the TCs is also related to the low-level moisture fields (Figure 39). The trailing cold wakes in the wake 3 and wake 4 experiments have reduced azimuthal mean mixing ratios between 36 h–72 h (~ 0.1 to 0.3 g kg^{-1}) below 1 km throughout the inner-core region that may be attributed in part to the reduced air-sea fluxes over the trailing cold wake regions. Interestingly, the crescent-shaped cold wake 4 (see Figure 14d) has increased moisture content ($> 0.3\text{ g kg}^{-1}$) at 4 – 7 km elevation near the center that may be attributed to less subsidence in the eye. The reduced secondary circulations in the wake 3 and wake 4 experiments are also reflected in slightly smaller moisture in the outflow layer. However, two regions of larger moisture are also simulated at the top of the boundary layer with a maximum near 3

RMW and in a deeper layer in the middle troposphere. The positive moisture anomaly region may be partly attributed to a reduced boundary layer inflow of moisture to the inner-core region, and thus less compensating subsidence and drying just above the boundary layer (Figure 39d and e). The space and time filtered mean moisture changes in Figure 39 are about an order of magnitude smaller compared to just the space filtered moisture difference between the wake and CNTL experiments. This is because the position and magnitude of the moisture changes fluctuate with time. The wake 3 and wake 4 experiments induced a deep layer of $\sim 1\text{-}3 \text{ g kg}^{-1}$ higher mixing ratio compared to the control experiments after 43 h such as the 49 h wake 3 – CNTL moisture change (Figure 40).

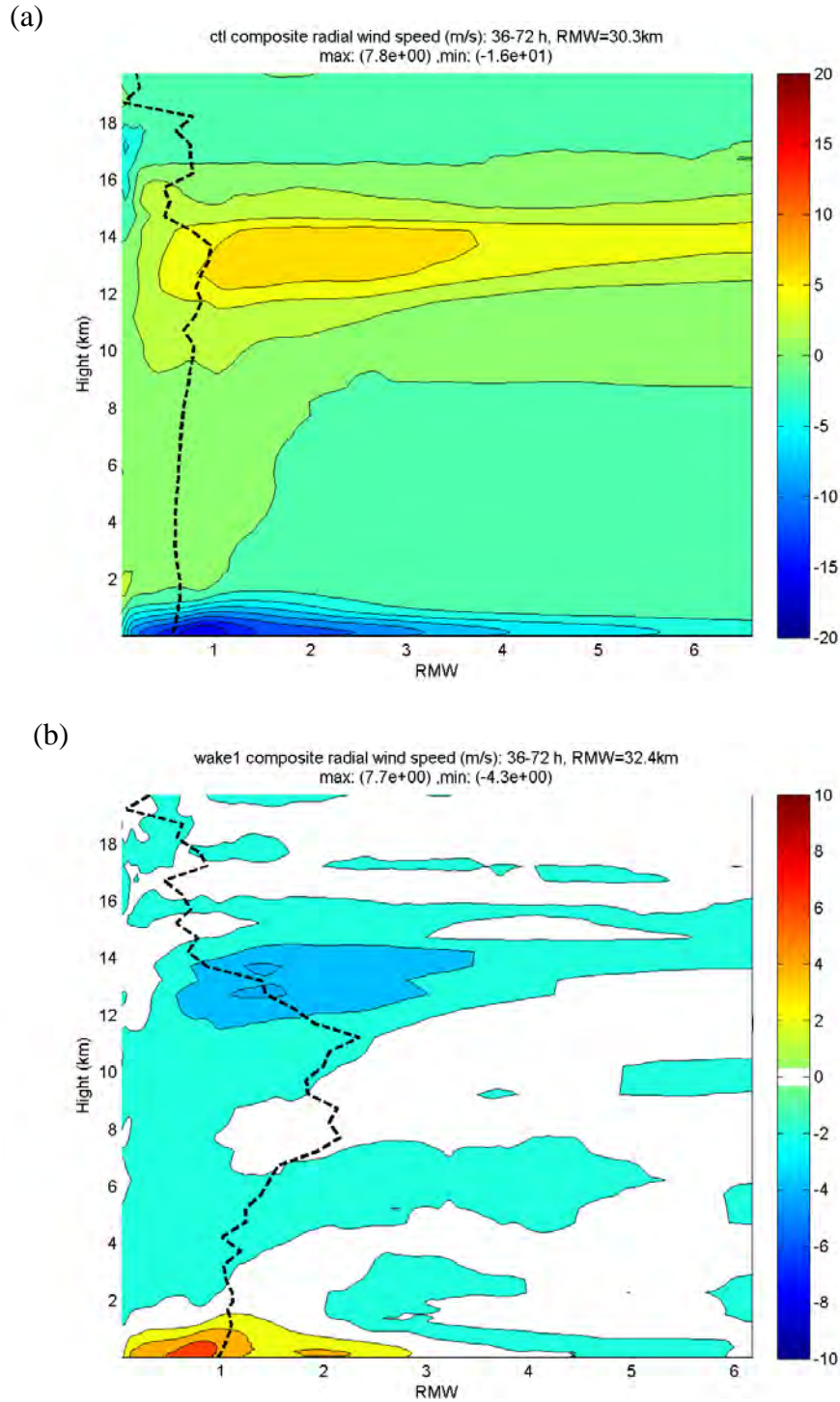
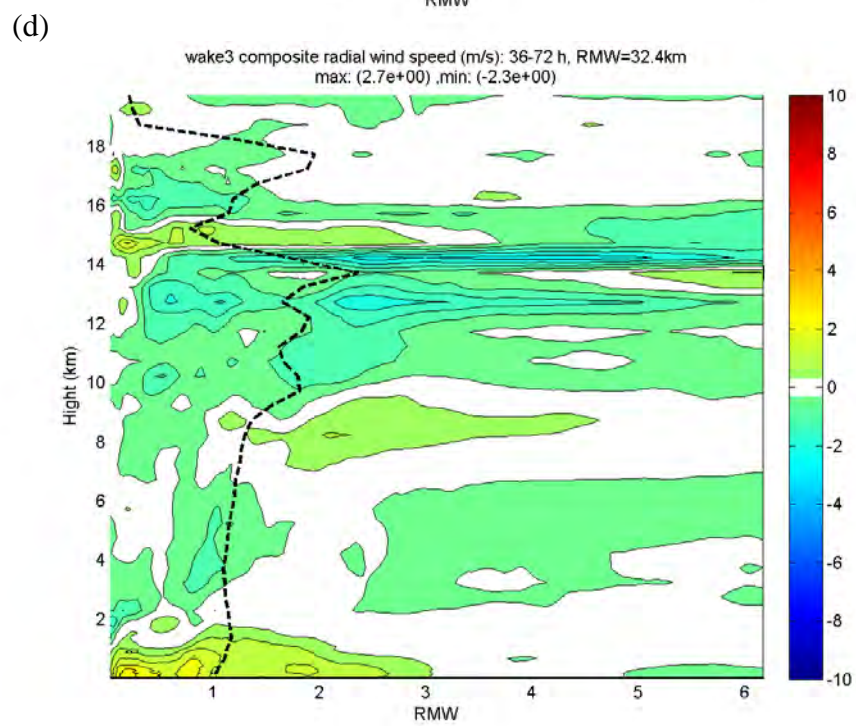
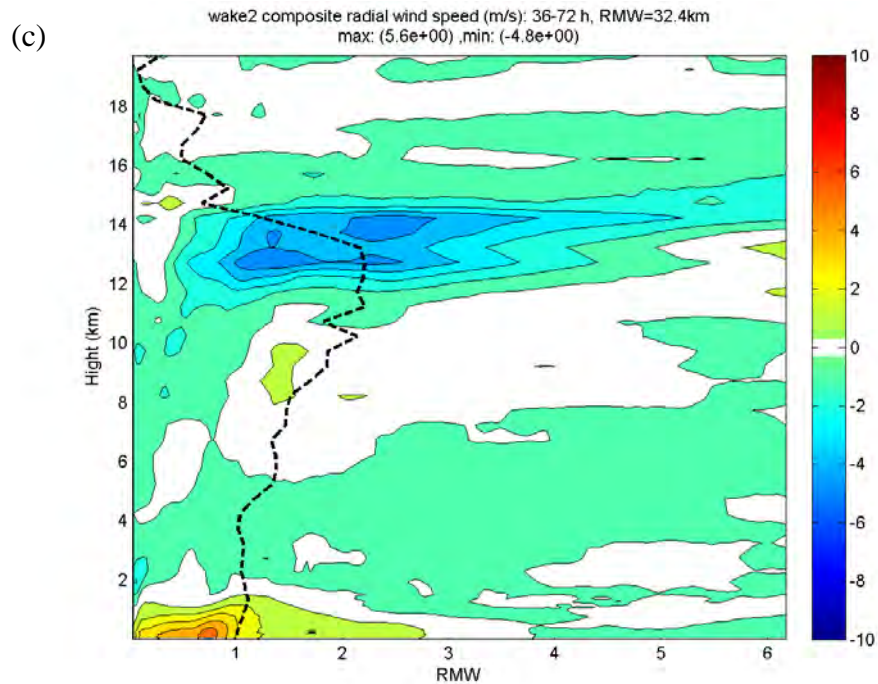
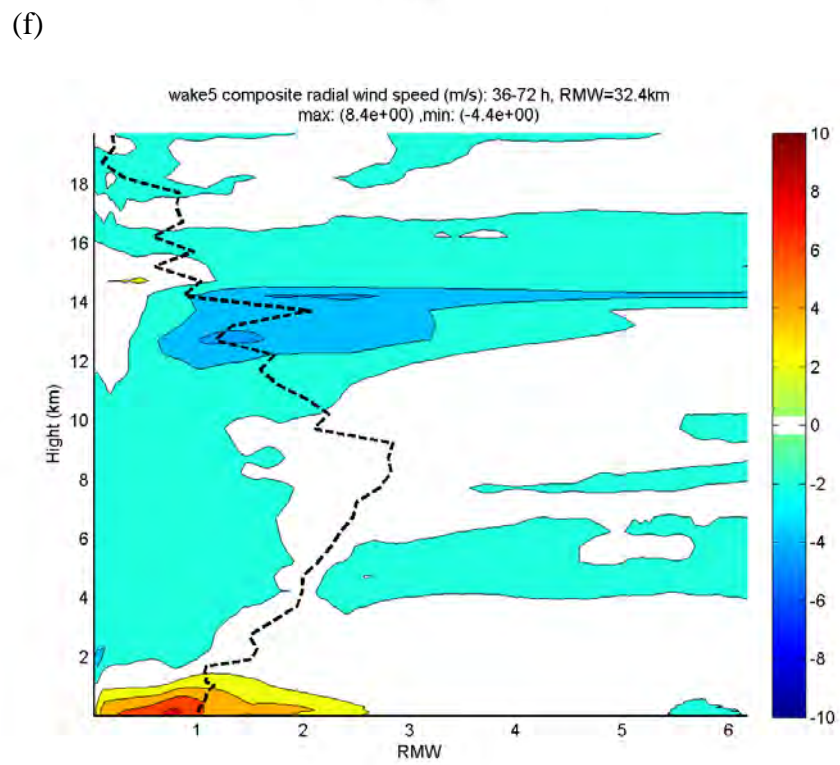
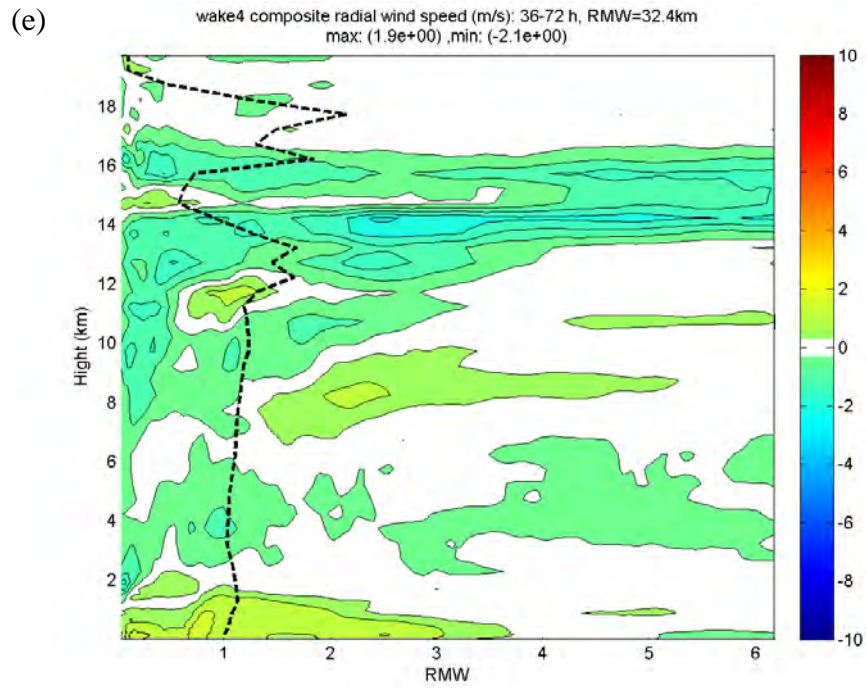


Figure 38. Composite of the 36 h – 72 h azimuthal-mean radial wind component (m s^{-1} ; scale on right) from the (a) CNTL experiment, and then the deviations from the CNTL for: (b) wake 1-CNTL, (c) wake 2-CNTL, (d) wake 3-CNTL, (e) wake 4-CNTL, and (f) wake 5-CNTL. The contour interval in panels (b) to (f) is 2 m s^{-1} and the scale is on the right.



(Figure 38 continued)



(Figure 38 continued)

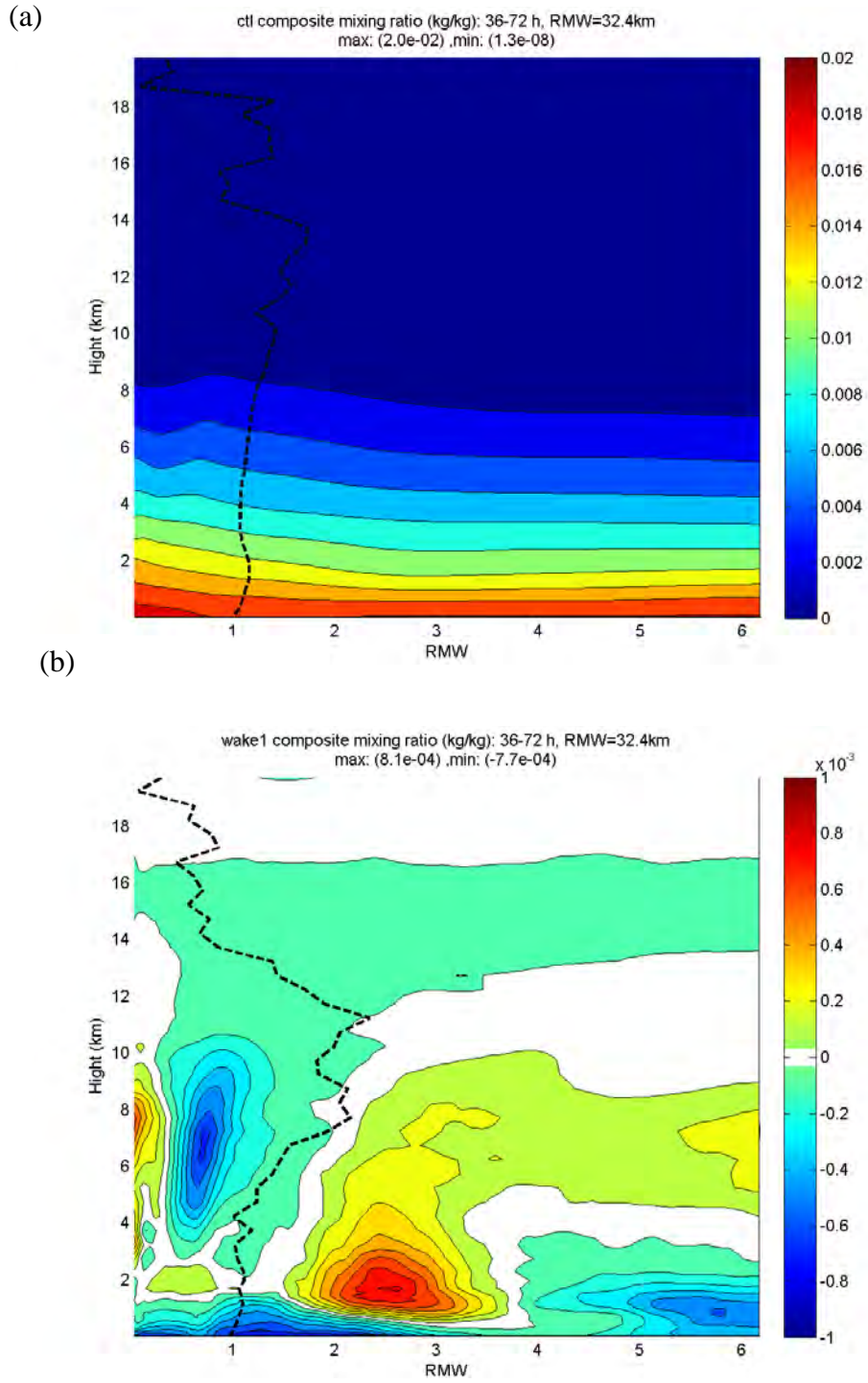
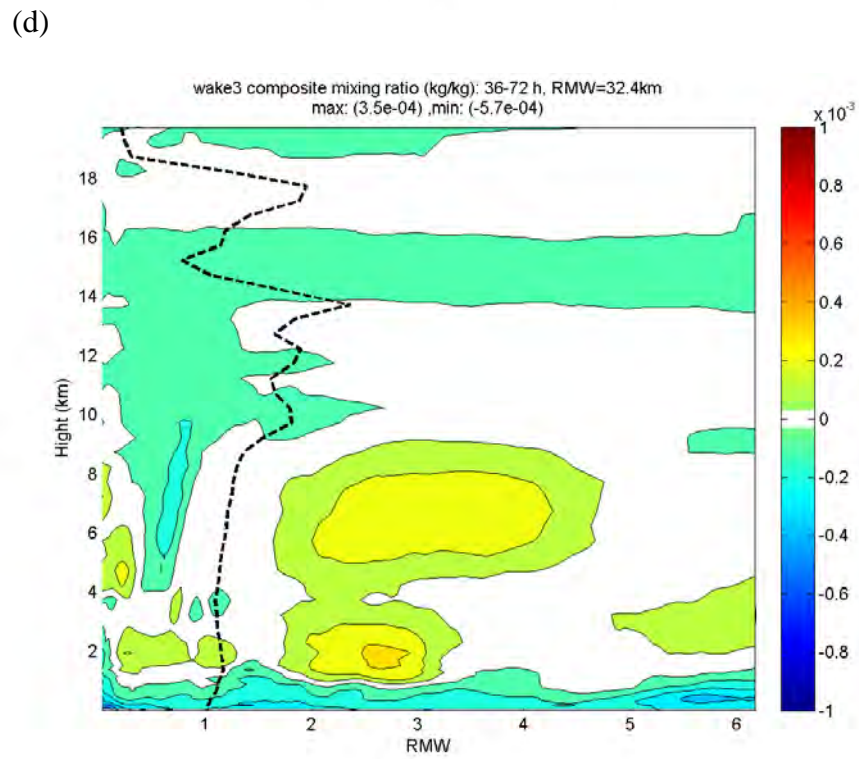
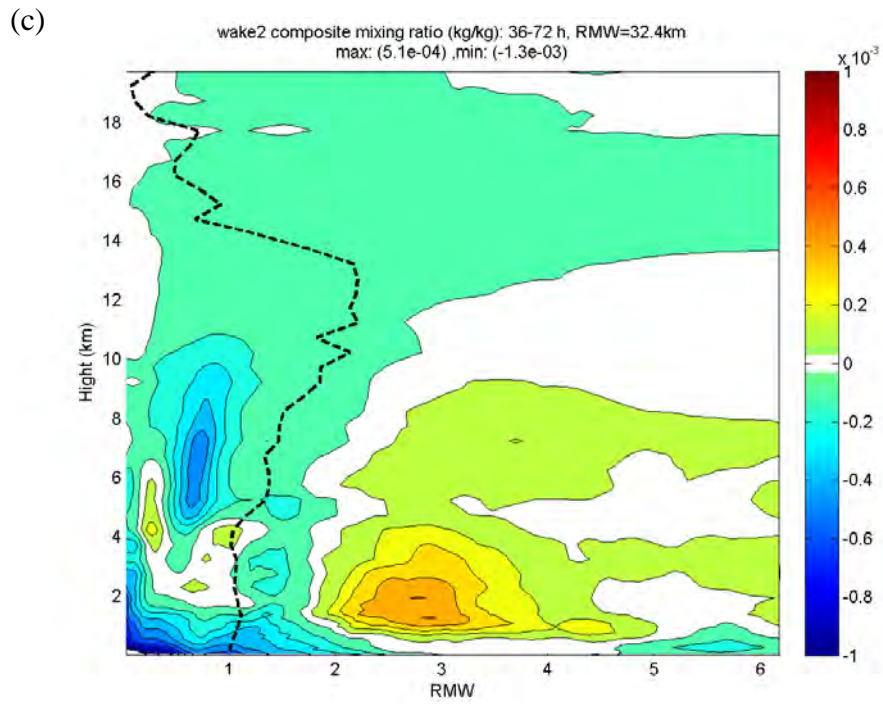
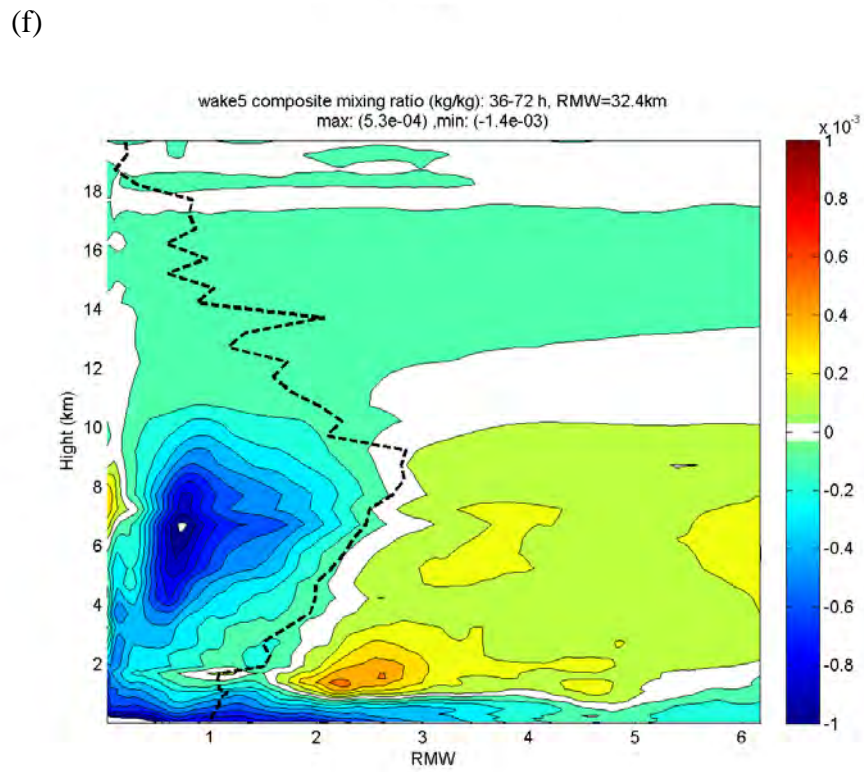
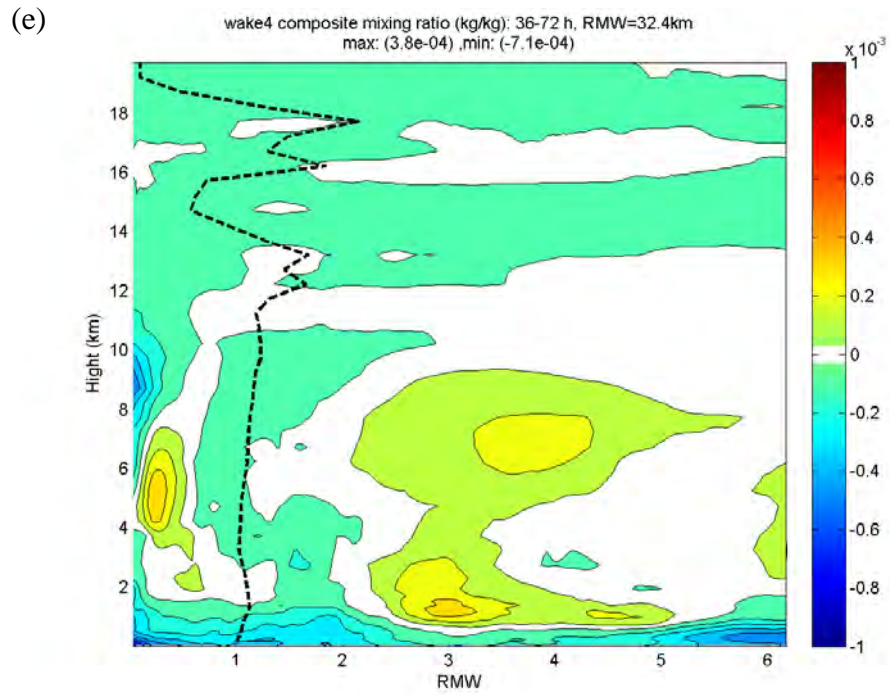


Figure 39. As in Figure 38, except for the water vapor mixing ratio (kg/kg) from the CNTL experiment in (a) and then the deviations from the CNTL for the wake 1 to wake 5 experiments in panels (b) to (f).



(Figure 39 continued)



(Figure 39 continued)

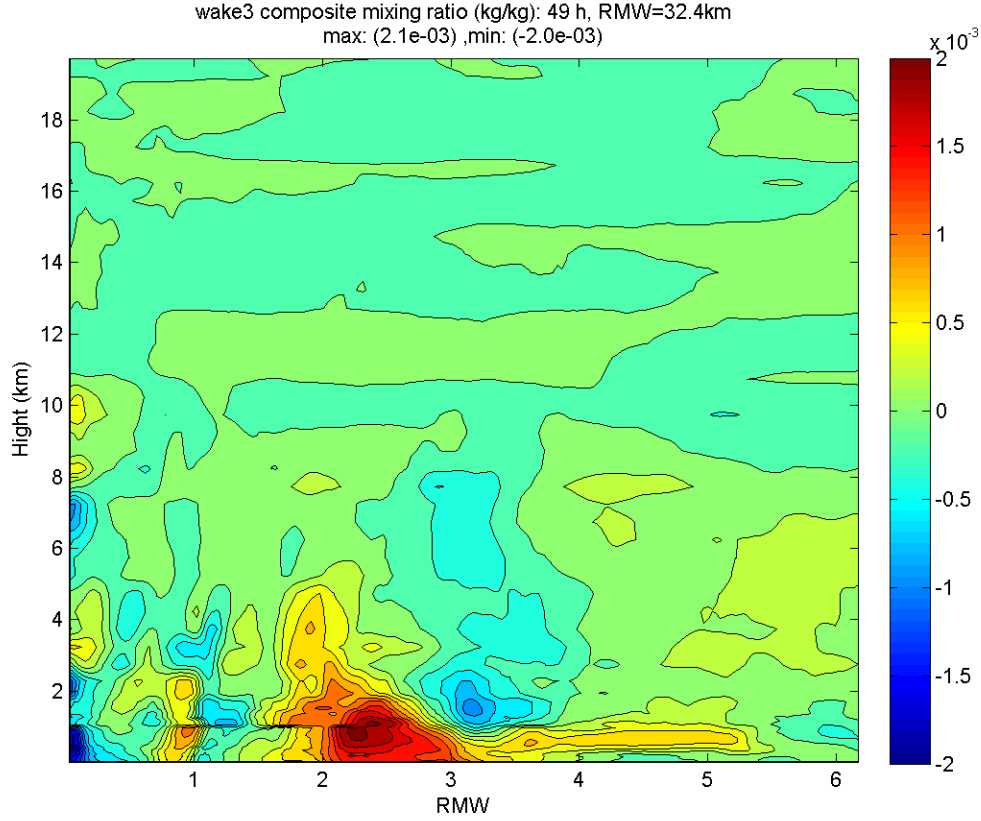


Figure 40. Composite of the wake 3 experiment 49 h azimuthal-mean mixing ratio (g kg^{-1} ; scale on right) deviation from the CNTL experiment.

However, the vertical velocity differences between the wake experiments and the CNTL simulation in this region are smaller than 0.1 ms^{-1} . Thus the contribution from a slightly reduced compensating subsidence from the wake 3 and wake 4 is likely small. Reduced moisture compared to the CNTL is particularly noted at low levels near the RMW, in the ascent region, within the RMW, and in the outflow layer for the wake 1 and wake 2 experiments, and especially for the wake 5 experiments (Figure 41b, c, and f). As above, reduced boundary layer inflow to the inner-core region likely leads to less compensating subsidence from above, which may have a small contribution to the positive moisture anomaly in the 1-4 km layer between 2-3 R_{max} for the wake 1, wake 2, and wake 5 experiments.

Although these are differences for the axisymmetric fields, the TC response for cold wakes with and without a trailing portion seem to suggest the trailing wake experiments have a larger advection of low-mid level moisture compared to the wake experiments without the trailing wake. Note the total enthalpy flux transfer from the ocean to the atmosphere in the wake 1 and wake 4 experiments are about the same (Figure 31), and yet the TC radial wind and moisture changes in these two experiments are quite different. This is another indication that there is a dynamic pathway induced by the trailing wake both inside and outside the RMW.

Composites of the radial pressure gradients from the CNTL and the wake 3 and wake 4 experiments indicate the wake 3 and wake 4 experiments have slightly smaller radial pressure gradients near the RMW compared to the CNTL (Figure 42). In the wake 1 (Figure 42b), wake 2 (Figure 42c), and wake 5 (Figure 42f) experiments without a trailing wake, the radial pressure gradients are considerably decreased compared to CNTL (Figure 42a). From gradient wind balance, the reductions of flux divergence in the wake 3 and wake 4 experiments should be balanced by changes in the pressure gradient, tangential and radial wind speeds compared to the CNTL experiment.

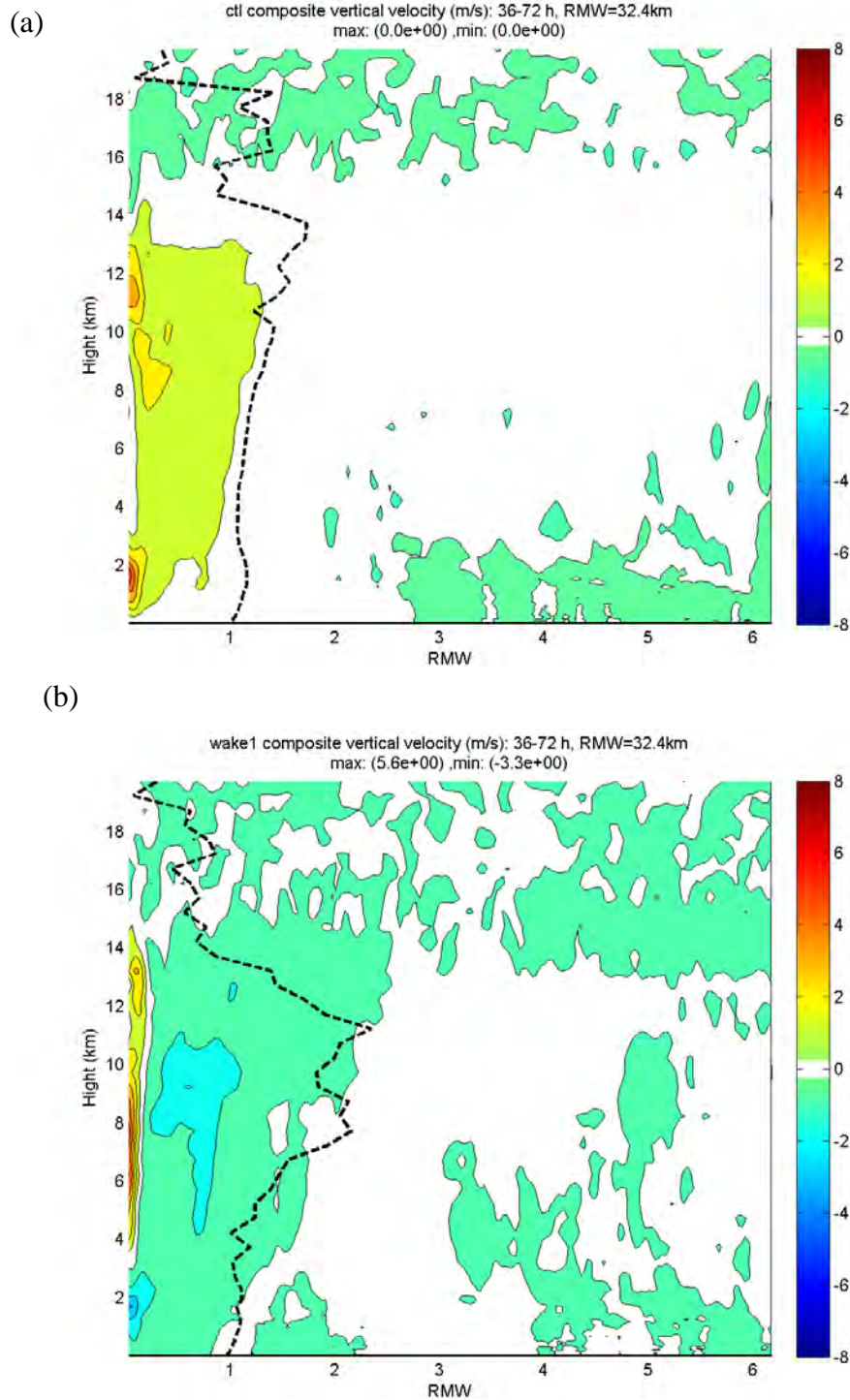
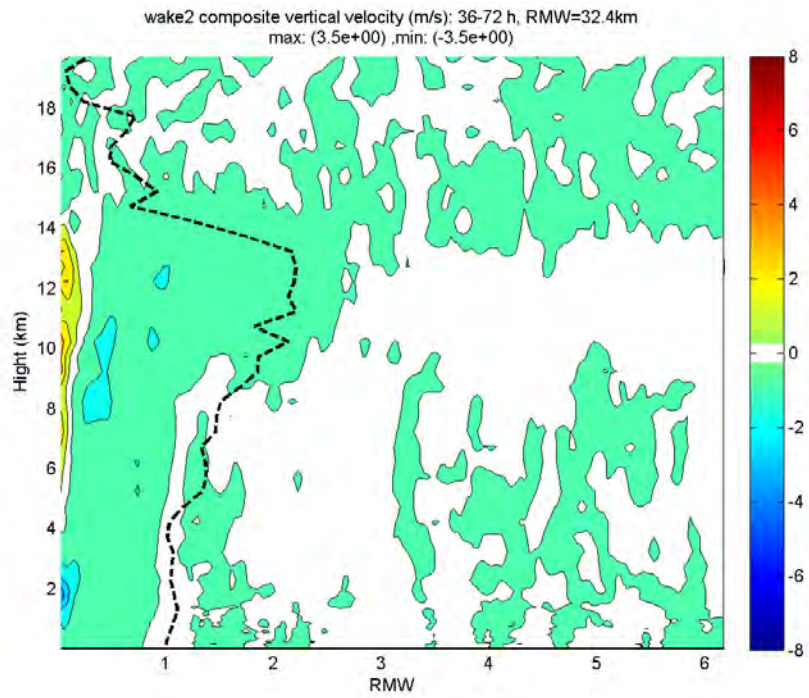
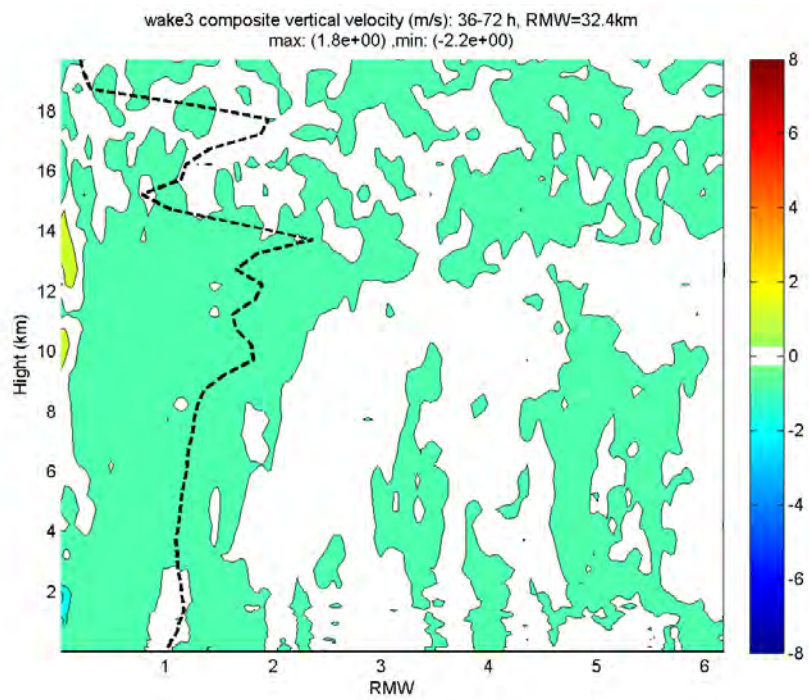


Figure 41. As in Figure 39, except for the vertical velocity (ms^{-1}) from the CNTL experiment in (a) and then the deviations from the CNTL for the wake 1 to wake 5 experiments in panels (b) to (f).

(c)



(d)



(Figure 41 continued)

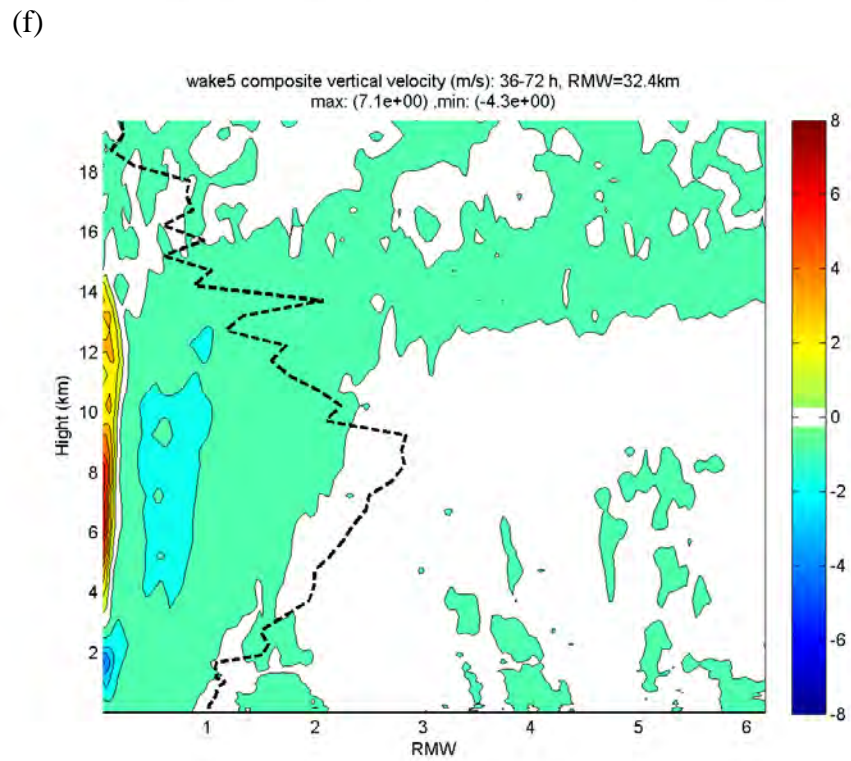
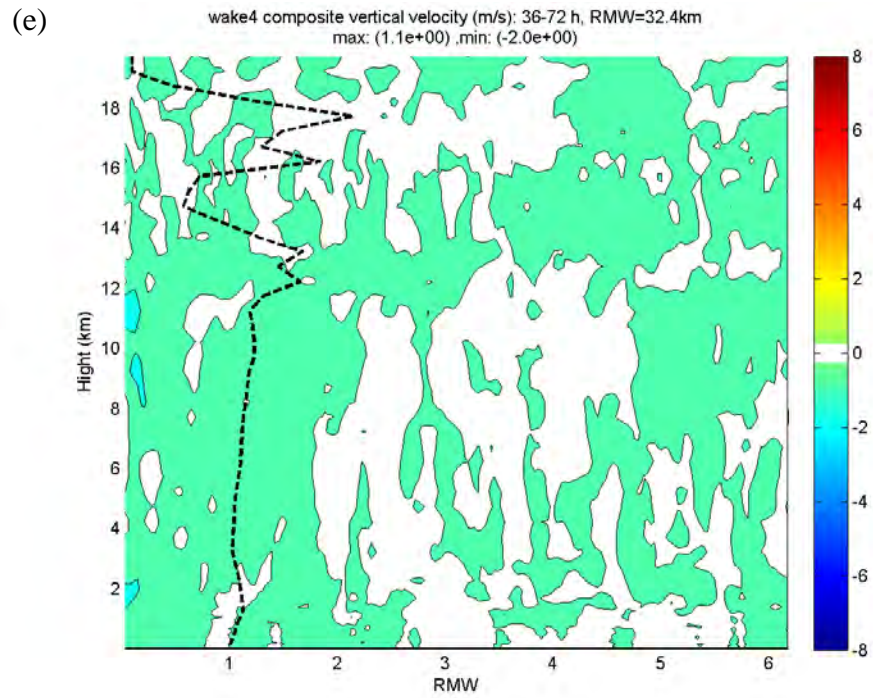


(Figure 41 continued)

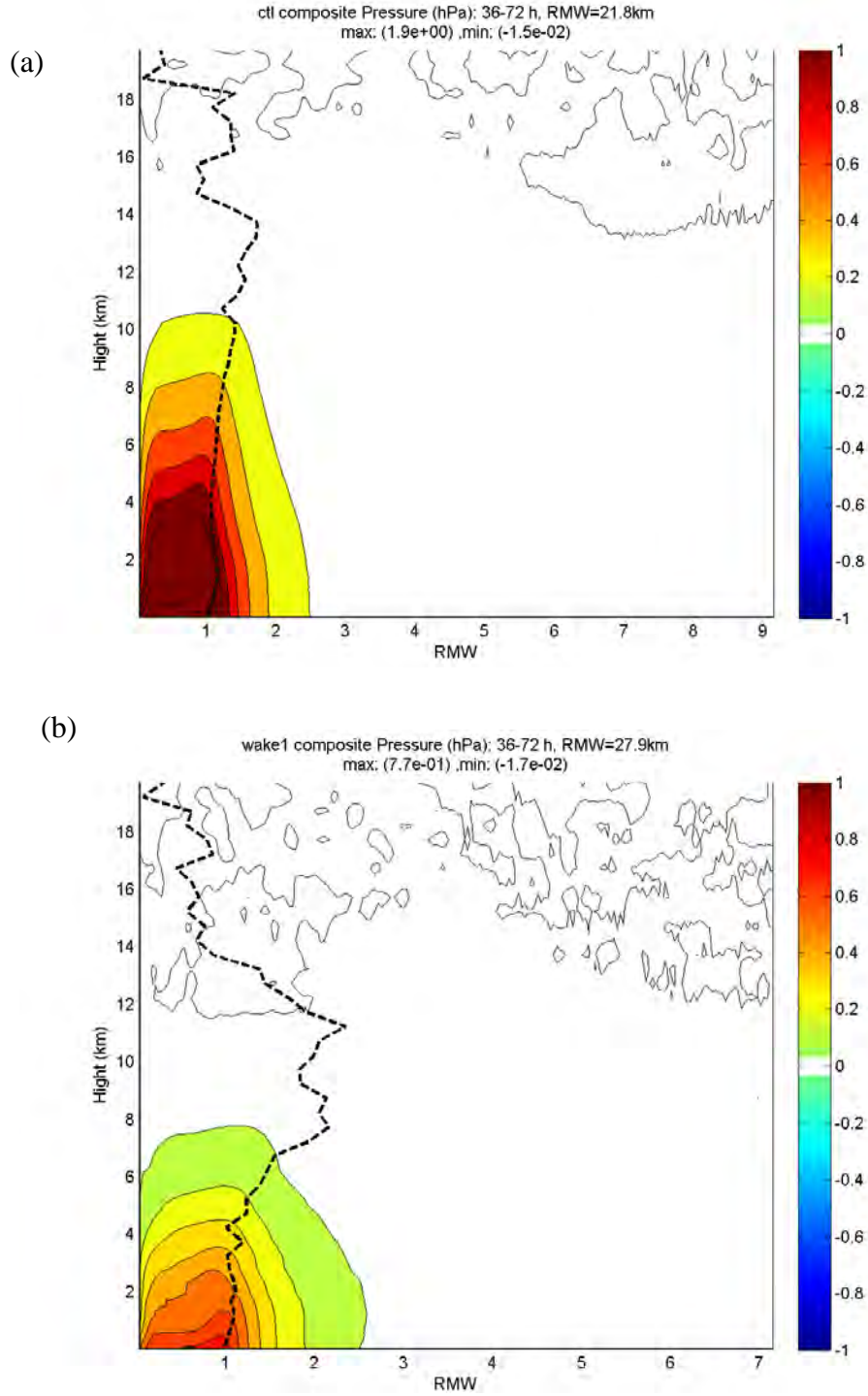
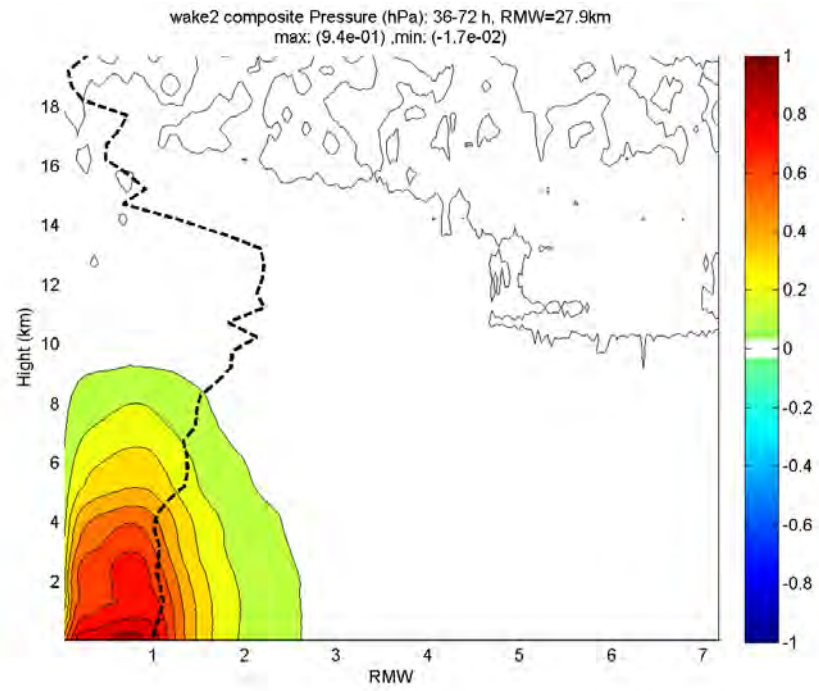
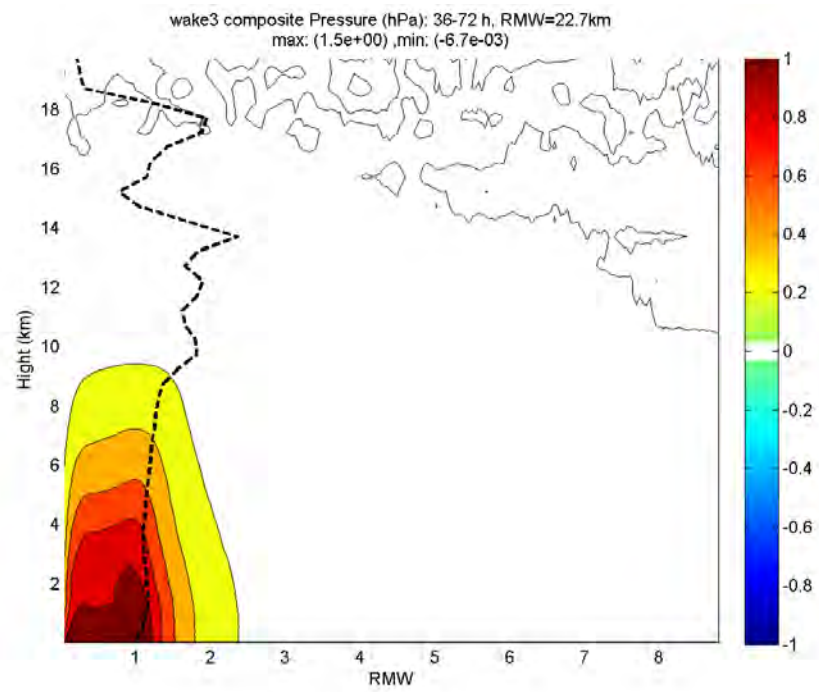


Figure 42. Composites of the azimuthal-mean radial pressure gradients (hPa/km) from (a) CNTL, (b) wake 1, (c) wake 2, (d) wake 3, and (e) wake 4, and (f) wake 5 experiments at 36-72 h.

(c)



(d)



(Figure 42 continued)

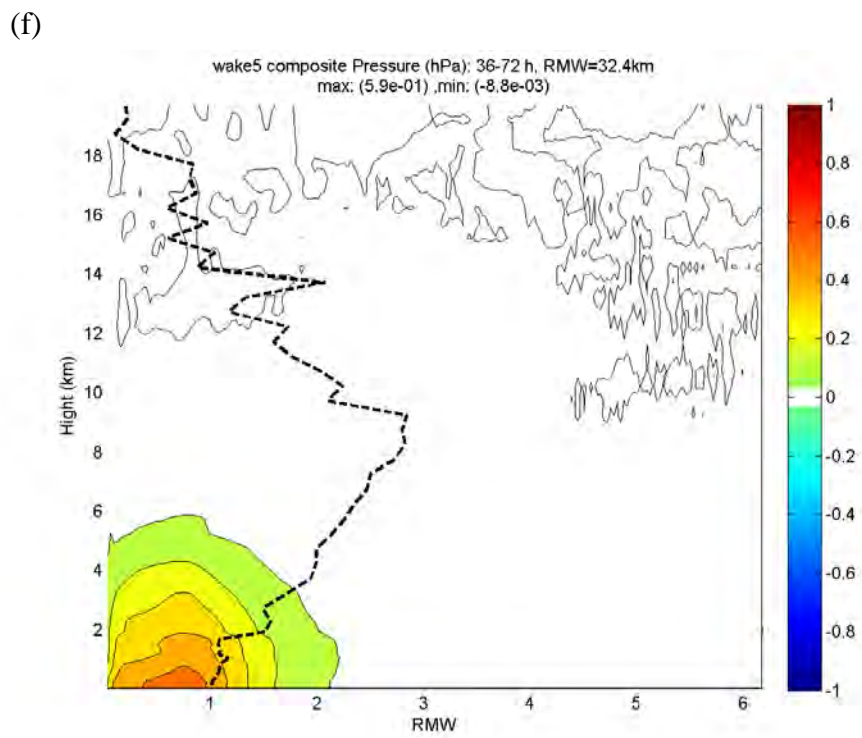
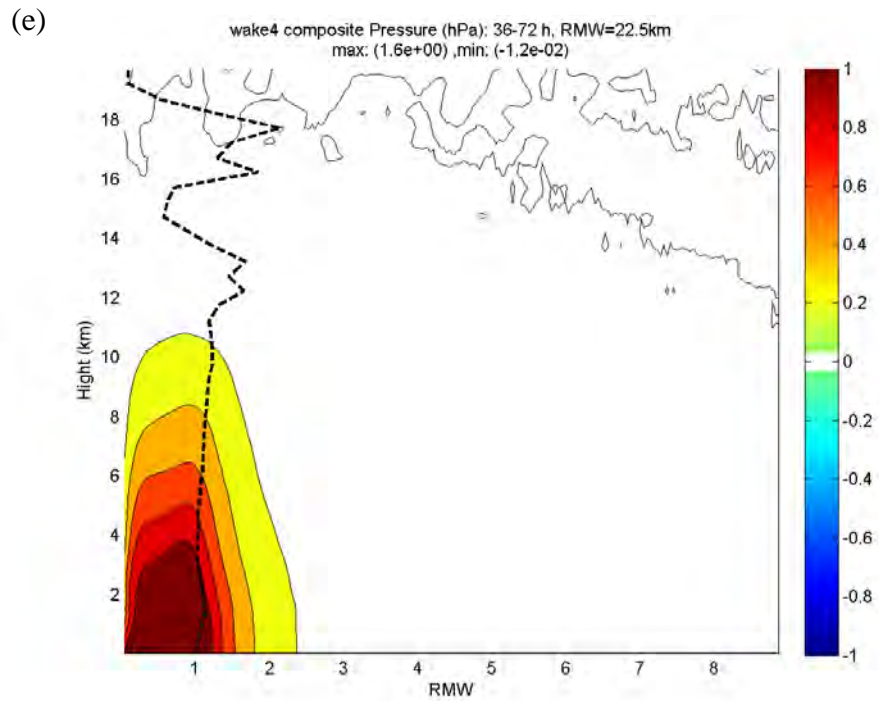


(Figure 42 continued)

B. ASYMMETRIC RESPONSE FROM WAKE COOLING

The asymmetric response of the TC to the cold wake forcing is displayed in plan views of the 850 hPa vorticity (red) superposed with 400 hPa (blue) vorticity for the under-eyewall CNTL, cold wake 1, wake 2, and wake 5 (Figure 43a,b,f) and trailing cold wake 3 and wake 4 experiments (Figure 43d-e). In all of these experiments, the 850 hPa vorticity exceeding $5 (10^{-4} \text{ s}^{-1})$ is concentrated within the RMW. For the wake 1 (full circle and 2°C), wake 2 (half circle and 4°C), and wake 5 (full circle and 4°C) experiments, the 850 hPa vorticity maximum also remains within the cold wake region, albeit with some wobbling. About six to nine hours after imposing these cold wakes at 36 h, the 400 hPa vorticity becomes organized in spiral bands in the outer radii. In these cold wake experiments, the 400 hPa vorticity bands expand outward with time. The outward expansion of the 400 hPa vorticity bands in the wake 2 experiment is somewhat slower than for the wake 1 and wake 5 experiments. Inner spiral 400 hPa vorticity bands that appear to be connected to a ring of vorticity around the center are simulated from about 69-72 h. For the wake 3 and wake 4 experiments that have a trailing wake, the time evolutions of the 400 hPa vorticity bands are more complicated than for the other wake experiments. Two primary outer vorticity bands develop after 45 h and persist until about 66-69 h. The outward propagations of the 400 hPa vorticity bands are slower and last longer than in the wake 1 experiment as these vorticity bands rotate around the eye.

(a)

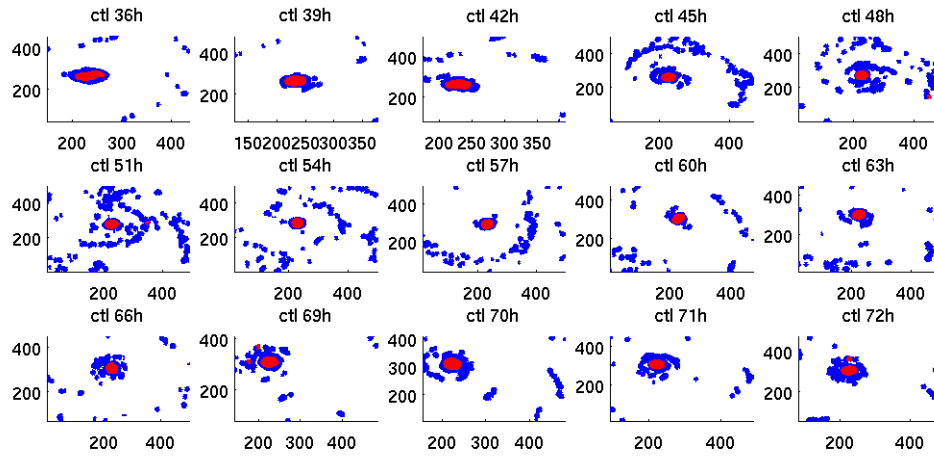
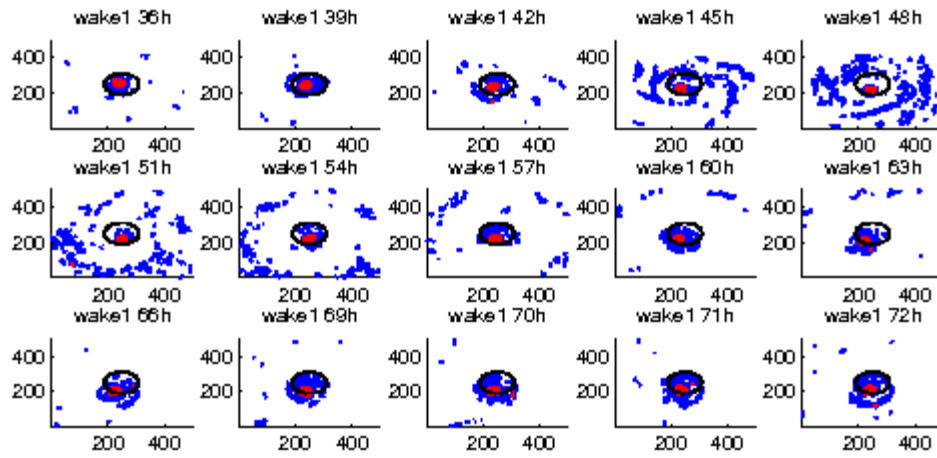
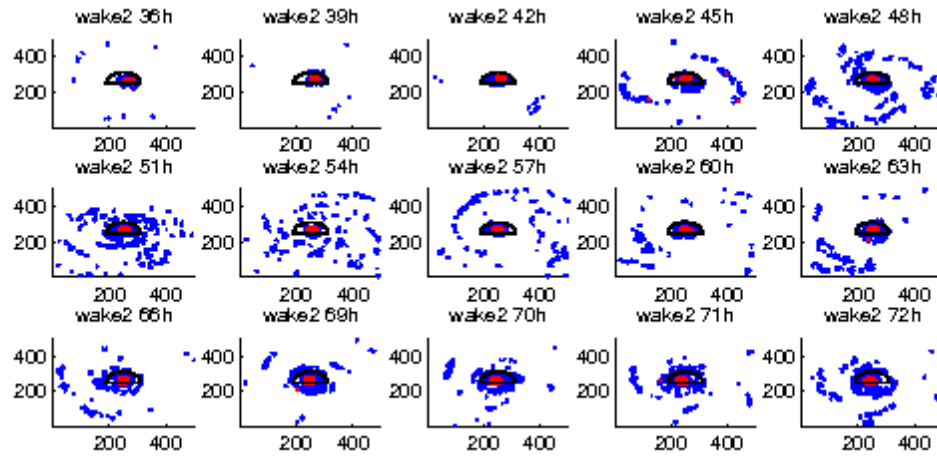


Figure 43. Time evolution at selected times from 36 h to 72 h of vorticity at 850 hPa (red) exceeding $5 (10^{-3} \text{ s}^{-1})$ and at 400 hPa (blue) exceeding $1 (10^{-3} \text{ s}^{-1})$ from (a) CNTL, (b) wake 1, (c) wake 2, (d) wake 5, (e) wake 3, and (f) wake 4 experiments. Black contour indicates the cold wake area.

(b)



(c)



(d)

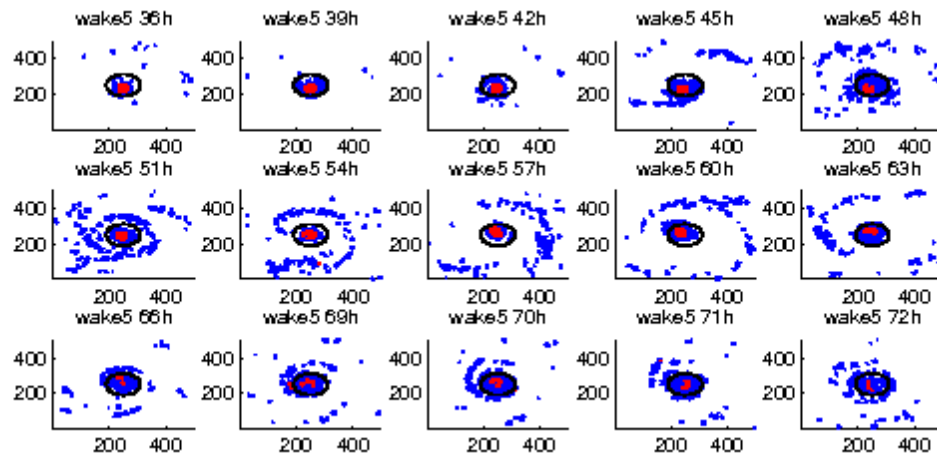
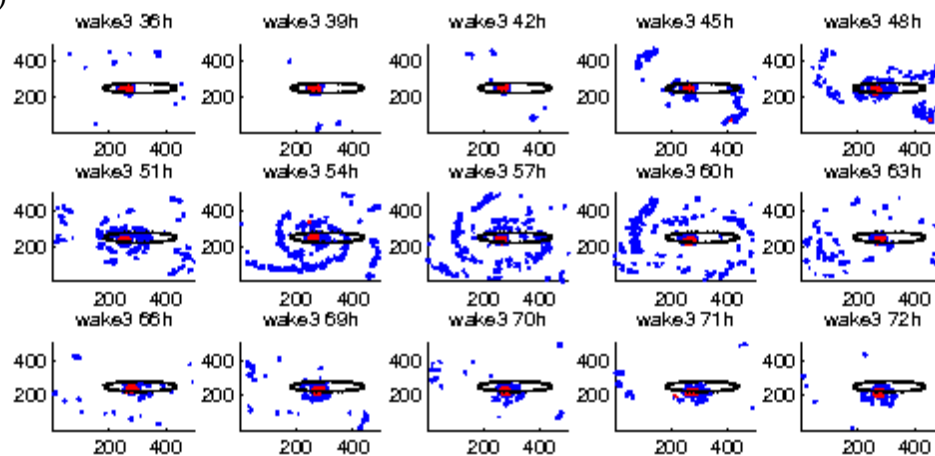


(Figure 43 continued)

(e)



(f)

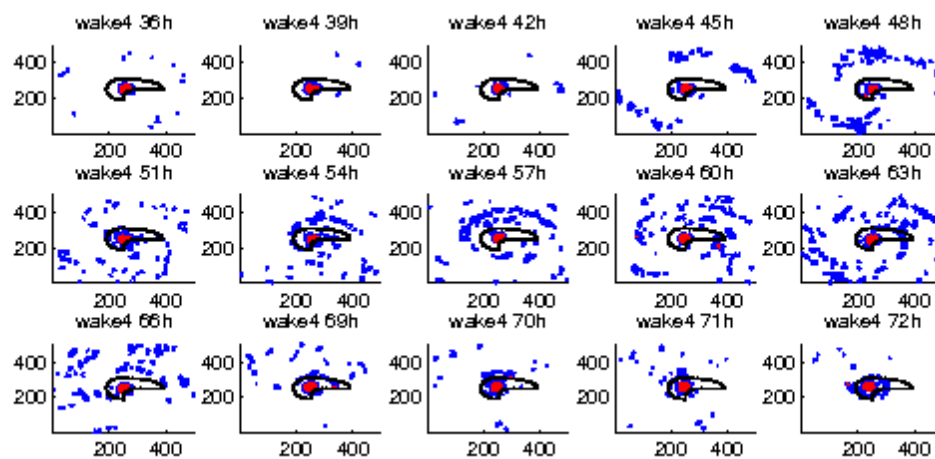


(Figure 43 continued)

The low-level vortex defined by the location of minimum SLP continues to wobble throughout the 36 – 72 h integration (Figure 44). The displacements of the vortex centers at 72 h for the CNTL, wake 1, wake 2, wake 3, wake 4, and wake 5 experiments are 42, 44, 29, 28, 32, and 19 km. Overall, the vortex movements induced by the cold wake are not large due to the constant Coriolis value and the absence of environmental vertical wind shear. The movement of low-level vortex in the no-shear, no environment flow, and f-plane case presented here may be related to the interaction of upper- and low-level potential vorticity on a horizontal plane (Gryanik and Tevs 1989; Flatau et al. 1994). After the TC vortex has adjusted to the cold wake at 48 h, the vortex moves southward in all of the wake experiments with subsequent northward and then eastward motion, which is an anticlockwise rotation.

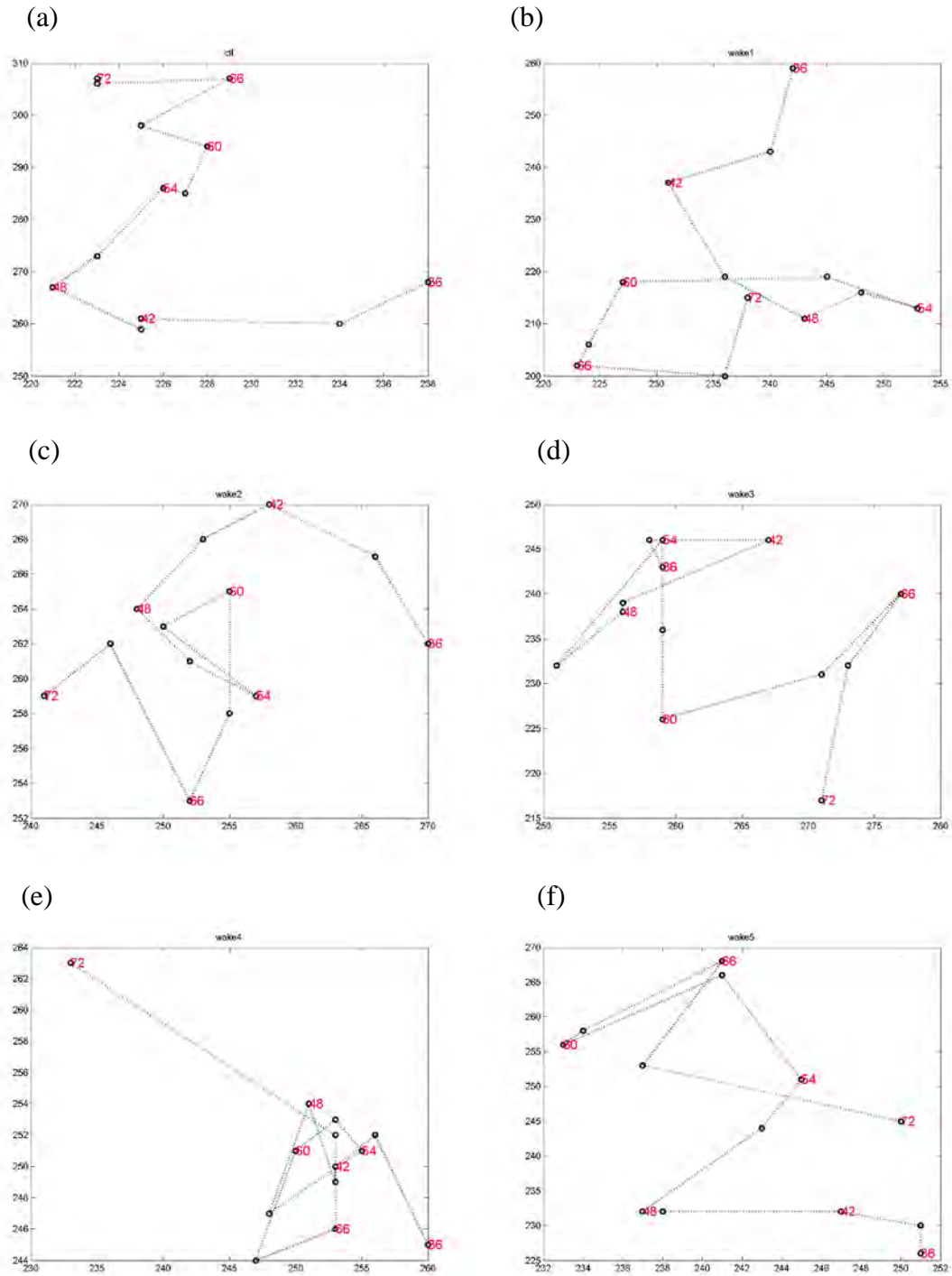


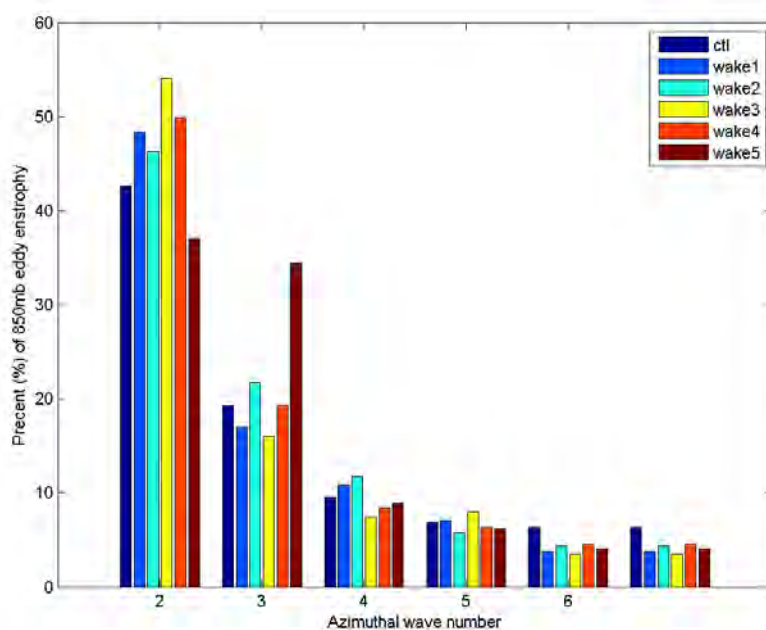
Figure 44. Low-level vortex tracks from (a) CNTL, (b) wake 1, (c) wake 2, (d) wake 3, (e) wake 4, and (f) wake 5 experiments. Black circles are the 3 hourly locations of vortex centers beginning at 36 h and ending at 72 h as indicated by the red numbers. Numbers along the ordinate and abscissa are grid 3 positions (km).

The inner and outer vorticity band patterns (Figure 44) are associated with the propagation of spiral rainbands. Previous studies suggest the low-frequency vortex Rossby waves (VRWs) and high-frequency inertial gravity waves (IGWs) are responsible for the outward propagation of the rainbands (Schechter 2008). Recently, two mixed vortex Rossby inertial gravity waves (mixed VRIGWs) modes were identified by Zhong et al. (2009), who showed the mixed VRIGWs tend to be limited to the eyewall region. By contrast, the VRWs and IGWs freely propagate between the inner and outer regions. Strong wave-wave interactions between wave numbers (WN) 1 and 2 in the eyewall region have also been demonstrated in the hydrostatic model study by Wang (2002).

To examine the TC flow asymmetries forced by the cold wakes, a similar azimuthal wave decomposition technique has been utilized as in those studies. The discretized Fast Fourier Transform (FFT) filtering is applied to decompose the fields between 36-72 h into the WN1-WN5 components. The azimuthal-mean at each radial distance is removed to define the perturbation (eddy) vorticity. An azimuthal-mean of the square of the perturbation vorticity and then a time mean is computed to obtain the azimuth-time mean eddy enstrophy at 25 km from the center (the mean RMW of all wake experiments).

The mean eddy enstrophy at 850 hPa from WN1-WN5 is shown in Figure 45a normalized by the total eddy enstrophy of each experiment. One striking feature is the decrease of WN1 and the increase of WN2 eddy enstrophy at 850 hPa in the wake 5 experiment (4 °C cold wake below the eye) that has the largest intensity decrease. The mean eddy enstrophy from WN1 (WN2) in the wake 5 experiment is 37% (34%) of the total eddy enstrophy. In the other wake experiments, the mean WN2 eddy enstrophy is much less than for the WN1 experiment. Similar features are simulated at the 400 hPa level (Figure 45b), where again a large portion (26%) of the WN2 enstrophy is found in the wake 5 experiment compared to the other wake experiments, which indicates a damped WN1 and an enhanced WN2 throughout a deep layer of the eyewall region in the wake 5 experiment.

(a)



(b)

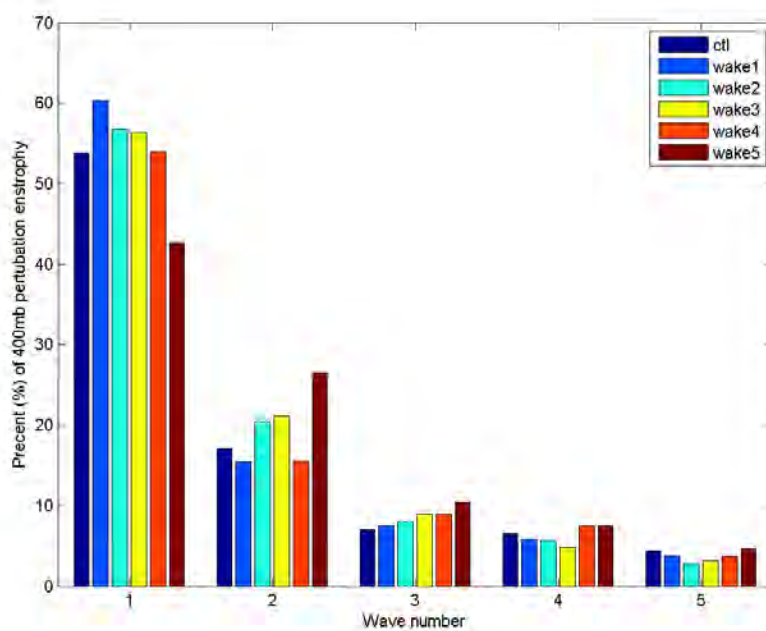


Figure 45. Histograms of eddy enstrophy percentage of the total enstrophy at 25 km radii from 36-72 h at (a) 850 hPa and (b) 400 hPa levels decomposed to WN1-WN5 components for the control and five wake experiments (see inset for bar definitions).

The Hovmöller azimuthal plot for the wake 5 experiment eddy vorticity at 25 km radius (Figure 46) indicates WN2 is propagating along the vortex mean cyclonic flow (upwind) when the wake 5 TC intensity has a temporary increase between 50-60 h, while the propagation is against the mean flow during the intensity decrease period. In all of the wake experiments, the WN2 has an alternating downwind/upwind propagation pattern related to the TC intensity fluctuations. In contrast, WN1 seems to propagate with the mean flow (Figure 47). The upwind/downwind propagation direction variations of WN2 also vary in frequency, which indicates the WN2 is dispersive. The stronger cold wake 5 and a cold wake-shape asymmetry (wake 2) appear to induce larger WN2 eddy vorticity response. Zhong et al. (2009) showed the two mixed VRIGW WN2 modes propagating with and against the mean flow. These waves have an inseparable wave dispersion characteristic. It is speculated that the changing of the WN2 azimuthal propagation direction and frequency is related to the interactions of the VRWs and the mixed VRIGWs.

An intriguing question is whether the spin-downs of the TC circulation in all of the five wake experiments relative to the CNTL experiment are related to the mean flow interaction with these propagating VRW, mixed VRIGW, and IGW that are revealed in the above WN1-WN5 decompositions. In particular, the rapid spin-down of the TC circulation in the wake 5 experiment compared to the other wake experiments may be related to active WN2 and higher wave numbers at and outside the RMW.

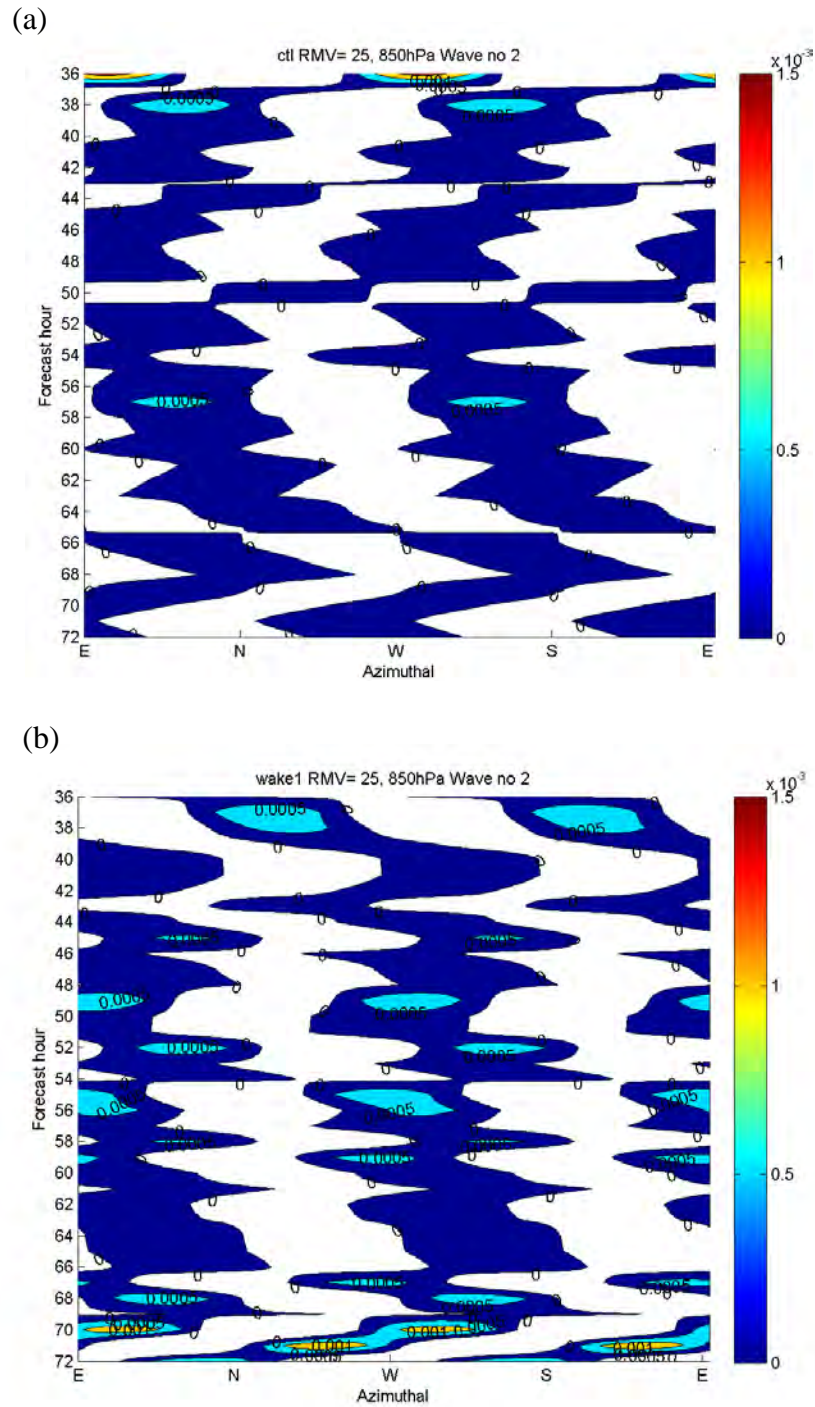
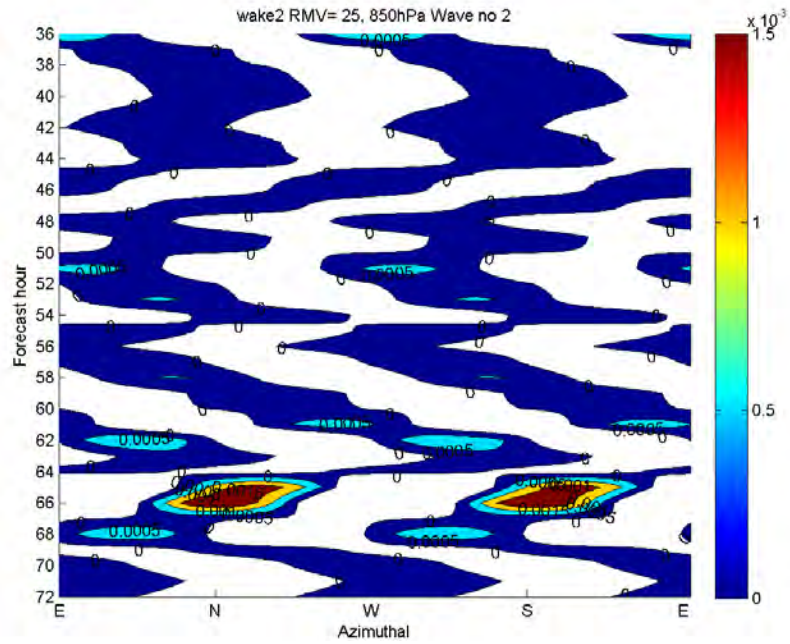
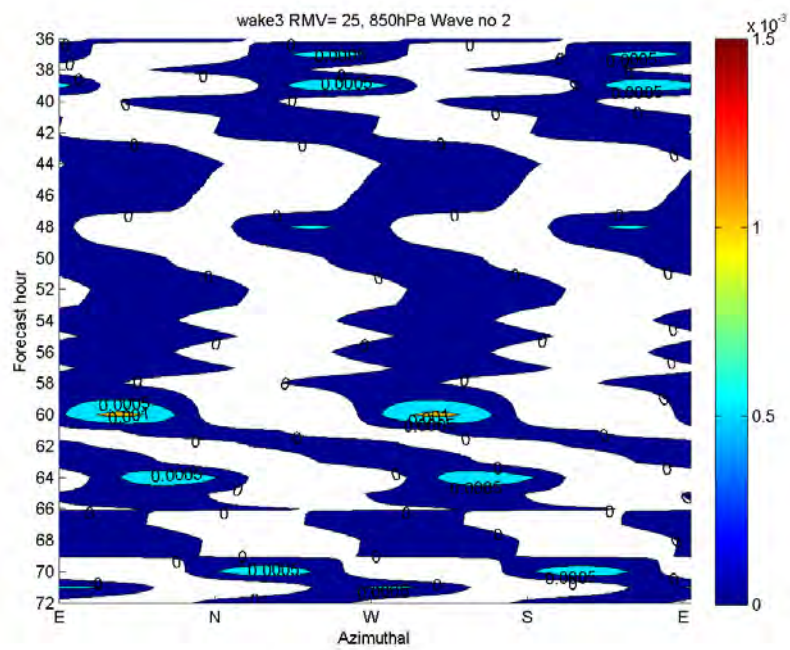


Figure 46. Time and azimuthal plot of wavenumber 2 eddy vorticity (s^{-1} ; scale on right) from (a) CNTL, (b) wake 1, (c) wake 2, (d) wake 3, (e) wake 4, and (f) wake 5 experiments. Only positive eddy vorticity is shown here. Positive slope (left to right with increasing time) means downwind propagation.

(c)

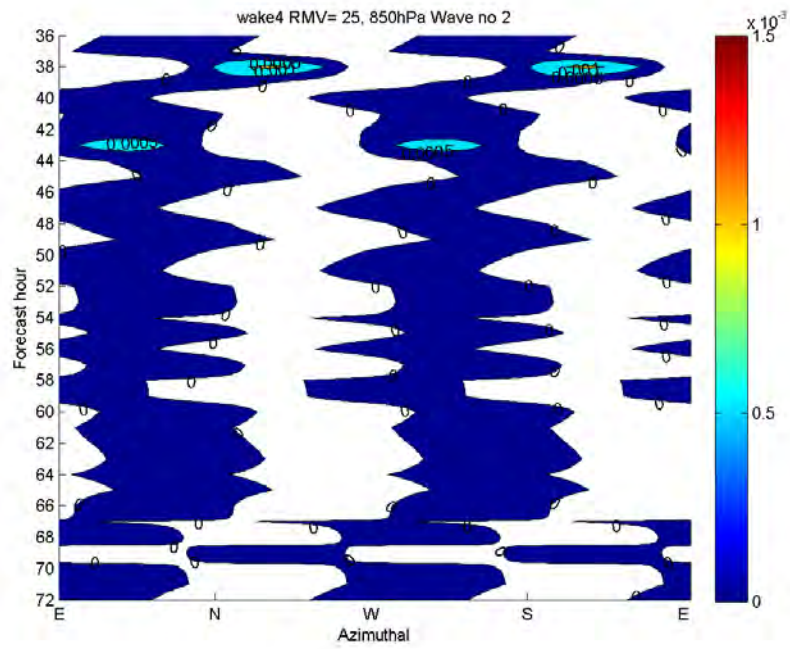


(d)



(Figure 46 continued)

(e)



(f)

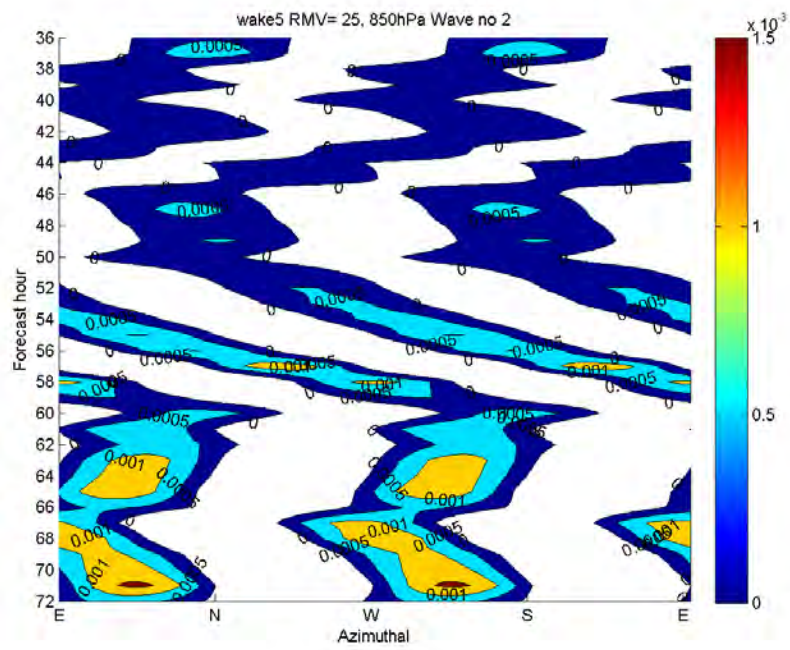


(Figure 46 continued)

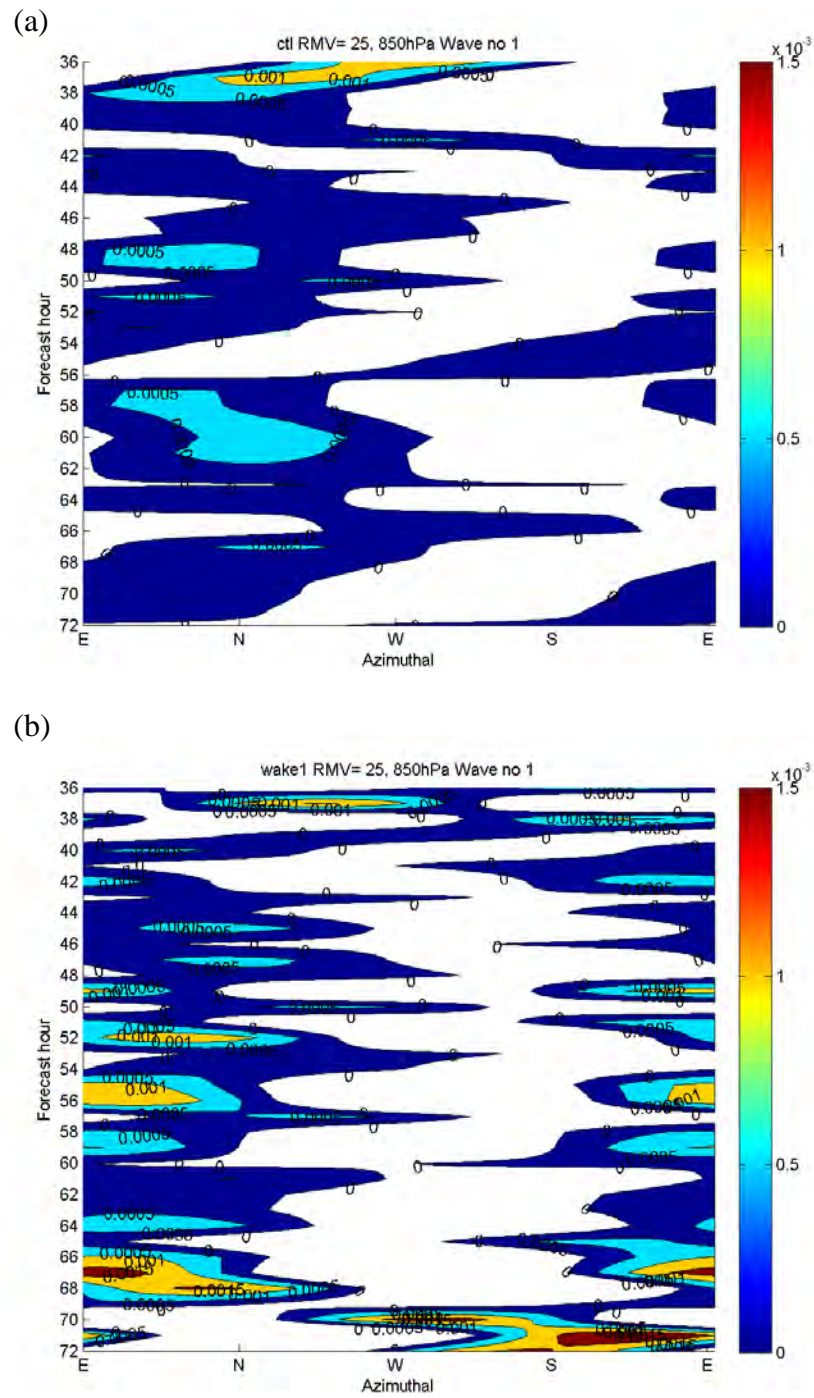
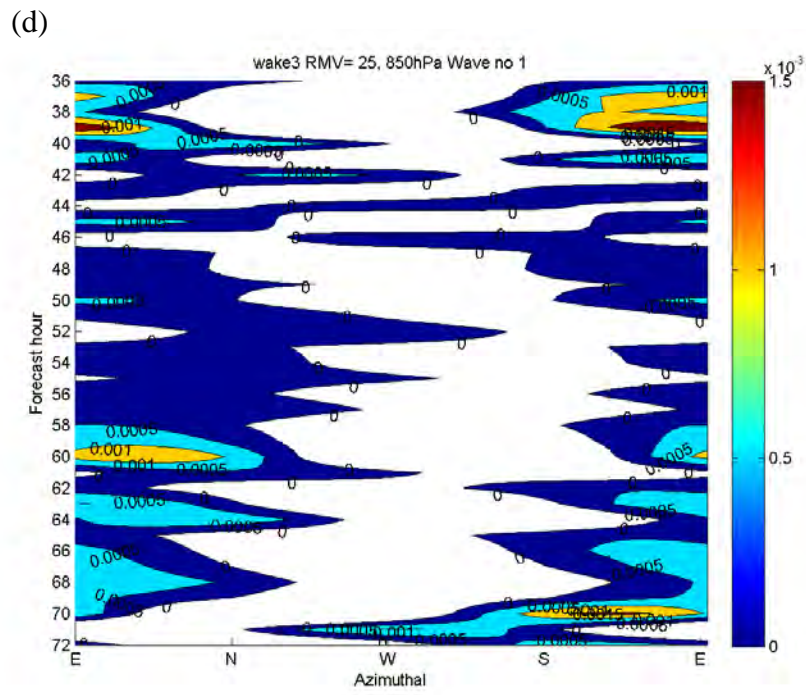
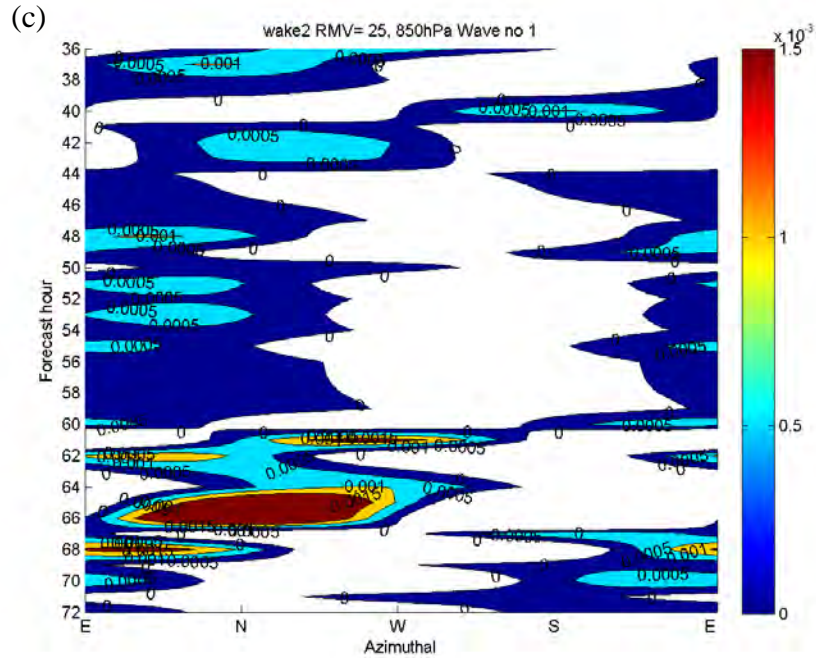
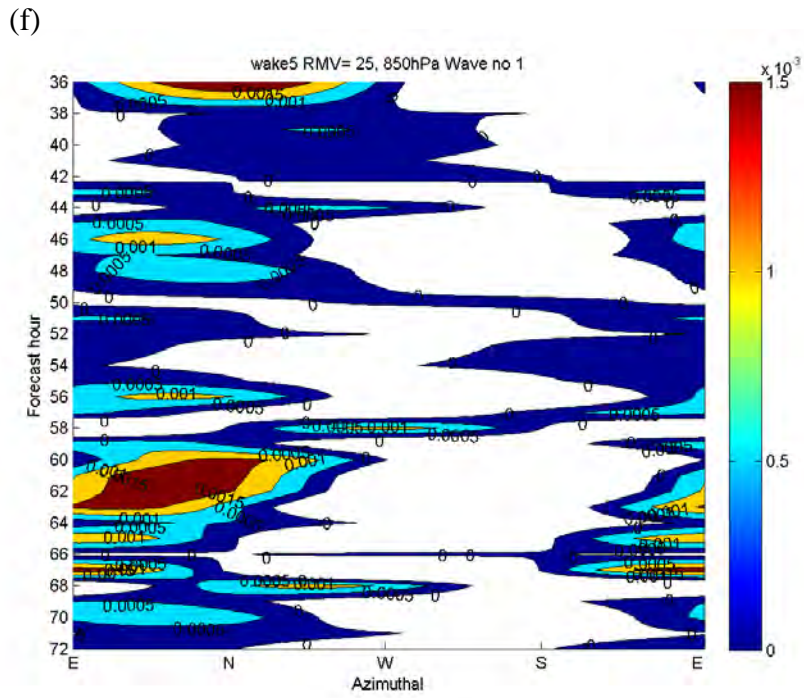
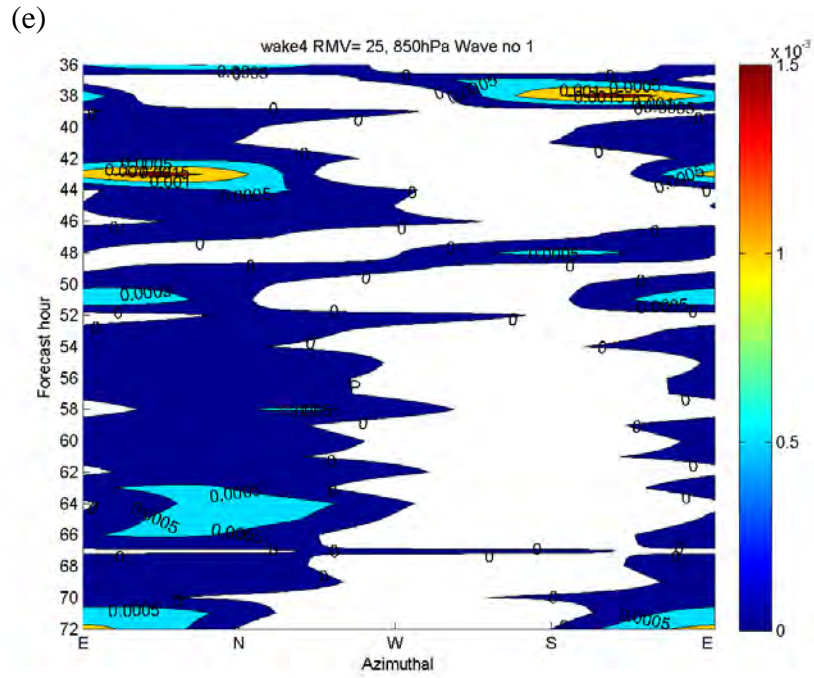


Figure 47. As in Figure 46, except for the wavenumber 1 eddy vorticity.



(Figure 47 continued)



(Figure 47 continued)

It is plausible that these waves near the RMW can extract energy from the mean vortex and transport it radially inward or outward. To further examine this possibility, the

mean time-radial Hovmöller plot of 850 hPa enstrophy from the wake 5 experiment indicates an eddy enstrophy presence in WN2 and WN3 near the RMW after 50 h when the wake 5 TC has a rapid decrease in intensity (Figure 48f). Whereas the WN1 enstrophy in wake 5 is very small, the other four wake experiments have dominant WN1 components at and inside RMW.

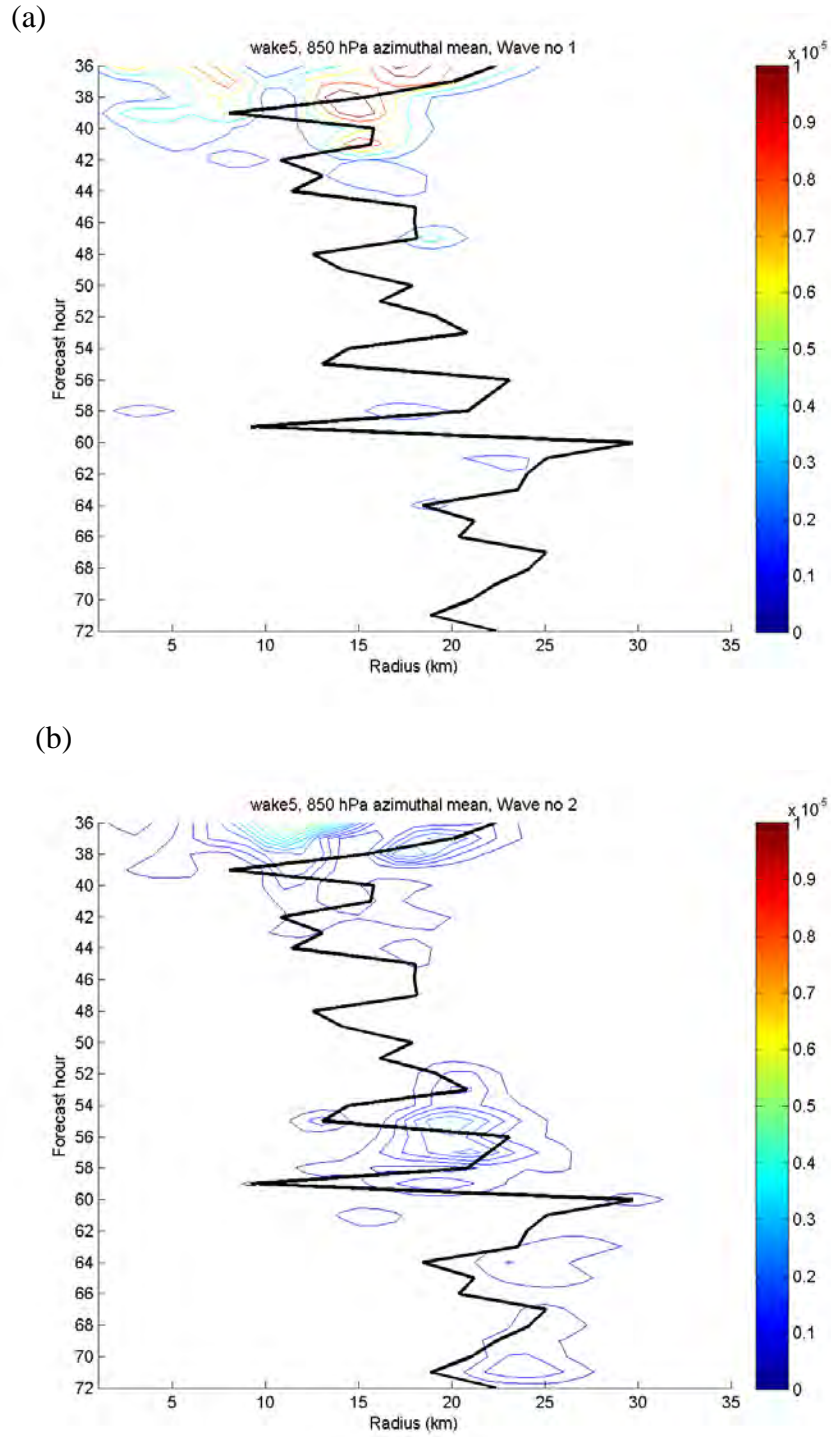
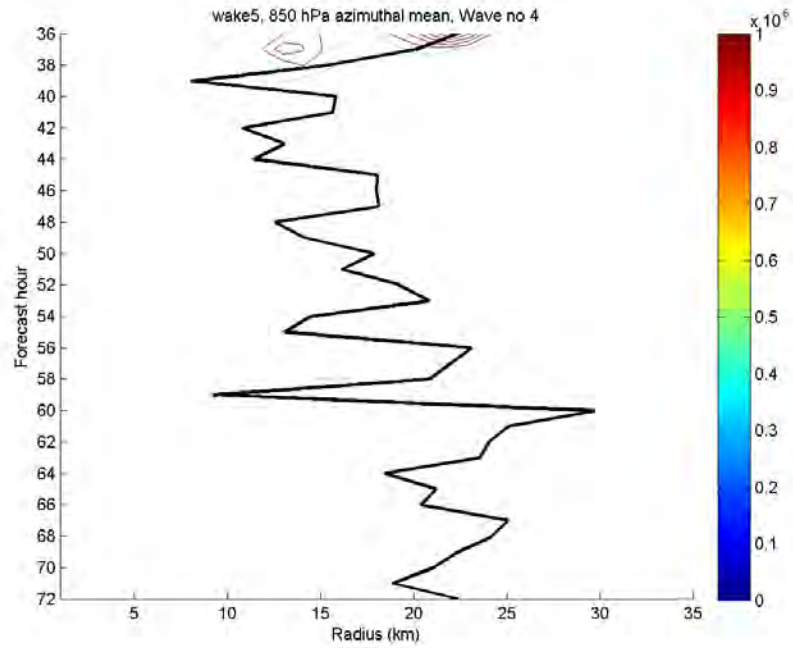
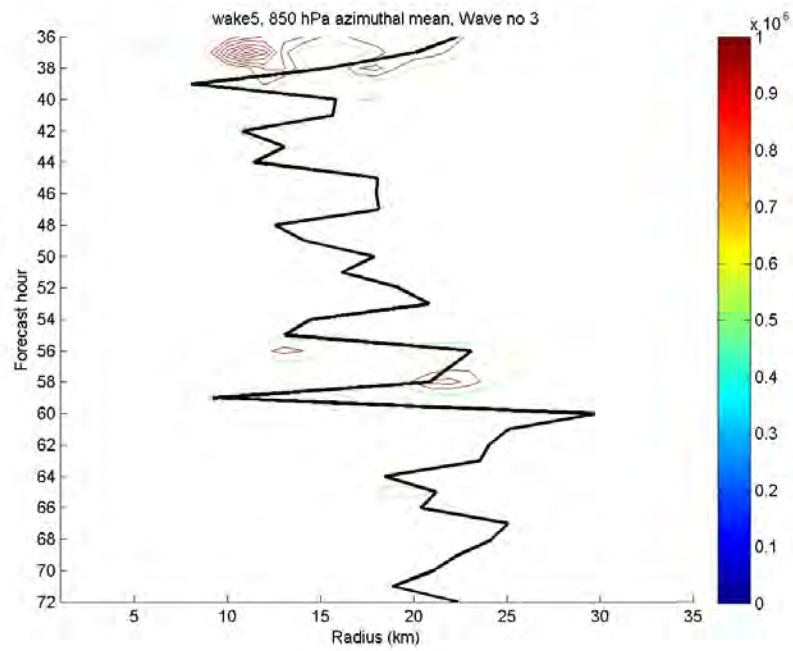


Figure 48. Time and radius plots of the wake 5 experiment eddy enstrophy decomposed into azimuthal (a)WN1, (b) WN2, (c) WN3, (d) WN4, and (e) WN5 at 850 hPa level. The black line represents the radius of maximum wind.

(c)



(d)



(Figure 48 continued)

(e)

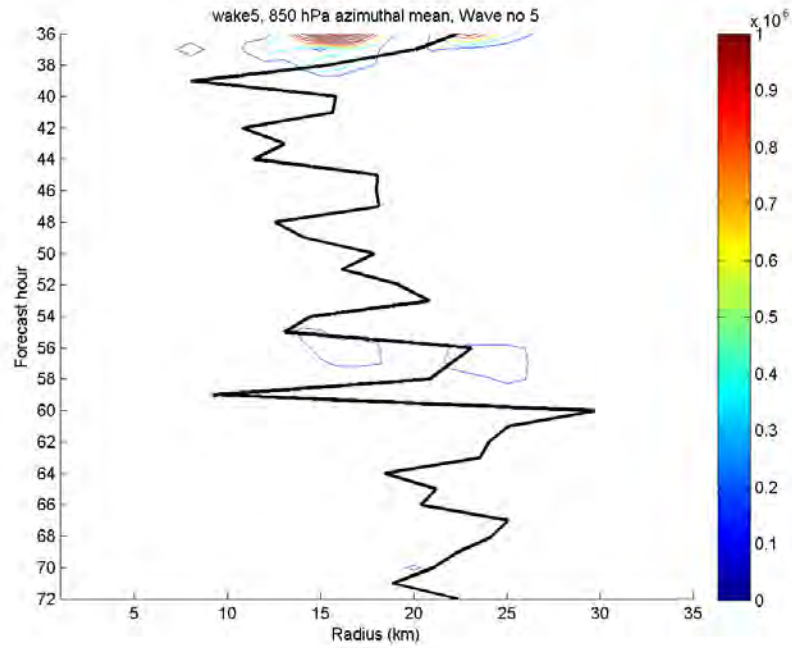


(Figure 48 continued)

(a)

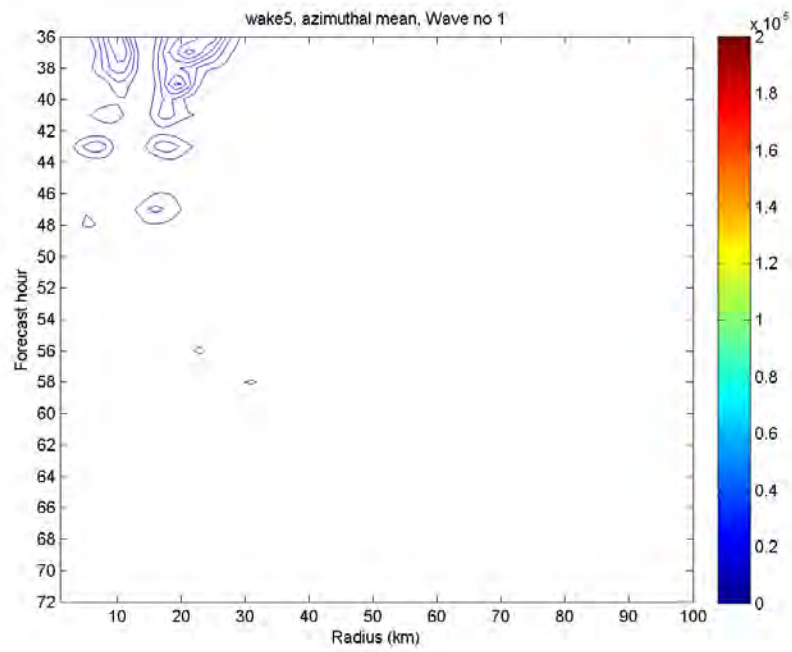
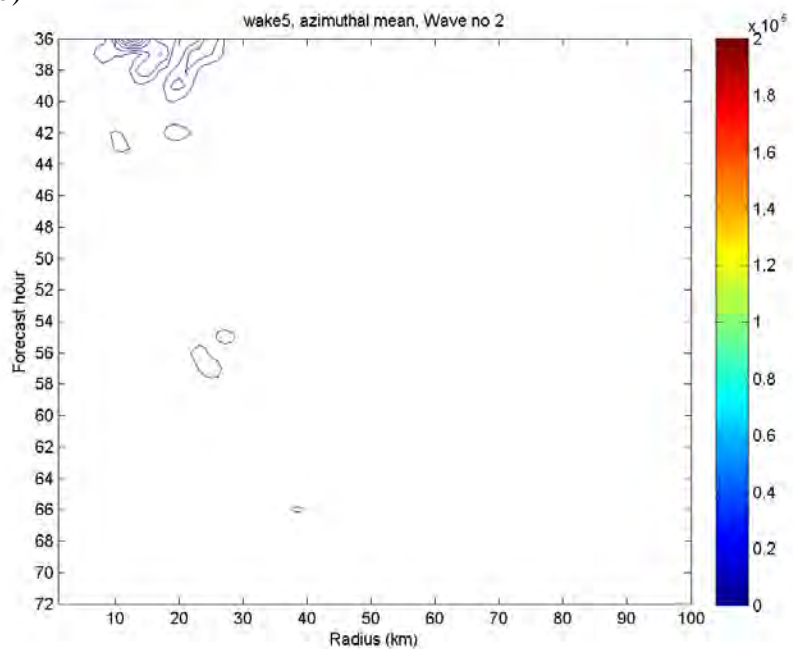
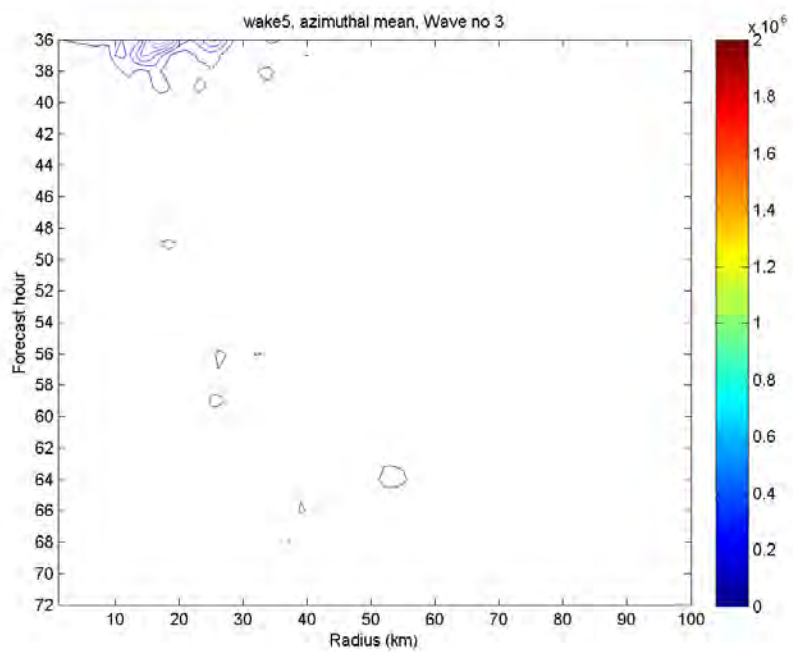


Figure 49. As in Figure 48, except for the 400 hPa levels.

(b)



(c)



(Figure 49 continued)

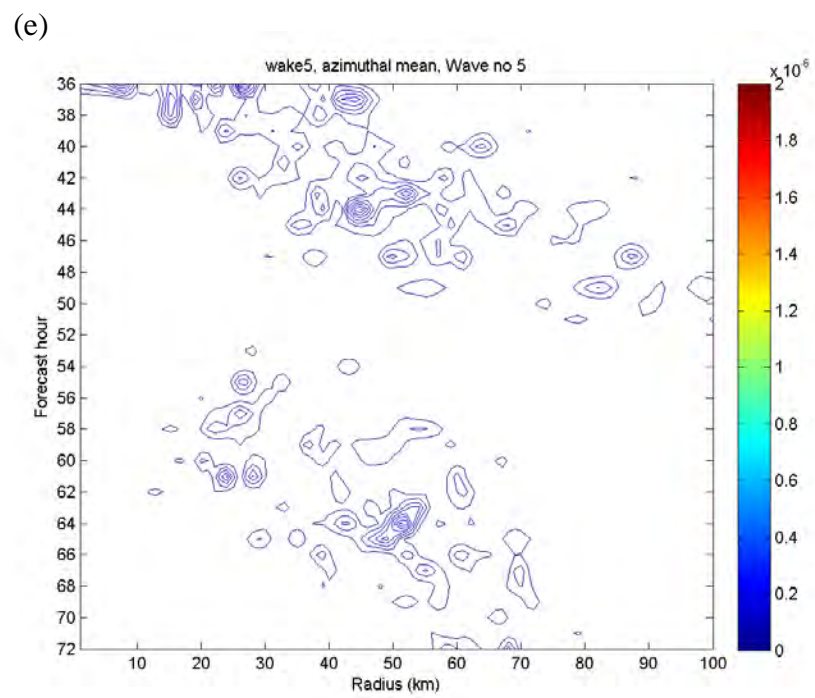
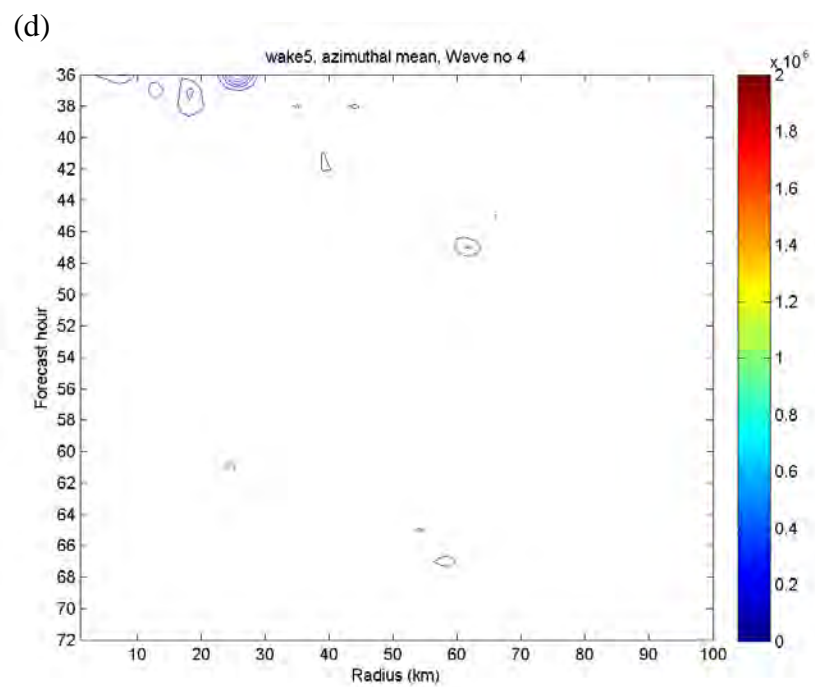


(Figure 49 continued)

In these experiments, the eddy transport of energy inward from the mean vortex at RMW to inside 10 km is mainly accomplished by WN1 (Figure 50). Note that the magnitudes of the WN1 850 hPa eddy enstrophy in the trailing wake 3 and wake 4 experiments are much higher in the inner-core region than for the three experiments that have cold wakes below the eyewall. Furthermore, the WN2-WN5 transports are occurring between 10-30 km radii. However, sporadic transports inside 10 km radii by WN2-WN5 also occur. These transports suggest the effect of the cold wakes below the eyewall is to damp the eddy WN1 component in the inner-core region. If the cold wake below the eyewall has a large magnitude, such as 4°C in the wake 2 and wake 5 experiments, an increase in the WN2 and WN3 eddy enstrophy occurs.

For the trailing wake 3 and wake 4 experiments, the WN1 eddy enstrophy inside 10 km prior to 50 h seems to indicate the inward transport of WN1 energy helps to maintain the TC intensity in wake 3 and wake 4 for a period of time after the coupling with these cold wakes. The subsequent reduction of WN1 enstrophy inside 10 km radii in the wake 3 and wake 4 experiments between 50-60 h corresponds to the period of intensity decreases. A similar WN1 pattern inside the RMW is also simulated in the wake 1 and wake 2 experiments, but with smaller magnitudes. Outside the RMW, the 850 hPa enstrophy is small for WN1-WN5 in all of the wake experiments.

The lack of outward wave transport beyond 30 km at 850 hPa is reversed at the 400 hPa level. An active outward propagation of enstrophy is simulated by the WN3-WN5 (Figure 51). The largest radially outward transport of 400 hPa eddy enstrophy by WN5 is simulated in the wake 5 experiment, and the smallest in wake 4 (crescent-shape wake). Note that the RMW curve in Figure 51 is not smooth, which may be due to unstable asymmetric circulations associated with the wobbling of the cyclonically rotating vortex.

At the 400 hPa level, the WN3-WN5 outward eddy enstrophy transports in the experiments without a trailing cold wake (wake 1, wake 2, and wake 5) are larger than in the trailing wake experiments (wake 3 and wake 4). Although in all of the wake experiments the WN3-WN5 components contain less than 10% of the total eddy enstrophy, their radial propagations may contribute as in the WN1-WN2 interactions to

the removal of kinetic energy from the mean vortex. The radial propagation of waves is limited in lower levels due to the stronger radial and vertical shear associated with the primary circulation and the low-level inflow from the secondary circulation. As the tangential wind decreases at mid-levels, the radial shear is smaller than at low levels. Therefore, wave packets at higher levels have less resistance to the radial movement because the inertial stability is less due to a weaker cyclonic rotation.

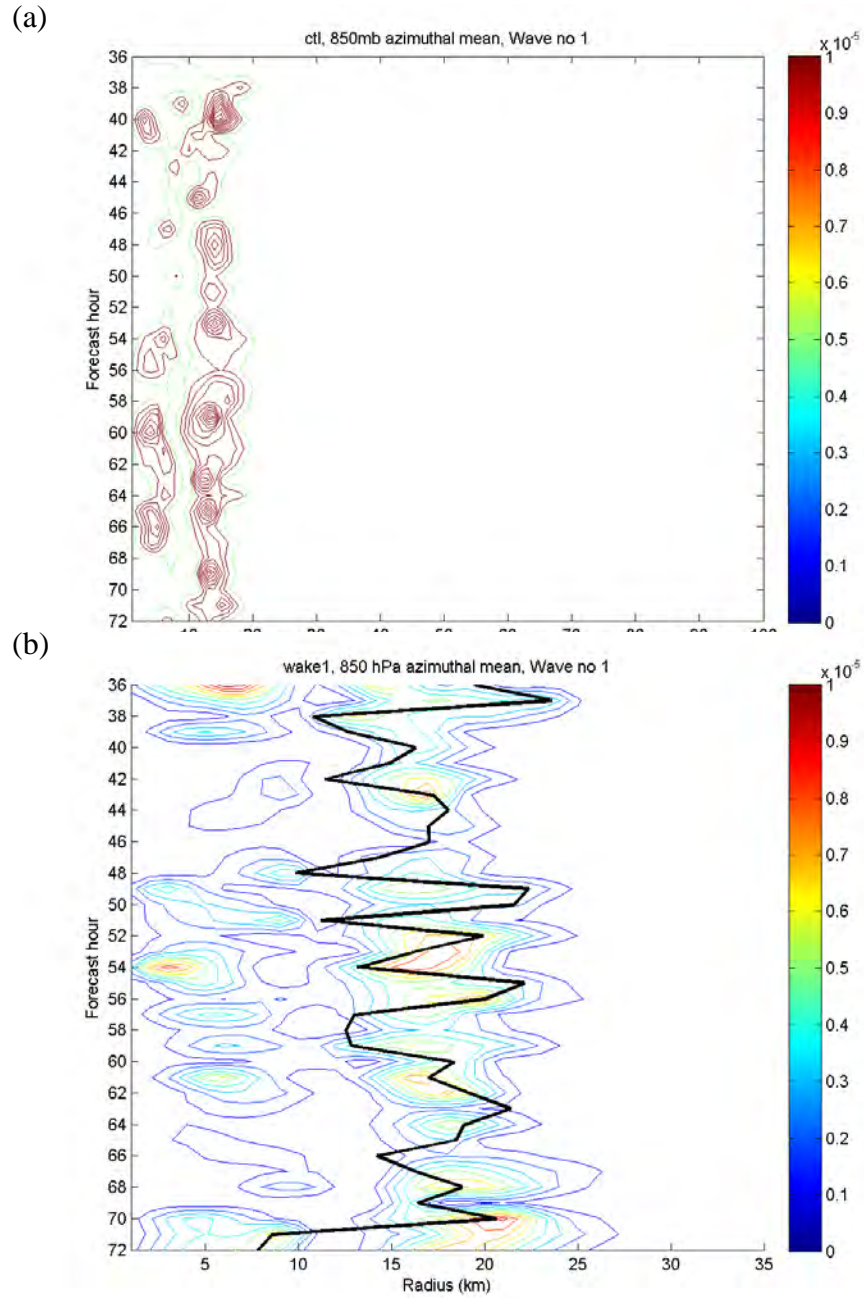
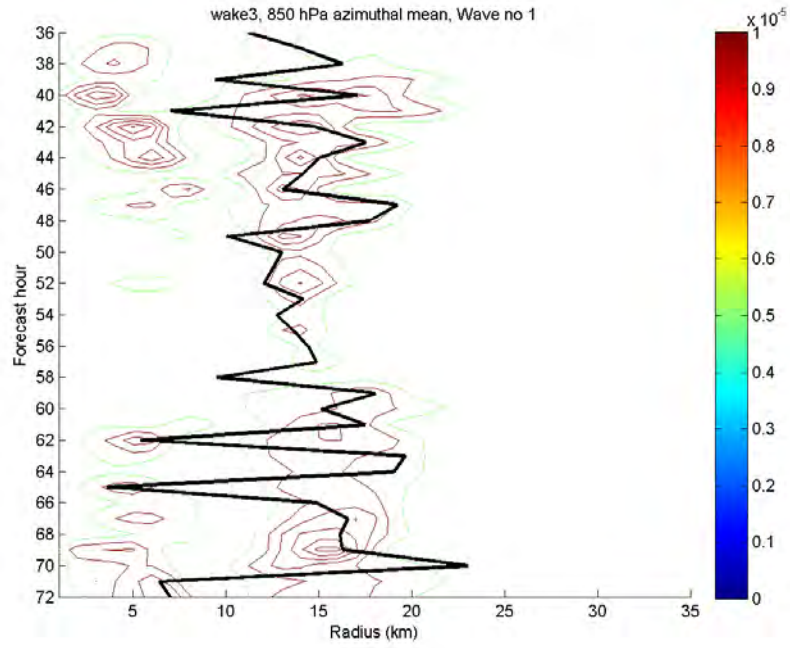
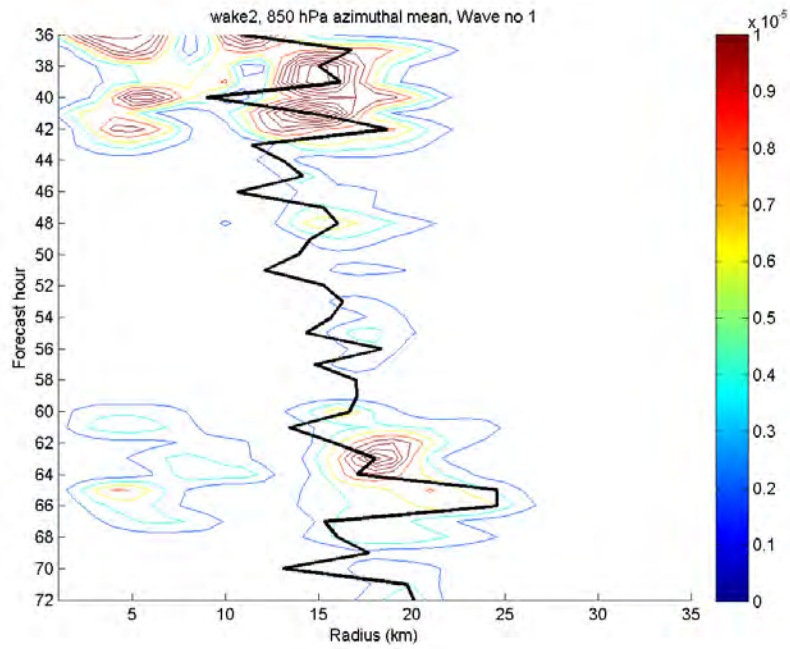


Figure 50. Time and radius plot of 850 hPa WN1 eddy enstrophy from (a) CNTL, (b) wake 1, (c) wake 2, (d) wake 3, (e) wake 4, and (f) wake 5 experiments. The contour interval is 10^{-4} s^{-2} . The black line represents the radius of maximum wind.

(c)

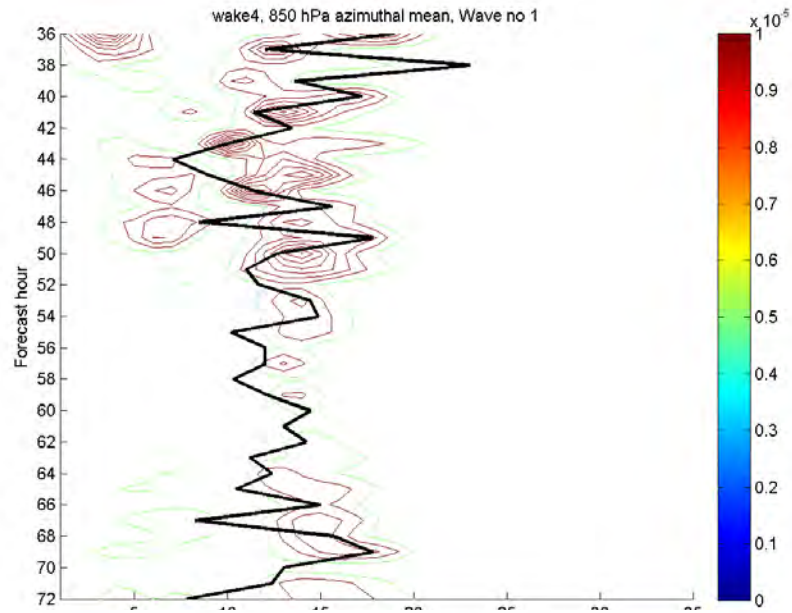


(d)



(Figure 50 continued)

(e)



(f)

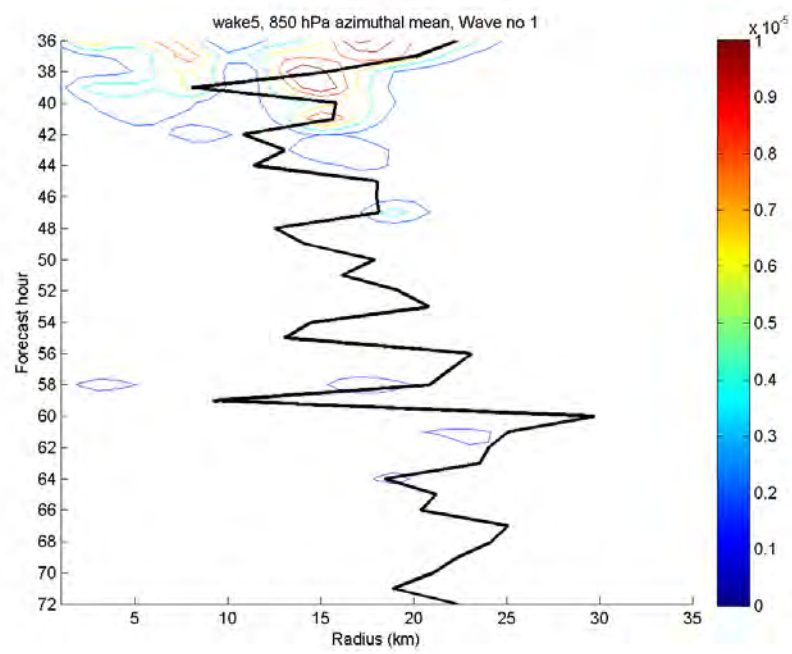


(Figure 50 continued)

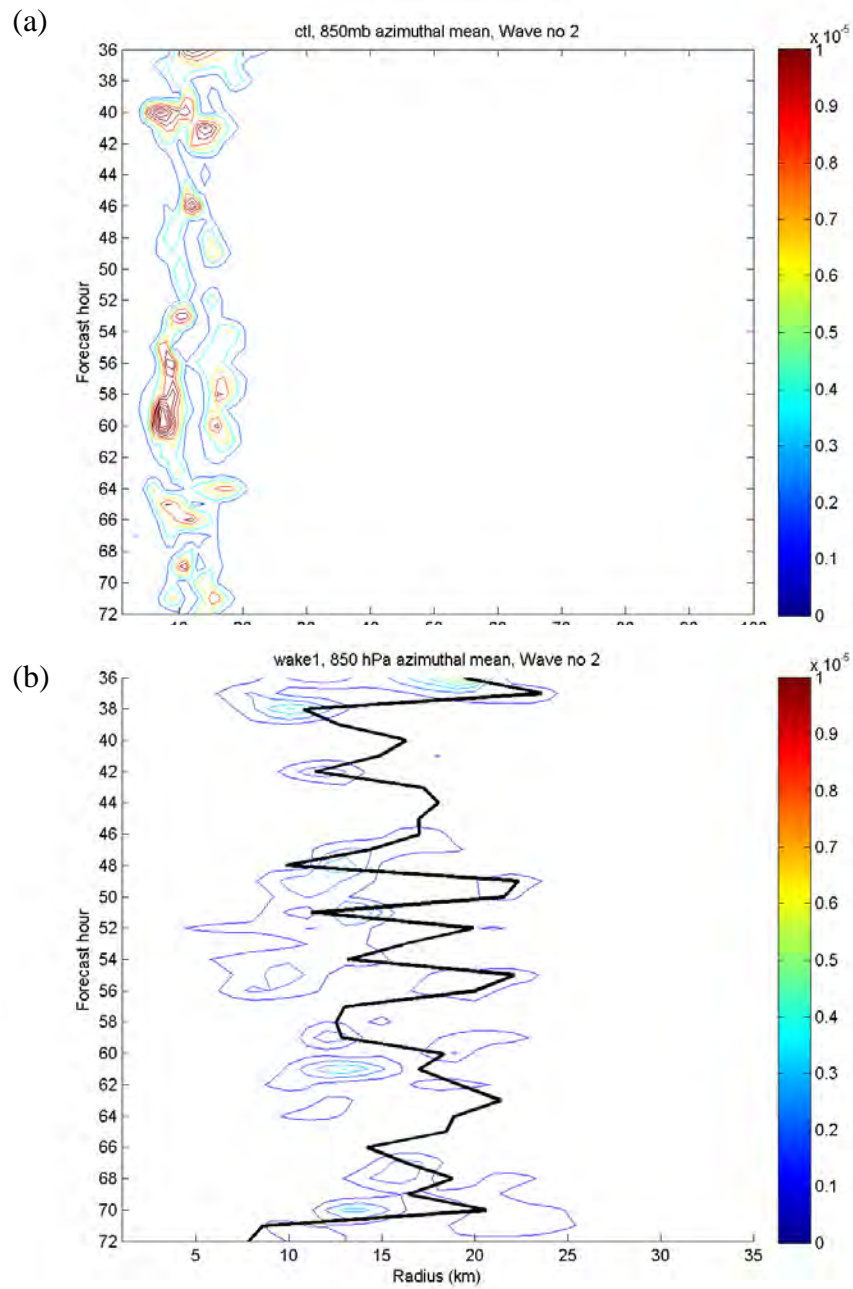
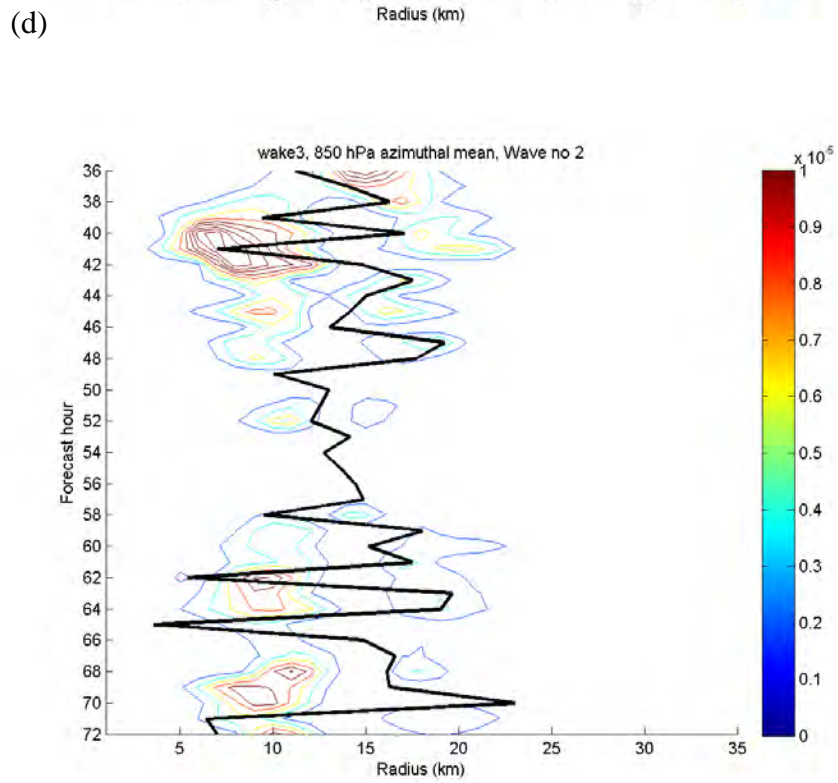
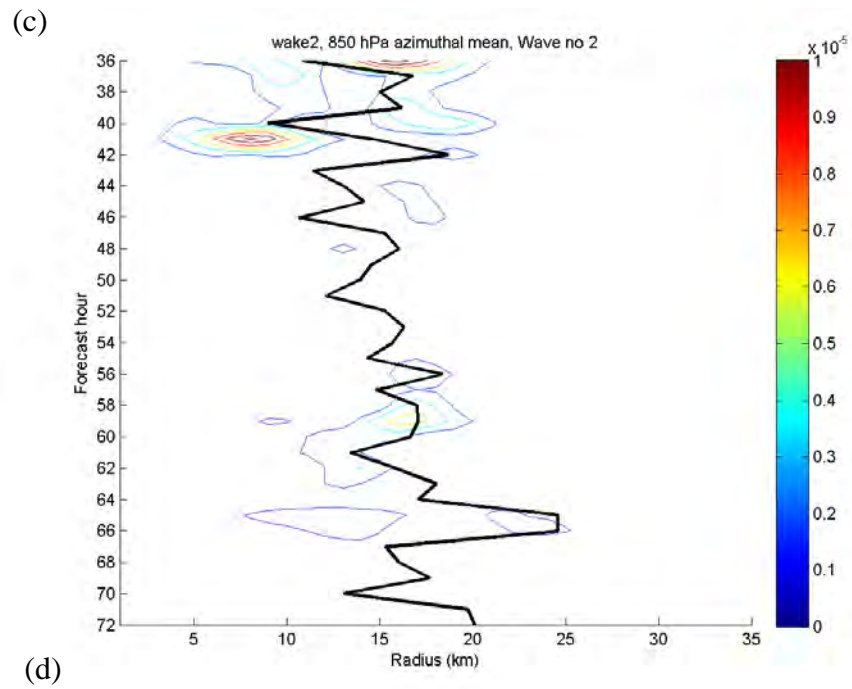
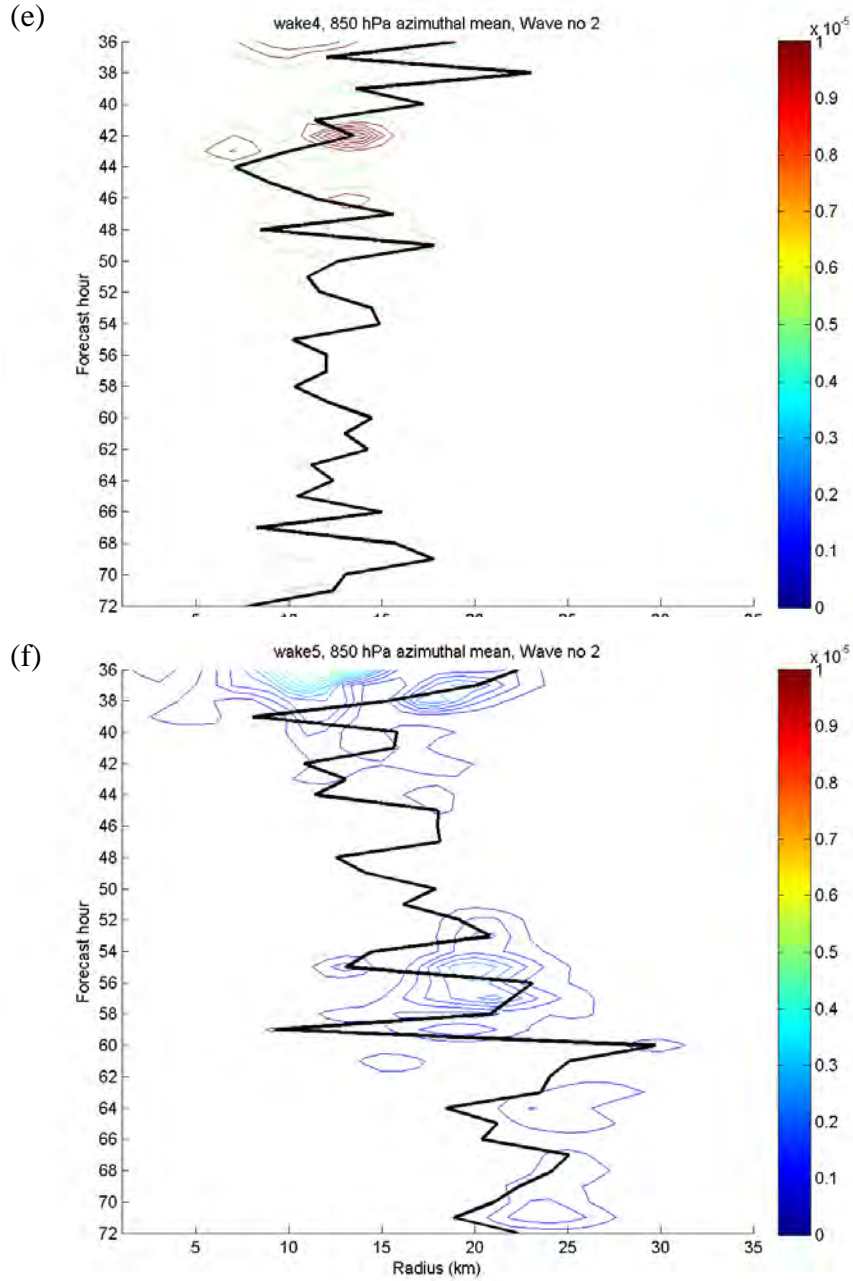


Figure 51. As in Figure 50, except for the wavenumber 2.



(Figure 51 continued)



(Figure 51 continued)

The propagations of the waves and the wave effects on the changes of the mean vortex state are affected by the radial shear in the vortex. From the linear VRW theory (Montgomery and Kallenbach 1997), the asymmetry and propagation direction of the

vortex Rossby waves are related to the sign of vortex beta term. Consider the vortex Rossby wave intrinsic frequency equation

$$\omega = n\Omega_0 + \frac{n}{R} \frac{\overline{\partial \zeta_0 / \partial r}}{\left(k^2 + n^2/R^2\right)} \quad (4)$$

where n and k are the azimuthal and radial wave numbers, R is the radius of maximum wind, $\overline{\partial \zeta_0 / \partial r}$ is the mean flow vortex beta, and $\Omega_0 = \frac{\overline{V_0}}{r}$ is the mean angular velocity. The vortex beta is the radial gradient of vortex vorticity, which is analogous to the planetary vorticity. When the vortex beta is greater (less) than zero, the VRW propagates along (against) the mean flow and increases (decreases) the wave frequency. Thus, the role of vortex beta is to oppose the radial shear to allow for the radial propagation of Rossby waves. For the mixed VRIGW, the intrinsic frequency is related to the quad root of the vortex beta. If beta is less than zero, the mixed VRIGW has an imaginary part and the waves are unstable, which then may have exponential growth. The intrinsic frequency of IGW is influenced by both the rotational and divergent components of flow and has a higher frequency than the vortex Rossby waves.

Comparing the CNTL mean radial gradient of 850 hPa vorticity (beta term) and radial gradient of tangential wind with the wake runs (Figure 52), the outward displacements of the radial gradient of tangential wind maxima and minima are positively correlated with the intensity variations in Figure 34. That is, the more intense vortices in the CNTL, wake 3, and wake 4 experiments have larger radial shears inside 10 km, and the weaker vortices in the wake 1, wake 2, and wake 5 experiments have smaller radial shears that are displaced farther out. Thus, the cold wakes shift the location of the maximum tangential wind as well as the vorticity gradients radially outward and increase the eye size in agreement with previous modeling studies (Chen et al. 2010). The wake 5 experiment has the smallest intensity and radial vorticity gradient inside the RMW, which is the region where the vortex beta is negative. This relationship suggests advection of vortex beta in this region opposes the mean flow and thereby decreases the mean vortex rotation. Negative vortex beta also contributes to the upwind propagation of VRW. As in

Montgomery and Kallenbach (1997), the advection of positive beta in the inner core will mix the high PV at the RMW inward to increase the mean vortex rotation.

The wave activity in the wake 3 experiment is different from that in the wake 4 experiment and also has a more uniform vortex beta inside the RMW as in wake 5. Since the TC in the wake 3 experiment has the highest intensity of all the wake experiments at end state and has almost no positive WN1 vortex beta in the inner-core region, the advection of positive vortex beta may not have contributed to the time delayed intensity decrease in the wake 3 experiment. Rather, the advection of vorticity from the mean vortex flux divergence probably played a larger role in maintaining the intensity in the wake 3 compared to the CNTL and wake 4 experiments.

Two plausible causes of WN1 damping are considered: unfavorable algebraic instability growth of the azimuthal WN1 perturbations, and WN1 to WN2 wave-wave interaction. The algebraic instability growth of azimuthal WN1 perturbations (Smith and Rosenbluth 1990; Nolan and Montgomery 2000; Nolan et al. 2001) requires two necessary conditions: the perturbation vorticity is inside the radius of maximum angular velocity, and there is more than one angular velocity maximum other than at the center of the vortex. When these two conditions are satisfied, the WN1 algebraic growth may arise from the decaying VRW that generates perturbation vorticity due to the interaction with the basic-state vorticity gradient to sustain a longtime growing mode. From equation (2.9) of Nolan and Montgomery (2000), the WN1 perturbation vorticity growth is dependent on the vorticity gradient via the relationship

$$\zeta_1(r, t) = \zeta_1(r, 0) - it \frac{\partial \bar{\zeta}}{\partial r} \int_r^\infty e^{-i\bar{\Omega}(\rho)t} h(\rho) d\rho \quad (5)$$

where $\bar{\Omega}$ is the angular velocity of the basic-state vortex, $\bar{\zeta}$ is the basic-state vorticity, ζ_1 is the perturbation vorticity, $h(\rho)$ is the initial condition, and t is time. A reduced vorticity gradient inside the maximum radius of angular velocity in the wake 3 and wake 5 experiments will then suppress the algebraic instability growth of the azimuthal WN1 perturbation.

The second possibility of a damped WN1 due to WN1-WN2 wave-wave interaction was suggested by Wang (2002a), who argued from a model PV budget analysis that the WN1 VRW potential vorticity (PV) is a significant source for WN2 VRW growth through nonlinear eddy processes. This nonlinear term [Wang 2002a, equation (6)] is:

$$J_E = \left(V_3' P' - \overline{V_3' P'} \right) - g \left(Q' \zeta_a' - \overline{Q' \zeta_a'} \right) + g \left(\nabla_3 \theta' \times F' - \overline{\nabla_3 \theta' \times F'} \right) \quad (6)$$

where V_3' and ∇_3 are the three-dimensional velocities and advection vectors, P is PV, Q is the diabatic heating rate, ζ_a is the three-dimensional absolute vorticity, θ is the potential temperature, and F is the friction. The quantities with overbars and primes are the means and perturbations, respectively. Wang (2002b) indicated there is a WN2 PV tendency from the nonlinear interaction with WN1 and concluded there must be a WN1 to WN2 PV transfer in the eyewall region. Since the perturbation magnitudes at higher wavenumbers are usually much smaller than for WN1, a simple scale analysis indicates that if there is wave-wave energy transfer, WN1 can contribute more to the WN2 nonlinear PV and vorticity tendency growth than would an upscale interaction from higher wavenumbers. Because there is a very small WN1 eddy enstrophy in the wake 5 experiment, the spin-down of the TC circulation from this WN1 to WN2 wave-wave interaction would be less likely than in the wake 3 experiment.

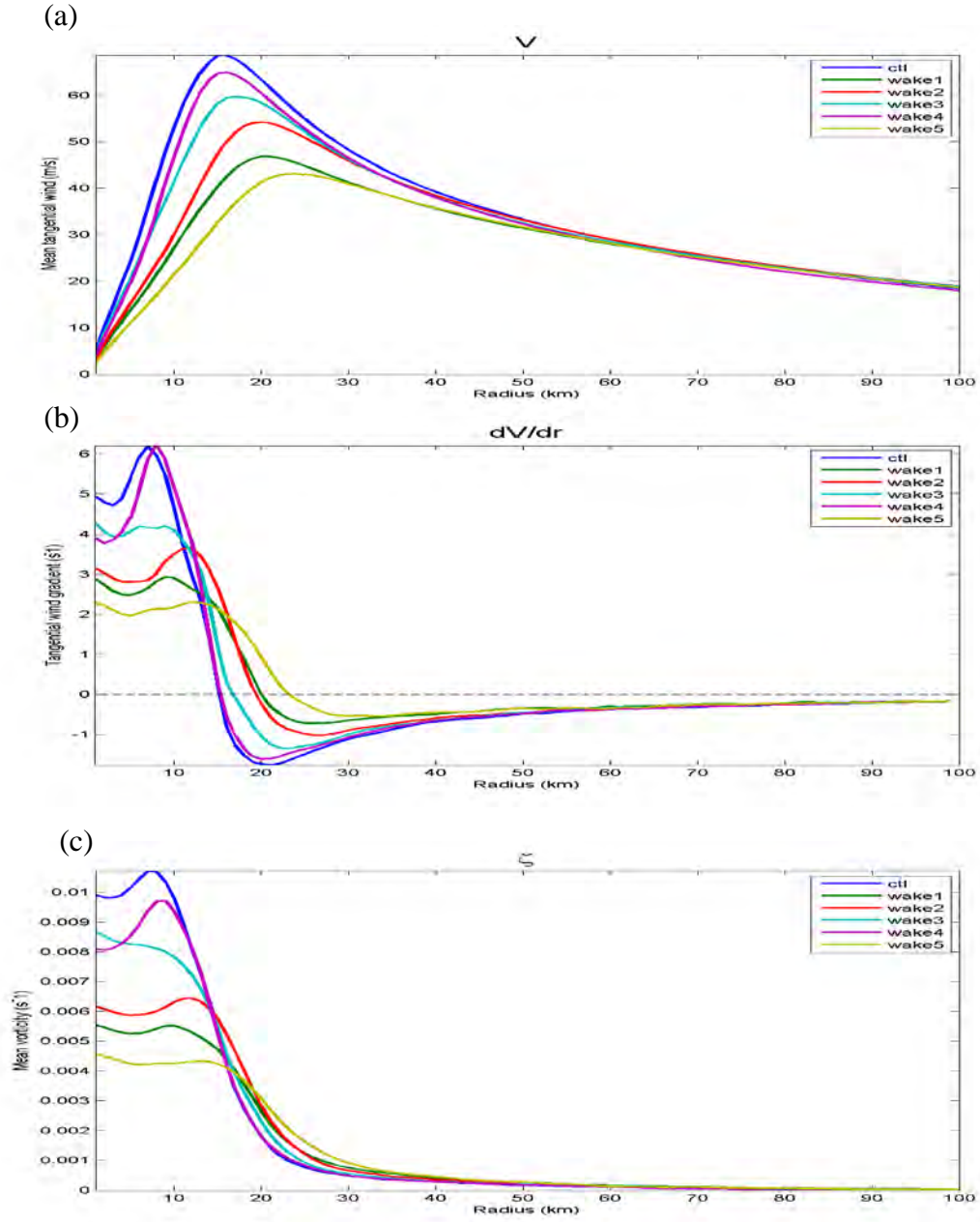
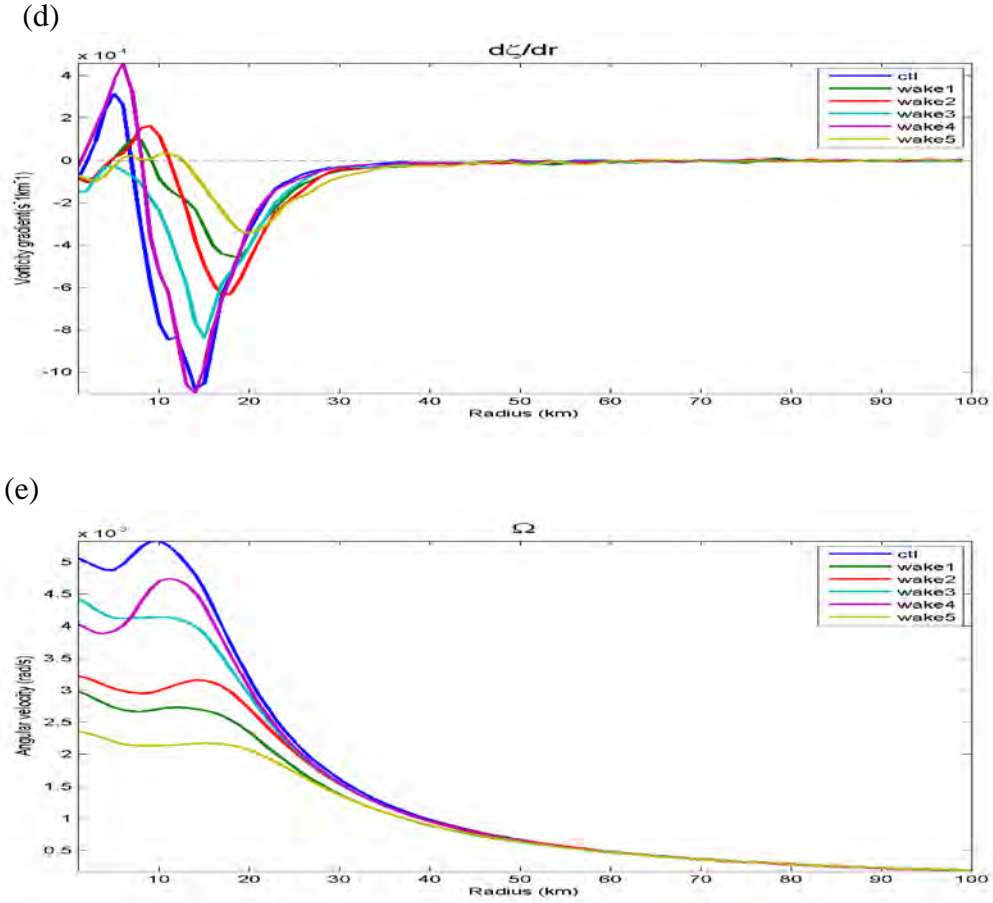


Figure 52. Radial distributions of 850 hPa azimuthal-mean (a) tangential wind ($m s^{-1}$), (b) tangential wind gradient (s^{-1}), (c) relative vorticity (s^{-1}), (d) relative vorticity gradient ($m^{-1}s^{-1}$), and (e) angular velocity ($rad s^{-1}$) from the various wake experiments (see inset for definitions).



(Figure 52 continued)

The cause of rapid spin-down of the TC intensity after the coupling with the cold wake 5 experiment compare to the other wake experiments may be related to the significant cooling below the eyewall. As noted above, the wake 5 experiment has smaller WN1 eddy enstrophy compared to the other wake experiments, which may be related to how the VRW also responds to the cold wake 5. Suppressed WN1 algebraic growth prevents the TC from maintaining the intensity without extraction of mean vortex kinetic energy or by interaction with asymmetric WN2 and higher wave numbers.

However, the WN1 damping mechanism does seem to be present in other wake experiments during their rapid spin-down phase (Figure 50). The waves in the wake 4 (crescent-shaped with a trailing wake) experiment have different characteristics from the other wake experiments. The wake 4 experiment has the smallest WN2 850 hPa eddy enstrophy, and most of its wave energy is in WN1.

Differences in the WN1 and WN2 responses in these wake experiments and in the CNTL experiments are probably a result of counter-acting effects from the three types of waves. Whereas the patterns of vorticity (Figure 48-Figure 51) are largely attributed to the propagation of VRW, the patterns of divergence reflect the propagation of IGWs or mixed VRIGWs. The relative magnitudes of WN2 divergence and vorticity for these three types of waves are very different. For IGWs, the divergence is 3-4 times larger than the vorticity. By contrast, the vorticity in the VRWs is 3-4 times larger than the divergence. For the mixed VRIGWs, the divergence and vorticity are of the same order of magnitude (Zhong et al. 2010).

The plan views of 850 hPa composite WN1 (Figure 53) and WN2 (Figure 54) vorticity and divergence fields indicates the cold wakes increase the divergence and decrease the vorticity components within the RMWs compared to the CNTL (Figure 53a and Figure 54a). For WN1, the wake 3 and wake 5 experiments both have a larger increases in the divergence than do the other wake experiments. The maximum divergence in the wake 3 and wake 5 experiments is $-1.1 \times 10^{-4} \text{ s}^{-1}$. However, the WN1 vorticity is still 1-3 orders of magnitude larger than the divergence in the CNTL and all of the wake experiments.

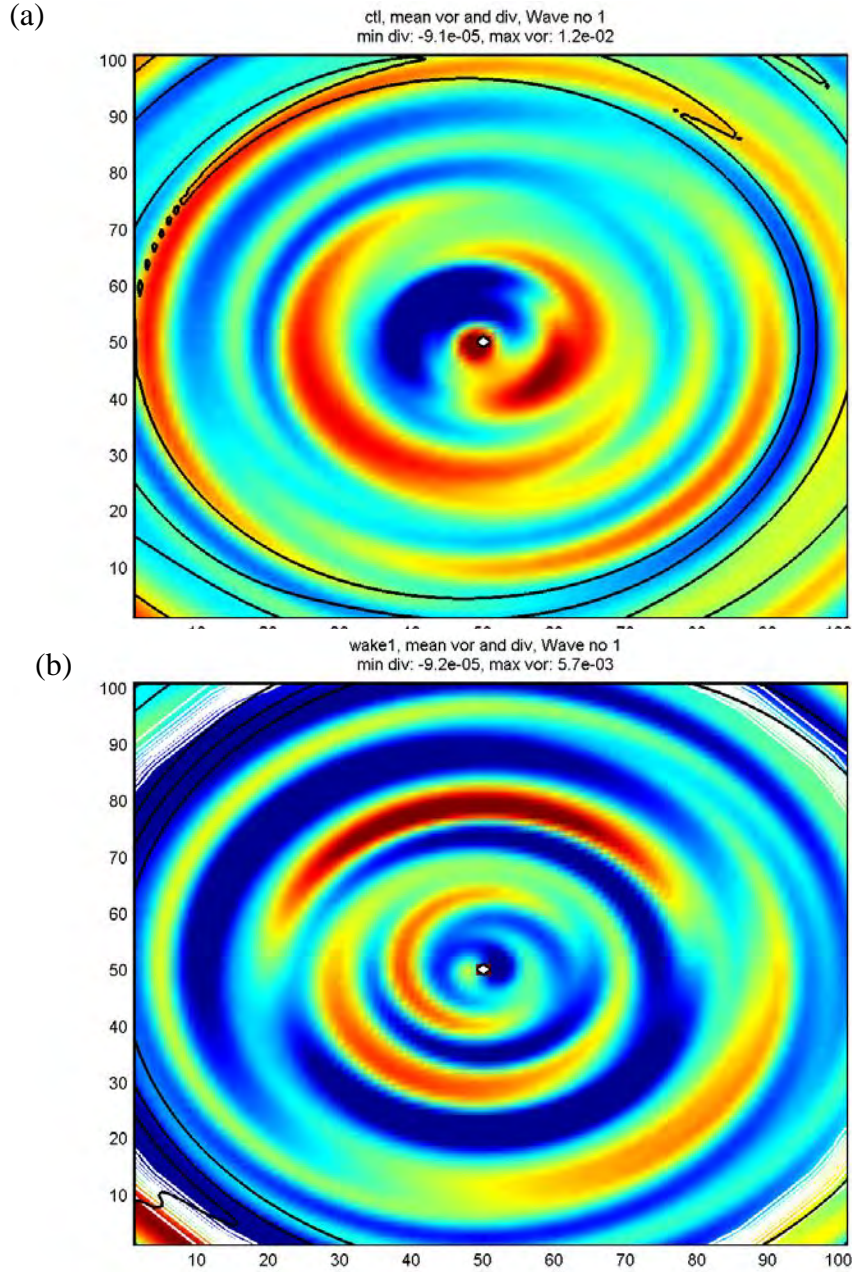
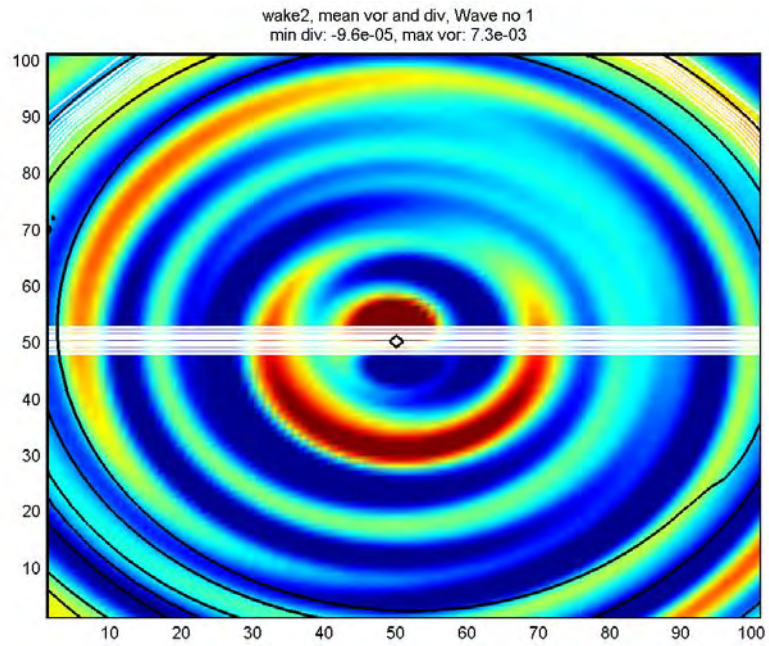
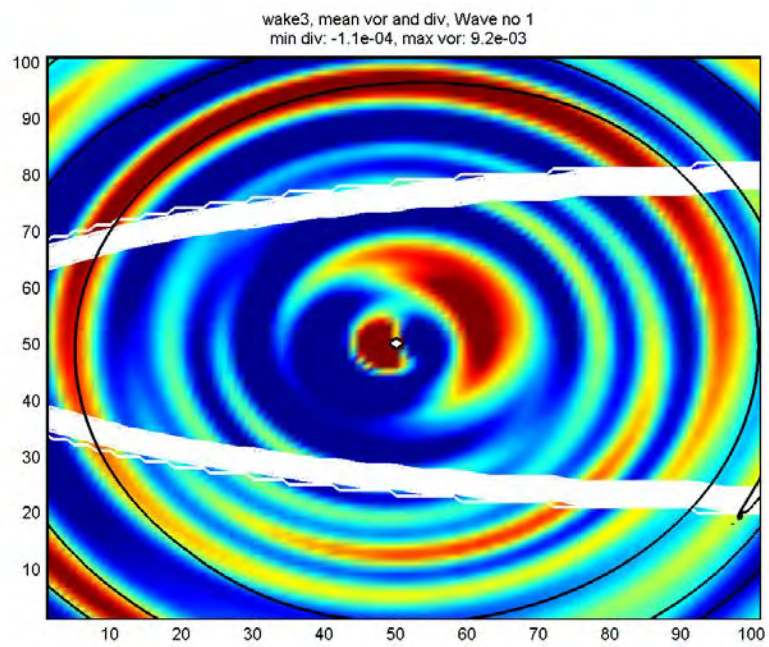


Figure 53. Plan views of composite wavenumber 1 divergence (color shaded) and vorticity (contoured) at 850 hPa level for the CNTL (upper-left) and the five wave experiments. The time period of the composite is from 36-72 h. The vorticity contour interval is $5 \times 10^{-5} \text{ s}^{-1}$ and the white contours mark the boundaries of each cold wake.

(c)



(d)



(Figure 53 continued)

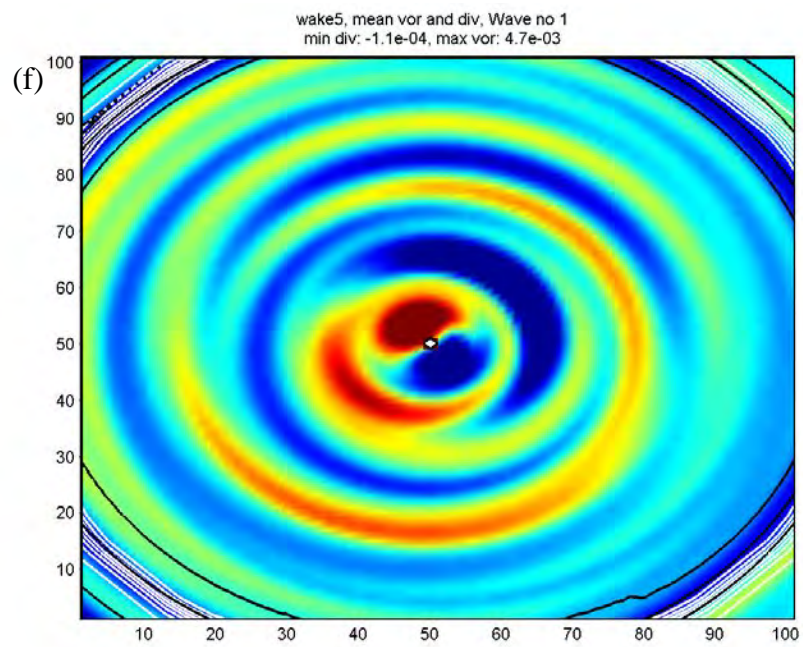
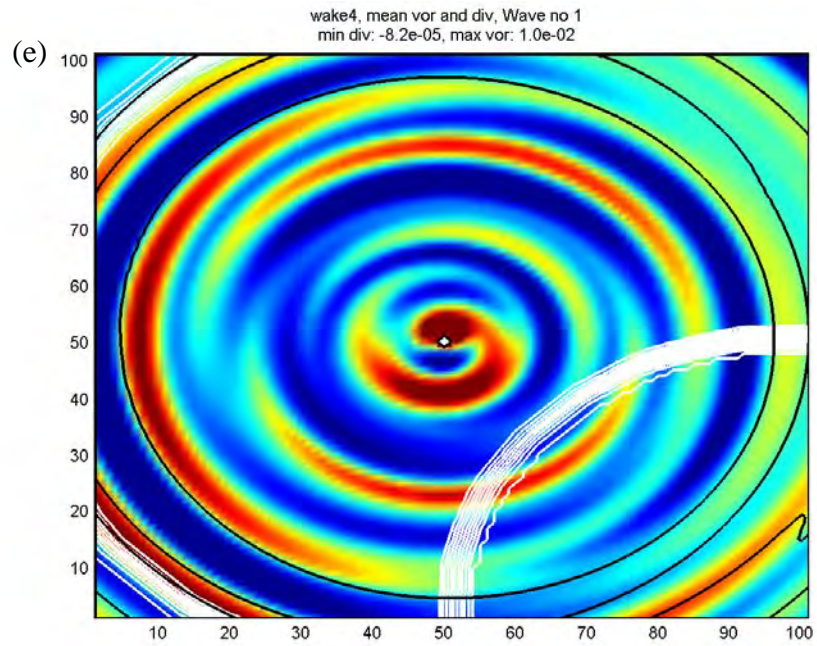


(Figure 53 continued)

A decrease in the vorticity and divergence ratio in the wake experiments also occurs for WN2 (Figure 54) and higher wavenumbers (not shown). In the WN2 and higher wavenumbers, the vorticity is about one order of magnitude larger than the divergence, which indicates the VRWs are the dominant mode inside the RMW. At outer radii, the increased divergence and decreased vorticity result in their values being about the same order of magnitude.

The horizontal distributions of composite WN1 divergence and vorticity responses to the cold wakes inside the RMW are different from those of WN2. These wake 1, wake 2, and wake 5 experiments have the WN1 positive vorticity everywhere within 50 km of the center, but with a smaller magnitude than for the CNTL. The WN1 divergence fields have a radial WN4 structure out to 50 km radius, but with no coherent pattern compared to the CNTL. The CNTL WN2 vortex has a baroclinic structure with convergence a quarter wavelength downwind from the vorticity couplets at the RMW. The baroclinicity at the 850 hPa level is reduced in the wake experiments as the vorticity couplets have rotated upwind to be closely coincident with the convergence couplets. The vorticity in the wake experiments is also extended downwind and outward compared to the CNTL experiment. This stretched vorticity pattern is attributed to the reduced vortex rotation in the wake experiments. The upwind propagation of the VRWs forces an outward and upwind rotation of the WN2 vorticity couplets.

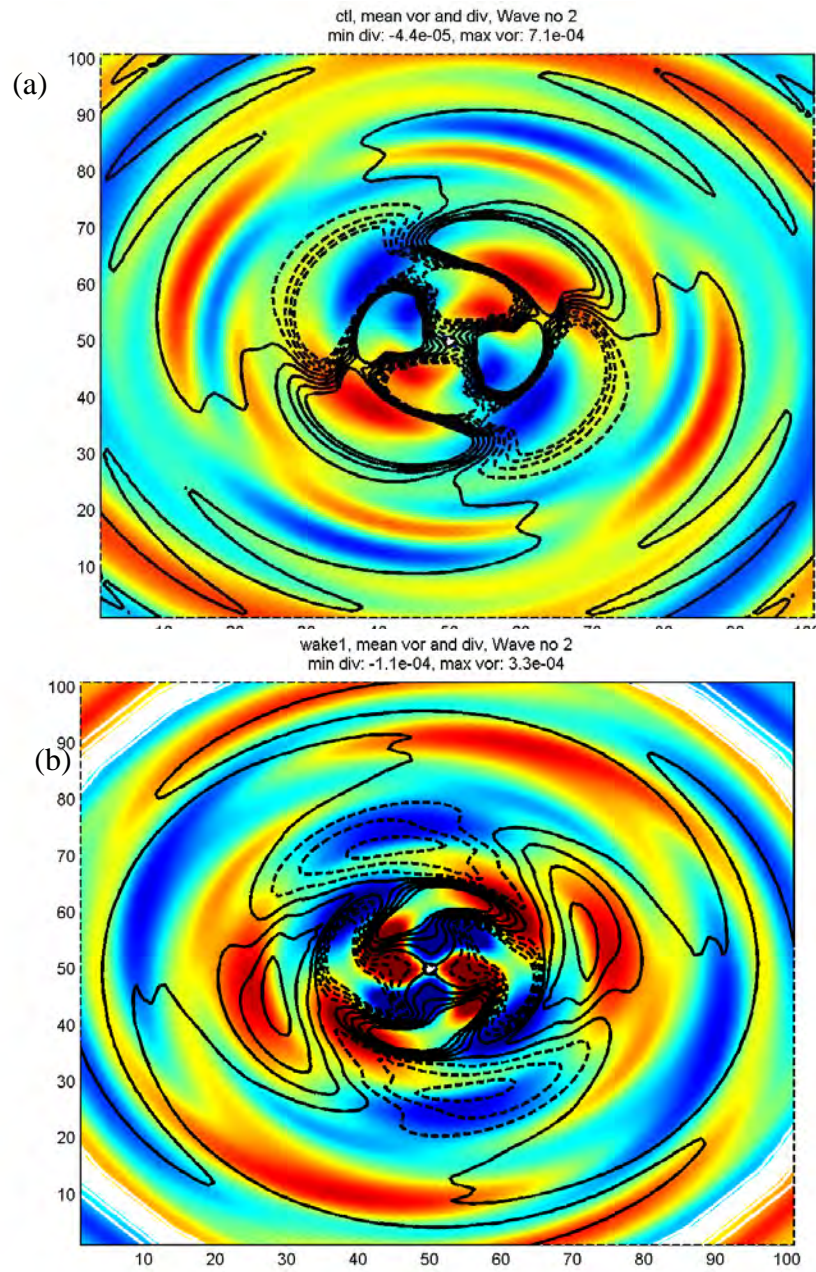
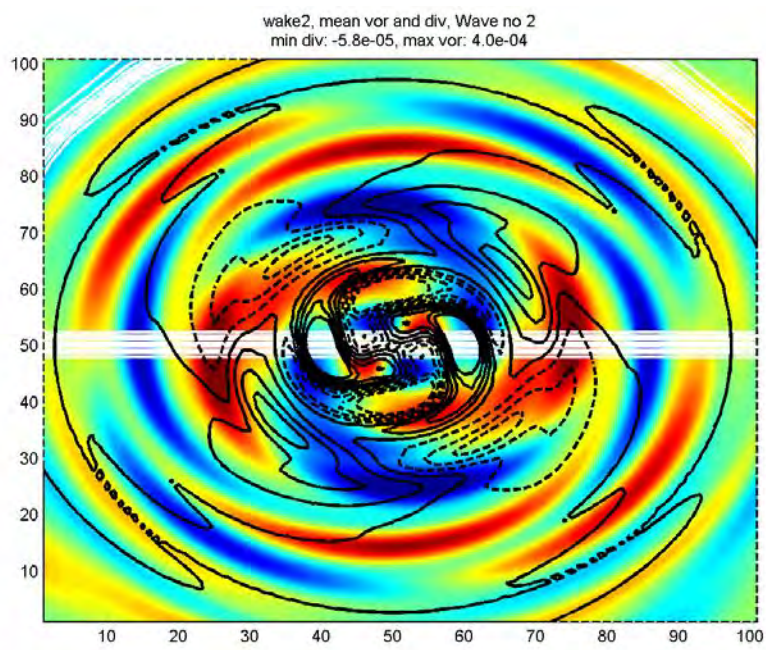
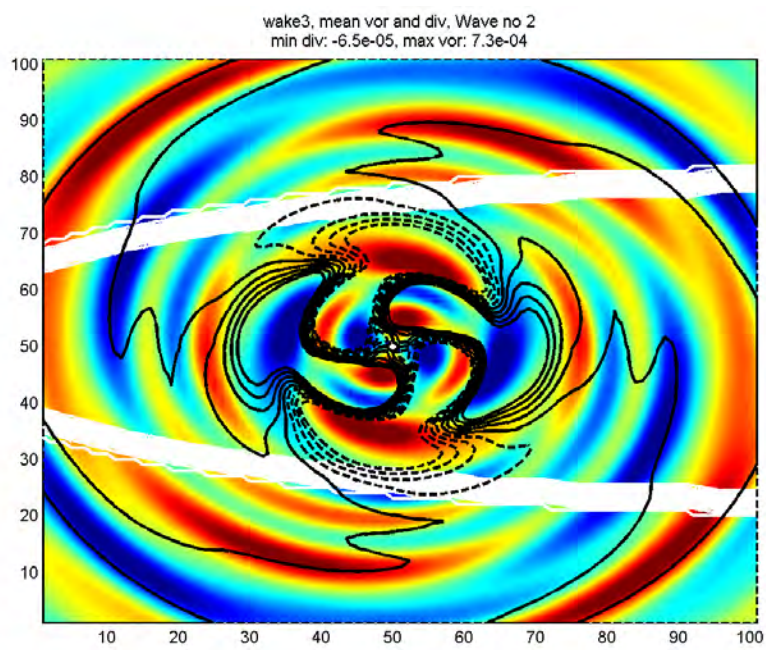


Figure 54. As in Figure 53, except for the wavenumber 2.

(c)

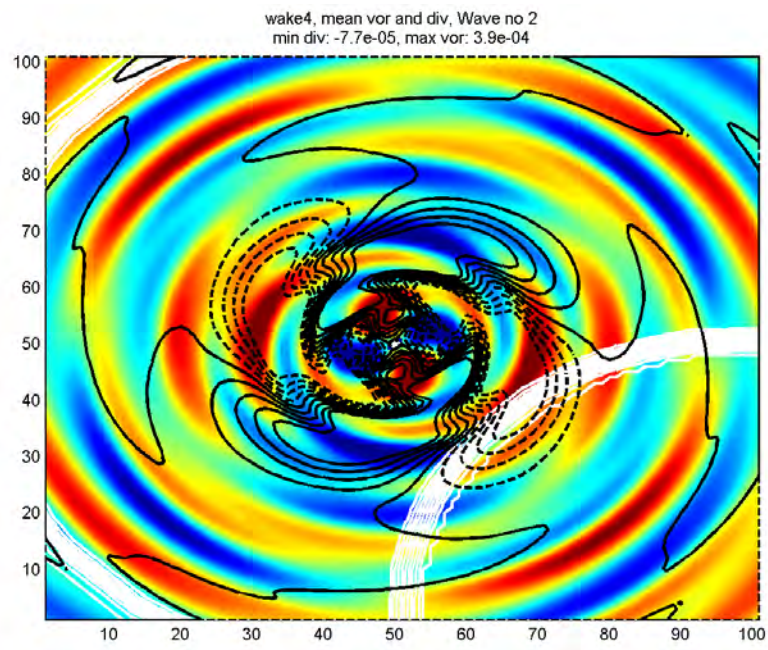


(d)



(Figure 54 continued)

(e)



(f)

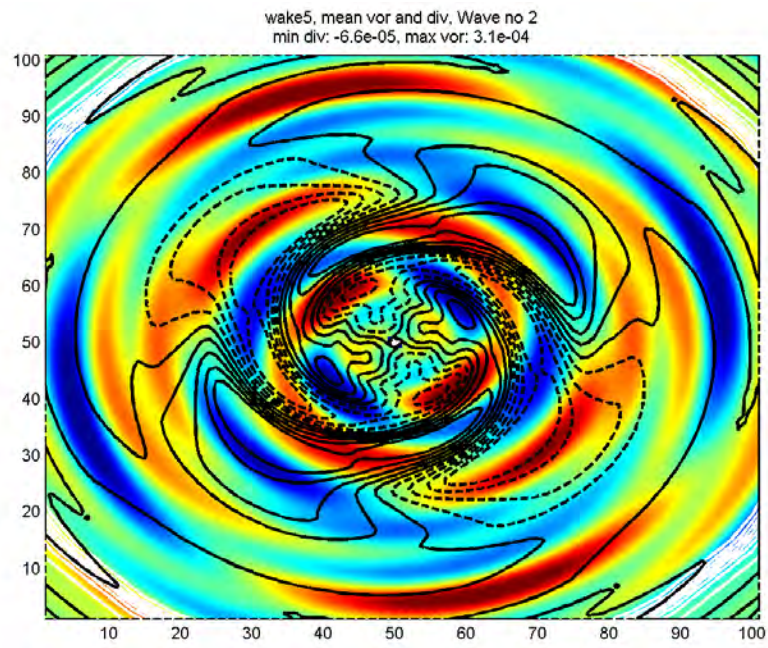


(Figure 54 continued)

Previously, it was demonstrated that the cold wakes excite inward and outward propagation of higher wavenumbers at 400 hPa, and the VRW propagates upwind. The azimuthal-height cross-section composite of vorticity and divergence of WN1 at the RMW (Figure 55) indicates the cold wake damps the vertical propagation of the VRWs compared to the CNTL experiment. The CNTL WN1 vorticity below (above) 700 hPa tilts downwind (upwind) with height. In the wake experiments, the WN1 vorticity upwind propagation below 700 hPa is faster than in the CNTL experiment. The WN1 divergence for the CNTL has a similar pattern as in the vorticity, but with less vertical tilt. In the wake 1, wake 3, and wake 4 experiments, the divergence tilts upwind with height to about 600 hPa. However, the wake 2 and wake 5 divergence tilts downwind with height.

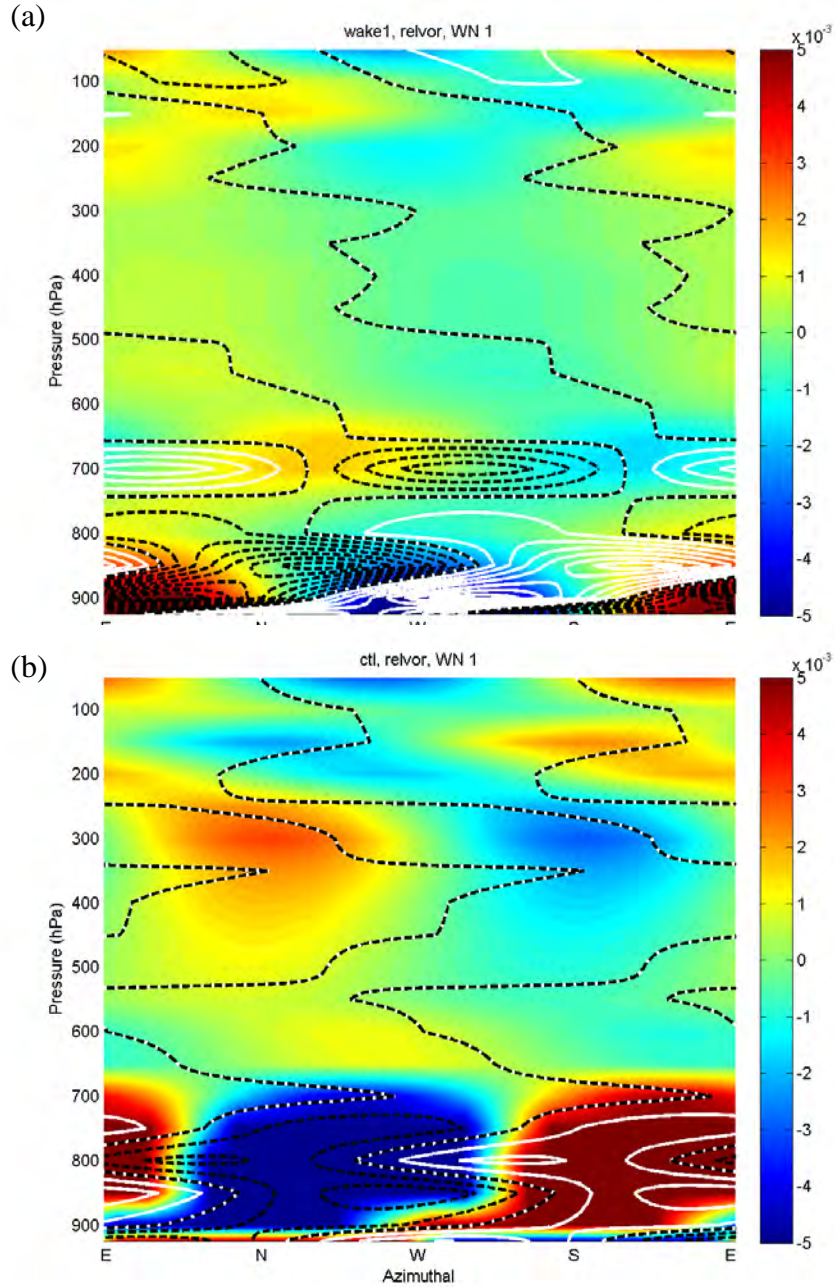
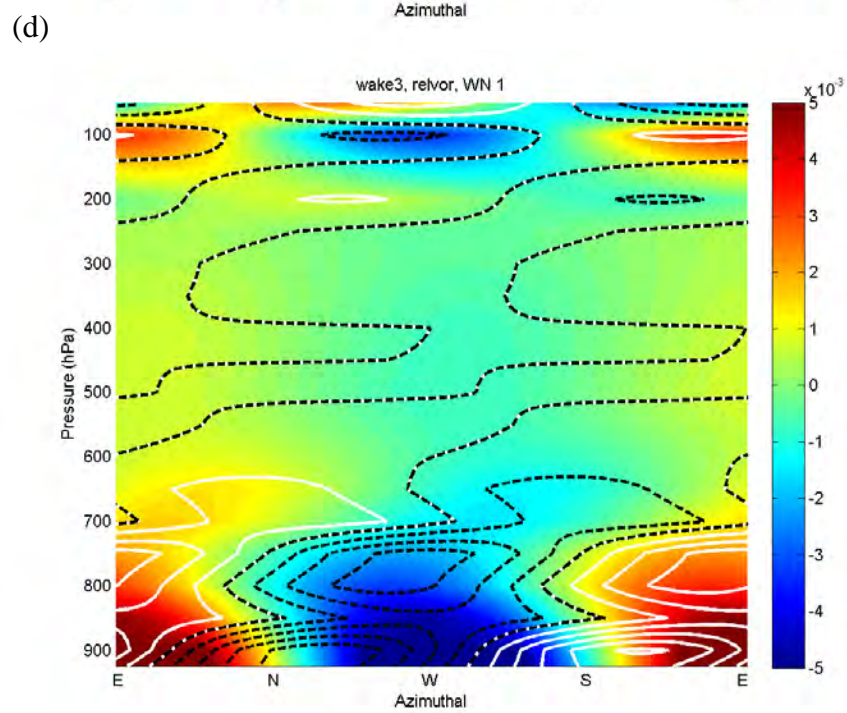
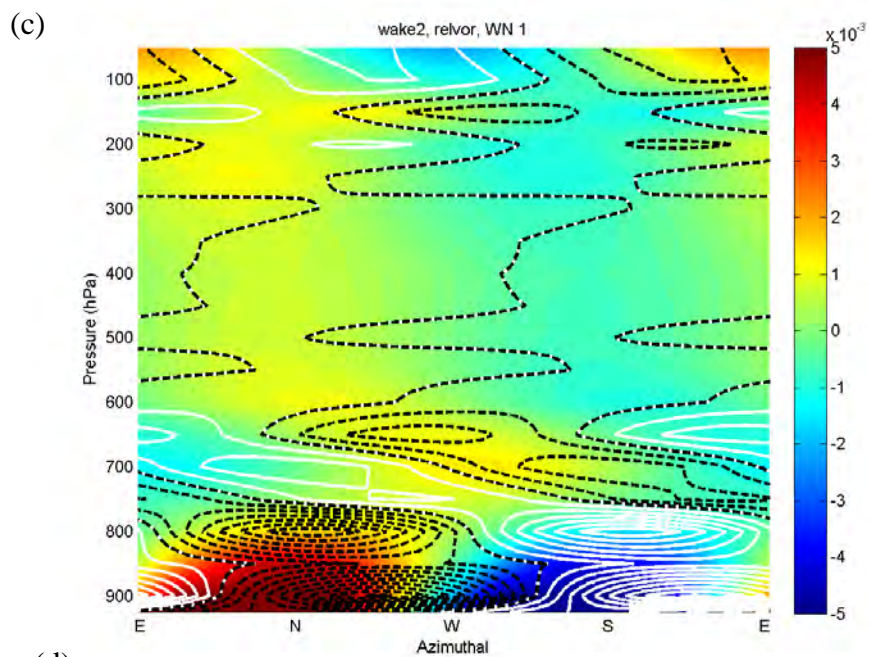
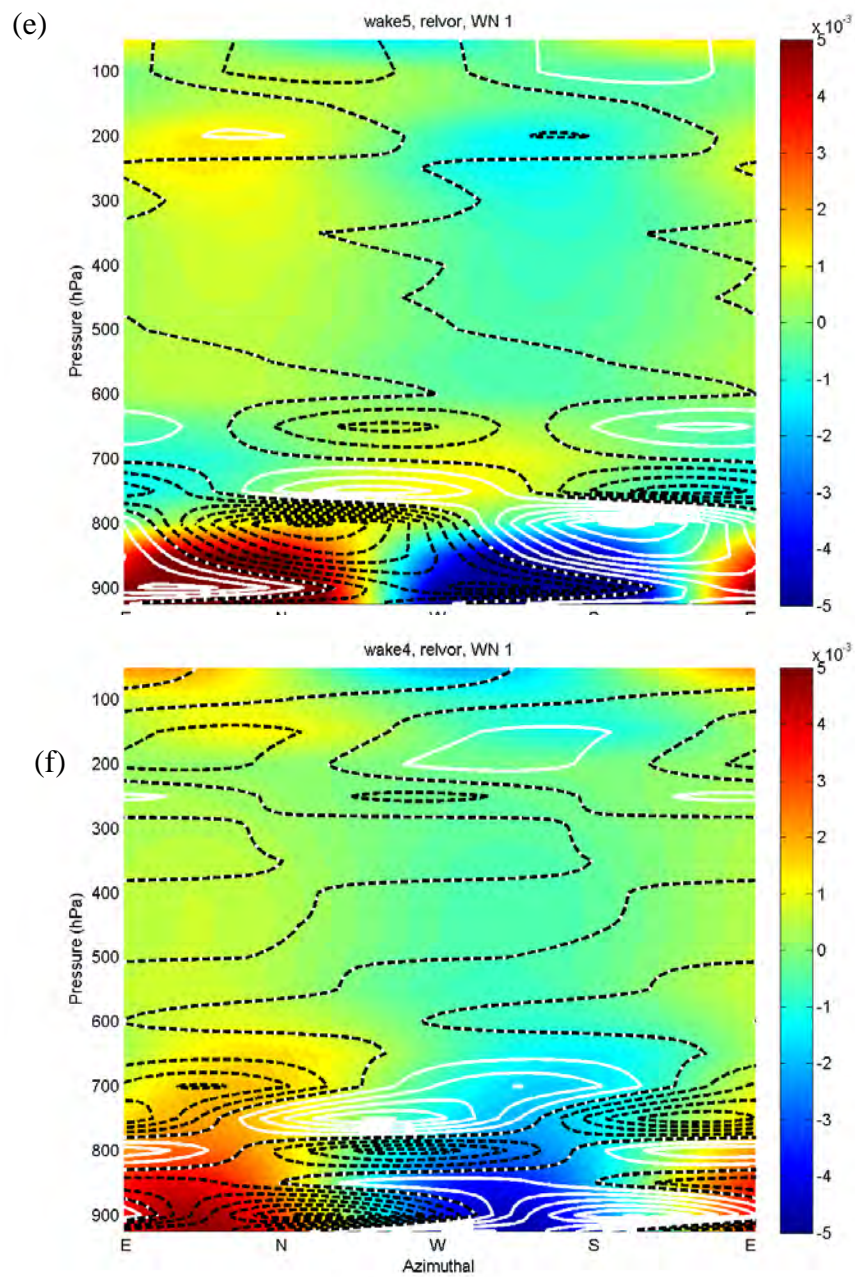


Figure 55. Azimuth-height cross-sections of composite WN1 vorticity (s^{-1} , color scale on right) and divergence (s^{-1} , solid white and dashed black contours) at RMW from (a) CNTL, (b) wake 1, (c) wake 2, (d) wake 3, (e) wake 4, and (f) wake 5 experiments. The contour interval is $2 \times 10^{-4} \text{ s}^{-1}$. The RMW for the CNTL experiment is 10 km and for the wake experiments is 25 km.



(Figure 55 continued)



(Figure 55 continued)

A similar vertical damping of the WN1 vorticity in the wake experiments occurs for the WN2 vorticity (Figure 56). The CNTL WN2 vorticity tilts downwind with height below 700 hPa, but then has little vertical tilt up to 300 hPa. In contrast, the WN2 vorticities in the wake experiments have an upwind tilt with height, which indicates an upward and upwind propagating VRW. The low-level WN2 divergence between 900-700 hPa has an upwind vertical tilt in the CNTL experiment. This upwind vertical tilt is reduced in the wake 1 experiment and changes to a downwind tilt in the wake 2 to wake 5 experiments, which suggests the gravity wave component of WN2 wave is propagating vertically faster than the mean wind at 900-700 hPa level. The asymmetry in the cold wake shapes also seems to affect the magnitude of the divergence. An increase in the divergence magnitude is simulated in the wake 2, wake 3, and wake 4 experiments compared to the wake 1 and wake 5 experiments. The wake 4 experiment has the largest WN2 divergence magnitude among the wake experiments.

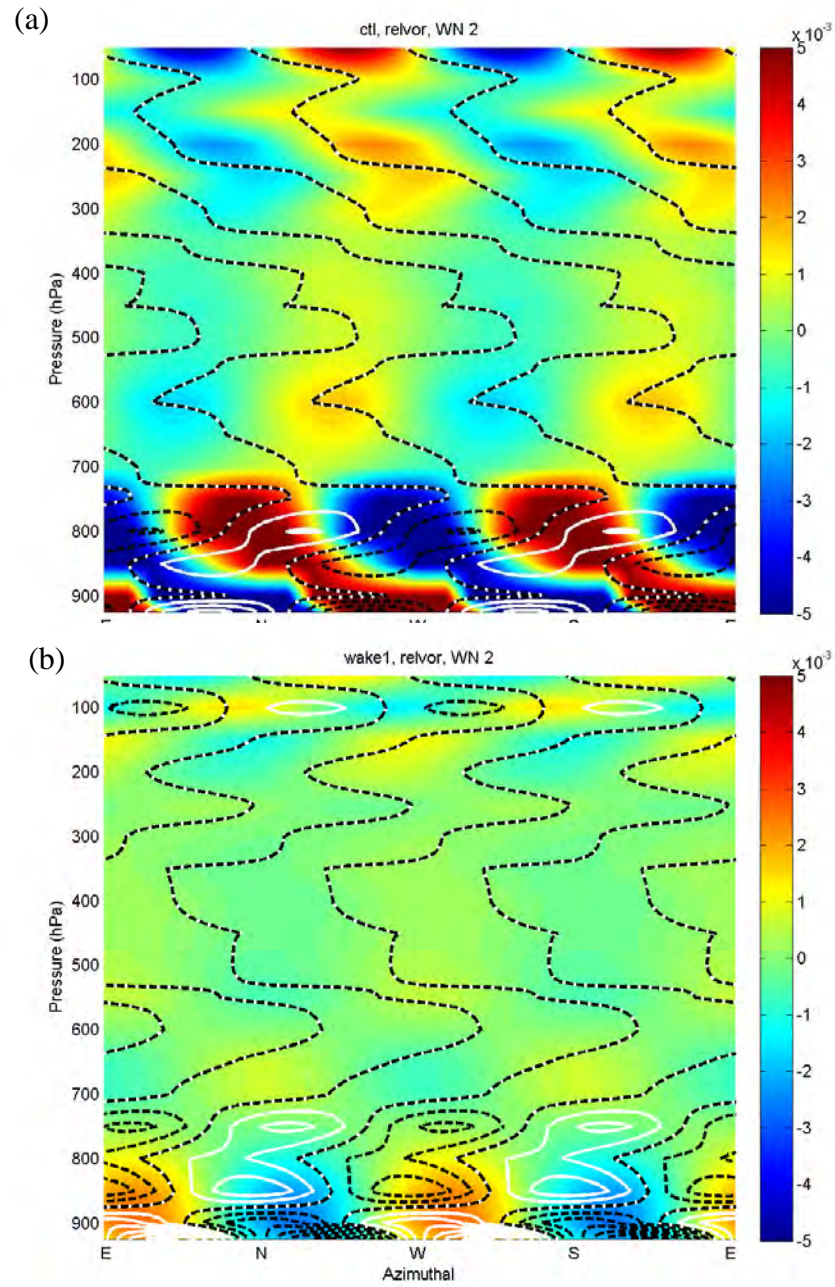
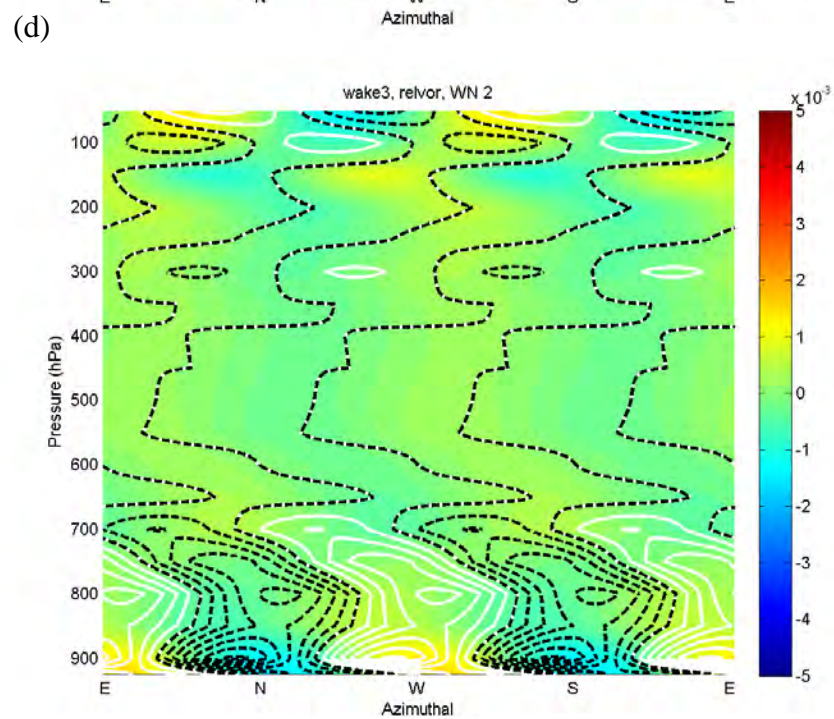
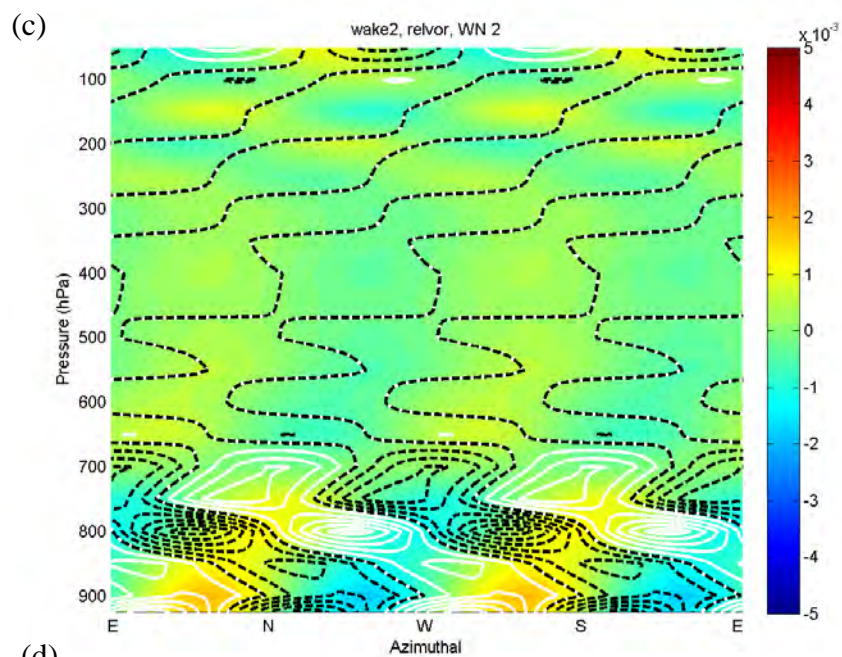
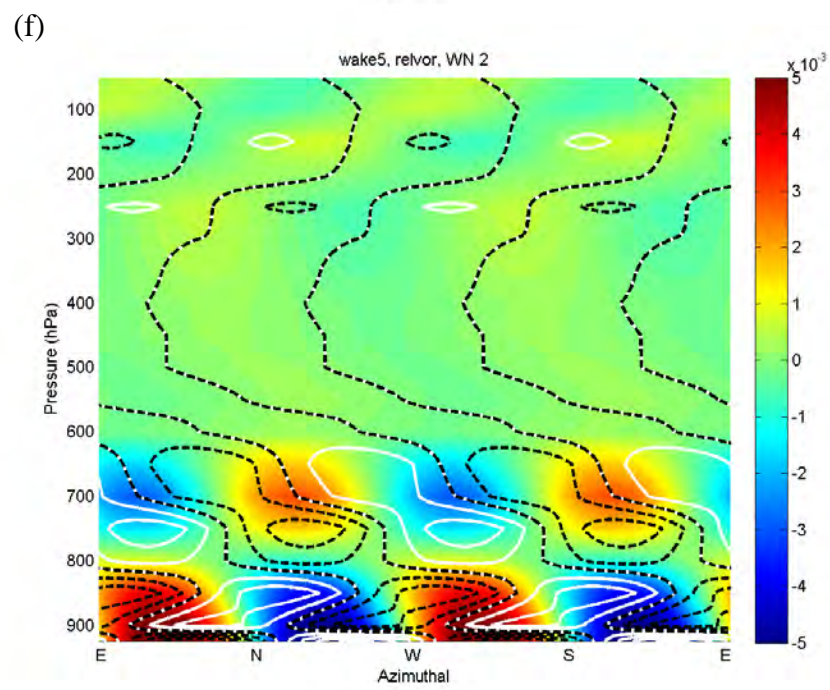
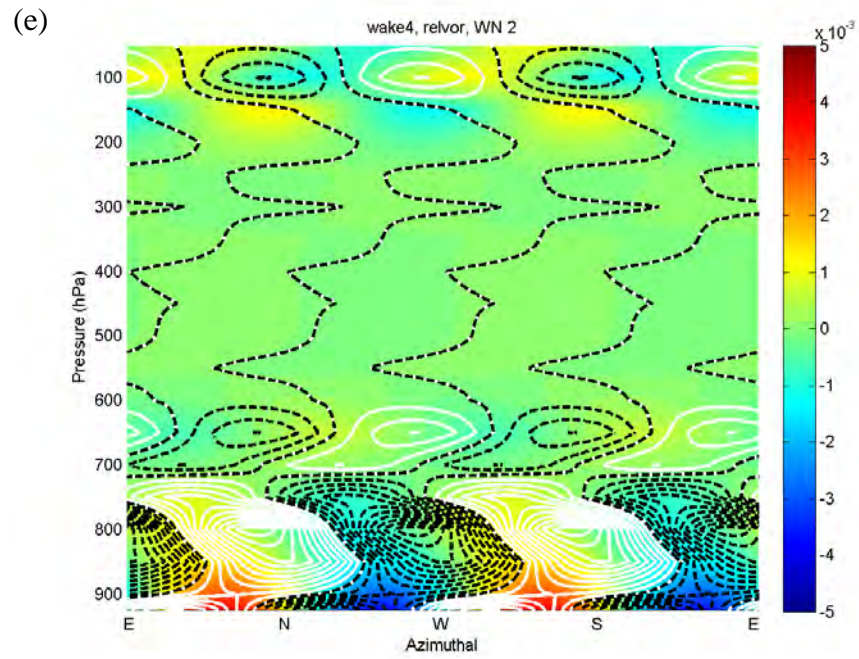


Figure 56. As in Figure 55, except for the WN2 vorticity and divergence.



(Figure 56 continued)



(Figure 56 continued)

The vertical and radial propagation of WN1 at 45° azimuthal angle is shown in Figure 57. The CNTL vorticity composite has a single positive vorticity column that is situated between 10-20 km radius and extends up to 200 hPa. Positive vorticity is also simulated inside 10 km, but is confined to below 750 hPa. In the wake experiments, the low-level positive vorticity is displaced radially outward to 20-30 km in the wake 1, wake 2, and wake 5 experiments. Positive vorticity above 700 hPa is reduced compared to the CNTL experiment. The WN1 vorticity is tilted slightly outward vertically in the wake experiments compared to the CNTL experiment. The WN1 divergence vertical tilt is more radially outward in the wake experiments and extends higher and has a larger magnitude than in the CNTL experiment.

The cold wakes have a larger impact on the vertical propagation of the WN2 compared to the CNTL experiment. The mid-level positive vorticity between 700-500 hPa inside the RMW is smaller in the wake experiments and the low-level positive vorticity is decoupled from the upper-level vorticity maximum. The low-level positive vorticity inside the RMW is also mostly confined to below 800 hPa (Figure 58). Thus, the effects of the cold wakes on the WN2 divergence are similar to those for the WN1 divergence in that the vertical and radial propagations of divergence are increased.

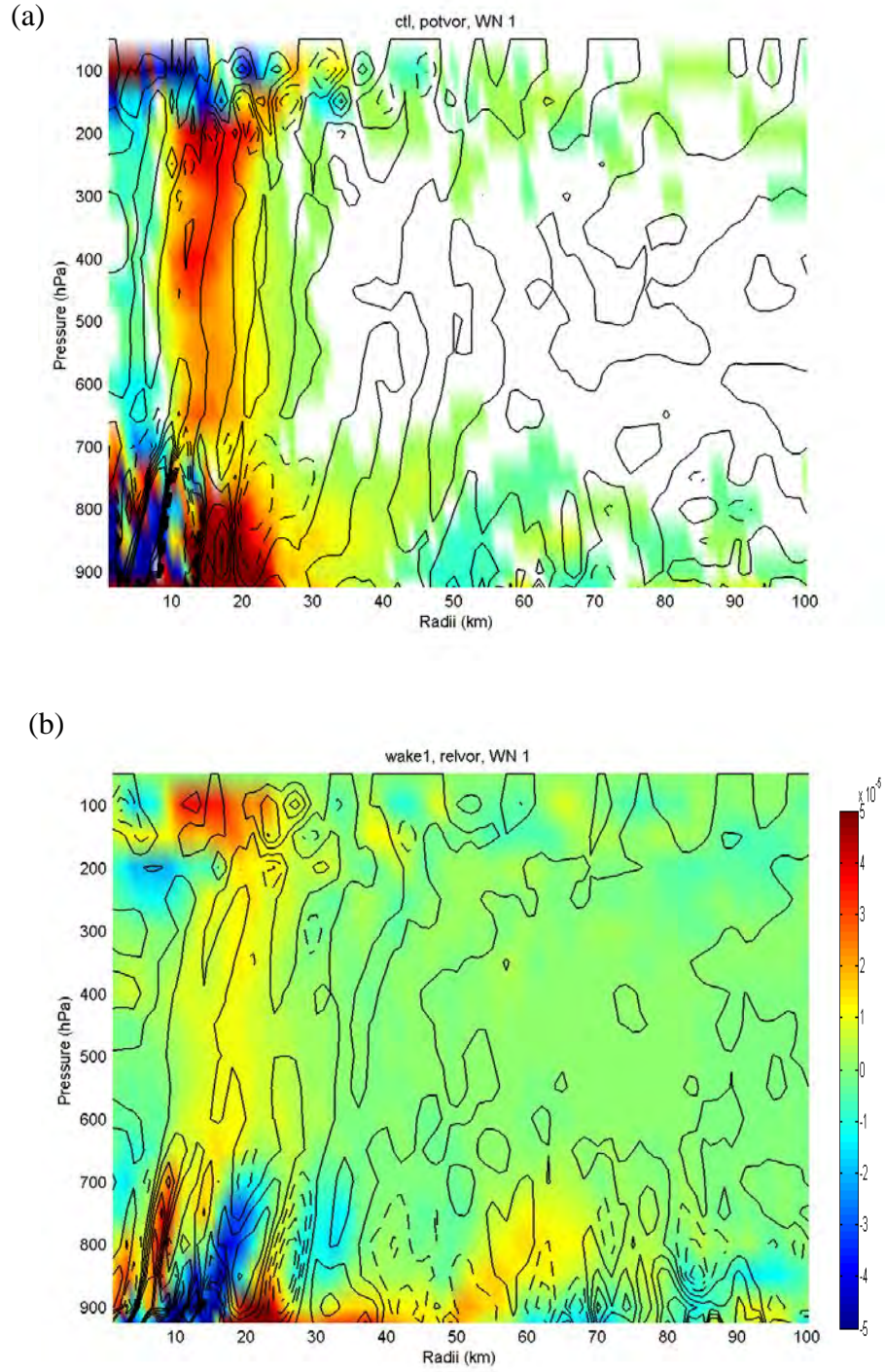
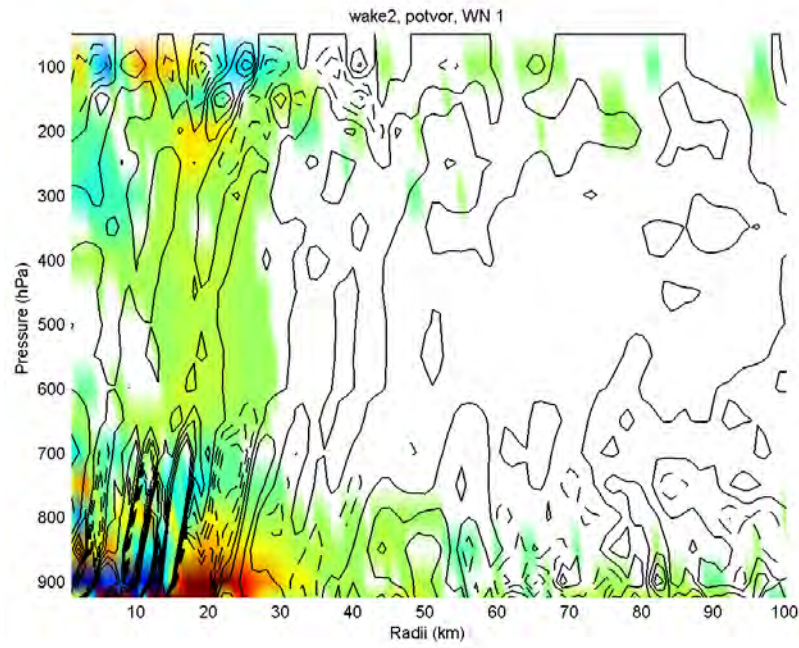
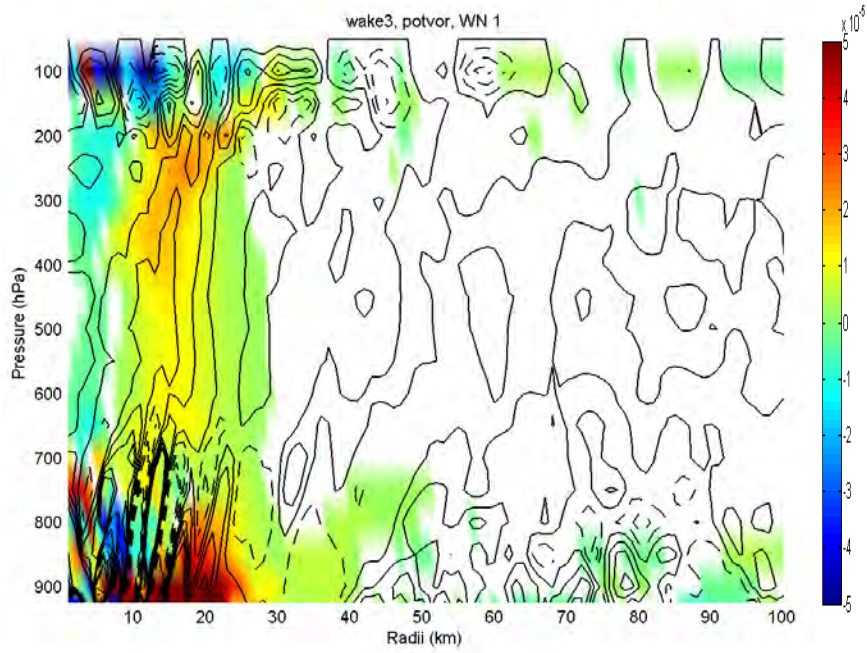


Figure 57. Radial-height cross-sections of WN1 composite vorticity (s^{-1} , color shaded) and divergence (s^{-1} , contours) from (a) CNTL, (b) wake 1, (c) wake 2, (d) wake 3, (e) wake 4, and (f) wake 5 experiments. The contour interval is $5 \times 10^{-4} \text{ s}^{-1}$.

(c)



(d)



(Figure 57 continued)

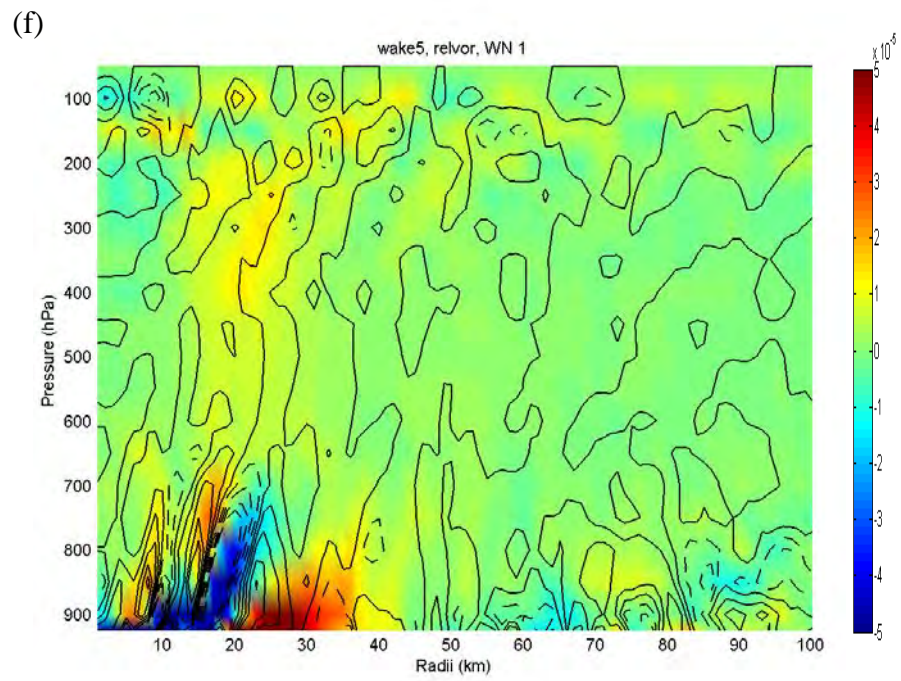
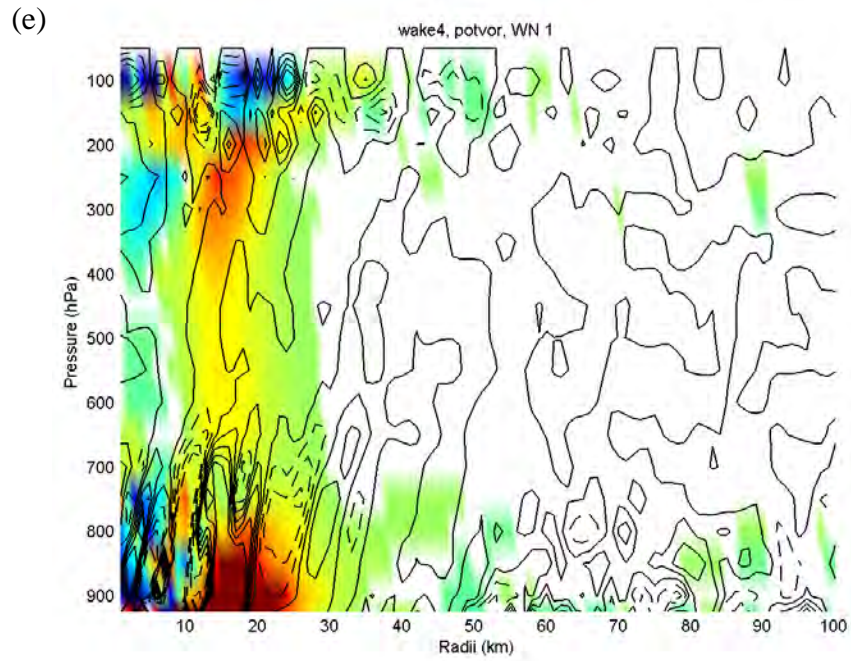


(Figure 57 continued)

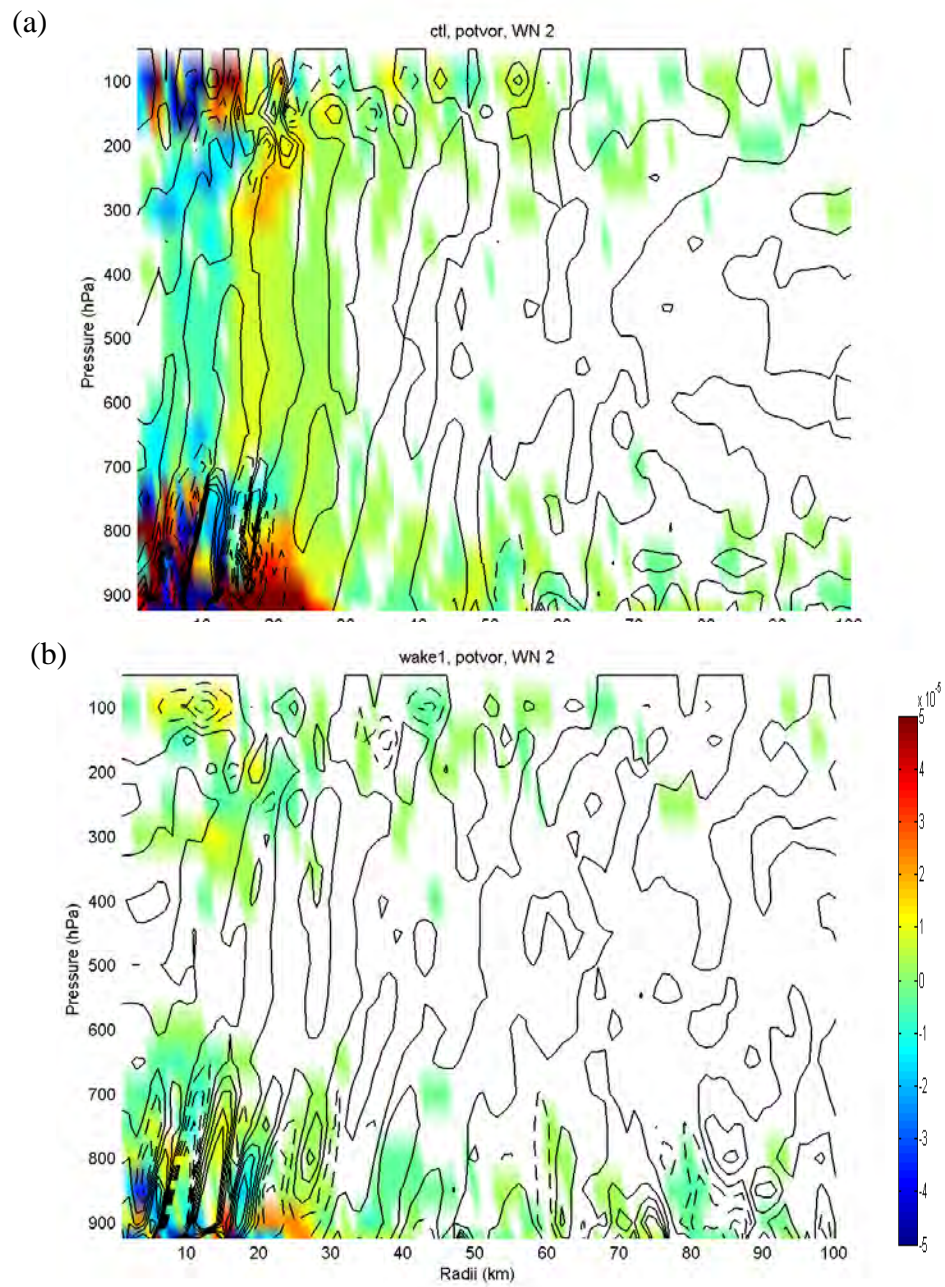
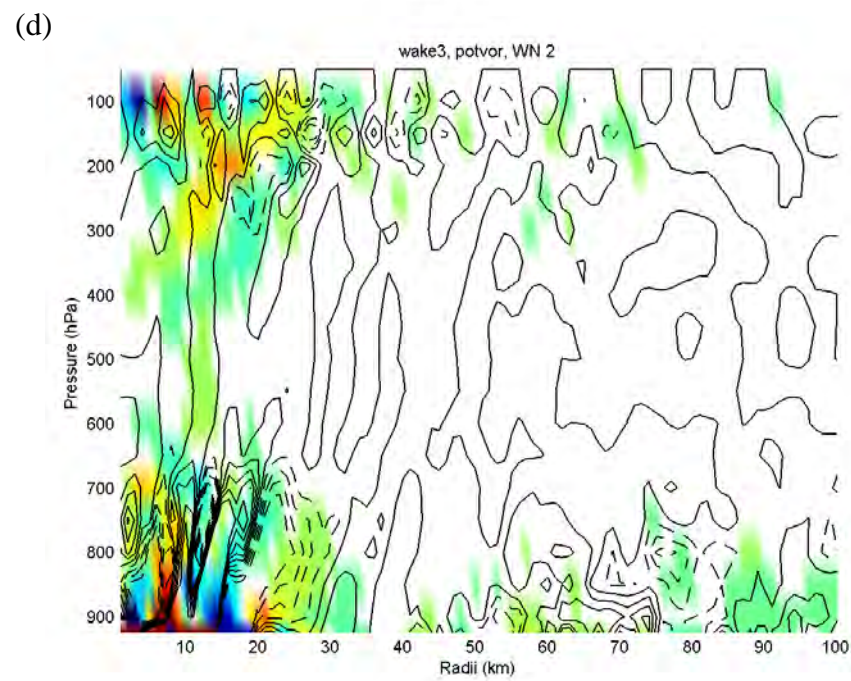
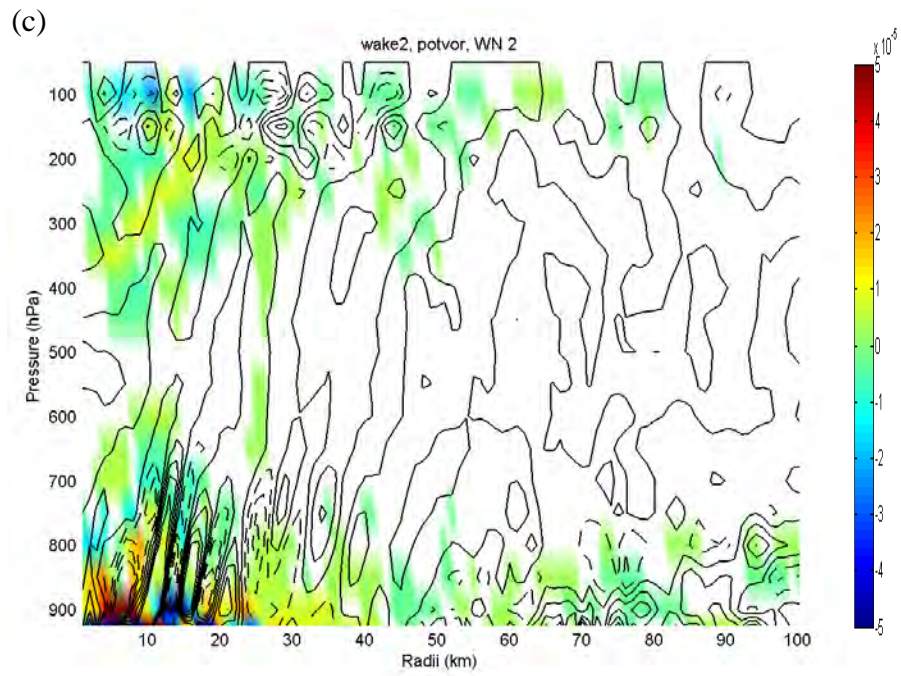
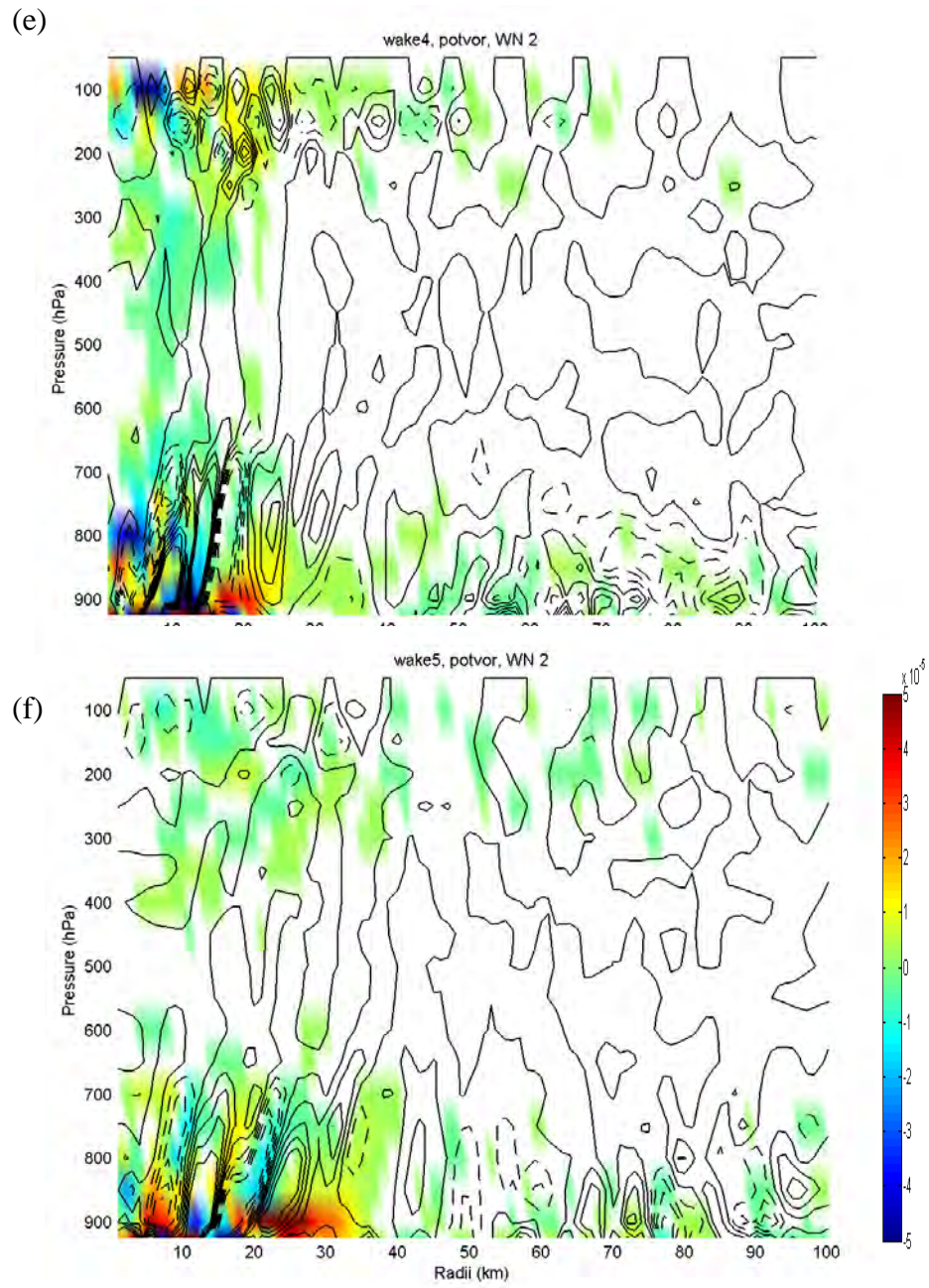


Figure 58. As in Figure 57, except for the WN2 vorticity and divergence.



(Figure 58 continued)



(Figure 58 continued)

C. ORIGIN OF WAKE JET

The objective in this section is to describe the origin of a “wake jet” as the low-level airstream in the tropical cyclone passes over its cold wake. Chen et al. (2010) first proposed the existence of a wake jet as the warm, moist airstream interacts with the cooler air over the ocean that has been modified by air-sea fluxes. Recently, Lee and Chen (2014) have also modeled the effects of the ocean cold wake and found a similar effect. In this section, the origin of the wake jet due to the modulation of the low-level flow over a long, narrow cold wake will be displayed with trajectory analyses. That is, these trajectory analyses were performed on the one-way coupled wake 3 experiment that had an elongated 2°C cold wake. Momentum budget analyses and air-sea flux calculations will then be performed to describe the physical mechanisms for the wake jet.

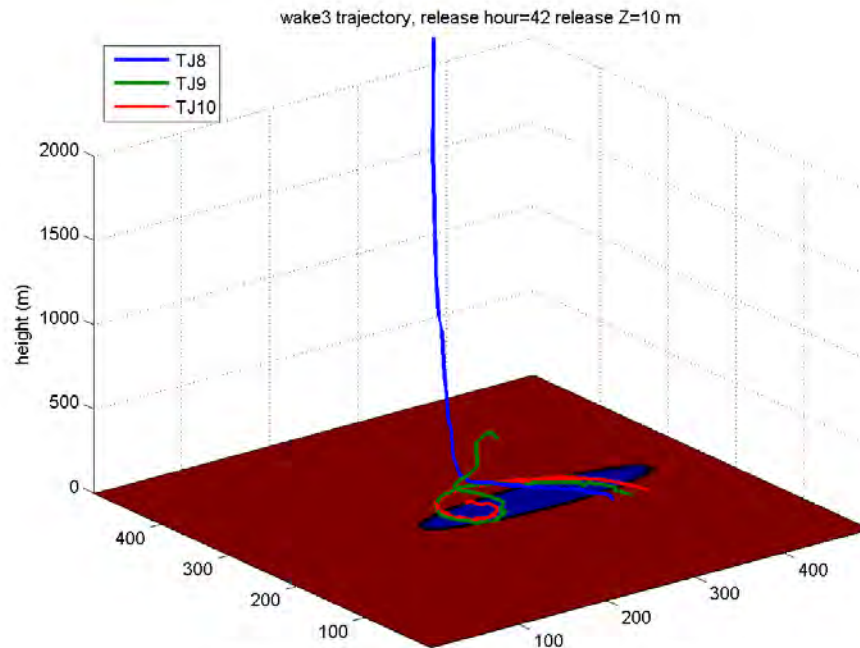
The deflections of air parcel trajectories due to the ocean cold wake in experiment wake 3 are obtained by calculating the forward trajectories with a two minute time interval. Ten trajectories were initiated 20 km apart along an east-west line starting around 50 km east of the initial TC center as determined by the minimum sea-level pressure. The trajectories are thus released just upwind from the cold wake at each of the lower 22 model vertical levels (10 m – 1000 m). These trajectories were released every hour between 30 h - 67 h during the simulation and tracked for 6 h (not shown). The trajectories closer to the TC center at the release time had different paths from trajectories released at outer radii in TC. Most of the air parcels released close to the TC center continue into the eyewall updrafts or passed into the subsidence region of the eye. By contrast, air parcels released at the outer radii experienced an increased vertical displacement with time and an increased inflow angle.

Of particular interest are the displacement of the outer three trajectories 8, 9, and 10 (hereafter referred to as TJ8, TJ9, and TJ10) that were released at 10 m height and at distance of 90, 110, and 130 km from the eye. The time evolutions of these three trajectories with 3 h release intervals are shown in Figure 59. At 42 h (Figure 59a), the end positions of TJ8 and TJ9 are in the eyewall updrafts, while TJ10 simply rotates around to the front-left quadrant of TC. For the release at 45 h (Figure 59b), TJ10 has a longer travel time over the cold wake than do TJ8 and TJ9. For the release at 48 h (Figure

59c), all three trajectories experience ascent over the cold wake with the largest ascent occurring for TJ9. Trajectories released from 50 m height are very similar to the trajectories released at 10 m height, except that TJ10 is also incorporated into the eyewall updrafts by the end of 6 h trajectory. Both TJ9 and TJ10 have an increased ascent magnitudes and inflow angles (Figure 60).

The weak ascent in TJ9 and TJ10 is forced by the formation of an atmospheric cold pool (ACP) in response to the underlying cold ocean wake. The time evolution of the ACP (Figure 61a) displayed along the N-S cross sections ~130 km east of the eye (Figure 61b) shows the time variation of the potential temperature up to 2 km height from 48 h – 72 h. Note that the variation of the ACP at this location is associated with the diurnal cycle and outward propagating rainbands. The time evolution of the sensible heat fluxes (Figure 62) are negative over the cold wake region at night times. During the day times, the sensible heat flux is positive over the wake. There is a distinct oscillation of rainbands on the diurnal time scale (Fig. 5.28). Dunion et al. (2014) showed observation evidence of a TC diurnal pulse that begins near the storm center at sunset each day and propagates outward until the following late afternoon. The model simulated rainbands, sensible heat flux over the wake, and the associated ACP also show this kind of diurnal variation. A larger and stronger ACP (Figure 62a-f, cooler color) means a longer travel time required for TJ10 to climb over this atmospheric cold dome.

(a) 42 h



(b) 45 h

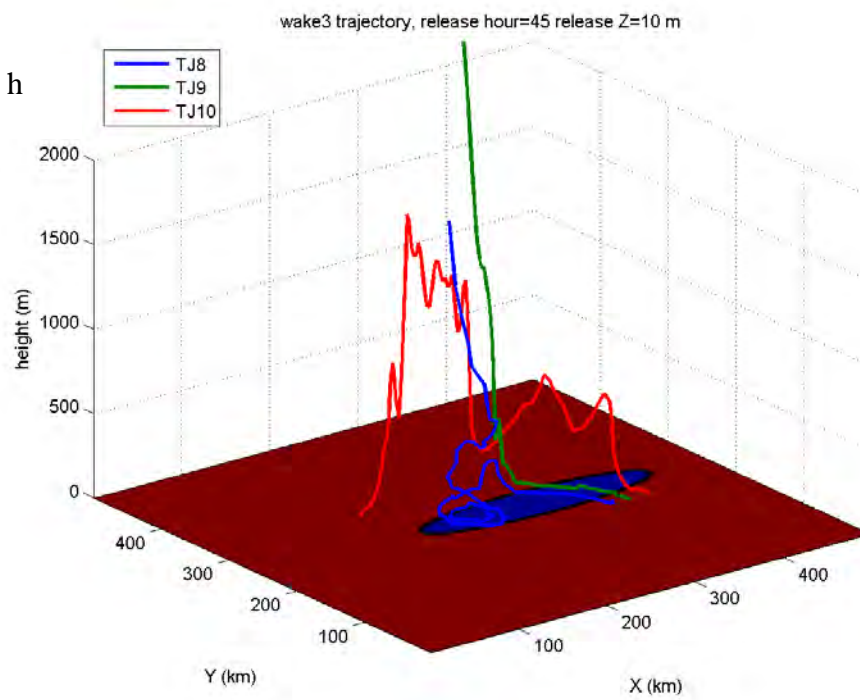
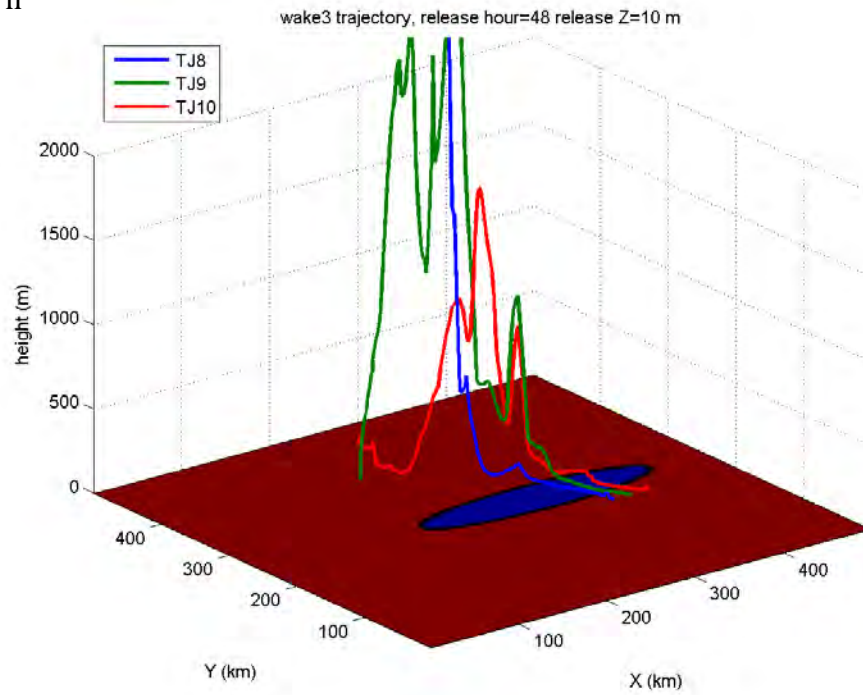
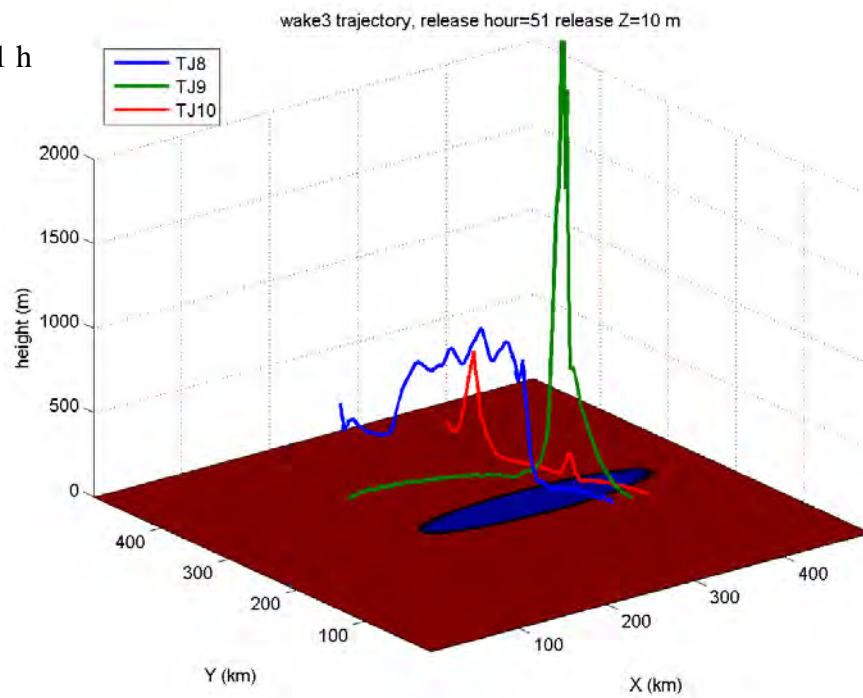


Figure 59. Six-hour evolutions of trajectories TJ8-TJ10 (see inset for definitions) released at (a) 42 h, (b) 45 h, (c) 48 h, and (d) 51 h.

(c) 48 h



(d) 51 h



(Figure 59 continued)

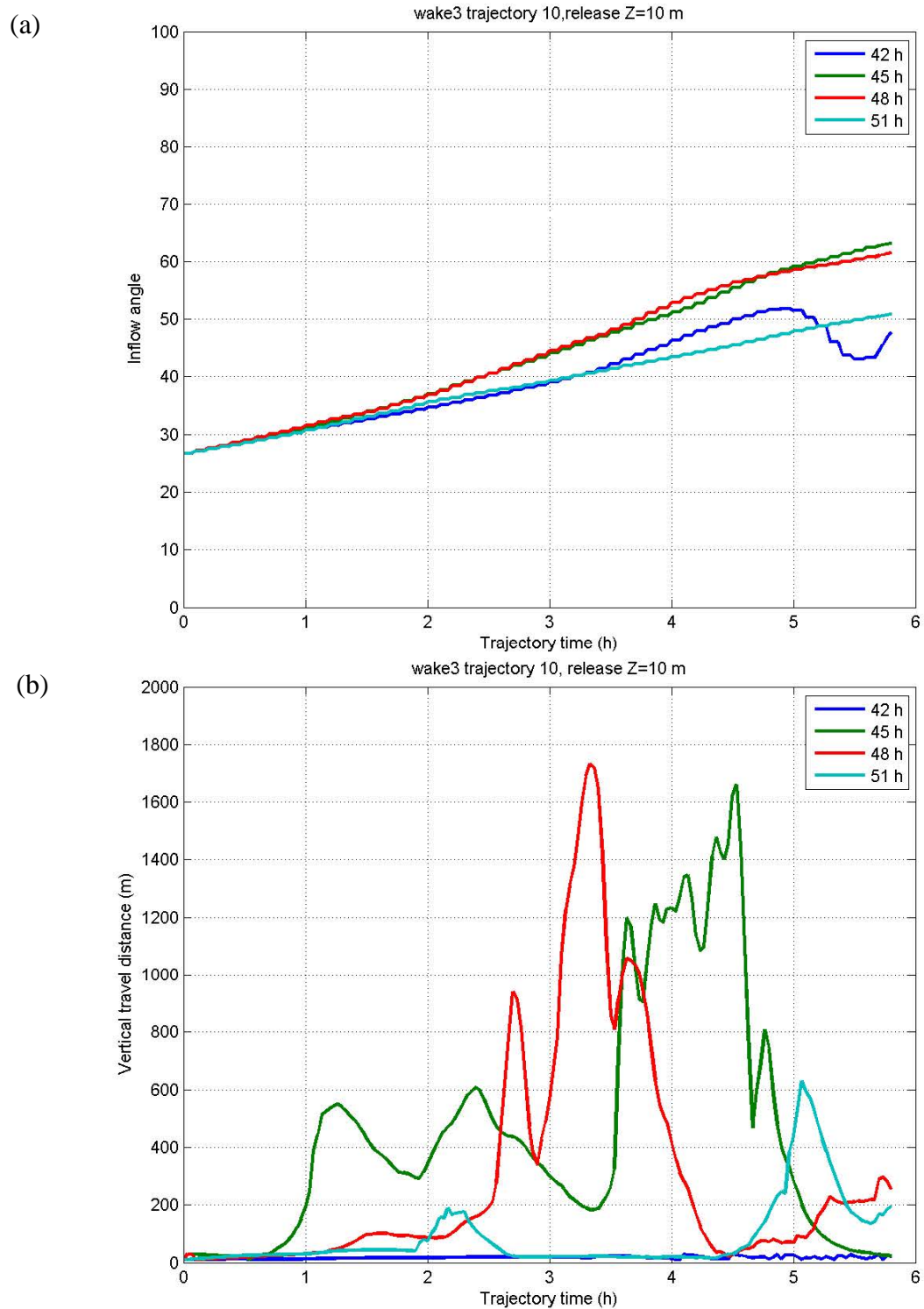
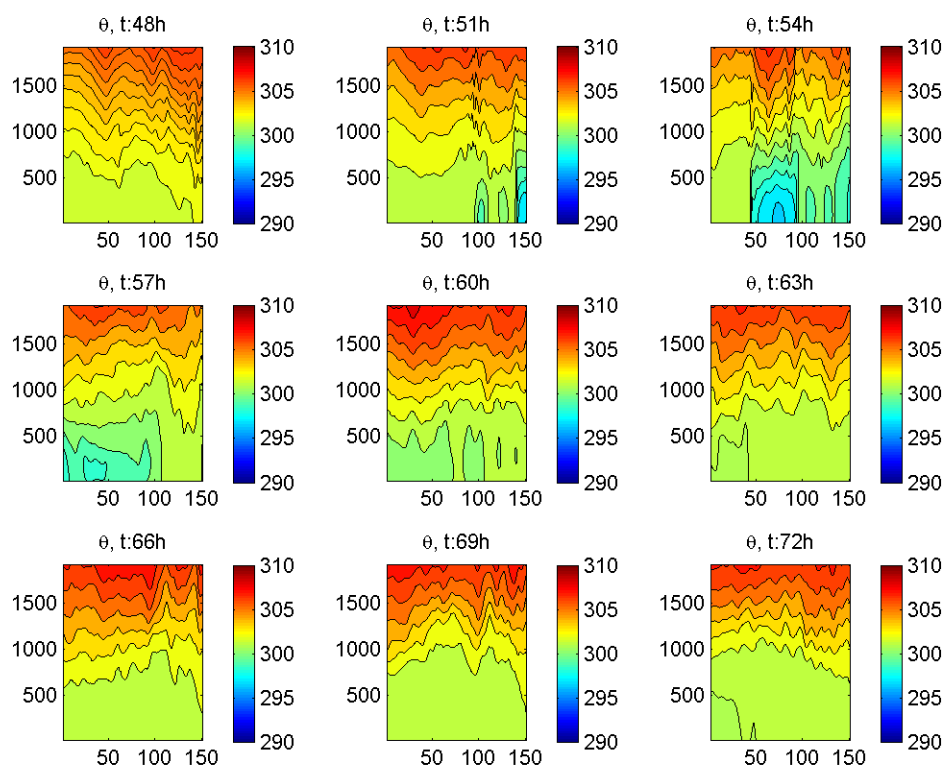


Figure 60. (a) Inflow angle ($^{\circ}$) and (b) vertical distance traveled (m) for the TJ10 releases between 42 h – 51 h.

(a)



(b)

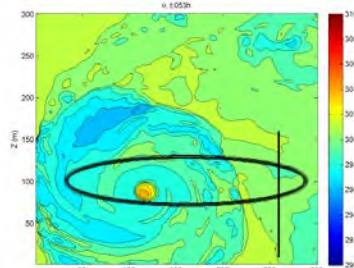


Figure 61. North-south cross sections of the wake 3 potential temperature every three hours from (a) 48 h – 72 h. (b) Location of the cross section with respect to the cold wake (black oval) and the plan view of the 48 h potential temperature ($^{\circ}\text{K}$, colored) averaged over the 1-2 km layer.

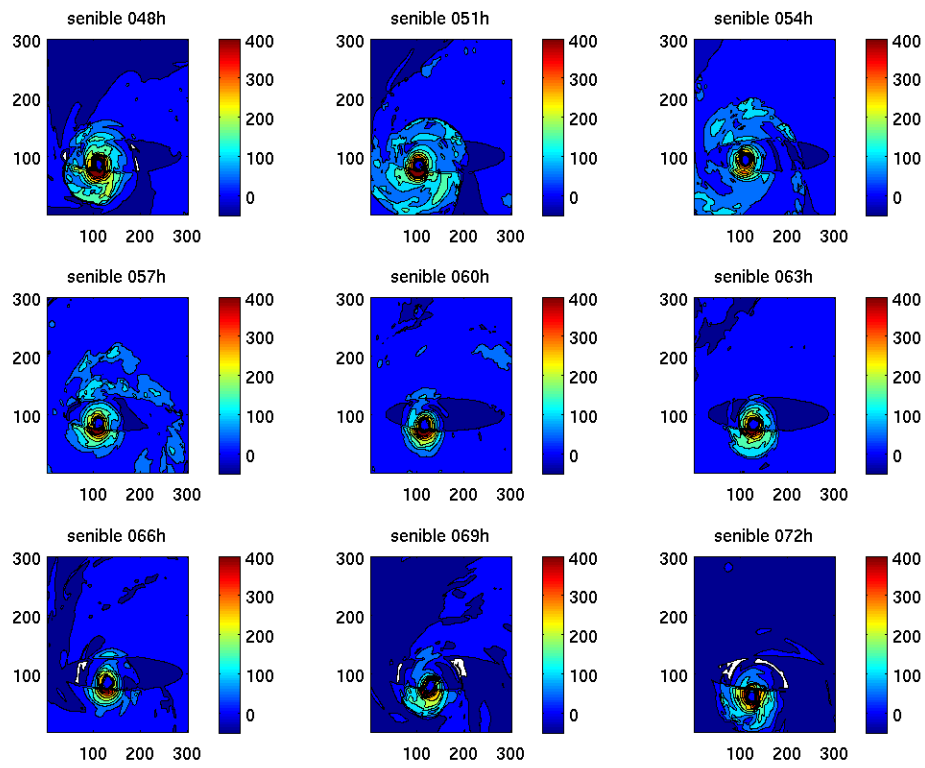


Figure 62. As in Figure 61, except for the sensible heat flux from -50 to 400 Wm^{-2} . The contour interval is every 50 Wm^{-2} .

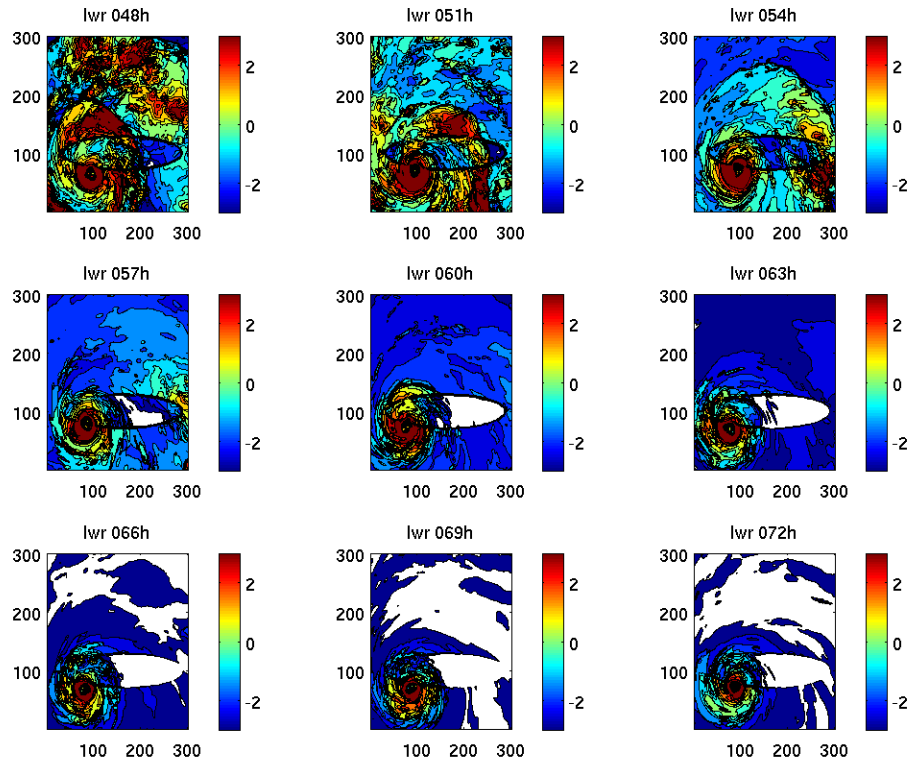


Figure 63. As in Figure 61, except for the long wave fluxes averaged over the lowest 500 m. The contour interval is every 0.5 Wm^{-2} .

These trajectories suggest as air parcels at outer radii travel over the cold wake region they experience an ascent, and this increased ascent is more pronounced at night time as the ACP above the cold wake continues to build as a result of increased negative sensible heat (Figure 62) and long wave fluxes (Figure 63) at night time. The outward propagating rainbands are also contributing to an increased strength of the ACP which then tends to offset the sensible and longwave fluxes that weaken the ACP. The evaporative cooling of the lower boundary layer from the rainbands reduces the air-sea temperature difference. In the rainband region, the long wave fluxes are positive due to increased moisture.

Another notable feature of the outer radii trajectories is an increase of inflow angle with trajectory travel time as the air parcels move over the cold wake region, which leads to a backing of the wind with height. In summary, there is a dynamical response to the thermodynamic forcing of the cold wake in the form of increasing wind speed over the wake, and especially at night time. Associated with this increased wind speed over the wake is an increased transport of moisture to the mid-levels just outside the eyewall region.

D. ANALYSIS OF MOMENTUM BUDGET

1. A Thought Experiment

The dynamic influence of the cold wake in the wake 3 experiment is diagnosed from an analysis of the momentum budget. To the first approximation, the momentum equation far outside the maximum wind radius and above the boundary layer is in gradient wind balance. However, in the planetary boundary layer the turbulent flux term is of the same order of magnitude as the other terms and cannot be neglected. In such a case, the momentum equation for the quasi-balanced radial wind component is:

$$fv_{rad} + \frac{v^2}{r} = \frac{\partial \phi}{\partial r} - \frac{\overline{\partial v'w'}}{\partial z} \quad (6)$$

where f is the Coriolis, v is the tangential wind speed, v_{rad} is the radial wind speed, r is

the distance to the center of the TC, $\frac{\partial \phi}{\partial r}$ is the pressure gradient force, ϕ is the

geopotential, and $\frac{\overline{\partial v'w'}}{\partial z}$ is the momentum vertical flux divergence. In this equation, the

horizontal turbulent momentum flux and the molecular viscosity are ignored. Thus it is a four-way balance among the Coriolis force, the centrifugal force, the pressure gradient force, and the turbulent momentum flux divergence.

In the model, the turbulent momentum flux is traditionally approximated as an eddy viscosity coefficient times the local vertical gradient of the mean wind such that the turbulent eddies act in a manner similar to molecular diffusion. Using the K and mixing length theories, the turbulent momentum flux in (5.1) is written as:

$$\frac{\partial \overline{v'w'}}{\partial z} = \frac{\partial}{\partial z} \left(-K_m \frac{\partial \bar{v}}{\partial z} \right) = \frac{\partial}{\partial z} \left(-l^2 \left| \frac{\partial \bar{v}}{\partial z} \right| \right) \quad (7)$$

where K_m is the eddy viscosity and l is the mixing length. The mixing length is typically empirically defined in the TC model and the magnitude of the turbulent momentum flux within the planetary boundary varies widely among different PBL schemes. However, the objective here is to understand the magnitude of the momentum flux term within our idealized TC cases and how that term may modulate the gradient wind balance in the presence of the cold wake. The variability of the momentum flux divergence will not be addressed in this study.

O'Neill (2010a, 2010b, 2012a, 2012b) recently confirmed the wind-SST coupling by using satellite and buoy observations. Numerical experiments by Spall (2007) suggested that a change in wind speed and direction across an idealized linear SST front is required to balance the Coriolis force due to the sudden change in turbulent mixing and because the boundary layer height of the flow is changed as it crosses the SST front. In Spall's simple SST front simulation, the changes in the pressure gradient term in the momentum equation for this condition are neglected because the adjustment time scale is much smaller than the time scale over which the pressure gradient can act on the flow. Spall (2007) found that winds blowing from warm to cold water tend to slow down and turn toward the lower background pressure gradient along the SST front, which leads to an acceleration of the wind speed. However, winds blowing from cold to warm water tend to first accelerate along the SST front, but then turn toward the higher background pressure gradient and thus decelerate. Therefore, the zonal and meridional wind changes forced by the SST front set up surface convergence and divergence regions downwind

from the front, which in turn induces a secondary circulation above the boundary layer due to thermal wind balance.

In the rotating TC fluid, the balance is different from the straight SST front problem discussed by Spall (2007). Inserting Eq. (7) into Eq. (6), results in the nonlinear balance Eq. (8) in which the change of flux divergence (term 4) must be offset by a change of either pressure gradient (term 3), Coriolis force (term 1), or centrifugal force (term 2):

$$f v_{rad} + \frac{v^2}{r} = \frac{\partial \phi}{\partial r} - \frac{\partial}{\partial z} \left(l^2 \left| \frac{\partial v}{\partial z} \right| \right) \quad (8)$$

Based on the argument of gradient wind balance at larger radii in the TC, the thought experiment for the interaction of the TC winds with the cold wake would indicate that as winds flow from the warm sector to the cold wake, the reduction of tangential wind and turbulent fluxes are balanced by increasing pressure gradient and/or Coriolis force. That is, either an increase of Coriolis force (increased radial wind toward the low center) or pressure gradient is required to balance the decrease in centrifugal force (decreased tangential wind) and momentum flux. It is also probable that both the pressure gradient force and Coriolis force increase to offset this reduction.

In the eyewall region the gradient wind balance is replaced by cyclostrophic balance, due to strong inertial motion, and the Coriolis force is neglected. Thus, the balance is between the pressure gradient force, the centrifugal force, and the momentum flux term. If the centrifugal force and momentum flux are reduced over the cold wake, the cyclostrophic balance implies an increased pressure gradient force over the wake (pressure is higher over the wake). Therefore in both the inner core and outer radii, the pressure gradient over the wake has to increase to satisfy the cyclostrophic and the gradient balance equations, respectively.

2. COAMPS Wake 3 Momentum Budget Analysis

To test the hypothesis that a low-level elevated wake jet will be generated in response of the change of flux divergence term to satisfy the gradient balance as the air flows across the cold wake SST gradient, the momentum budget is performed for the wake 3 experiment, which has a long trailing wake. In COAMPS, the horizontal momentum budget in Cartesian coordinate are expressed as the sum of the local change, geostrophic forcing that is related to the horizontal pressure gradient, damping, horizontal advection, vertical advection, Coriolis, vertical mixing, and horizontal diffusion. The momentum budget terms are transformed to cylindrical coordinate for the momentum budget analysis.

Vertical profiles of the radial wind budgets upwind, over, and downwind of the wake at the radial distance of 150 km are shown in Figure 64. The negative total tendency of the radial wind (yellow) over the wake between 500 m – 1000 m elevation is contributed by the pressure gradient (magenta), vertical advection (red), and vertical mixing (cyan). There is a decrease of the radial inflow from the vertical mixing over the wake compare to the locations upwind and downwind from the wake. The change from the vertical advection term (red) from small to large and to very small across the wake is also evident. The contribution from the Coriolis (blue) is small for all three locations.

The tangential wind budgets have larger negative tendencies than for the radial wind. The terms with the largest contribution to this spin down of the tangential wind upwind from the wake are the horizontal and vertical advection. Over the wake, the decrease of tangential wind tendency is from the vertical advection and pressure gradient. Downwind of the wake, the horizontal advection, Coriolis, and pressure gradient terms all contribute to a decrease in the tangential wind speed.

At outer radii over the wake above 300 m, most terms in these budget analyses except the Coriolis contribute to an increase of the negative radial wind inflow tendency (Figure 64b). The vertical advection and horizontal pressure gradient (geostrophic) are the two largest terms over the wake. The increased radial wind tendency is well correlated with the horizontal advection term upwind (Figure 64a) and downwind (Figure

64c) from the wake above the warmer ocean. In the tangential wind budget (Figure 65) the total tangential wind tendency above 300 m follows the horizontal advection term as well. Over the wake (Figure 65b), increasingly low-level tangential wind tendency below 250 m is not simulated at upwind (Figure 65a) and downwind (Figure 65c) warmer ocean locations, where the tangential wind is reduced (negative tendency) throughout the vertical column above 1 km height.

(a)

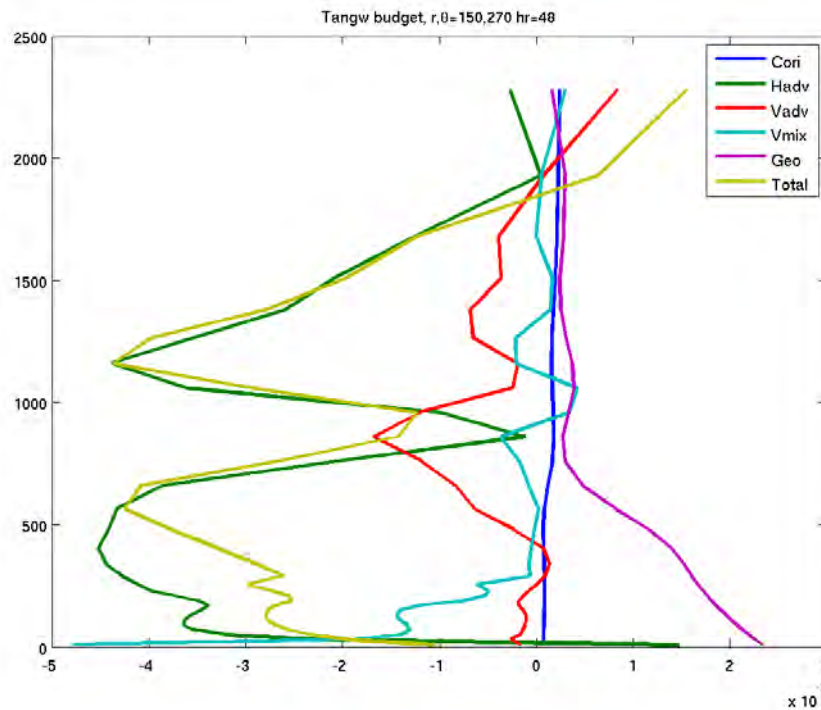
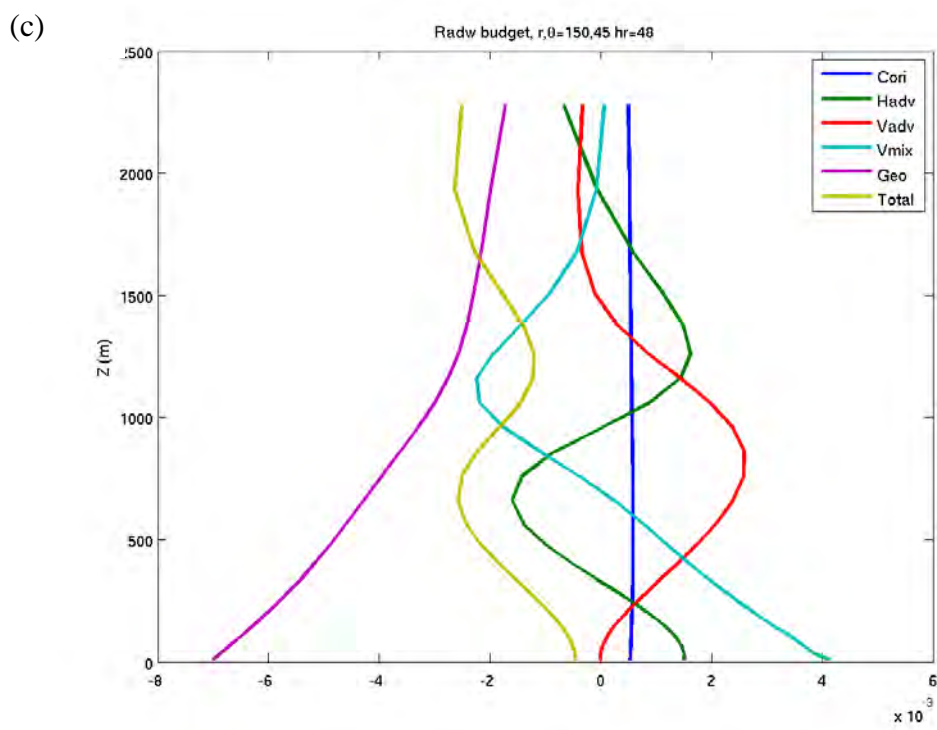
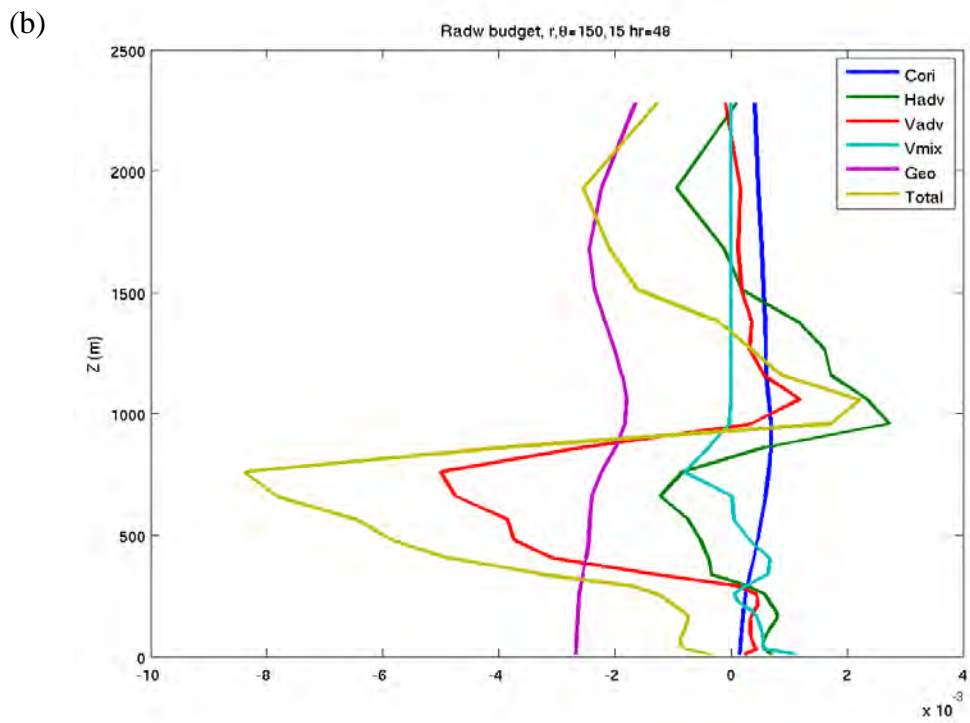
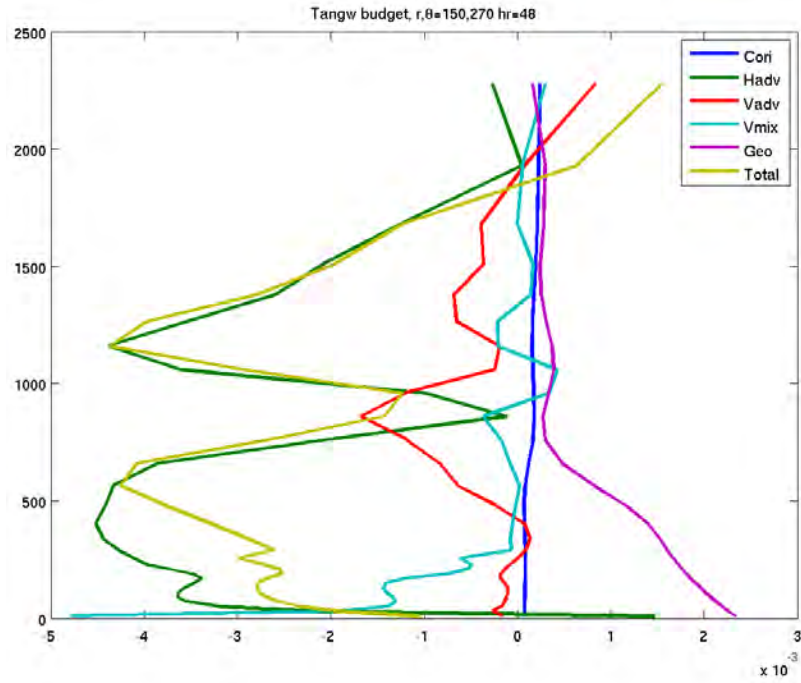


Figure 64. Wake 3 experiment 48 h radial wind (ms^{-1}) budgets (a) upwind, (b) over, and (c) downwind from the cold wake at a radius 150 km from the eye. The budget terms are the total tendency (yellow), pressure gradient (magenta), horizontal advection (green), vertical advection (red), and Coriolis (blue), and vertical mixing (cyan).



(Figure 64 continued)

(a)



(b)

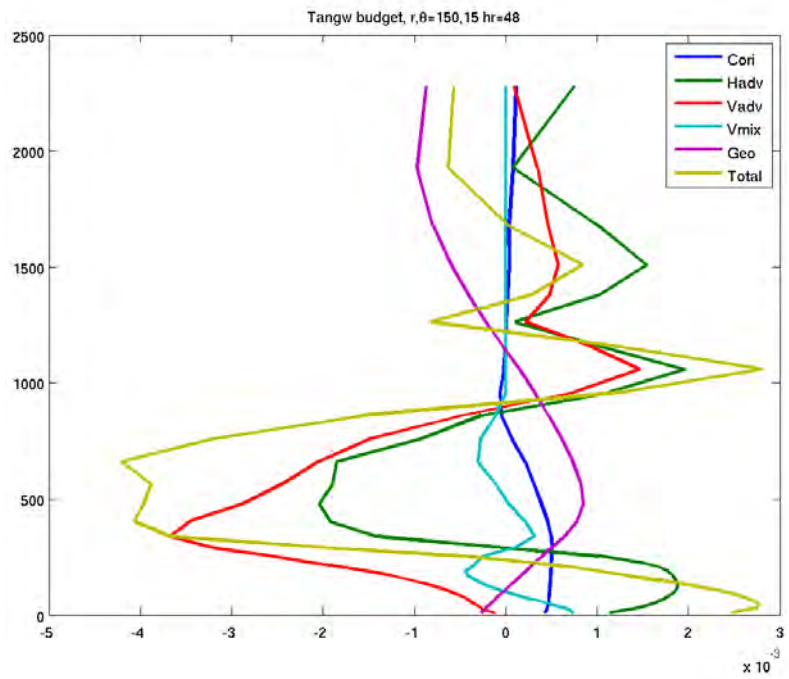
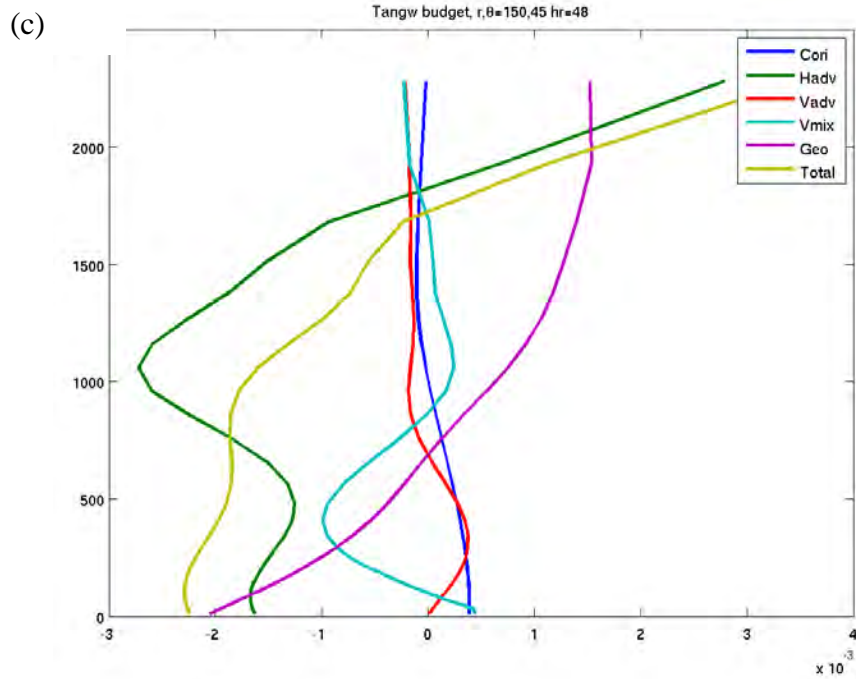


Figure 65. As in Figure 64, except for the tangential wind budget.



(Figure 65 continued)

The momentum budgets at 48 h (Figure 66 and 67) at 30 km from the eye are quite different from the budget at 150 km. Over and downwind from the wake, the radial inflow tendency is close to zero (Figure 66) as the pressure term is balanced by the vertical mixing and horizontal advection. At the location upwind from the wake, the pressure and vertical mixing terms contributed positively to the inflow below 1 km. The net tendency for the tangential wind (Figure 67) is negative near the eyewall. Since the wake covers the entire region at 30 km radius, the vertical mixing term is negative. The vertical advection and Coriolis terms are small compared to horizontal advection, mixing, and the pressure gradient terms. The horizontal pressure gradient has a positive contribution to the tangential wind budget over and downwind from the wake, but the net tangential wind tendency is negative owing to a large negative horizontal advection term contribution.

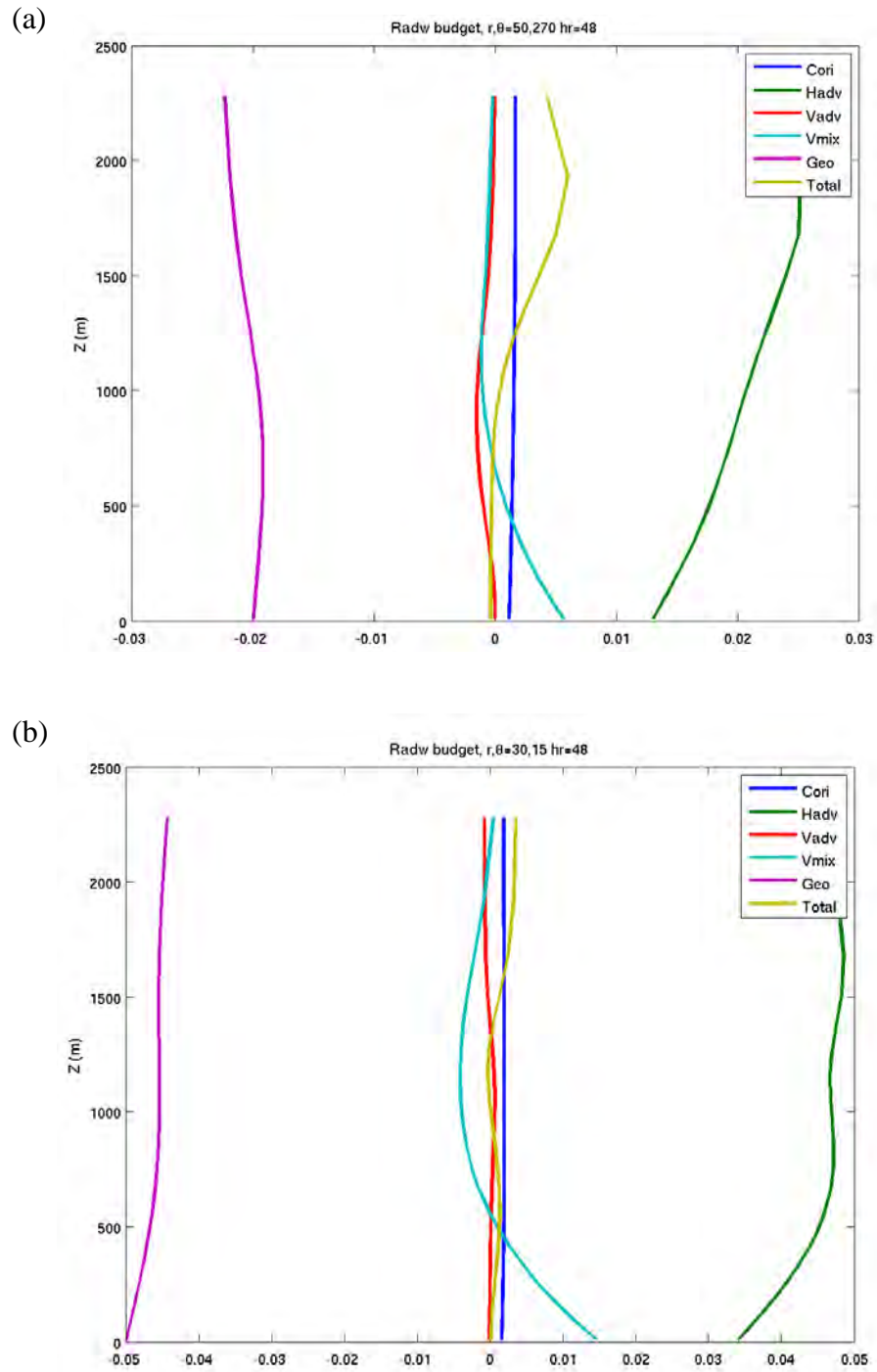
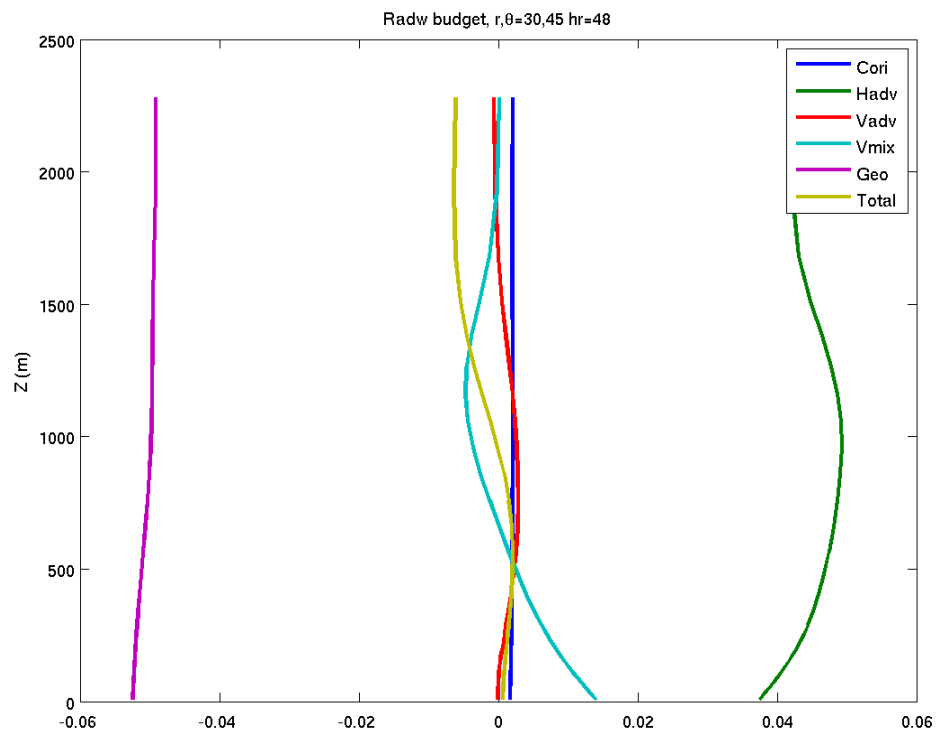


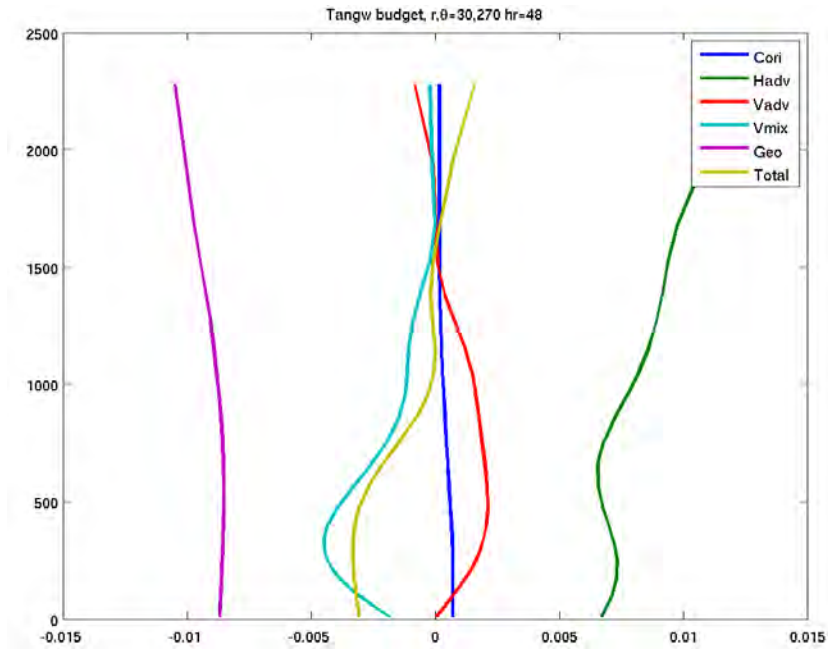
Figure 66. As in Figure 64, except for the radial wind budget at 30 km from the eye.

(c)



(Figure 66 continued)

(a)



(b)

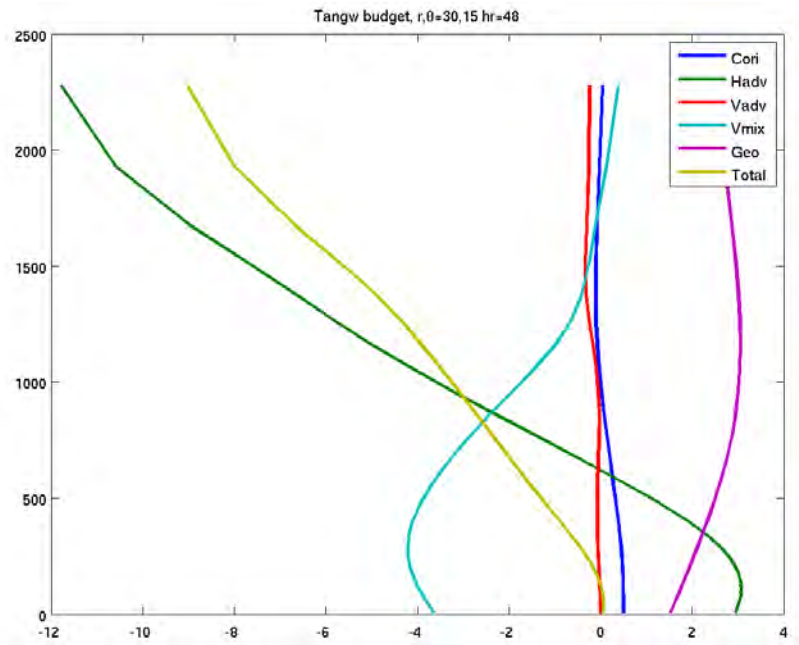
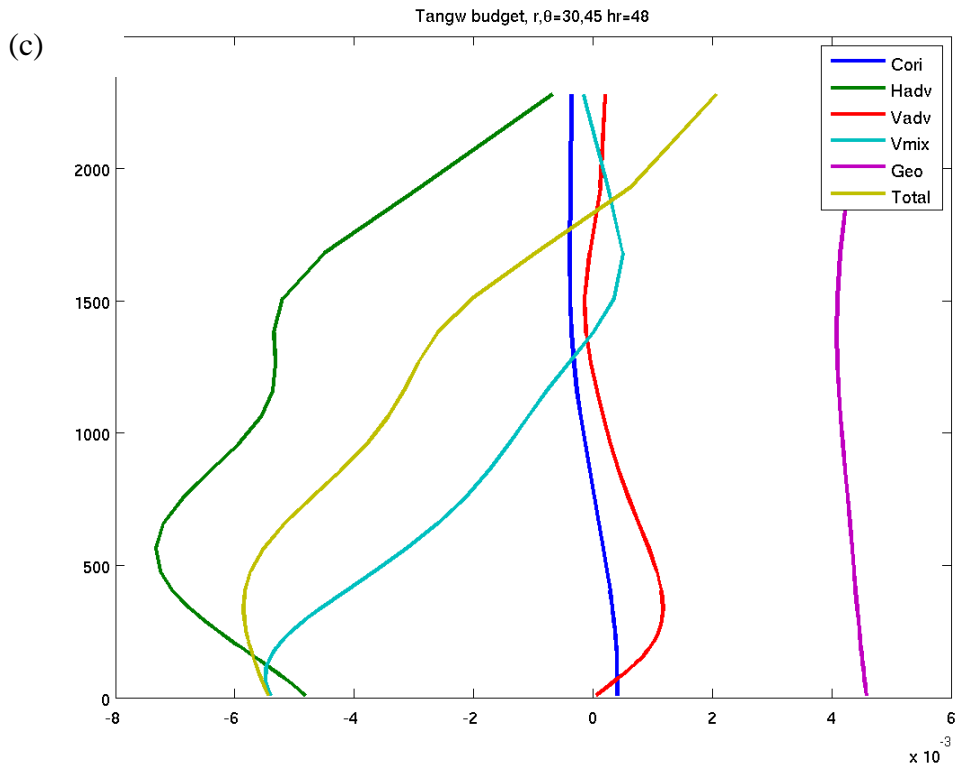


Figure 67. As in Figure 66, except for the tangential wind budget at 30 km from the eye.



(Figure 67 continued)

A similar radial and tangential wind momentum budget analysis is now performed following the trajectory 10 (TJ10) released at 48 h. As TJ10 passes across the wake, the increase of radial inflow tendency is attributed to a large vertical advection term at the leading edge of the wake (Figure 68a). This vertical advection is roughly balanced by the horizontal advection and pressure gradient of the opposite sign, and thus there is only a small increase of the radial inflow tendency. Over the center of the wake, the pressure gradient and vertical mixing terms have a positive contribution to the radial inflow tendency, while the horizontal advection is balanced by the vertical advection, and the contribution from the Coriolis is close to zero. The tangential wind budget (Figure 68b) shows the increased negative tangential wind tendency over the wake below 250 m is mostly due to the horizontal advection and pressure gradient contributions.

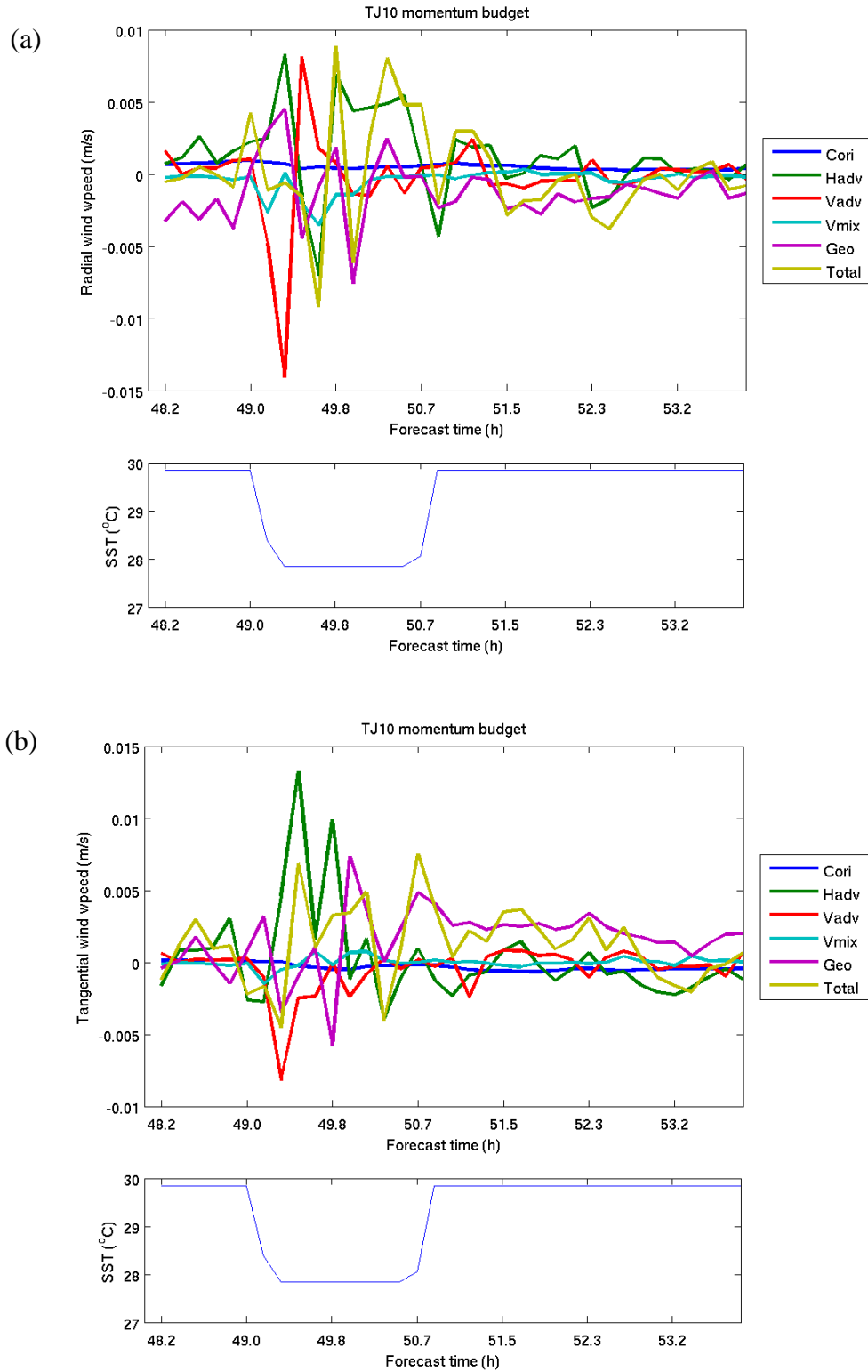


Figure 68. (a) Radial wind and (b) tangential wind budgets following trajectory 10 air parcel across the cold wake.

In summary, the analyses of the momentum budget suggest there is a distinctive dynamic flow response as air parcels at outer radii passes through the long ocean cold wake region. Over the wake, both the horizontal and vertical advection terms are large, but they have an opposite signs. The three largest terms contributing to an increase of radial inflow are the horizontal advection, pressure gradient, and vertical mixing, while the Coriolis term is small. Thus, the reduction of the turbulence flux as air parcels pass through the cold wake induce an increase of the radial wind tendency through adjustment of the pressure gradient and horizontal advection. This increased low-level radial inflow in conjunction with weak moist ascent therefore increases the moisture transport into the eyewall region, which can sustain the deep convection. Thus, the dynamic response leading to the wake jet in the long trailing wake 3 experiment tends to offset the expected thermodynamic response of a TC intensity decrease from the SST decreases below the eye.

3. Analysis of Surface Fluxes

The primary thermodynamic factor that impacts the TC intensity from the wake cooling is the reduction of the enthalpy flux transport from the ocean. The 36 h - 72 h surface fluxes averaged over the region within five RMW from the one-way coupled wake 1 - wake 5 experiments have sensible (latent heat) fluxes that vary from 7510 (88168) to 17065 (137960) Wm^{-2} compared to the control simulation (Figure 69). The reductions of enthalpy fluxes for all five wake experiments range from 30%-60% in the first 12 h (36 h – 48 h) after the coupling with the ocean begins. The two long trailing wake 3 and wake 4 experiments have the smallest (~30-40%) enthalpy flux reduction during this time period.

To relate the TC intensity change to the enthalpy flux, the mean potential vorticity, maximum tangential wind, and the enthalpy flux in the lowest 2 km are normalized by the 36 h control values of the same variables. The day time and night time normalized intensity and averaged enthalpy fluxes within 5 RMW between 36 h – 72 h are compared in Figure 70. Given the same normalized enthalpy flux of 0.5 from the ocean, the intensities of these one-way coupled wake experiments varied widely. The range of normalized mean potential vorticity (maximum tangential wind) is about 0.4-2.0 (0.8-1.7).

The irregularly shaped wakes 2, 3, and 4 tend to be associated with higher intensities than do wake 1 and wake 5. The relationship between a fixed storm enthalpy flux and intensity change due to the five cold wakes seems to indicate that other factors than the enthalpy flux averaged over 5 RMW may also play a role in the intensity modulation. As for the diurnal influence on the normalized intensity, the intensity is slightly higher during the day time (Figure 70 a and c) versus during the night time (Figure 70 b and d), which is attributed to the interaction of TC circulation and clouds with radiation. The normalized intensity does have a better relationship with the normalized enthalpy flux averaged within one RMW (Figure 72). Thus for these one-way coupled with TC experiments the intensity reduction over the cold wake is indeed strongly related to the amount of enthalpy flux in the inner-core region.

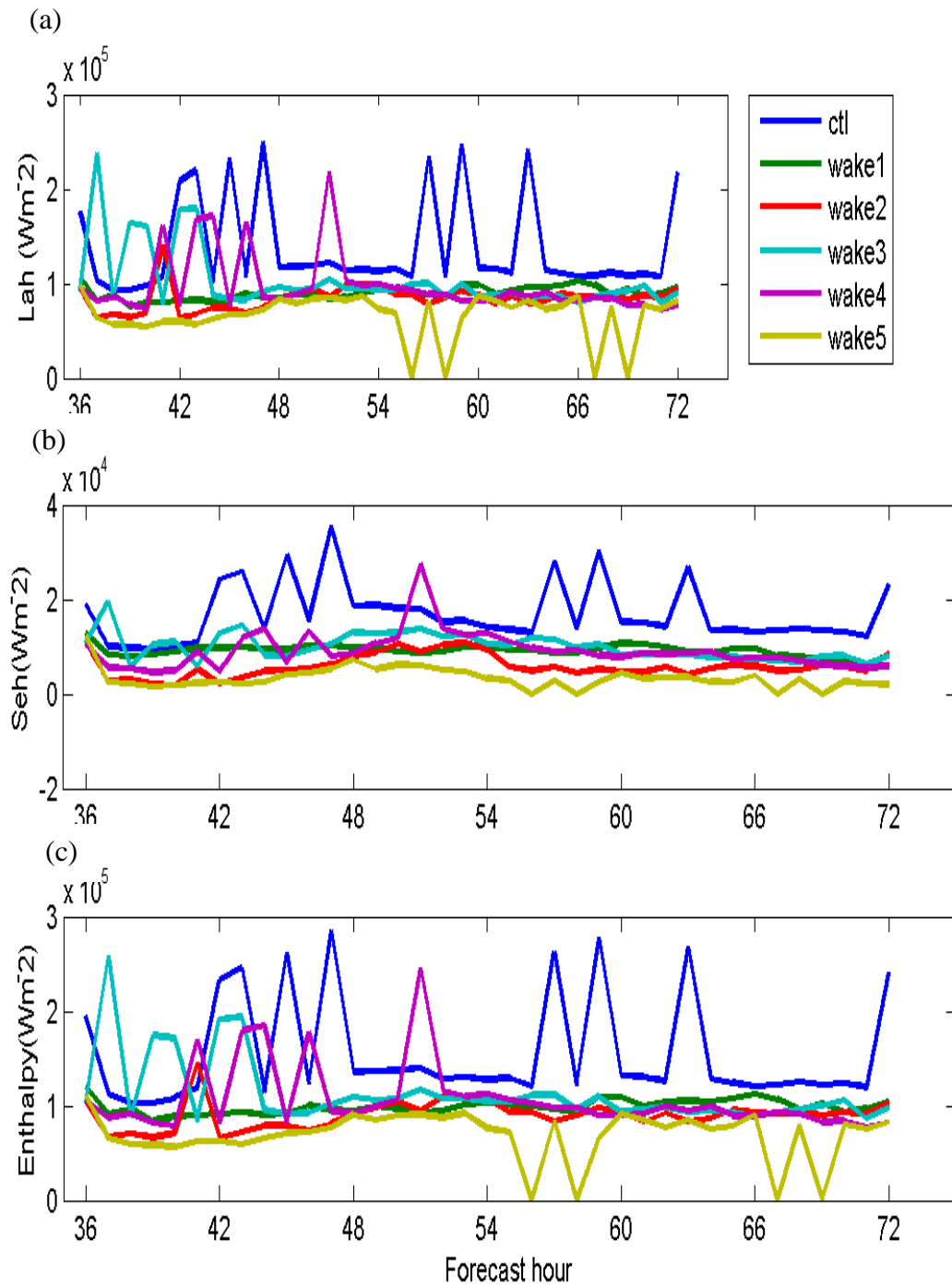


Figure 69. Azimuthal-mean (a) latent heat flux, (b) sensible heat flux, and (c) total enthalpy flux averaged within five RMW for the control and the five one-way coupled wake experiments (see inset). The unit for the fluxes is 10^5 Wm^{-2} for (a) and (c), but 10^4 Wm^{-2} for (b).

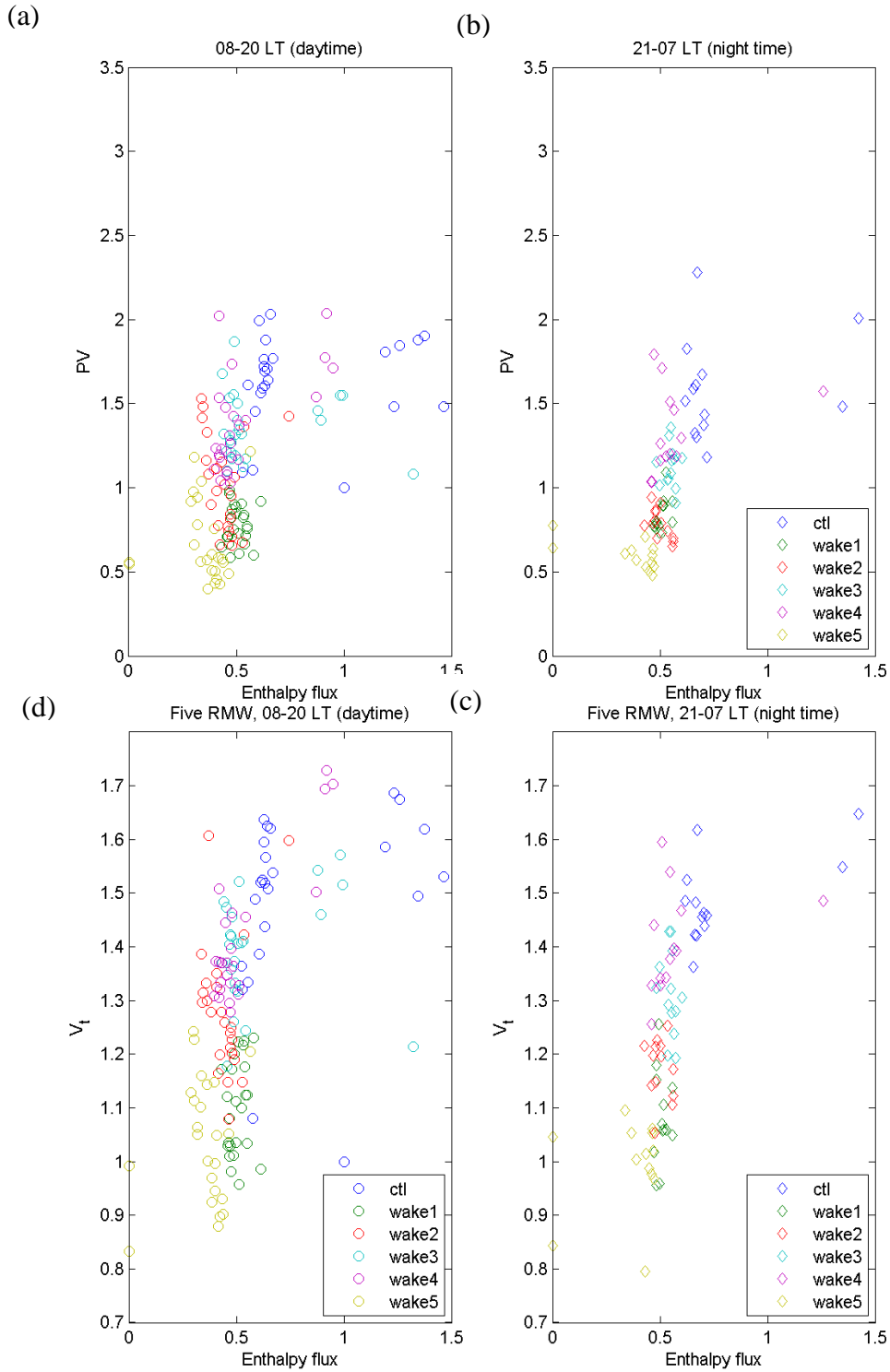


Figure 70. Scatter plots of (a) day time and (b) nighttime normalized potential vorticities, (c) day time and (d) night time normalized maximum tangential wind speeds in the lowest 2 km versus normalized enthalpy flux averaged within 5 RMW. The symbol colors (see insets) indicate the one-way coupled wake experiments and the control (ctl) simulation.

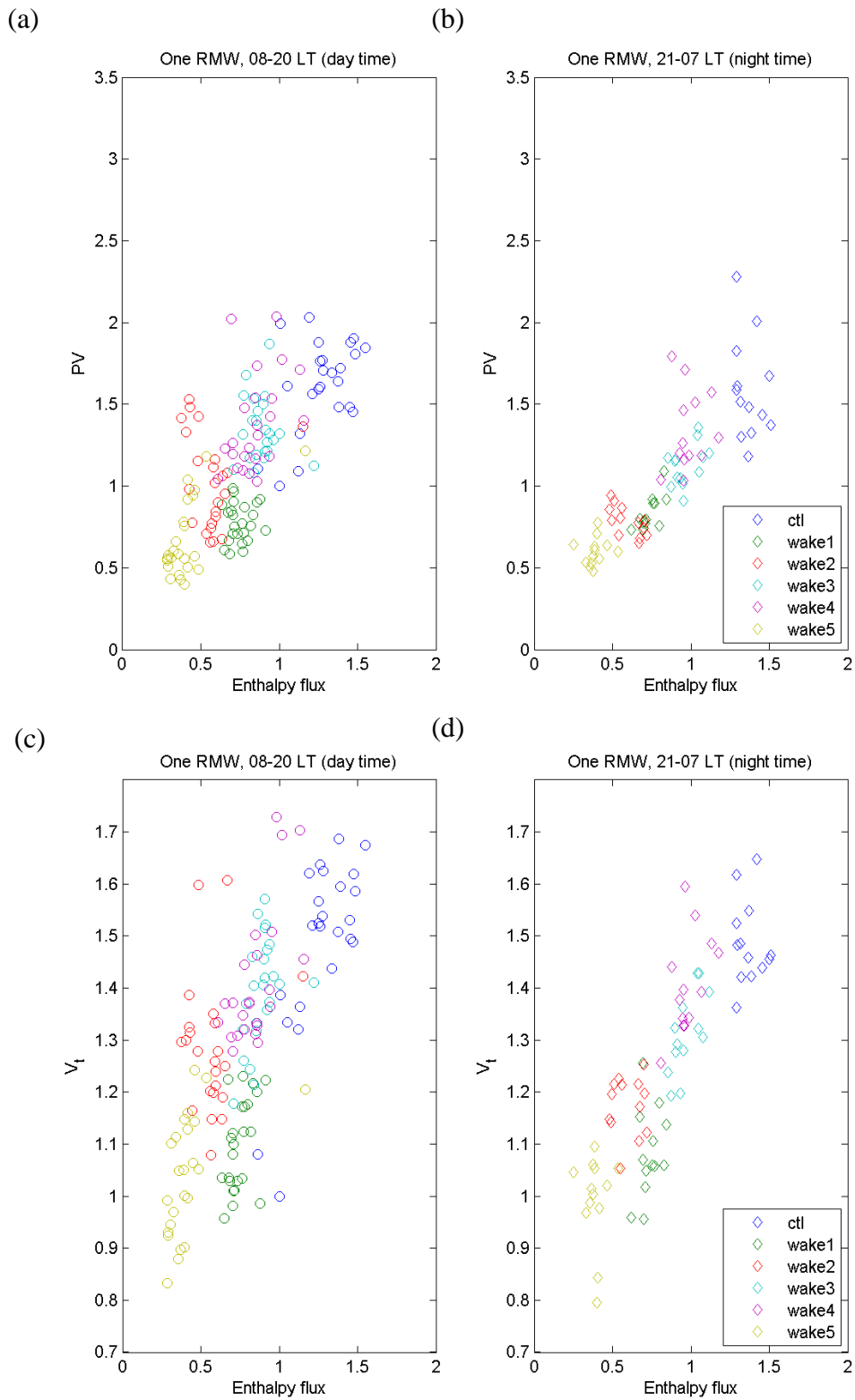


Figure 71. As in Figure 70, except for averaged within one RMW.

THIS PAGE INTENTIONALLY LEFT BLANK

VI. TWO-WAY AIR-OCEAN COUPLED SIMULATIONS

To investigate how the two-way air-ocean coupling response differs from the one-way coupled response simulated in Chapter V, hypotheses I-III are re-examined using a two-way air-ocean coupled framework. Two sets of two-way coupled experiments are conducted with a 5 m s^{-1} (hereafter referred to as EXPA) and a 2 m s^{-1} (hereafter referred to as EXPB) westward TC translation speed. The horizontal resolutions of the two atmospheric domains for these coupled experiments are 9 km and 3 km, while the horizontal resolution of the ocean domain is 3 km. The 3 km domain covers an area of $\sim 2200 \times 2200 \text{ km}^2$. The initial atmospheric temperature and moisture profiles of the coupled experiments are identical to the one-way control simulations described in Chapter III except there is a vertically uniform background easterly wind to move the model-simulated TC toward the west. The ocean is at rest initially using the mean Typhoon Fanapi pre-storm temperature and salinity profiles described in Chapter III (Figure 15).

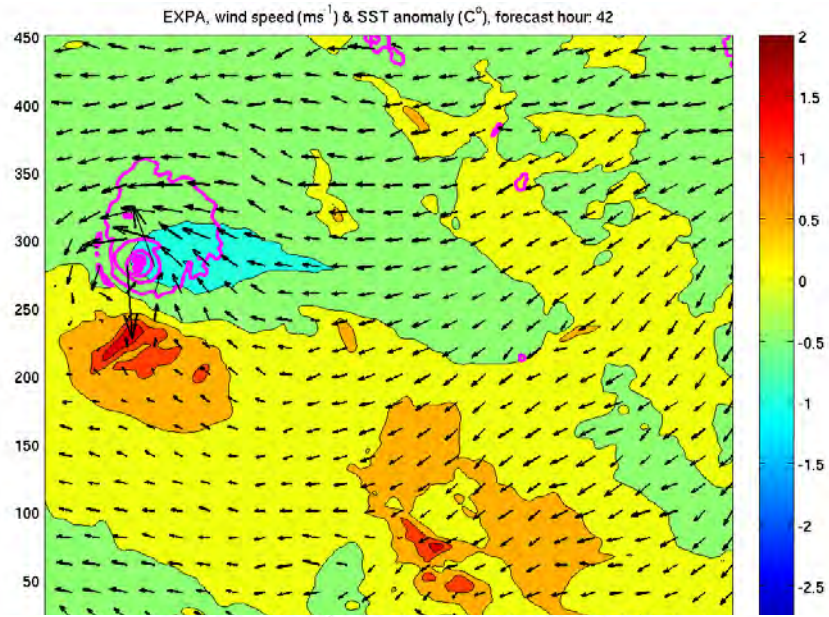
The model is first integrated for 36 h without the air-ocean coupling, which allows for a trailing ocean cold wake to develop in the rear-right quadrant along the model-simulated TC track. After 36 h, the two-way coupling is turned on with a coupling interval of every 6 min. Since the ocean feedback to the atmosphere interaction is not turned on until 36 h, this procedure allows the spin-up of the model-simulated TC to CAT3 intensity without the influence of the cold ocean wake. Two similar experiments as in EXPA and EXPB but using a fixed SST of 303°K (hereafter referred to as uncoupled uncEXPA and uncEXPB) are integrated to illustrate the differences between TCs in coupled and uncoupled simulations.

A. COMPARISON OF COUPLED AND UNCOUPLED SIMULATIONS

Comparisons of cold wakes forced by EXPA and EXPB at 42 h are shown in Figure 72. At this time, the SST anomalies within the radius of maximum wind from these two simulations are about -1.1°C and -2.4°C , respectively. At the end of 72 h forecast (not shown), EXPB has a cold anomaly of -3.7°C . The magnitudes of the EXPB

cold anomalies are similar to the one-way coupled wake 3 and wake 4 experiments discussed in Chapter V. The magnitudes of the cold anomalies in the coupled experiments are influenced by the TC translation speed, stability of the initial ocean profile, and mixed layer depth. The EXPA experiment has a much longer trailing cold wake due to a faster background wind speed (5 m s^{-1}) than EXPB (2 m s^{-1}) experiment. As a result, cooling beneath the eyewall and the trailing cold wake in the EXPA experiment are smaller compared to EXPB experiment. These simulations are consistent with the early TC cold wake studies by Chang and Anthes (1978) and Price (1981), and illustrate again that the TC translation speed is one of the major factors that control the size and location of the trailing cold wake with respect to the TC track given the same upper-ocean density profile.

(a)



(b)

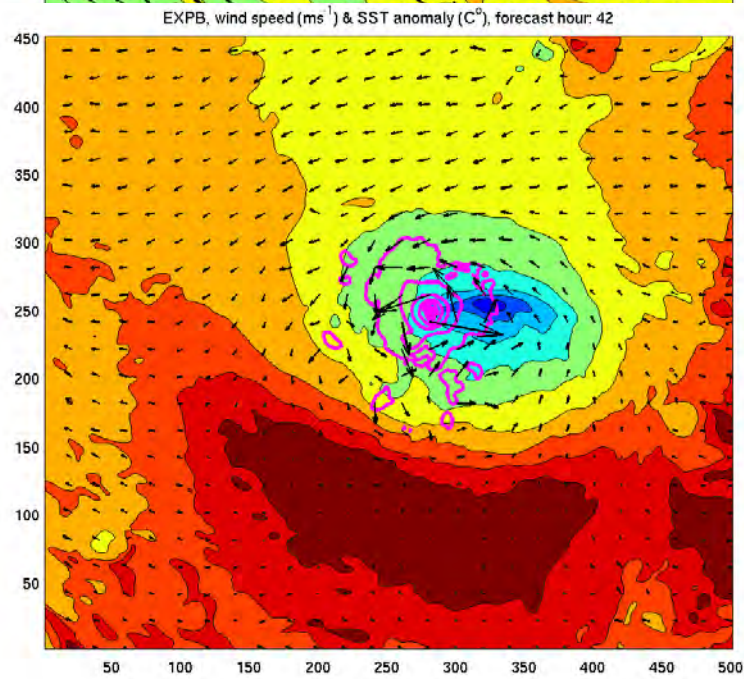


Figure 72. Sea-surface temperature anomaly ($^{\circ}\text{C}$, color shading bar on right) and 10 m wind speeds (m s^{-1} , magenta contours) from (a) EXPA and (b) EXPB simulation after 42 h. The contour interval for the SST anomaly is 0.5°C and for wind speed is 5 m s^{-1} . The 10 m wind vectors are plotted every 20 grid points.

As in the one-way coupled experiments in Chapter V, more wake cooling under the eyewall results in a weaker intensity in the coupled experiments (Figure 73). The maximum 10 m wind speeds from EXPA, EXPB, uncEXPA, and uncEXPB simulations are 68.2, 63.6, 65.6, and 73 m s⁻¹, respectively. The steep decrease in maximum wind speed in the EXPA and uncEXPA simulations after 62 h is due to the model-simulated TC moving out of the western boundary of grid 2 domain. Interestingly the intensity for the coupled EXPA is higher than for the corresponding uncoupled uncEXPA, while the intensity in EXPB is lower than in the uncoupled uncEXPB, but the intensity decrease is delayed by almost 12 h after the simulated TC experienced the cold wake at 36 h. The size and magnitude of the cold wake in EXPB are close to the one-way coupled wake 3 and wake 4 experiments. Those wake 3 and wake 4 experiments had a 2 °C cold anomaly and there was a 14 h time delay of the intensity decrease in those two simulations (see Chapter V section A).

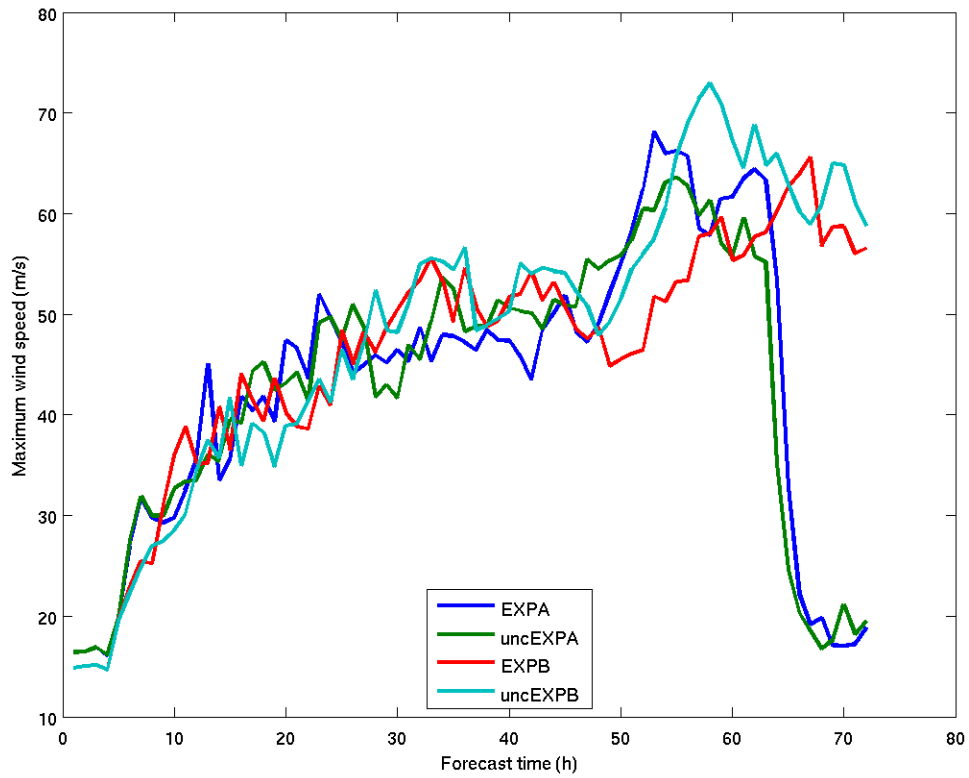


Figure 73. Time series of the maximum wind speeds (m s^{-1}) from the coupled EXPA and EXPB and the uncoupled uncEXPA and uncEXPB experiments (see inset). The coupling with the ocean in EXPA and EXPB starts at 36 h.

These two-way coupled versus uncoupled intensity comparisons are similar to the one-way coupled versus uncoupled experiment previously discussed in Chapter V. Note that the intensity changes in the two-way coupled experiments are the cumulative effect of the cold ocean interaction with its TC, which includes the nonlinear interaction of the two-way coupling with the model physics. These two-way coupled responses agree with the one-way coupled experiments in that the magnitudes of cooling underneath the eyewall and the aspect ratios of the trailing cold wake play a role in modulating the TC intensity. The sensitivity of the TC intensity to the aspect ratio of the cold wake has not been previously discussed in the literature.

The asymmetric response of the two-way coupled TC to the cold wake forcing is displayed in plan views of the 850 hPa vorticity (red) superposed with 400 hPa (blue) vorticity for the EXPA and EXPB experiments (Figure 74). In both the EXPA and EXPB experiments, an outward expansion of the 400 hPa vorticity bands is simulated. Note also that the 400 hPa vorticity bands in EXPB are one order of magnitude weaker than the one-way coupled wake 3 and wake 4 experiments (Figure 18). This is because the maximum intensity of the EXPB experiment is less than in wake 3 and wake 4 experiments.

The vertical tilt of the vortex defined by the displacements of the 850 hPa and 400 hPa vorticity centers in EXPB is smaller than in EXPA (Figure 75). The increased vortex vertical tilt in EXPA in association with a weaker cooling underneath the eyewall compared to the EXPB experiment is different than the one-way coupled wake experiments. The increased rainband development to the left of the EXPA track in the warmer SST region causes the shift of the 400 hPa vorticity centers toward the south. In both the EXPB and uncEXPB experiments, the low-level vortex defined by the location of the minimum SLP continues to rotate anticlockwise while moving westward until 60 h. When the simulated TC intensity experienced another upward trend of intensity increase between 60 – 66 h, the EXPB minimum SLP centers moved about 30 km due southwestward with little rotation (Figure 76). As in the one-way coupled wake experiments (see Fig. 5.10), the two-way coupled EXPB and uncEXPB simulations have a similar cycloidal path at 850 hPa that rotates anticlockwise with time (Figure 77).

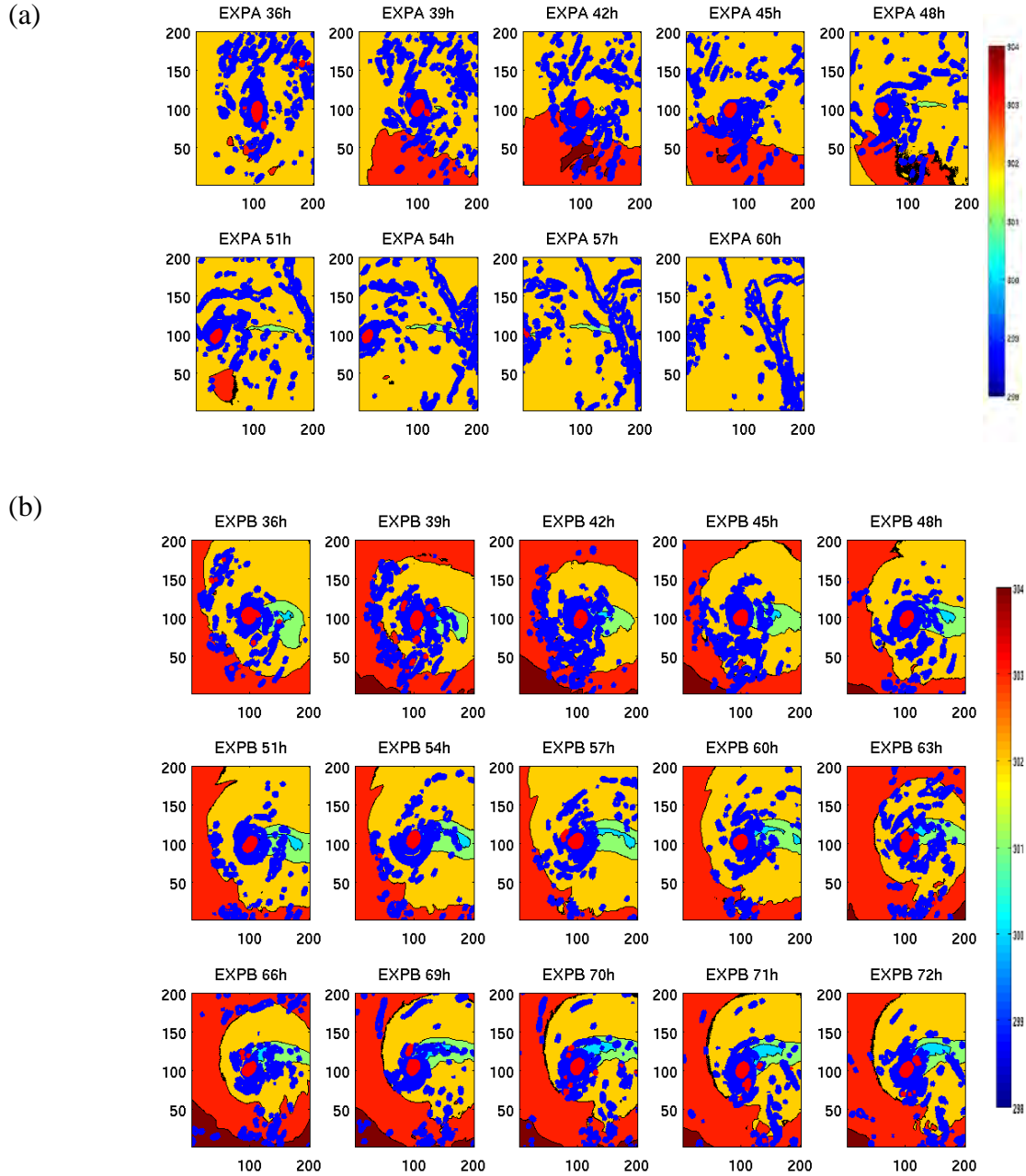


Figure 74. Time evolution at selected times of 850 hPa vorticity (red) exceeding $1 \text{ (} 10^{-3} \text{ s}^{-1} \text{)}$ and 400 hPa vorticity (blue) exceed $1 \text{ (} 10^{-4} \text{ s}^{-1} \text{)}$ from (a) 36 h to 60 h from EXPA experiment and (b) 36 h to 72 h from EXPB experiment. Color shadings indicate the cold wake area with contour interval of $1 \text{ } ^\circ\text{C}$. The domain is re-centered around the TC eye in (a) from 36 h – 42 h and in (b) from 36 h – 72 h.

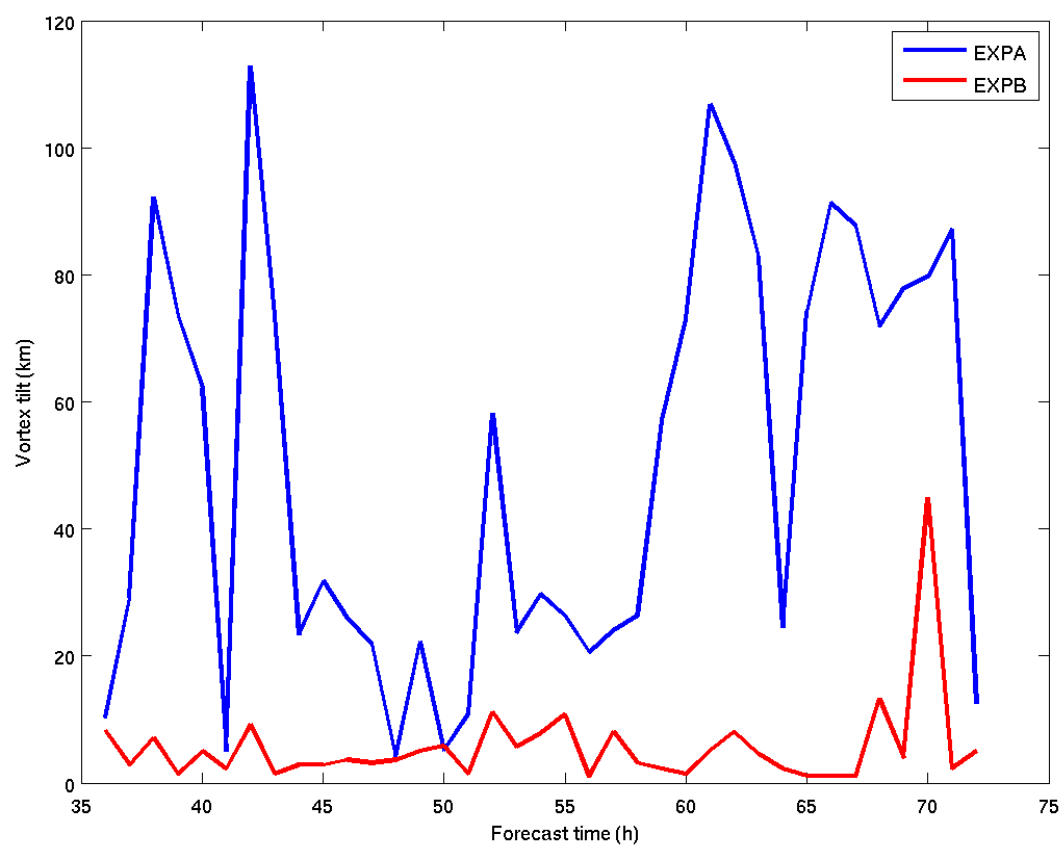
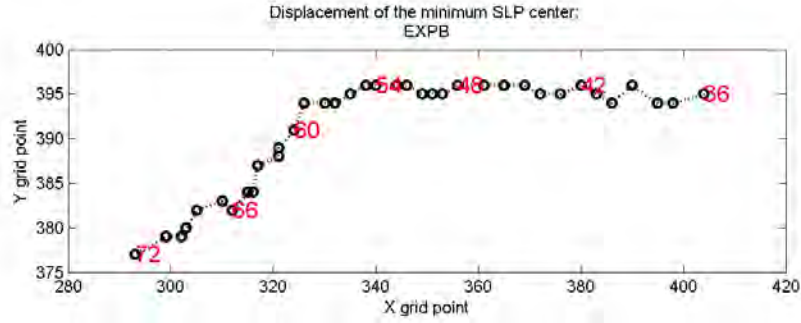


Figure 75. Vertical vortex tilt of the 850 hPa and 400 hPa vortex centers from 36 h to 72 h in EXPA and EXPB experiments (see inset for definition).

(a)



(b)

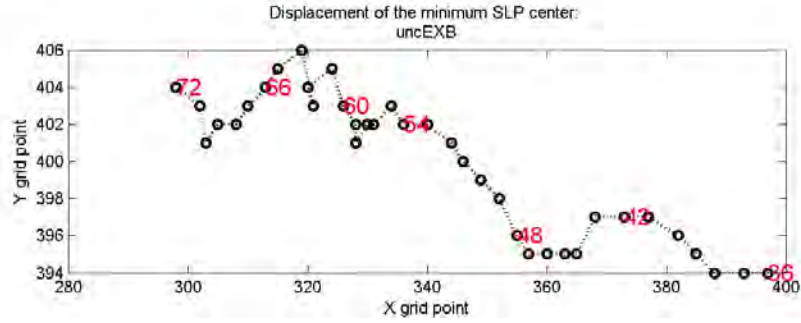
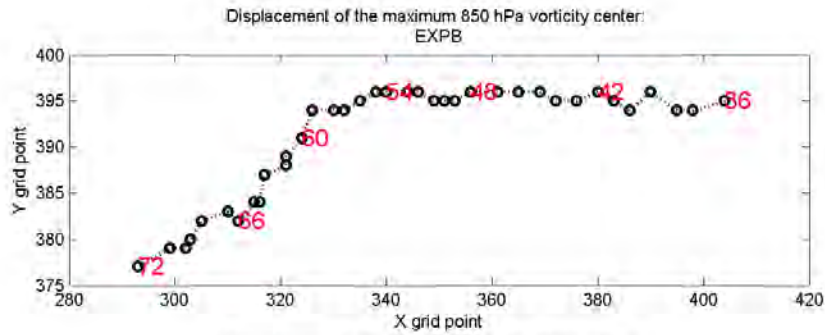


Figure 76. Displacement each hour from 36 h through 72 h of the minimum SLP centers for (a) EXPB and (b) uncEXPB experiments.

(a)



(b)

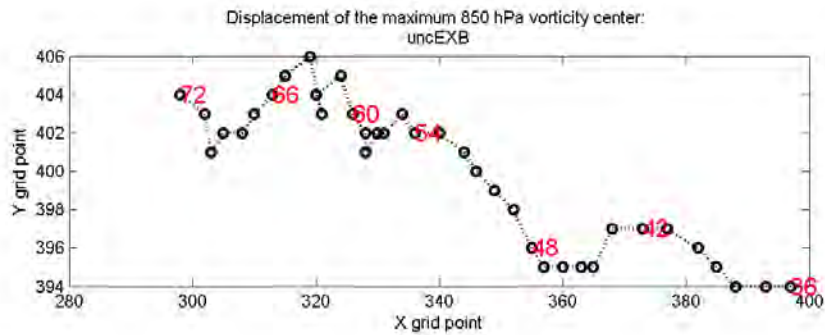


Figure 77. As in Figure 76, except for the 850 hPa maximum vorticity center. Note that the scale on the ordinate is much smaller than on the abscissa.

The 36 h – 60 h azimuthal mean differences of the radial wind speed and water vapor mixing ratio between the two-way coupled simulations and their control uncoupled simulations are shown in Figure 78. Compared to uncEXPA, the azimuthal mean of the radial wind between 36 h - 60 h in the EXPA experiment has an increase of $< 1 \text{ m s}^{-1}$ low-level radial inflow below 1 km height and within 5 RMW (Figure 78a). Outside the 5 RMW, there is a very large area of a small ($< 2 \text{ m s}^{-1}$) increase in the radial wind speed from the surface to up to 10 km height. A moisture increase of less than 2 g kg^{-1} mixing ratio is simulated inside the eyewall up to 10 km height. Outside the eyewall, two regions with moisture increases occurred between 2-15 RMW and 5 – 30 RMW (Figure 78b).

In the stronger wake cooling EXPB experiment, the differences in the radial wind speed and moisture are similar to the EXPA-uncEXPA differences, but with smaller magnitudes. Comparing EXPB with uncEXPB, the increase in the low-level inflow extends to 10 RMW (Figure 78c) and most of the moisture increase occurs above the boundary layer (Figure 78d). The atmospheric responses to the wake cooling in these two-way coupled experiments are similar to the one-way wake experiments. That is, the cold wake induces a broad area of larger moistening above the boundary layer. However, the increase of moisture in the two-way coupled simulation also occurred within the boundary layer. In the two-way coupled EXPB simulation, the increase of low-level radial inflow extended farther out to 10 RMW compared to all of one-way coupled wake experiments. The one-way coupled experiments in Chapter V also had an increased transport of the moisture in the TC boundary layer that may be attributed to the elongated cold wake versus a broader cold wake.

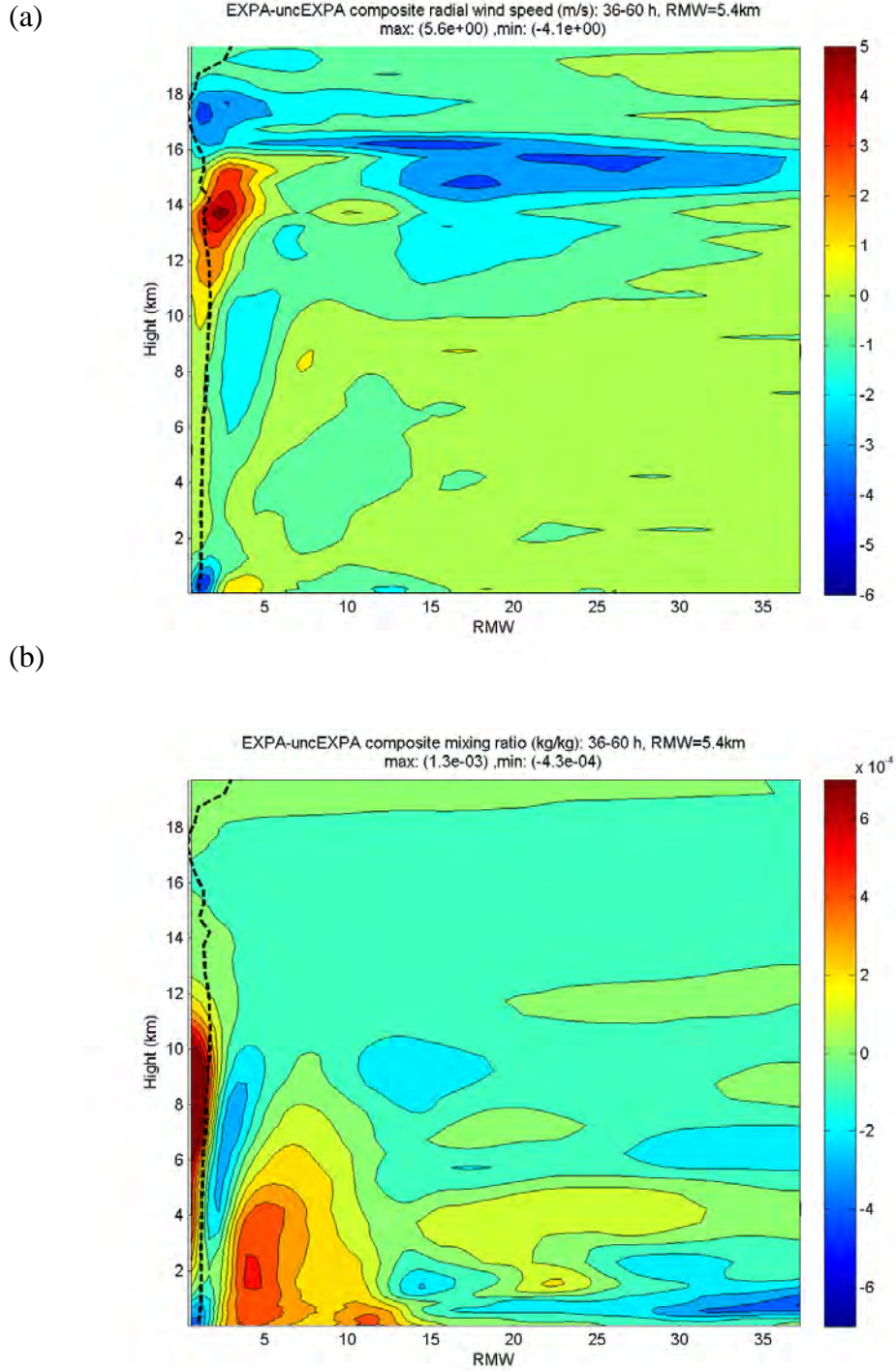
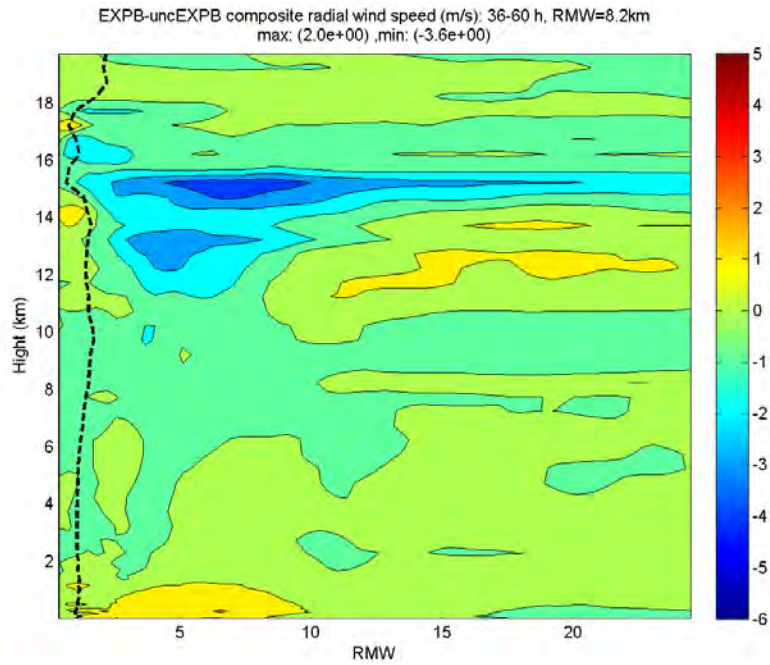
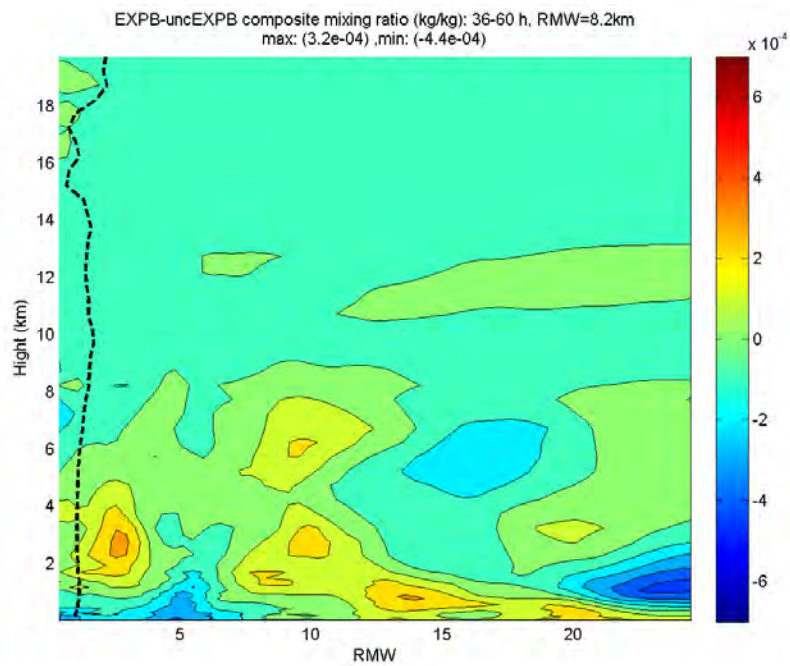


Figure 78. Composite radial wind speed (m s^{-1}) and mixing ratio (kg kg^{-1}) anomalies from EXPA (a and b) and EXPB (c and d). The contour interval is 1 m^{-1} for the wind speed and $0.5 \times 10^{-4} \text{ kg kg}^{-1}$ for the mixing ratio.

(c)



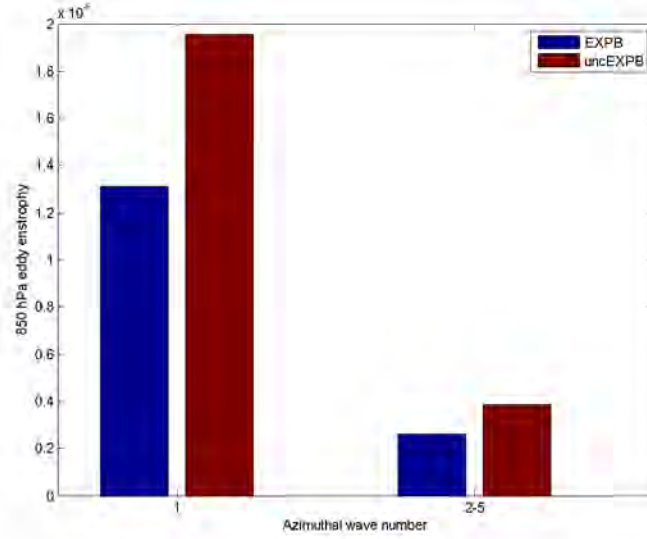
(d)



(Figure 78 continued)

Recall from Chapter V that the TC response in the wake 1-5 experiments was characterized by an increase of normalized 850 hPa eddy enstrophy in azimuthal wavenumber two (WN2) at the radius of maximum wind due to an exchange with the total eddy enstrophy. Similar to those one-way coupled experiments, the slow-moving two-way coupled EXPB has the same behavior compared to uncEXPB (Figure 79a). The EXPB has a few percent larger growth of the TC eddy enstrophy in 850 hPa WN2 compared to uncEXPB. At the 400 hPa level (not shown), the increase of eddy enstrophy shifts to WN3. The two-way coupled EXPB has about 5% more growth in WN3 than in the uncEXPB. Although these differences are small, the agreement of the two-way coupled experiments with the one-way coupled experiments indicates again that there is a dispersion of the vortex Rossby wave energy to higher wave numbers. For both EXPB and uncEXPB, the ratio of eddy enstrophy from WN1 and residual (WN2 and higher wave numbers) at 850 hPa is about 5:1 (Figure 79b), which is higher than for the one-way coupled wake 3 and wake 4 experiments (see Figure 45). It is difficult to determine if this difference is due to the effect of the two-way coupling or because of the differences in cooling magnitudes between the one-way coupled and fully coupled simulations.

(a)



(b)

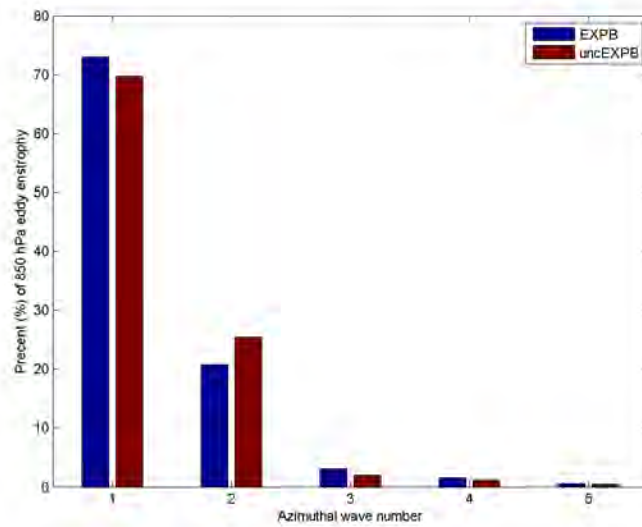


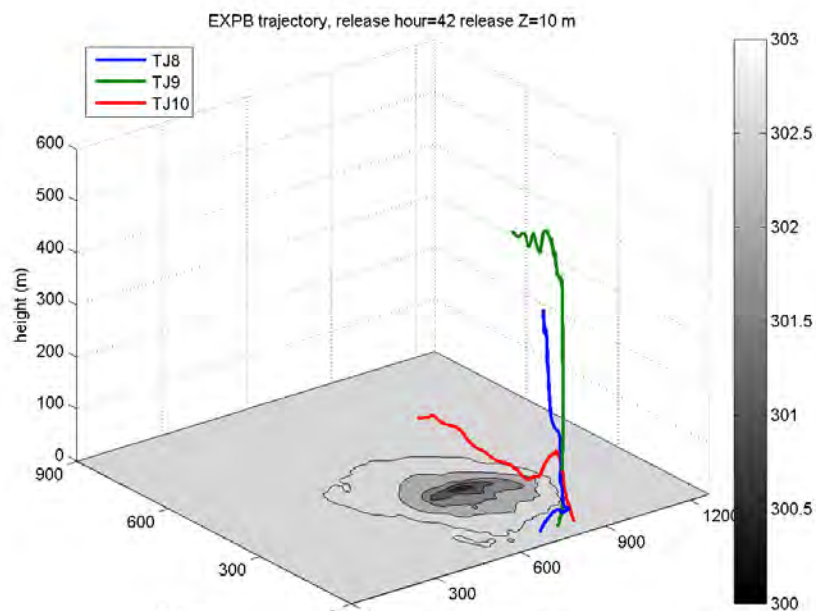
Figure 79. (a) Magnitude of the mean azimuthal 850 hPa eddy enstrophy for EXPB and uncEXPB simulations (see inset for definitions) from WN1 and WN2-5, and (b) Normalized wave eddy enstrophy in wave numbers 1 to 5 with respect to the total enstrophy.

The WN1 and WN2 vorticity and divergence patterns at 850 hPa in the two-way coupled EXPB and uncoupled uncEXPB experiments also had similar structures. A broader outward expansion of the vorticity and divergence bands in the EXPB simulation compared to the uncEXPB is attributed to the wake cooling. Note also that WN1 and WN2 maximum vorticity and divergence in EXPB are lagged by about a quarter of wavelength.

B. TRAJECTORY AND MOMENTUM BUDGET ANALYSES OF EXPB EXPERIMENT

The deflections of air parcel trajectories due to the ocean cold wake in the EXPB experiment are analyzed for ten trajectories released from the 10 m height upwind from the cold wake. These trajectories were placed 60 km apart and released at fixed positions between 42 h – 51 h in 3 hour intervals and tracked for 11 h. Similar to the wake 3 forward trajectories TJ8-TJ10 discussed in Chapter V section C, the three outer radii trajectories from the EXPB experiment experienced an ascent over the cold wake as the simulated trailing cold wake continue to expand (Figure 80). As the simulated EXPB TC moves southwestward with time, the initial release positions of TJ8-TJ10 are farther away from the eye. However, because the ocean cold wake also expands southward, the release locations of TJ8-TJ10 are within the edge of the cold ocean wake by the 48 h release time. Notice that the inflow angle of TJ10 increased with time as TJ10 travels across the model simulated cold wake (Figure 81a). The maximum vertical travel distance of TJ10 decreased with a later release time due to a weaker wind speed as the model simulated TC eye moved farther to the west (Figure 81b). Thus the trajectories of EXPB experiment at the outer radii experienced a similar ascending path and increased turning of the flow inward toward the eye as in the trajectory of TJ10 in the one-way coupled wake 3 experiment.

(a)



(b)

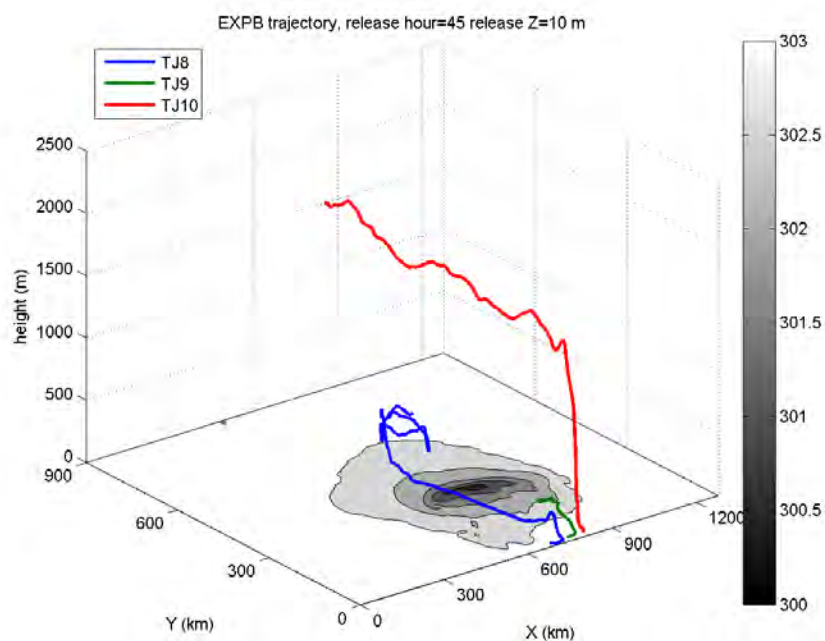
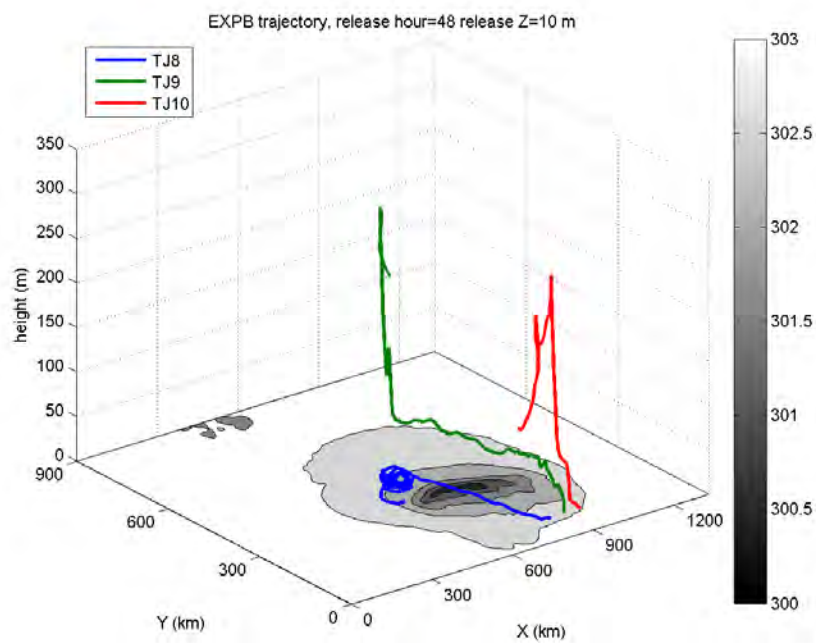
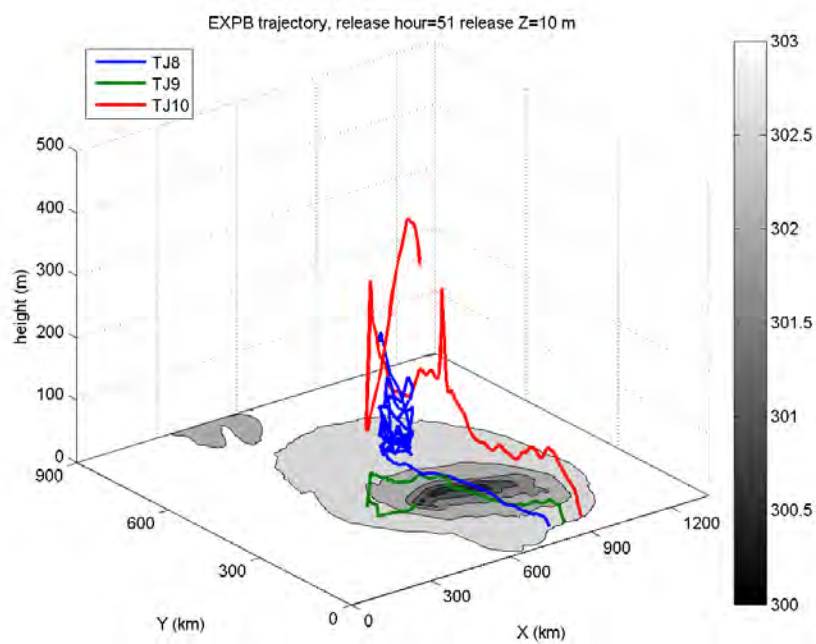


Figure 80. Eleven-hour evolutions of trajectories TJ8-TJ10 (see inset for definitions) released at (a) 42 h, (b) 45 h, (c) 48 h, and (d) 51 h. The shaded area is the SST distribution in the coupled EXPB experiment at the release time with a contour interval of 0.5 °C.

(c)

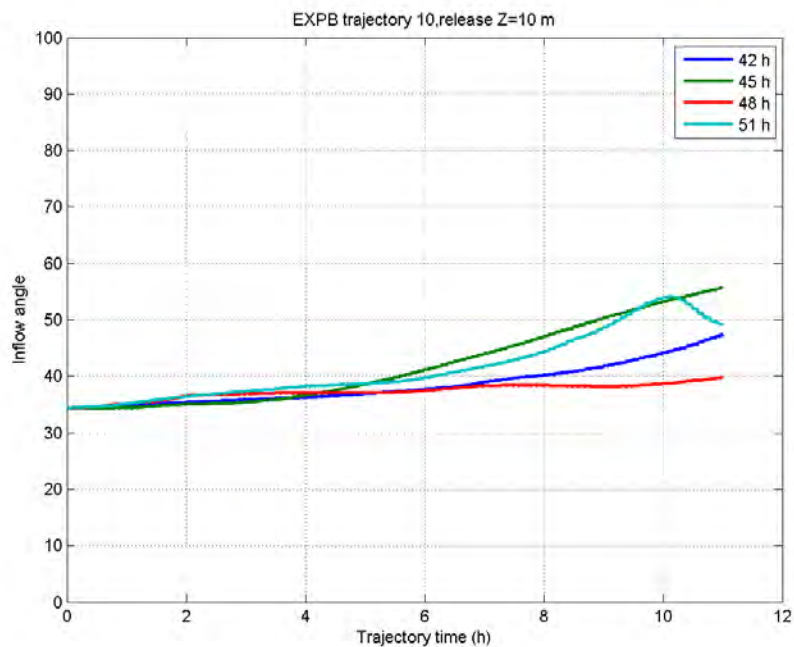


(d)



(Figure 80 continued)

(a)



(b)

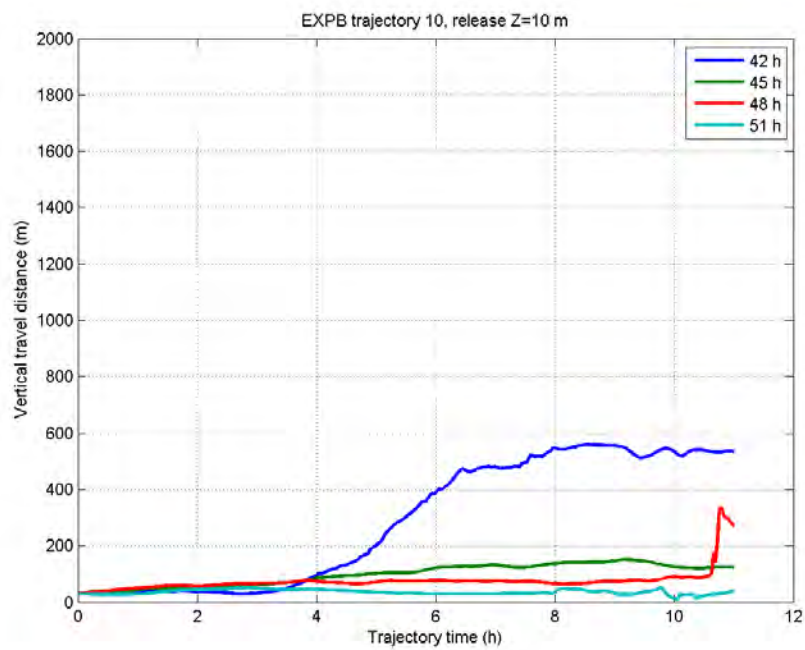


Figure 81. Plot of TJ10 (a) inflow angle ($^{\circ}$) and ascent distance (m) during the same 11 h trajectories as in Figure 80.

The momentum budget along the TJ10 trajectory released at 42 h from the EXPB experiment shows that as TJ10 approached the leading edge of the cold wake the largest contributions to the tangential (Figure 82a) and radial (Figure 82b) wind speed tendency change is from the pressure gradient and horizontal advection terms. The pressure gradient term tends to increase the radial inflow and decrease the tangential wind tendency. When trajectory TJ10 continued across the cold wake, the horizontal advection term increased in magnitude. However, the vertical advection term is nearly zero until TJ10 passed over a region of larger SST cooling over the coldest portion of the wake. At these locations, the sign of the vertical advection term is negative, which has a positive contribution that tends to increase the radial inflow. However, the magnitude of the vertical flux divergence term is much smaller than the pressure gradient and the two advection terms. Thus the impact of the flux divergent term to the increase of the radial inflow is secondary in the two-way coupled EXPB experiment despite a smaller SST gradient at the edge of the cold wake in EXPB experiment compared to the one-way coupled wake 3 experiment. The three largest terms that contribute to the change of tangential and radial winds in the two-way coupled EXB experiment are the pressure gradient, horizontal advection, and vertical advection. The pressure gradient has the largest contribution to the radial wind speed tendency increase. Therefore, the momentum balance in the two-way coupled EXB experiment is consistent with the one-way coupled wake 3 experiment.

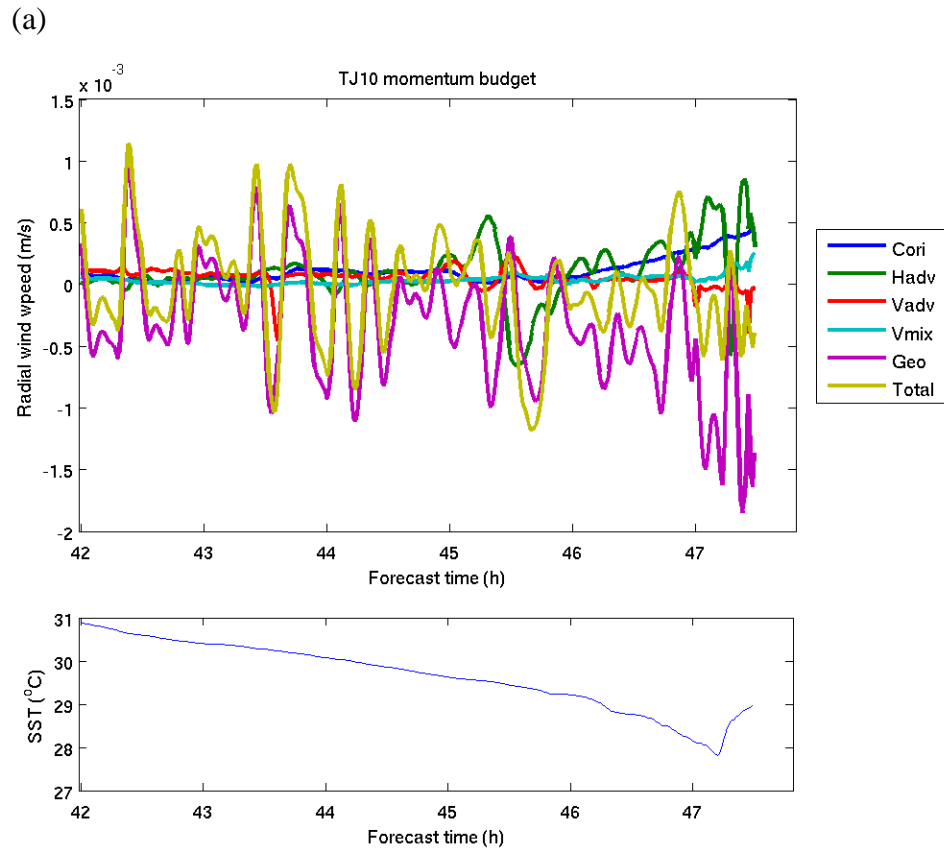
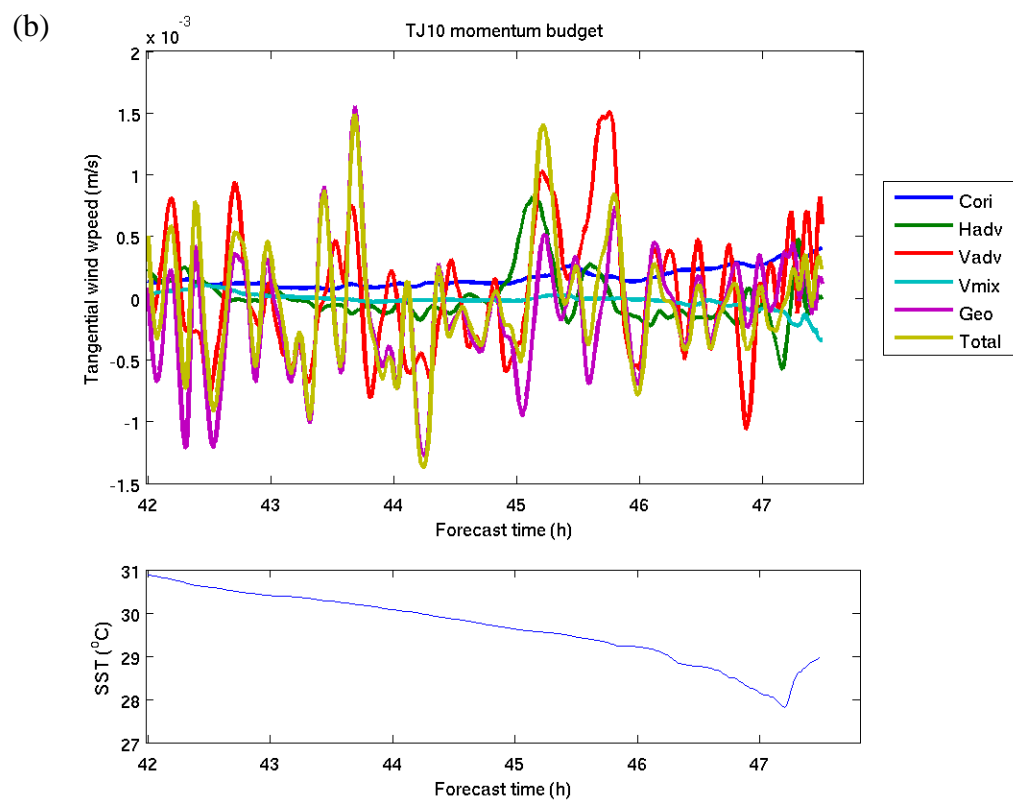


Figure 82. (a) Tangential wind and (b) radial wind budgets from two-way coupled EXPB experiment following trajectory 10 air parcel across the cold wake.



(Figure 82 continued)

C. ANALYSIS ON THE POTENTIAL TEMPERATURE SURFACE

The relationships among the pressure change, increased inflow, vertical motion, and clouds are analyzed on a potential temperature surface. The winds in the EXPB experiment on the 302 °K surface (magenta vectors in Figure 83) have a cyclonic turning near the center of the model-simulated TC. In the outer radii, the cyclonic turning is smaller in regions ahead of the ocean cold wake but the flow directions over the cold wake have a larger inward turning. This larger turning angle of the flow on the 302 °K surface over the wake is consistent with the trajectory analysis. Compared to the uncoupled uncEXPB wind directions on the 302 °K surface at the same time (42 h), the cold wake induced an increased flow toward the model-simulated TC center between grid points 380-400 (black arrows in Figure 83). Farther out where the air parcels are crossing the tailing portion of the wake, there are regions of the upward motion (red contours in Figure 83) where the differences in the wind vectors are also large. Between 37 h – 42 h, the outer convective cells are forming downwind from the cold wake (white contours in Figure 83).

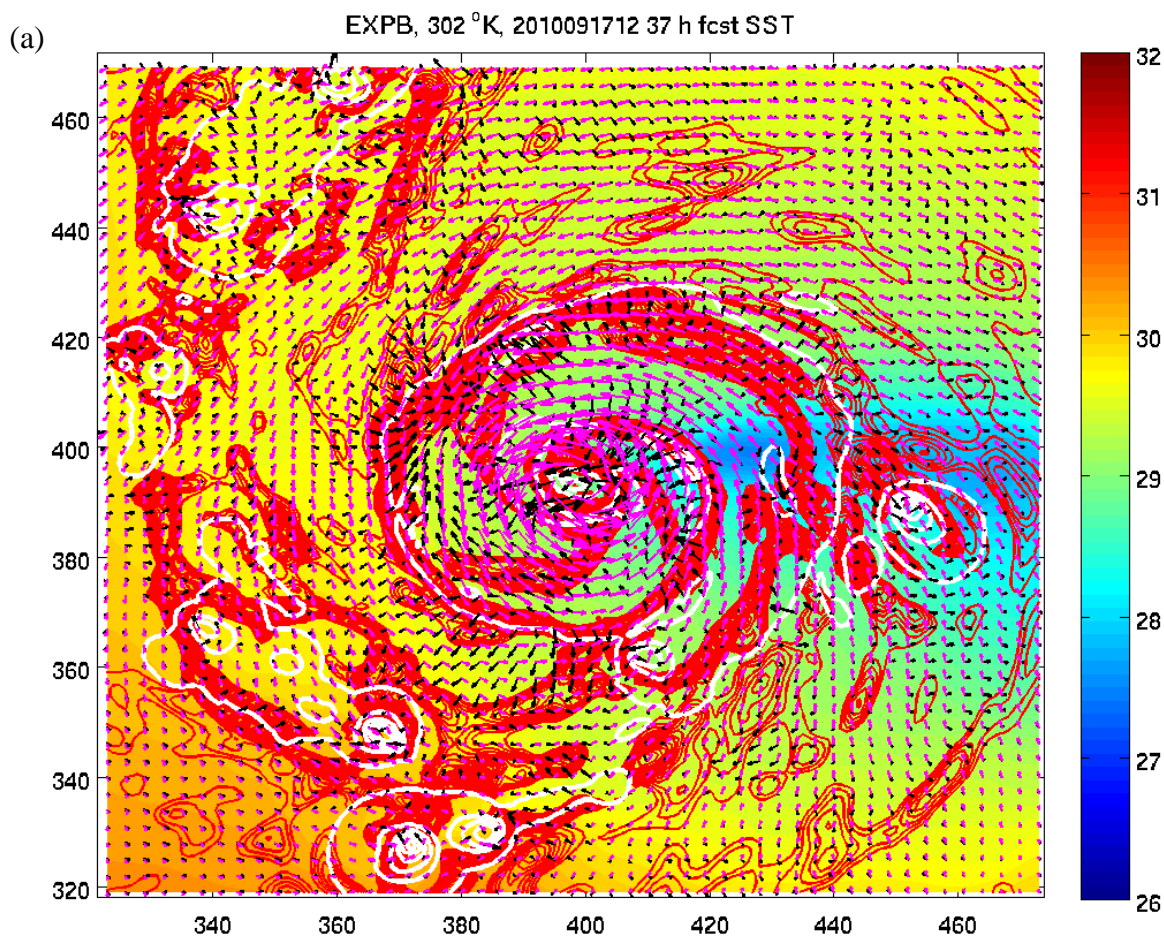
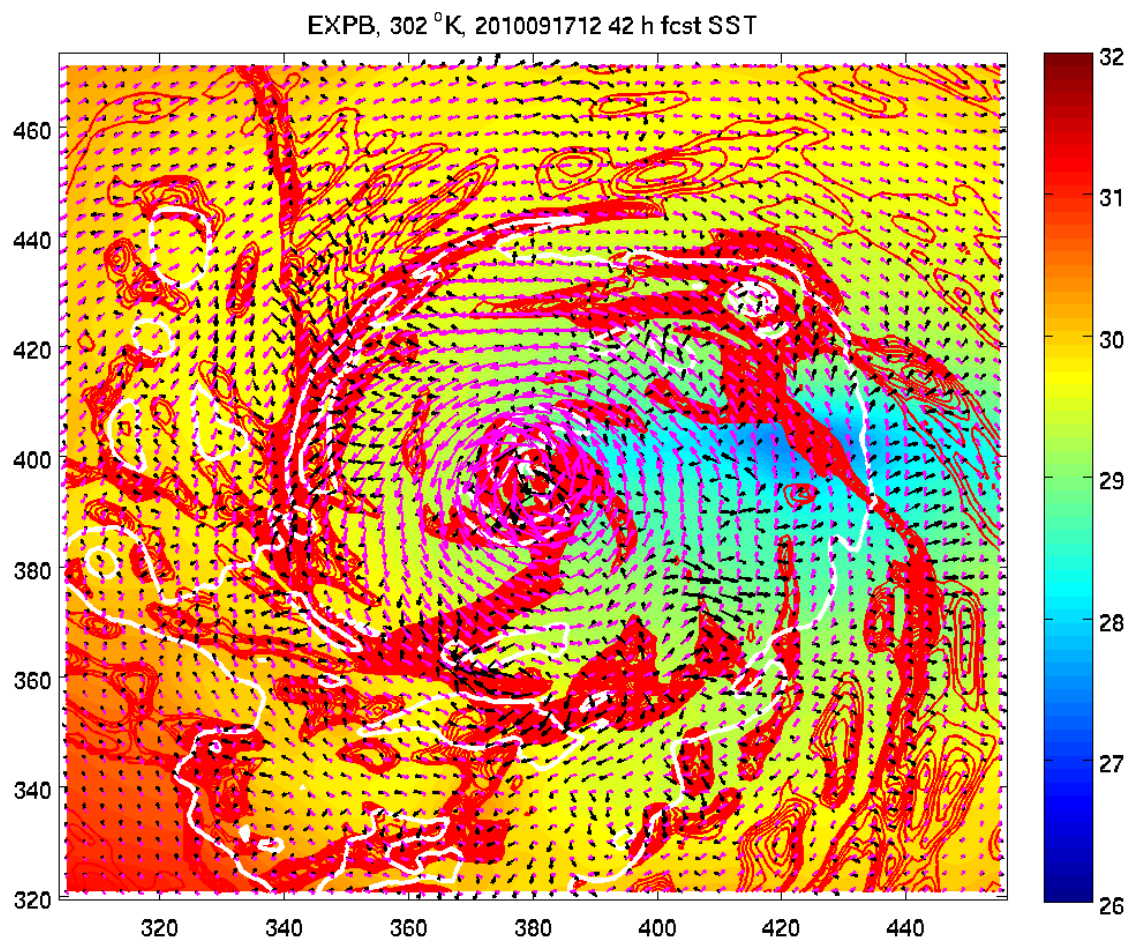


Figure 83. Low-level winds (m s^{-1} , magenta vectors), upward vertical velocity (m s^{-1} , red contours), and the column-integrated mixing ratio (kg kg^{-1} , white contours) at (a) 37 h and (b) 42 h on the 302 °K potential temperature surface from the EXPB experiment. The upward vertical velocity contour interval is 0.2 m s^{-1} from 0.2 to 3 m s^{-1} . The column integrated mixing ratio contour interval is 0.1 kg kg^{-1} from 0.001 to 3 kg kg^{-1} . The black arrows represent the wind differences between the EXPB and uncEXPB experiments.

(b)



(Figure 83 continued)

D. ANALYSIS OF THE SURFACE FLUXES

For the two-way coupled experiments, the relationships between TC intensity and enthalpy fluxes are more complicated than in the one-way coupled experiments. These differences arise from how the two-way coupling interacts with the model nonlinear physics. For example, the sensible heat flux under the eyewall for the coupled experiment EXPB is less than in its control uncEXPB, but the latent heat fluxes can sometimes exceed the latent heat fluxes in the control experiment (Figure 84a). Because these latent heat fluxes are nearly an order of magnitude larger than the sensible heat fluxes, the trends for the enthalpy fluxes are similar to the latent heat fluxes (Figure 84c).

The day-time and night-time EXPA and EXPB normalized maximum tangential winds are compared with the enthalpy fluxes averaged within one and five RMW in Figure 85. The night-time normalized maximum tangential winds versus normalized enthalpy fluxes averaged within five RMW are clustered near a value of 0.4 for EXPA and a value of 0.7 for EXPB (Figure 85b). However, the rest of the plots in Figure 85a, c, and d do not have a similar relationship to the enthalpy fluxes averaged either over one RMW or 5 RMW. Instead, they tend to have increased normalized maximum tangential winds with increased normalized enthalpy fluxes. The lack of a relationship between intensity and enthalpy fluxes averaged over five RMW at night-time is consistent with the one-way coupled wake experiments shown in Figure 70c.

In summary, the aforementioned discussions of the two-way coupled experiments demonstrate that the model-simulated TC response from the two-way coupled experiments is consistent with the one-way coupled wake experiments. Both the two-way coupled and one-way coupled experiments have a similar azimuthal mean and asymmetric structure. Associated with the wake-forced dynamic response in TC circulation and moisture is the structure change of the vortex Rossby waves and inertial gravity waves. As the low-level boundary inflow crosses the ocean cold wake, air parcels can be deflected upward and turned toward the center of TC, which seems to help retain the moisture within and above the boundary layer.

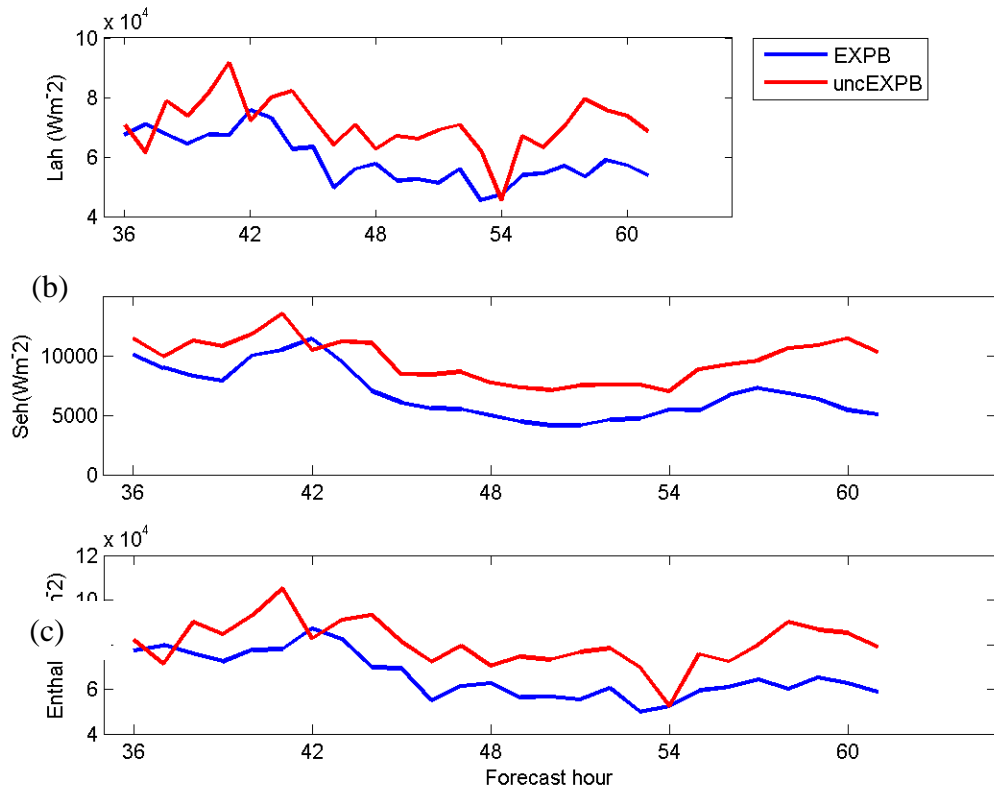


Figure 84. Azimuthal-mean (a) latent heat flux, (b) sensible heat flux, and (c) total enthalpy flux averaged within five RMW for experiment EXPB and uncoupled uncEXPB (see inset). The unit for the fluxes is 10^5 Wm^{-2} for (a) and (c), but 10^4 Wm^{-2} for (b).

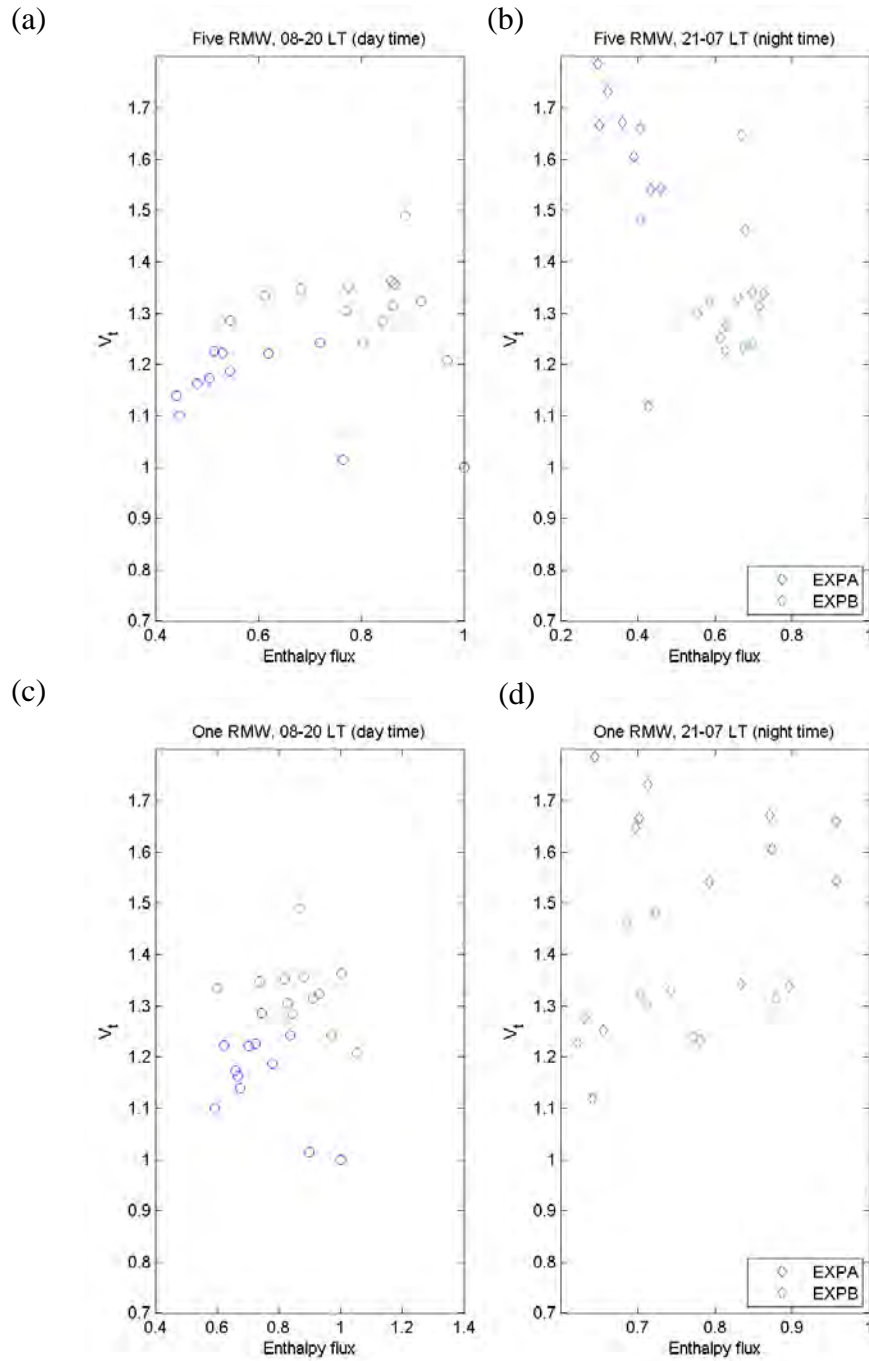


Figure 85. Scatter plots of (a) day-time and (b) night-time normalized maximum tangential wind speeds in the lowest 2 km versus normalized enthalpy flux averaged within 5 RMW for the two-way coupled experiment EXPA and EXPB (see insets). (c) and (d) as in (a) and (b), except for the average within one RMW.

THIS PAGE INTENTIONALLY LEFT BLANK

VII. SUMMARY AND DISCUSSION

One of the difficulties in interpreting the real-data TC-ocean model forecasts is the isolation of processes governing the TC response versus from the air-sea interaction. A novel approach in this dissertation is to combine the air-ocean coupled modeling framework with the COAMPS capability to systematically study the fundamental nature of the TC response to an ocean wake in a simple setup on a f -plane, no vertical shear, and no differential radiation effects in the horizontal. The objective is first to examine the interaction of the TC circulation with various idealized cold wakes in a series of one-way coupled numerical model experiments using the state-of-the art one-way coupled COAMPS-TC. Then two-way air-ocean coupled model simulations that generate somewhat similar cold wakes are analyzed in the same manner as for the one-way coupled model simulations.

Despite a large body of literature that discusses the TC structure and intensity changes owing to air-sea interaction or describes the ocean response to passing TCs, several key questions need to be further studied: What are the key physical processes in the TC response to the ocean cooling during the storm stage? How do the location relative to the TC center and the shape of the ocean cold wake affect the TC intensity change? To address these questions, the responses in model-simulated CAT3-5 TCs are examined in an ocean cold wake parameter space that includes the cold wake magnitude, shape, and location. Key advancements in understanding have been achieved through validation of the following three hypotheses:

- Hypothesis I: The TC intensity is sensitive to the location and magnitude of the wake relative to the track. A cold wake centered underneath the TC core has more important impacts on reducing the intensity than a cold wake located to the right or left of the TC center.
- Hypothesis II: Differential surface enthalpy fluxes over the ocean cold wake introduce an asymmetric structure in the TC circulation. In a certain region of moderate winds outside the radius of maximum wind, the cold wake forces a low-level wake jet that is deflected toward the center of the storm. The strength of the wake jet depends on the magnitude of the wake cooling.

- Hypothesis III: The TC intensity reduction due to the cold wake may arise dynamically from the growth of vortex Rossby and baroclinic waves excited by the cold wake at the expense of the mean vortex as well as by thermodynamic influences resulting from a change in the surface enthalpy fluxes over the colder water.

A. HYPOTHESIS I

Five one-way coupled and two two-way coupled experiments were compared to their control simulations to understand the TC response to the cold wake magnitude and shape. For the one-way coupled wake experiments, the magnitude of these idealized cold wakes is either 2°C or 4°C colder than the surrounding area and is held constant through the model integration. The total areal coverage of each cold wake in these five cases is roughly similar, except the smallest cold wake 2 has half the areal coverage underneath the eyewall, but the cold wake magnitude of 4°C is twice as large as in three of the other wake experiments. The areal coverage of the one-way coupled wake cooling underneath the eyewall varies from a full to partial coverage. In the two-way coupled experiments, the maximum wake cooling anomalies range from ~ 1 to 2 °C.

Analyses of the axisymmetric and asymmetric characteristics of the TC thermodynamic and dynamic response to the wakes were performed using the azimuthal mean of composites with respect to the TC center and an azimuthal wave decomposition of wavenumbers 1 to 5. Both the one-way and two-way coupled experiment reveal that the wakes underneath the eyewall region are more efficient in spinning down the TC than a trailing wake, which is in agreement with the conventional view and validates hypothesis I: “A cold wake centered underneath the TC core has more important impacts on reducing the intensity than a trailing cold wake.”

The primary thermodynamic factor that impacts TC intensity from the atmospheric cooling over the cold wakes is the reduction of the enthalpy flux transport from the ocean. In the one-way coupled experiments within an area of five RMW, the ratio of the enthalpy flux reduction compared to the control experiment is ~44-52% (a range of 40-60%) in the first 12 h of coupling for the 2°C (4°C) cold wakes. The two long trailing wakes and the wake 2 case have the smallest (30-40%) enthalpy flux reduction. However, the reduction of intensity in the two long trailing wakes experiments was

delayed for more than 12 h despite the areal coverage of the cold anomaly being roughly the same as in the wake 1 experiment. A similar delay in the intensity reduction also occurred in the two-way coupled experiments that have a trailing wake.

These results suggest a more complicated TC dynamic response from the cold wake forcing compared to a direct thermodynamic impact, which is contrary to the WHISHI thermodynamic point of view of an immediate response to the SST under the eyewall (Emanuel 1986; Bender and Ginis 2000). That is, the WHISHI argument assumes a direct positive feedback between wind speed and enthalpy flux, which implies the reduction of the wind speed is solely due to the reduction of the enthalpy flux. In all of the wake experiments, the imposition of the cold wake, and thus a reduction in the surface fluxes, did not immediately reduce the surface wind speed. The delayed response in intensity for the trailing wake cases implies a continued transport of moist inflow air into the eyewall updrafts that tends to offset the negative effect of decreasing enthalpy flux from the ocean. The delayed intensity responses may also indicate a dynamic pathway contributes to the time delay in the TC spin-down.

The asymmetric nature of the atmospheric response to the cold wake is studied using wavenumber decomposition. The model simulations indicate a dynamic pathway of the TC spin-down from wake cooling is through the dispersion of the vortex Rossby and inertial gravity (IG) waves. In the one-way coupled wake 5 experiment with the 4°C cold wake, the immediate intensity response is through a severe damping of the wavenumber1 vortex Rossby waves. Because of the weaker radial vorticity gradient inside the radius of maximum angular velocity, suppression of the algebraic instability growth of the azimuthal WN1 perturbation prevents the TC from maintaining the intensity without extraction of mean vortex kinetic energy or by interaction with the asymmetric WN2 and higher wave numbers.

The increased activity of the WN2 and higher waves in the eyewall region in all of the wake experiments indicates the wake cooling induces trapped discrete vortex Rossby wave (DVRWs). Accompanying these trapped DVRWs is an increased radial propagation of divergence in all wake simulations compared to the control. In these simulations, the wake cooling also enhanced the generation and radial propagation of IG

waves. At a certain radial distance from the eyewall at outer radii, the ratio of the peak divergence to the vorticity approaches unity where the DVRW transitions to an IG according to the linear theory of Schechter (2008). Schechter (2008) noted that the emission of IG waves can sometimes create a spontaneous imbalance (SI) that favors the IG radiation pumping by exceeding the threshold for critical layer damping of DVRWs. In such a case, the DVRWs will amplify at the critical layer in which the angular rotation frequency of the cyclone equals the angular phase velocity of the mode to conserve the pseudo-angular momentum. The excitement of DVRWs is required to balance the removal of angular momentum by the IG waves away from the eyewall, and thus leads to the growth of the TC asymmetry.

Similar to the 1 km horizontal resolution one-way coupled trailing wake experiments, the 3 km horizontal resolution two-way coupled experiments that move with a 5 m s^{-1} or 2 m s^{-1} uniform easterly background flow also produce a trailing wake. The faster moving two-way coupled experiment induces $\sim 1^\circ\text{C}$ of cooling, while the slower moving two-way coupled experiment has a cold anomaly of about 2.4°C . The TC response to the wake cooling is not as strong as those in the one-way coupled experiments that have a similar wake cooling magnitude, which may in part be due to a lower horizontal grid resolution used in the two-way coupled simulation to allow for a larger domain. Nevertheless, the two-way coupled experiments in general do agree with the one-way coupled experiments.

An important implication from the validation of hypothesis I, which has not been discussed in the literature before, is these experiments provide some useful information as to where to deploy ocean sensors in order to improve the TC intensity forecast. Based on the aforementioned findings from the numerical wake experiments, the shape of the cold wake in addition to its cooling magnitude is an important characteristic to observe. In addition to the typical alpha flight pattern for sensor deployment, a long flight path parallel to trailing wake plus a lawnmower pattern several times across the trailing wake would improve the initialization of the ocean cold wake and boundary layer structure above the wake for the TC intensity forecast.

These numerical simulations suggest more uniform wake cooling that is confined to the eyewall region induces rapid intensity reductions compared to the wakes that have a more irregular shape, such as a partial eyewall coverage or a long trailing tail. It has been shown previously in the literature, and confirmed in these two-way coupled experiments, that whether the wake has a long trailing part is largely influenced by the TC translation speed. In the real atmosphere, factors that affect the TC translations speed are more complicated than these two-way coupled experiments with no vertical shear.

B. HYPOTHESIS II

Both the one-way and two-way coupled wake experiments show the axisymmetric TC response for cold wakes is to increase the low-level radial inflow. For the cold wake experiment with a long trailing portion, the increased low-level inflow originates farther outward. Both the one-way and two-way coupled experiments that have a trailing wake induced a $0.1\text{--}0.3\text{ g kg}^{-1}$ low- to mid-level moisture increase outside the RMW compared to their control and to those cold wake experiments without a trailing wake. Trajectories and a momentum budget analysis between the RMW and outer radii reveal the air parcels can be deflected toward the eye as these air parcels travel across the cold wake.

Cross-sections of potential temperature and equivalent potential temperature across the wake at the RMW and outer radii indicate that the ACP developed over the ocean cold wake is stronger during night-time. Variations in the ACP strength are modulated by passing cold downdrafts from outward propagating spiral rainbands and the diurnal short wave and long wave radiation influences. Air parcels that are more buoyant than the ACP will be mechanically lifted and ascend over the ACP to follow the constant potential temperature or equivalent potential temperature surfaces to conserve the dry static or moist static energy. A slantwise moist ascent over the ACP may also exist. With sufficient ascent, convective towers may be triggered in the warm, moist airstream.

A momentum budget following the air parcel trajectories in the one-way coupled wake 3 experiment reveals an increased pressure gradient and vertical mixing contribution over the wake. While the horizontal and vertical advection terms are also large over the wake, these terms tend to have opposite signs and the net contribution to

the radial inflow tendency from these advection terms is small. The contribution to the increased inflow from the Coriolis term is also small compared to these other terms. The largest momentum budget terms that contribute to the increase of radial inflow tendency in the two-way coupled EXPB experiment are from the pressure gradient, horizontal advection, and vertical advection. In disagreement with the one-way coupled wake 3 experiment, the flux divergence term is smaller compared to these three other terms in the two-way coupled EXPB experiment due to a smaller SST gradient at the edge of the cold wake.

In the two-way coupled EXB experiment, as the air parcels travel across the cold wake the vertical advection term is nearly zero until the air parcels reached a steeper SST gradient. At outer radii well beyond the RMW, the TC wind above the boundary layer is in gradient wind balance. The radial wind momentum budget analysis indicates that this balance is achieved through the change of pressure gradient, flux divergence, and the horizontal and vertical advection. In the two-way coupled simulation, the pressure gradient term has the largest contribution to the increase of radial wind speed tendency over the wake. As a result, an axisymmetric composite mean $1\text{-}2\text{ m s}^{-1}$ increase of low- to mid- level inflow occurred above the cold wake (referred to as the “wake jet” owing to the location of the increased secondary circulation over the ocean cold wake) that is induced in response to an imbalance among these four terms.

A very recent study by Lee and Chen (2014) also found evidence of an enhanced boundary layer inflow into the inner core over the wake region. However, their tracer and trajectory analysis showed that increased model-simulated inflow is confined to the stable lower boundary layer over the wake. A larger inflow angle is associated with the increased low-level inflow across the model-simulated wake in the TC south-east quadrants. They suggested that the increased low-level inflow offsets the decrease of enthalpy fluxes from the wake cooling. Their results also suggested a region of depressed rain area downstream from the cold wake in their coupled experiment. Air-ocean coupling decreased the coverage of the rainband convection downstream from the wake by 40% - 50% and overall they note a 20% - 25% decrease in coverage of the convection compared to the uncoupled simulation.

The flow response induced by the cold wake examined by Lee and Chen (2014) is similar to the one-way and two-coupled wake experiments discussed here that have a long trailing cold wake. Details of the inflow characteristics in these long-trailing wake experiments differ from those of Lee and Chen (2014) both in terms of the depth of the increased inflow and the suppression of the rainband activity downstream from the wake. Compared to the uncoupled one-way and two-way control experiments, the depth of the increased inflow in the axisymmetric composite from the long trailing wake experiments extends to mid-levels with the largest increase of inflow in the 1 - 2 km layer. Associated with the increased inflow is a slight increase of moisture. The suppression of the simulated rainbands downwind from the wake by Lee and Chen (2014) does not appear to be a ubiquitous feature of all simulations.

The one-way and two-way coupled wake experiments presented in this dissertation show that the wake cooling underneath the eyewall region increases the asymmetric components of the upper-level divergence and alters the position of the centers of maximum low-level convergence which are noted to rotate counterclockwise in the coupled runs. This in turn alters the evolution of the outward propagation of the rainbands. In conjunction with the diurnal cycle from cloud-radiation interaction, the rainbands in the coupled long trailing wake experiments are thus not necessarily any more suppressed than the uncoupled experiments in the region downwind from the wake. Rainbands in the coupled experiments still developed downwind and over the wake region but have a different temporal propagation than the uncoupled control simulations.

The deeper wake jet in both the idealized cold wake experiments and the fully coupled experiments is an indication that there is a dynamic pathway induced by the trailing wake both near and outside the RMW. These results validate the Hypothesis II: “Differential surface enthalpy fluxes over the ocean cold wake introduce an asymmetric structure in the TC circulation. In a certain region of moderate winds outside the radius of maximum winds, the cold wake forces a low-level wake jet that is deflected toward the center of the storm. The strength of the wake jet depends on the magnitude of the wake cooling.”

The model simulations presented here suggest the need for additional observations over the cold wake to further elucidate and validate the structural changes in the hurricane dynamics and behavior described. One suggestion is to include high temporal and spatial resolution dropsondes both along the wake and across the wake. Such additional observations would supplement current observational strategies that have yet to address the implications of the wake-induced changes in the atmospheric circulations and potentially the ocean circulations as well. Current observation platforms may not properly characterize the TC boundary layer inflow changes across its cold wake due to rain contamination in scatterometer winds or lack of temporal and spatial resolution from in-situ dropsonde observations across and along the cold wake. It is often the case that modeling results such as these lead to improved observing strategies that reveal important new aspects of the circulation that can further help isolate the underlying dynamics as well as improve coupled model validation efforts. Future observational studies on the flow response over the cold ocean wake is needed to quantify the changes imposed by the ocean cold wake.

C. HYPOTHESIS III

Results from the validation of the hypotheses I and II indicate that the TC intensity change can occur thermodynamically from the enthalpy flux and diurnal heating cycle, and dynamically by the wake jet and VRWs. For the strongest cold wake 5 experiment, there is an increasing asymmetry in DVRWs and IG wave emission, which suggests that both pathways contribute to the vortex spin-down in the wake 5 experiment. Furthermore, the TC intensities in these one-way coupled wake experiments vary widely even for roughly the same amount of normalized enthalpy flux of 0.5 from the ocean within 5 RMW. The ranges of mean low-level potential vorticity and maximum tangential wind normalized by the 36 h control values are about 0.8-1.7 and 0.5-3. If these normalized intensities are compared with normalized enthalpy fluxes within one RMW, then a trend of increasing enthalpy fluxes to increasing intensity is more evident than when the fluxes averaged over five RMW.

A similar enthalpy flux relationship with the intensity change also occurred in the two-way coupled experiments, which is another indication that intensity reduction is strongly affected by the amount of wake cooling in the eyewall region. As for the diurnal influence on the normalized intensity, the intensity is slightly higher during day-time versus during night-time, which may be due to the interaction of TC with radiation as well as the enthalpy fluxes.

These uncoupled wake 1-wake 5 simulations tend to validate hypothesis III: “The TC intensity reduction due to cold wake may arise dynamically from the growth of vortex Rossby and baroclinic waves excited by the cold wake at the expense of the mean vortex as well as by thermodynamic influences resulting from a change in the surface fluxes over the colder water.” The dispersion of WN2 and higher wavenumbers is smaller in the two-way coupled experiments. However, the increases of WN1 and WN2 divergence in the two-way coupled experiments are consistent with the one-way coupled experiments.

Conceptual Model of Model-Simulated TC interaction with Its Cold Wake

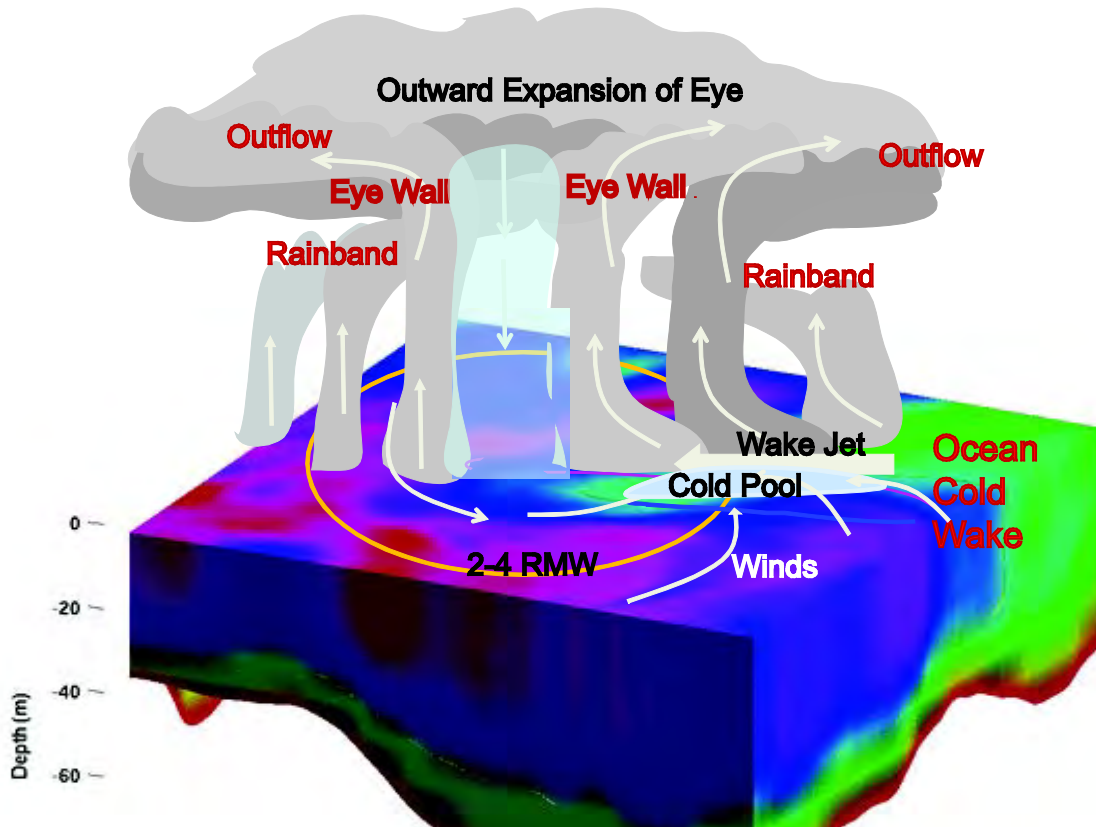


Figure 86. Conceptual model of the physical processes affecting the atmospheric response in a TC moving from right to left while interacting with an ocean cold wake (green color) and the atmospheric cold pool (light blue) above that cold wake. In addition to the thermodynamic processes related to a reduction in the enthalpy flux from the ocean to the TC boundary layer, a dynamic response of a low-level wake jet leads to inflow of moist air that delays or offsets the thermodynamic response to the cold wake. The gray shading depicts the locations of clouds, and the blue column represents the eye of the TC. The white arrows are the winds. The cooling underneath the eyewall forces an outward expansion of the eyewall.

In summary, the main new findings presented in this dissertation can be summarized as illustrated by the conceptual model (Figure 86), which outlines the physical processes governing the model-simulated TC interaction with its cold wake. First, these processes include complex dynamical pathway induced by the ocean cold wake that act in concert with the enthalpy flux to modulate the TC intensity change. Second, the shape and location of the wake are relevant to the TC intensity change because they affect the time delay of the vortex spin-down. A long trailing wake or irregularly shaped wake within the eyewall region forces a dynamic response that tends to offset the negative effect of reduced enthalpy flux and increase the time delay of the vortex spin-down. Third, a $1 - 2 \text{ m s}^{-1}$ increase of low- to mid- level inflow referred to as the “wake jet” occurs above an atmospheric cold pool that is induced by the reverse sensible flux transfer over the trailing cold wake that is augmented by negative long wave fluxes at night-time. As the low-level boundary level boundary inflow crosses the ocean wake, air parcels can be deflected upward and turned toward the center of TC, which helps retain the moisture within and above the boundary layer. Fourth, a strong 4°C cold wake underneath the eyewall significantly damps the vorticity gradient in the eyewall region, which in turns forces the TC to transition from an unstable annulus ring vortex to a stable Rankine-like vortex. The wavenumber 1 VRW is reduced and is replaced by amplifying DVRWs and an increase in spiral rainband activity associated with the IG wave emission.

The significance of this dissertation stems from the discovery that a dynamic pathway that governs the time scale of the TC intensity reduction due to interaction with its cold wake, which has not been previously shown in the literature. This discovery has been made possible from an advancement in the state-of-the-art, high-resolution, coupled atmospheric-ocean model at the Naval Research Laboratory-Monterey. The transition of this advanced model to operations will improve predictions of TCs that continually threaten U. S. Navy ships and Department of Defense bases.

THIS PAGE INTENTIONALLY LEFT BLANK

LIST OF REFERENCES

- Andreas, E. L., P. O. G. Persson, J. E. Hare, J. E., 2008: A bulk turbulent air-sea flux algorithm for high-wind, spray conditions. *J. Phys. Oceanogr.*, **38**(7), 1581-1596.
- _____, L. Mahrt, and D. Vickers, 2012: A new drag relation for aerodynamically rough flow over the ocean. *J. Atmos. Sci.*, **69**, 2520-2537.
- Bao, J.-W., C.W. Fairall, S. A. Michelson, and L. Bianco, 2011: Parameterizations of sea-spray impact on the air-sea momentum and heat fluxes. *Mon. Wea. Rev.*, **139**, 3781-3797.
- Bell M. M., M. T. Montgomery, and K. A. Emanuel, 2012: Air-sea enthalpy and momentum exchange at major hurricane wind speeds observed during CBLAST. *J. Atmos. Sci.*, **69**, 3197-3222.
- Bender, M.A. and I. Ginis, 2000: Real-Case Simulations of Hurricane–Ocean Interaction Using A High-Resolution Coupled Model: Effects on Hurricane Intensity, *Mon. Wea. Rev.*, **128**, 917-946.
- Black, P. G., R. L. Elsberry, L. K. Shay, R. P. Partridge, and J. D. Hawkins, 1988: Atmospheric boundary layer and oceanic mixed layer observations in Hurricane Josephine obtained from air-deployed drifting buoys and research aircraft. *J. of Atmos. and Oceanic Technology*, **5**(6), 683-698.
- _____, E.A. D'Asaro, W.M. Drennan, J.R. French, P.P. Niiler, T.B. Sanford, E.J. Terrill, E. J. Walsh, and J. A. Zhang, 2007: Air-sea exchange in hurricanes: Synthesis of observations from the Coupled Boundary Layer Air-Sea Transfer Experiment. *Bull. Amer. Meteor. Soc.*, **88**, 357-374.
- Bolton, D., 1980: The computation of equivalent potential temperature. *Mon. Wea. Rev.*, **108**, 1046-1053.
- Carr III, L. E., and R. T. Williams, 1989: Barotropic vortex stability to perturbations from axisymmetry. *J. Atmos. Sci.*, **46**(20), 3177-3191.
- Chan, J. C., and J. D. Kepert, 2010: Global perspectives on Tropical cyclones: From science to mitigation, **4**, World Scientific, Eds. 2.
- Chang, S. W., and R. A. Anthes, 1978: Numerical simulations of the ocean's nonlinear, baroclinic response to translating hurricanes. *J. Phys. Oceanogr.*, **8**(3), 468-480.
- _____, and _____, 1979: The mutual response of the tropical cyclone and the ocean. *J. Phys. Oceanogr.*, **9**, 128-135.

- Chen, S., J. Cummings, J. Doyle, R. Hodur, T. Holt, C.-S. Liou, M. Liu, J. Ridout, J. Schmidt, and W. Thompson, A. Mirin, and G. Sugiyama, 2003: COAMPS version 3 model description Naval Research Laboratory Memorandum Report, NRL/PU/7500-03-448, 143 pp.
- _____, T.J. Campbell, H. Jin, S. Gaberšek, R.M. Hodur, and P. J. Martin, 2010: Effect of two-way air-sea coupling in high and low wind speed regimes. *Mon. Wea. Rev.*, **138**, 3579–3602.
- _____, T. J. Campbell, S. Gaberšek, J. Hao, and R. Hodur, 2011: Next generation air-ocean-wave Coupled Ocean/Atmosphere Mesoscale Prediction System (COAMPS). *NRL Review* (available at <http://www.nrl.navy.mil/research/nrl-review/>).
- _____, S. Gaberšek, J. D. Doyle, J. Cook, P. Chu, P. R. A. Allard, E. Rogers, Wittmann, W. Nuss, 2014: Validation Test Report for the Coupled Ocean/Atmosphere Mesoscale Prediction System (COAMPS) Version 5.0: Air/Wave Component Validation. Naval Research Laboratory Memorandum Report, NRL/MR/ 7533-9526, 68 pp.
- Chia-Ying Lee and Shuyi S. Chen, 2012: Symmetric and Asymmetric Structures of Hurricane Boundary Layer in Coupled Atmosphere-Wave-Ocean Models and Observations. *J. Atmos. Sci.*, **69**, 3576-3594.
- _____, and _____, 2014: Stable Boundary Layer and Its Impact on Tropical Cyclone Structure in a Coupled Atmosphere-Ocean Model. *Mon. Wea. Rev.*, **142**, 1927–1944.
- Cione, J. J., and E. W. Uhlhorn, 2003: Sea surface temperature variability in hurricanes: Implications with respect to intensity change. *Mon. Wea. Rev.*, **131**, 1783-1796.
- Craik, A. D. D., 1977: The generation of Langmuir circulations by an instability mechanism. *J. Fluid Mech.*, 81(02), 209-223.
- Craig, P. D., and M. L. Banner, 1994: Modeling wave-enhanced turbulence in the ocean surface layer. *J. Phys. Oceanogr.*, **24**, 2546-2559.
- Cummings, J. A., 2005: Operational multivariate ocean data assimilation. *Quart. J. Royal Met. Soc.*, **131**, 3583-3604.
- Daley, R., and E. Barker, 2001: NAVDAS: Formulation and diagnostics. *Mon. Wea. Rev.*, **129**, 869-883.
- D'Asaro, E. A., T. B. Sanford, P. P. Niiler, and E. J. Terrill, 2007: Cold wake of Hurricane Frances. *Geophys. Res. Lett.*, **34**, L15609, doi:10.1029/2007GL030160.

- Davies, H., 1976: A lateral boundary formulation for multi-level prediction models. *Quart. J. Roy. Meteor. Soc.*, **102**, 405-418.
- Dickey, T., D. Frye, J. McNeil, D. Manov, N. Nelson, D. Sigurdson, and R. Johnson, 1998: Upper-ocean temperature response to Hurricane Felix as measured by the Bermuda testbed mooring. *Mon. Wea. Rev.*, **126**, 1195-1201.
- Drennan, W. M., J. A. Zhang, J. R. French, C. McCormick, and P. G. Black, 2007: Turbulent fluxes in the hurricane boundary layer. Part II: Latent heat flux. *J. Atmos. Sci.*, **64**, 1103-1115.
- Doyle, J. D., 2002: Coupled atmosphere–ocean wave simulations under high wind conditions. *Mon. Wea. Rev.*, **130**, 3097-3099.
- _____, Y. Jin, R. Hodur, S. Chen, H. Jin, J. Moskaitis, J., Reinecke, J. Schmidt, and S. Wang, 2012: Real time tropical cyclone prediction using COAMPS-TC. *Advances in Geosciences*, **28**, 15-28.
- Donelan, M.A., B.K. Haus, N. Reul, W.J. Plant, M. Stiassnie, H.C. Graber, O.B. Brown and E.S. Saltzman, 2004: On the limiting aerodynamic roughness of the ocean in very strong winds. *Geophys. Res. Lett.*, **31**, 18.
- _____, M. Curcic, S. S. Chen, and A. K. Magnusson, 2012: Modeling waves and wind stress. *J. Geophys. Res.*, **117**, doi:10.1029/2011JC007787.
- Dunion, J. P., and C.S. Marron, 2008: A reexamination of the Jordan mean tropical sounding based on awareness of the Saharan Air Layer: Results from 2002. *J. Climate*, **21**, 5242-5253.
- _____, 2011: Rewriting the climatology of the tropical North Atlantic and Caribbean Sea atmosphere. *J. Climate*, **24**, 893-908.
- _____, C. D. Thorncroft, and C. S. Velden, 2014: The tropical cyclone diurnal cycle of mature hurricanes. *Mon. Wea. Rev.* (in press).
- Eliassen, A., 1952: Simplified dynamic models of the atmosphere, designed for the purpose of numerical weather prediction. *Tellus*, **4**, 145-156.
- Emanuel, K.A., 1986: An air-sea interaction theory for tropical cyclones. Part I: Steady-state maintenance. *J. Atmos. Sci.*, **43**, 585-605.
- Fairall, C., E. Bradley, J. Hare, A. Grachev, and J. Edson, 2003: Bulk Parameterization of Air-Sea Fluxes: Updates and Verification for the COARE Algorithm, *J. Climate*, **16**, 571–591.

- _____, M. L. Banner, W. L. Pierson, W. Asher, and R. P. Morison, 2009: Investigation of the physical scaling of sea spray spume droplet production. *J. Geophys. Res.*, **114**, C10001, doi:10.1029/2008JC004918.
- Fan, Y., I. Ginis, and T. Hara, 2009a: The effect of wind-wave-current interaction on air-sea momentum fluxes and ocean response in tropical cyclones. *J. Phys. Oceanogr.* **39**, 1019-1034.
- _____, I. Ginis, T. Hara, C. W. Wright, and E. J. Walsh, 2009b: Numerical simulations and observations of surface wave fields under an extreme tropical cyclone. *J. Phys. Oceanogr.* **39**, 2097–2116.
- _____, I. Ginis, and T. Hara, 2010: Momentum flux budget across the air-sea interface under uniform and tropical cyclone winds. *J. Phys. Oceanogr.*, **40**(10), 2221-2242.
- Flatau, M., W. H. Schubert, and D. E. Stevens, 1994: The role of baroclinic processes in tropical cyclone motion: The influence of vertical tilt. *J. Atmos. Sci.*, **51**, 2589-2601.
- Frank, W. M., and E. A. Ritchie, 1999: Effects of environmental flow upon tropical cyclone structure. *Mon. Wea. Rev.*, **127**, 2044–2061.
- _____, and _____, 2001: Effects of vertical wind shear on the intensity and structure of numerically simulated hurricanes. *Mon. Wea. Rev.*, **129**, 2249–2269.
- Hendricks, E. A., W. H. Schubert, R. K. Taft, H. Wang, and J. P. Kossin, 2009: Life cycles of hurricane-like vorticity rings. *J. Atmos. Sci.*, **66**(3), 705-722.
- Gosnell, R., C. W. Fairall, and P. J. Webster, 1995: The sensible heat of rainfall in the tropical ocean. *J. Geophys. Res.: Oceans* (1978–2012), **100**(C9), 18437-18442.
- Gray W. M., E. Ruprecht, and R. Phelps, 1975: Relative humidity in tropical weather systems. *Mon. Wea. Rev.*, **103**, 685-690.
- Gryanik, V. M., and M. V. Tevs, 1989: Dynamics of singular geostrophical vortices in a N-level model of the atmosphere (ocean). *Izvestiya atmospheric and oceanic physics*, **25**, 179-188.
- Hack, J. J., and W. H. Schubert, 1986: Nonlinear response of atmospheric vortices to heating by organized cumulus convection. *J. Atmos. Sci.*, **43**, 1559-1573.
- Haus, B. K., D. Jeong, M. A. Donelan, J. A. Zhang, and I. Savelyev, 2010: Relative rates of sea-air heat transfer and frictional drag in very high winds. *Geophys. Res. Lett.*, **37**.
- Hendricks, E. A., W. H. Schubert, R. K. Taft, H. Wang, and J. P. Kossin, 2009: Life cycles of hurricane-like vorticity rings. *J. Atmos. Sci.*, **66**, 705-722.

- Hodur, R.H., 1997: The Naval Research Laboratory's Coupled Oceanic/Atmospheric Mesoscale Prediction System (COAMPS). *Mon. Wea. Rev.*, **125**, 1414-1430.
- Holland, G. , 2008:. A revised hurricane pressure-wind model. *Mon. Wea. Rev.*, **136**(9), 3432-3445.
- Hong, X., S. W. Chang, S. Raman, L. K. Shay, and R. Hodur, 2000: The interaction between Hurricane Opal (1995) and a warm core ring in the Gulf of Mexico. *Mon. Wea. Rev.*, **128**, 1347-1365.
- Jacob, S. D., L. K. Shay, A. J. Mariano, and P. G. Black, 2000: The 3D oceanic mixed layer response to Hurricane Gilbert. *J. Phys. Oceanogr.*, **30**(6), 1407-1429.
- , and Shay, L. K., 2003: The role of oceanic mesoscale features on the tropical cyclone-induced mixed layer response: A case study. *J. Phys. Oceanogr.*, **33**(4), 649-676.
- , and C. J. Koblinsky, 2007: Effects of precipitation on the upper-ocean response to a hurricane. *Mon. Wea. Rev.*, **135**, 2207-2225.
- Jaimes, B., and L. K. Shay, 2010: Near-inertial wave wake of Hurricanes Katrina and Rita over mesoscale oceanic eddies. *J. Phys. Oceanogr.*, **40**, 1320-1337.
- Jarosz, E., D. A. Mitchell, D. W. Wang, and W. J. Teague, 2007: Bottom-up determination of air-sea momentum exchange under a major tropical cyclone. *Science*, **315**, 1707-1709.
- Jeong D., B. K. Haus, and M. A. Donelan, 2012: Enthalpy transfer across the air–water interface in high winds including spray. *J. Atmos. Sci.*, **69**, 2733-2748.
- Jin, Y., W. Thompson, S. Wang, and C. Liou, 2007: A numerical study of the effect of dissipative heating on tropical cyclone intensity. *Weather and Forecasting*, **22**, 950-965.
- Jones, S. C., 1995: The evolution of vortices in vertical shear: Initially barotropic vortices. *Quart. J. Roy. Meteor. Soc.*, **121**, 821–851.
- , 2000a: The evolution of vortices in vertical shear. II: Large scale asymmetries. *Quart. J. Roy. Meteor. Soc.*, **126**, 3137–3159.
- , 2000b: The evolution of vortices in vertical shear. III: Baroclinic vortices. *Quart. J. Roy. Meteor. Soc.*, **126**, 3161–3185.
- Jordan, C.L., 1958: Mean soundings for the West Indies area. *J. Meteor.*, **15**, 91-97.
- Kain, J.S., and J. M. Fritsch, 1990: A one-dimensional entraining/detraining plume model and its application in convective parameterization. *J. Atmos. Sci.*, **47**, 2784-2802.

- Kain, J.S., 2004: The Kain–Fritsch convective parameterization: An update. *J. App. Met.*, **43**, 170-181.
- Kantha, L.H., and C. A. Clayson, 2004: On the effect of surface gravity waves on mixing in the oceanic mixed layer. *Ocean Model*, **6**, 101-124.
- Klemp, J. B., and R. B. Wilhelmson, 1978: The simulation of three-dimensional convective storm dynamics. *J. Atmos. Sci.*, **35**, 1070-1096.
- Knaff, J. A., and R. M. Zehr, 2007: Reexamination of tropical cyclone wind-pressure relationships. *Weather and Forecasting*, **22**, 71-88.
- Kossin, J. P., and W. H. Schubert, 2001: Mesovortices, polygonal flow patterns, and rapid pressure falls in hurricane-like vortices. *J. Atmos. Sci.*, **58**, 2196-2209.
- Kossin, J. P., and W. H. Schubert, 2004: Mesovortices in Hurricane Isabel. *Bull. Amer. Meteor. Soc.*, **85**, 151-153.
- Langmuir, I., 1938: Surface motion of water induced by wind. *Science*, **87**(2250), 119-123.
- Large, W. G., and S. Pond, 1981: Open ocean momentum flux measurements in moderate to strong winds. *J. Phys. Oceanogr.*, **11**, 324–336.
- Lee, C.-Y., and S. S. Chen, 2012: Symmetric and asymmetric structures of hurricane boundary layer in coupled atmosphere-wave-ocean models and observations. *J. Atmos. Sci.*, **70**, 3576-3594.
- _____, and S. S. Chen, 2014: Stable Boundary Layer and Its Impact on Tropical Cyclone Structure in a Coupled Atmosphere–Ocean. *Mon. Wea. Rev.*, **142**(5), 1927-1944
- Leibovich, S., 1983: The form and dynamics of Langmuir circulations. *Annual Review of Fluid Mechanics*, **15**, 391-427.
- Leibovich, S., and D. Ulrich, 1972: A note on the growth of small-scale Langmuir circulations. *J. Geophys. Res.*, **77**, 1683-1688.
- Lin, I. I., C. C. Wu, I.-F. Pun, and D.-S. Ko, 2008: Upper-ocean thermal structure and the western North Pacific category 5 typhoons. Part I: Ocean features and the category 5 typhoons' intensification. *Mon. Wea. Rev.* **136**, 3288-3306.
- _____, I.F. Pun, and C. C. Wu, 2009: Upper-ocean thermal structure and the western North Pacific category 5 typhoons. Part II: Dependence on translation speed. *Mon. Wea. Rev.*, **137**, 3744-3757.

- Liou, C.-S., and K. D. Sashegyi, 2011: On the initialization of tropical cyclones with a three-dimensional variational analysis. *Natural Hazards*. DOI: 10.1007/s11069-011-9838-0.
- Liu, B., H. Liu, L. Xie, C. Guan, and D. Zhao, 2011: A coupled atmosphere-wave-ocean modeling system: Simulation of the intensity of an idealized tropical cyclone. *Mon. Wea. Rev.*, **139**(1), 132-152.
- Liu, M., J. E. Nachamkin, and D. L. Westphal, 2009: On the improvement of COAMPS weather forecasts using an advanced radiative transfer model. *Wea. and Forecasting*, **24**, 286-306.
- Longuet-Higgins, M. S., and R. W. Stewart, 1964: Radiation stresses in water waves; A physical discussion, with applications. In *Deep Sea Research and Oceanographic Abstracts*, Elsevier Publishing, **11**, 529-562 pp.
- Lorsolo, S., J. A. Zhang, F. Marks Jr., and J. Gamache, 2010: Estimation and mapping of hurricane turbulent energy using airborne Doppler measurements. *Mon. Wea. Rev.*, **138**, 3656-3670.
- Lynch, P., and Huang, X. Y., 1992: Initialization of the HIRLAM model using a digital filter. *Mon. Wea. Rev.*, **120**, 1019-1034.
- Martin, P.J., 2000: Description of the Navy coastal ocean model version 1.0, Naval Research Laboratory Memorandum Report, NRL/FR/7322-00-9962.
- Mahrt L., D. Vickers, E. L. Andreas, and D. Khelif, 2012: Sensible heat flux in near-neutral conditions over the sea. *J. Phys. Oceanogr.*, **42**, 1134-1142.
- Mellor, G. L., and T. Yamada, 1974: A hierarchy of turbulence closure models for planetary boundary layers. *J. Atmos. Sci.*, **31**, 1791-1806.
- Melville, W. K., F. Veron, and C. J. White, 2002: The velocity field under breaking waves: Coherent structures and turbulence. *J. Fluid Mech.*, **454**, 203-233.
- Montgomery, M. T., and R. J. Kallenbach, R. J., 1997: A theory for vortex rossby-waves and its application to spiral bands and intensity changes in hurricanes. *Quart. J. Roy. Meteor. Soc.*, 123(538), 435-465.
- Moon, I.-J., T. Hara, and I. Ginis, 2004a: Effect of surface waves on air-sea momentum exchange. Part I: Effect of mature and growing seas. *J. Atmos. Sci.*, **61**, 2321–2333.
- _____, I. Ginis, and T. Hara, 2004b: Effect of surface waves on air-sea momentum exchange. Part II: Behavior of drag coefficient under tropical cyclones. *J. Atmos. Sci.*, **61**, 2334–2348.

- _____, I. Ginis, and T. Hara, 2004c: Effect of surface waves on Charnock coefficient under tropical cyclones. *Geophys. Res. Lett.*, **31**(20).
- _____, I. Ginis, T. Hara, and B. Thomas, 2007: A physics-based parameterization of air–sea momentum flux at high wind speeds and its impact on hurricane intensity predictions. *Mon. Wea. Rev.*, **135**, 2869–2878.
- Mrvaljevic, R. K., P. G. Black, L. R. Centurioni, Y.-T. Chang, E. A. D'Asaro, S. R. Jayne, and C. M. Lee, 2013: Observations of the cold wake of Typhoon Fanapi (2010). *Geophys. Res. Lett.*, **40**, 316–321.
- Nolan, D. S., and M. T. Montgomery, 2000: The algebraic growth of wavenumber one disturbances in hurricane-like vortices. *J. Atmos. Sci.*, **57**, 3514–3538.
- Nolan, D. S., M. T. Montgomery, and L. D. Grasso, 2001: The wavenumber-one instability and trochoidal motion of hurricane-like vortices. *J. Atmos. Sci.*, **58**, 3243–3270.
- O'Neill, L. W., D. B. Chelton, S. K. Esbensen, and F. J. Wentz, 2010a: The effects of SST-induced surface wind speed and direction gradients on midlatitude surface vorticity and divergence. *J. Climate*, **23**, 255–281.
- _____, S. K. Esbensen, N. Thum, R. M. Samelson, and D. B. Chelton, 2010b: Dynamical analysis of the boundary layer and surface wind responses to mesoscale SST perturbations. *J. Climate*, **23**, 559–581.
- _____, 2012a: Wind speed and stability effects on the coupling between surface wind stress and SST observed from buoys and satellite. *J. Climate*, **25**, 1544–1569.
- _____, D. B. Chelton, and S. K. Esbensen, 2012b: Covariability of surface wind and stress responses to sea-surface temperature fronts. *J. Climate*, **25**, 5916–5942.
- Prasad, T. G., and Hogan, P. J., 2007: Upper-ocean response to Hurricane Ivan in a 1/25 nested Gulf of Mexico HYCOM. *Journal of Geophysical Research: Oceans* (1978–2012), **112**, C4.
- Powell, M. D., P. J. Vickery, and T. A. Reinhold, 2003: Reduced drag coefficient for high wind speeds in tropical cyclones. *Nature*, **422**, 279–283.
- Price, J.F., 1981: Upper ocean response to a hurricane. *J. Phys. Oceanogr.*, **11**, 153–175.
- Robert, A. J., 1966: The investigation of a low order spectral form of the primitive meteorological equations. *J. Meteor. Soc. Japan*, **44**, 237–245.
- Rogers, R., S. Lorsolo, P. Reasor, J. Gamache, and F. Marks, 2012: Multiscale analysis of tropical cyclone kinematic structure from airborne Doppler radar composites. *Mon. Wea. Rev.*, **140**(1), 77–99.

- Sanford, T. B., J. F. Price, and J. B. Girton, 2011: Upper-ocean response to Hurricane Frances (2004) observed by profiling EM-APEX floats. *J. Phys. Oceanogr.* **41**, 1041-1056.
- Schade, L. R., and K. A. Emanuel, 1999: The ocean's effect on the intensity of tropical cyclones: Results from a simple coupled atmosphere–ocean model. *J. Atmos. Sci.*, **56**, 642-651.
- Schechter, D. A., 2008: The spontaneous imbalance of an atmospheric vortex at high Rossby number. *J. Atmos. Sci.*, **65**, 2498-2521.
- Shay, L. K., P. G. Black, A. J. Mariano, J. D. Hawkins, and R. L. Elsberry, 1992: Upper ocean response to Hurricane Gilbert. *J. Geophys. Res.: Oceans* (1978–2012), **97**(C12), 20227-20248.
- Smith, J. A., 1992: Observed growth of Langmuir circulation. *J. Geophys. Res.: Oceans* (1978–2012), **97**, 5651-5664.
- Smith, R. A., and M. N. Rosenbluth, 1990: Algebraic instability of hollow electron columns and cylindrical vortices. *Physical Review Letters*, **64**, 649.
- Smith, S.R., J. A. Cummings, P. Spence, S. N. Carroll, C. Rowley, O. M. Smedstad, P. Chu, B. Lunde, J. Shriver, and R. Helber, 2011: Validation test report for the Navy Coupled Ocean Data Assimilation 3D Variational Analysis (NCODA-VAR) system, Version 3.43. NRL Memorandum Report NRL/MR/7320-11-9363.
- Smith, T.A., S. Chen, T. Campbell, E. Rogers, S. Gabersek, D. Wang, S. Carroll, and R. Allard, 2012: Ocean-wave coupled modeling in COAMPS-TC: A study of Hurricane Ivan (2004). *Ocean Dynamics*, **69**, 181-194.
- Spall, M.A., 2007: Midlatitude wind stress-sea surface temperature coupling in the vicinity of oceanic fronts. *J. Climate*, **20**, 3785-3801.
- Sullivan, P. P., L. Romero, J. C. McWilliams, and W. K. Melville, 2012: Transient evolution of Langmuir turbulence in ocean boundary layers driven by hurricane winds and waves. *J. Phys. Oceanogr.*, **42**(11), 1959-1980.
- Vincent, E. M., M. Lengaigne, G. Madec, J. Vialard, G. Samson, N. C. Jourdain, C. E. Menkes, S. Jullien, 2012: Processes setting the characteristics of sea surface cooling induced by tropical cyclones. *J. Phys. Oceanogr.: Oceans* (1978–2012), **117**(C2).
- Wang, Y., 2002a: Vortex Rossby waves in a numerically simulated tropical cyclone. Part I: Overall structure, potential vorticity, and kinetic energy budgets. *J. Atmos. Sci.*, **59**, 1213-1238.

- _____, 2002b: Vortex Rossby waves in a numerically simulated tropical cyclone. Part II: The role in tropical cyclone structure and intensity changes. *J. Atmos. Sci.*, **59**, 1239-1262.
- Wu, C. C., C. Y. Lee, and I. I. Lin, 2007: The effect of the ocean eddy on tropical cyclone intensity. *J. Atmos. Sci.*, **64**, 3562-3578.
- Zhang, J.A., W. M. Drennan, P. G. Black, and J. R. French, 2009: Turbulence structure of the hurricane boundary layer between the outer rainbands. *J. Atmos. Sci.*, **66**, 2455-2467.
- Zhong, W., D. L. Zhang, and H. C. Lu, 2009: A theory for mixed vortex Rossby-gravity waves in tropical cyclones. *J. Atmos. Sci.*, **66**(11), 3366-3381.
- Zhu, H., U. Wolfgang, and S. K. Roger, 2004: Ocean effects on tropical cyclone intensification and inner-core asymmetries. *J. Atmos. Sci.* **61**, 1245-1258.

INITIAL DISTRIBUTION LIST

1. Defense Technical Information Center
Ft. Belvoir, Virginia
2. Dudley Knox Library
Naval Postgraduate School
Monterey, California